UNIVERSITY OF SOUTHAMPTON

MICRO-IMPEDANCE CYTOMETRY

by

Catia Bernabini

A thesis submitted in partial fulfillment for the
degree of Doctor of Philosophy

in the
Faculty of Engineering, Science and Mathematics
School of Electronics and Computer Science

December 2010

UNIVERSITY OF Southampton

UNIVERSITY OF SOUTHAMPTON

ABSTRACT

FACULTY OF ENGINEERING, SCIENCE AND MATHEMATICS
SCHOOL OF ELECTRONICS AND COMPUTER SCIENCE

Doctor of Philosophy

MICRO-IMPEDANCE CYTOMETRY

by Catia Bernabini

Electrical impedance spectroscopy is a non-invasive and label free technique that allows for rapid counting and characterisation of particles in suspension based on their response to applied AC potentials. In recent years, lab-on-a-chip technologies have been developed to enable single-cell impedance detection and a wide range of impedance-based microfluidic devices have been reported. Despite the number of contributions and the achievements of this field, micro-impedance cytometry still suffers from a lack of sensitivity and specificity compared to traditional flow cytometry, which limits the potential commercialization of microfluidic impedance devices. While impedance measurements of beads and cells are well established, discrimination between particles that are very similar in size or detection of small particles (around 1 μm in diameter) such as bacteria, still represents a difficult task.

A number of issues limit the sensitivity and specificity of these microfluidic systems. Primarily, the sensitivity is governed by the dimension of the sample analysis volume. A small volume gives a high sensitivity, but this can lead to practical problems, including fabrication and clogging of the device. In addition, the spatial location of each particle needs to be controlled accurately within the field. Therefore, an efficient and accurate method for focussing the particles in the centre of the electric field is important. In this thesis, a micro-impedance cytometer for the detection of small particles and bacteria and for the discrimination of particles that are very similar in size is presented. The device consists of a microfluidic channel where two pairs of microfabricated electrodes are provided to perform differential measurements of single particles in suspension at high speed. Different electrode configurations and different techniques for focussing the sample within the detection region of the device are investigated in order to improve the sensitivity of the system without reducing the dimensions of the microfluidic channel.

Detection at a volume ratio of particle to an estimated sensing volume of 0.007% and discrimination of 1 μm and 2 μm diameter polystyrene beads and E. coli are demonstrated. The micro-impedance cytometer is also proven to be a reliable and effective system to investigate and determine the unknown dielectric properties of particles in suspension, such as polyelectrolyte microcapsules.

Declaration of Authorship

I, Catia Bernabini, declare that this thesis entitled:

MICRO-IMPEDANCE CYTOMETRY

and the work presented in it are my own. I confirm that:

- This work was done wholly or mainly while in candidature for a research degree at this University
- Where any part of this thesis has previously been submitted for a degree or any other qualification at this University or any other institution, this has been clearly stated
- Where I have consulted the published work of others, this is always clearly attributed
- Where I have quoted from the work of others, the source is always given. With the exception of such quotations, this thesis is entirely my own work
- I have acknowledged all main sources of help
- Where the thesis is based on work done by myself jointly with others, I have made clear exactly what was done by others and what I have contributed myself
- Parts of this work have been published as:

    1. **Micro-impedance cytometry for detection and analysis of micron-sized particles and bacteria.**
    Catia Bernabini, David Holmes and Hywel Morgan., *Lab on a Chip* **11**, 407, (2011).
    2. **Single-Colloidal Particle Impedance Spectroscopy: Complete Equivalent Circuit Analysis of Polyelectrolyte Microcapsules.**
    Tao Sun, Catia Bernabini and Hywel Morgan., *Langmuir*, **26**, 3821, (2010).

3. **Micro-impedance spectroscopy for detection and discrimination of bacteria and microparticles.**
   Bernabini, C., Holmes, D. and Morgan, H., in *Proc Micro Total Analysis Systems*, Jeju, Korea, 2009.

4. **On-Chip Impedance spectroscopy of pH-responsive Polyelectrolyte Microcapsules.**
   Bernabini, C., Holmes, D., Bedard, M., Sukhorukov, G. B. and Morgan, H., in *Proc Micro Total Analysis Systems*, San Diego, USA, 2008.

Catia Bernabini

December 2010

Contents

List of Figures

List of Tables

Nomenclature and Abbreviations

$\mathbf{F}$	Force
$\mathbf{O}$	Torque
$\mathbf{E}$	Electric field
$\mathbf{H}$	Magnetic field
$\mathbf{D}$	Electric flux density (Displacement)
$\mathbf{B}$	Magnetic flux density
$\mathbf{J}$	Current density
$\mathbf{r}$	Spatial vector
ϕ	Electric potential
V	Voltage
t	Time
Δt	Transit time
A	Surface area
Q	Charge
d	Distance
q	Unit charge
C	Capacitance
i	Imaginary unit number, $i = \sqrt{-1}$
σ	Conductivity
f	Frequency
ω	Angular frequency, $\omega = 2\pi f$
λ	Wavelength
λ_d	Debye wavelength
q_e	Electron change
μ_0	Vacuum magnetic permeability, $\mu_0 = 4\pi \times 10^{-7}\,\mathrm{H/m}$
ε_0	Vacuum dielectric permittivity, $\varepsilon_0 = 8.85 \times 10^{-12}\,\mathrm{F/m}$
ε	Dielectric permittivity, $\varepsilon = \varepsilon_1 + i\varepsilon_2$
ϵ_r	Relative dielectric permittivity
ϵ'	Real part of complex permittivity
ϵ''	Imaginary part of complex permittivity

ϵ_∞	Relative permittivity at infinite frequency
ϵ_s	Relative dielectric permittivity in DC field
ϵ_p	Particle permittivity
ϵ_m	Medium permittivity
χ	Electric susceptibility
α	Total polarisability
α_e	Electric polarisability
α_a	Atomic polarisability
α_o	Orientational polarisability
α_i	Interfacial polarisability
σ	Conductivity
σ_0	Limiting low frequency conductivity
σ'	Real part of complex conductivity
σ''	Imaginary part of complex conductivity
σ_s	Conductivity in DC field
σ_p	Particle conductivity
σ_m	Medium conductivity
η	Viscosity
z	Ion valence
k_B	Boltzmann constant
ζ	Zeta potential
R_m	Medium resistance
R_{mem}	Membrane resistance
R_i	Cytoplasm resistance
R_{DL}	Double layer resistance
R_b	Particle resistance
R_{sh}	Resistance of the shell
C_m	Medium capacitance
C_i	Cytoplasm capacitance
C_{DL}	Double layer capacitance
C_b	Particle capacitance
C_{sh}	Capacitance of the shell
C_{mem}	Specific capacitance of the membrane
G_{mem}	Specific conductance of the membrane
τ	Relaxation time constant
τ_{MW}	Maxwell-Wagner relaxation time constant
τ_p	Charge relaxation time constant of the particle
τ_m	Charge relaxation time constant of the medium
f_{MW}	Maxwell-Wagner relaxation frequency

f_{cross}	Crossover frequency
R	Particle radius
A_{rot}	Time-averaged torque
R_{rot}	Time-averaged torque
k	Scaling factor
Φ	Volume fraction
Z	Complex impedance
Z_{re}	Real part of the complex impedance
Z_{im}	Imaginary part of the complex impedance
Y	Complex admitance
C_{mix}	Complex capacitance of a mixture
G_f	Geometric cell constant
g	Gap
l	length
h	Height
w	width
κ	Debye length
U	Potential energy
U_{EDF}	Total interaction energy

1D	One Dimensional
2D	Two Dimensional
3D	Three Dimensional
AC	Alternate Current
BSA	Bovine Serum Albumin
CCD	Charge-Coupled Device
CM	Clausius-Massotti Factor
CPA	Constant Phase Element
CV	Coefficient of Variation
DC	Direct Current
DEP	Dielectrophoresis
DL	Diffuse Layer
DLS	Dynamic Light Scattering
DNA	Desoxyribo Nucleic Acid
E.coli	Escherichia Coli
ECM	Equivalent Circuit Model
EDL	Electrical Double Layer
EIS	Electrical Impedance Spectroscopy
EOF	Electro-Osmotic Flow

FACS	Fluorescence-Activated Cell Sorting
FEM	Finite Element Method
FITC	Fluorescein Isothiocyanate
iHP	Inner Helmholtz Plane
IPTG	Isopropyl β-D-1-Thigalactopyranoside
IR	Infrared
LB	Langmuir-Blodgett
LbL	Layer-by-Layer
MDCK	Madin-Drby Canine Kidney
MOSFET	Metal Oxide Semiconductor Field Effect Transistor
nDEP	Negative Dielectrophoresis
OD_{600}	Optical Density at 600 nm
oHP	Outer Helmholtz Plane
PAH	Poly (Allylamine Hydrochloride)
PBS	Phosphate Buffer Saline
PCD	Printed Circuit Board
PCS	Photon Correlation Spectroscopy
pDEP	Positive Dielectrophoresis
PDMS	Polydimethyl Siloxane
PE	Polyelectrolyte
PEEK	Poly ether Ether Ketone
PMT	Photomultiplier Tube
PS	Polystyrene
PSD	Particle Size Distribution
PSS	Poly (Styrene Sulfphonate)
RF	Radio Frequency
ROT	Electrorotation
ST	Stern Layer
UV	Ultraviolet

Acknowledgements

I would like to thank Prof Hywel Morgan, my supervisor, for the great opportunity to carry out this work. I am really grateful for all the support, advices and guidance he gave me through all these years, for his enthusiasm, dedication and passion for science.

Thanks to Nicolas Green, my second supervisor, for the useful discussions.

Many thanks to Dr Tao Sun for the important contributions to this work, his kindness and generosity.

Thanks to Dr David Holmes, for his valuable help and experience, and to Shady Gawad, for the helpful discussions.

Thanks to Prof Gleb Sukhorukov and his team at the Max Plank Institute of Colloids and Interfaces, for giving me the opportunity to visit their lab and for sharing their knowledge. Especially, thanks to Dr Matthieu Bedard and Dr Daria Andreeva for their assistance during my visit.

Many thanks to Dr Tracey Newman, for the useful discussions and the help given in many occasions.

My thanks to my friends and colleagues from the Biolectronics group (past and present) for the great time I had with them, their help and support. Thanks to Andrew Whitton, Barbara Cortese, Daniel Spencer, David Barat, Diego Morganti, Federico Thei, Ferran Revilla, Giuseppe Benazzi, Katie Chamberlain, Mairi Sandison, Marco Peca, Mark Friddin, Marta Lombardini, Michele Zagnoni, Nefeli Tsaloglou, Nurul Yunus, Pablo Garcia, Robert Zmijan, Raphael Tornay , Rupert Thomas, Sam Birtwell, Sara Aghdaei, Shahanara Banu, Soichiro Tsuda, Veronica Hollis, Xi Huang, Xiaojun Han. Among them, special thanks go to Giuseppe and Diego, for the long days we spent together in the lab, and to Barbara and Marta for their invaluable friendship. Many thanks to all my friends in Southampton and in particular to Davide Magagna and Francesca Placanica. Thanks to Robert Simpson, Nadia Vahdati and Francesca Parmigiani, for the nice time living together.

I wish to thank my family, the Italian, the Mexican, and the French one! Especially, I would like to thank Lucilla and Adelmo, my parents, who have always supported me. Special thanks also to Silvia and Paolo, Martina and Alessandro.

Finally, thanks to Rodrigo, for his patience, his love and support during all these years.

A Olimpio

"The creation of something new is not accomplished by the intellect but by the play instinct acting from inner necessity. The creative mind plays with the objects it loves."

C. G. Jung

Chapter 1

Single cell micro-impedance cytometry

1.1 Introduction

Electrical impedance spectroscopy (EIS) is a non-invasive and label-free technique that measures the electrical properties of particles in suspension in response to applied AC potentials. Typically, impedance measurements are performed by applying a small AC excitation voltage to the suspension of particles held in a measurement unit. The unit is provided with electrodes and the current passing through the system is measured as a function of the frequency. The first examples of impedance measurements on suspension of biological particles were reported by Hober [19, 20, 21], who measured the conductivity of erythrocytes, and Fricke [22, 23, 24] who calculated the membrane capacitance and thickness by measuring canine red blood cells. Measurements on lysing erythrocytes were shown in [25]. Cole and Cole measured the impedance of single oocytes [26, 27, 28] and measurements of single Nitella cells were reported in [29]. Since this early work, there has been a large number of contributions to the field and comprehensive reviews of the topic can be found in [30, 31, 10, 32, 33]. In recent years, the advent of lab-on-a-chip technologies led to the development of devices characterised by having features of the same size of the particles under study and which can be employed for analysis of single biological cells in a similar way to commercial flow cytomters. The benefits deriving from the miniaturisation of biological and chemical analysis devices compared to the more traditional macro-scale laboratory techniques are several. First of all, the analysis of the response of single cells, instead of a population of cell, allows for the detection of rare events that would disappear in the averaged result from

bulk experiments, as non-standard distribution of events are averaged by bulk experiments and thus are not represented correctly [34, 35]. Besides, the amount of samples and reagents required is considerably reduced, which results in a simplification of the analysis procedure, a decrease in the related laboratory costs and an improvement of the response times. A reduction in size allows for the development of integrated systems where a number of operations such as cell culturing, sample preparation, detection and monitoring of reactions, can be performed automatically on the same device. The automation of the analysis procedure using equipment easy to operate is essential for the development of point-of-care diagnostic. In this contest, electric analysis offers a number of advantages over more conventional optical detection. While conventional optical systems are expensive and require precise alignment of the components, electronic detection is more suitable for the integration on microchips as expensive lenses and detectors are not required. In the last twenty years, a large number of microfluidic devices for impedance-based detection and characterisation of biological particles in suspension have been developed. Developed a as miniaturised counterpart of traditional coulter devices, on-chip electrical detection systems have been extended to AC analysis, like classical impedance spectroscopy systems.

This chapter will review the recent progress in the field of microfluidic impedance cytometry. After presenting the Coulter counter principles, significant publications on micro-Coulter counters and micro-impedance cytometers are reviewed. This is followed by examples of impedance devices for the measurements of trapped cells. Contributions on cell analysis by AC electrokinetics techniques are also reported. Finally, a brief review on fluorescence base micro-flow cytometry which is an alternative to impedance detection and also the most well established on-chip detection technique, is presented.

1.2 Coulter counter

Since its invention in 1953, the Coulter counter has become one of the most well established technologies for counting and sizing biological cells and colloidal particles in suspension, giving the major contribution to the development of automated cell-counting, with applications in haematology, microbiology and industrial particle analysis.

The technique relies on the simple principle of passing individual particles suspended in an electrolyte solution through a sensing aperture as shown in Figure 1.1 [36]. The flow is normally forced by a pressure difference across the aperture whose size typically ranges from several microns to a few millimetres. Two electrodes are positioned at both ends of the aperture and a constant ionic current is passed through it. The transit of a particle through the aperture causes the displacement of conductive fluid and increases

the resistance of the aperture. This increase in resistance corresponds to a transient decrease in the current that is registered as a pulse. The number of such pulses gives a count of the particles in suspension and when the volume of liquid is known, the concentration of the sample can be obtained. As the magnitude of the pulse is proportional to the amount of fluid displaced, and thus to the volume of the particle, this technique can also provide information on particle size.

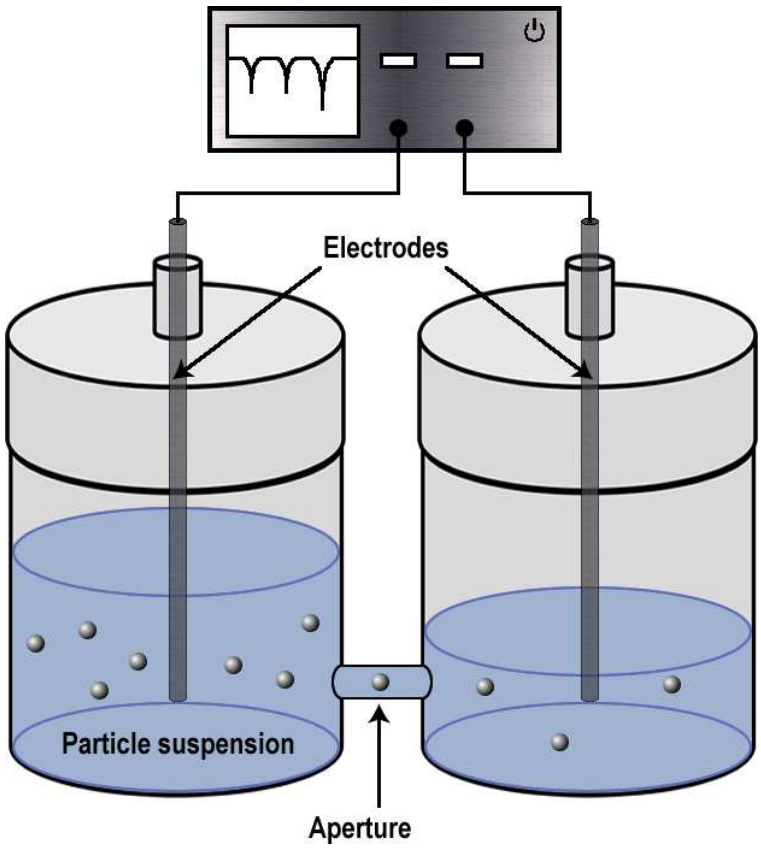

FIGURE 1.1: Diagram illustrating the working principles of the Coulter counter. A suspension of particles or biological cells is forced to flow through a sensing aperture where a current path exists. By measuring the current variation caused by their passage through the aperture, particles and biological cells are individually counted and sized.

The relative simplicity and the high sensitivity of the method contributed to the rapid development and commercialisation of Coulter devices which have widely been used to count and size a variety of particles, including erythrocytes and leukocytes [37], bacteria, tissue culture cells, algae, pollen, and yeast [38, 39]. At present, Coulter counters are regularly employed for diagnostic purposes involving the study of transmission and proliferation of diseases [40] and activity of cancer cells [41].

One of the limitations of the technique is that only particles with sizes of the order of the aperture dimensions can be detected. Measurement of small particles requires higher instrument sensitivity, which can be provided with the smaller apertures. On

the other hand, the aperture has to be big enough to allow the passage of the largest particle in suspension. Commercially available Coulter instruments operate within a size range that goes from 400 nm to 1200 μm diameter particles and at a detection rate of several thousands particles per second [39]. Resistive pulse sensing techniques have been successfully applied to the measurements of nano-particles by using nano-pores etched in an artificial membrane [42] or inorganic nanotubes [43]. Several examples have been reported so far, they include detection of colloidal particles [44, 45, 46] protein molecules [42], DNA [47, 48, 49, 50, 51] and viruses [52].

In general, the Coulter analysis technique is limited to the use of DC or low frequency voltages. Measurements at these frequencies provide only information on size of the particles. A biological cell at DC or low frequency appears to be a perfect insulator because of the high membrane capacitance, and thus it resembles a microsphere of similar size. In order to obtain information related to other properties besides the volume, such as cell membrane and the internal composition of the cell, it is necessary to extend the classic Coulter method to measurements at higher frequency values. There are few examples in the literature reporting the simultaneous measurement of low and high frequency impedance changes from individual cells passing through an orifice [53, 54, 55]. For example, by applying DC and 4.5 MHz frequency voltages Hoffman et al. could detect both the resistance and capacitance of microspheres and biological cells in suspension, and differentiate intact cells from cells with damaged plasma membrane [56]. Commercial instruments for the RF sensing of single cells or particles have been developed by Sysmex [57] and Beckman Coulter [39].

1.3 Micro Coulter counters

The first example of miniaturized Coulter counter was reported by Larsen in 1997 [58]. This device consisted of a planar microfluidic channel etched in silicon and covered with glass. Micro-electrodes for four-point particle measurements were fabricated on the bottom of the channel and fluidic inlets were provided for the hydrodynamic focusing of the sample. A similar device was reported few years later by Koch et al. [1] which proposed the integration of different features, such as filters, in a single device Figure 1.2. In both cases, no experimental data was reported.

After these two early attempts, only few examples of miniaturised Coulter counters have been reported in the literature. From a general review of the devices shown so far it can be observed that there are two major trends in on-chip resistive pulse sensing. One is to use small apertures or artificial pores to sense the passage of suspended particles while they cross the aperture [59, 60, 2, 61], the other one is to measure particles while

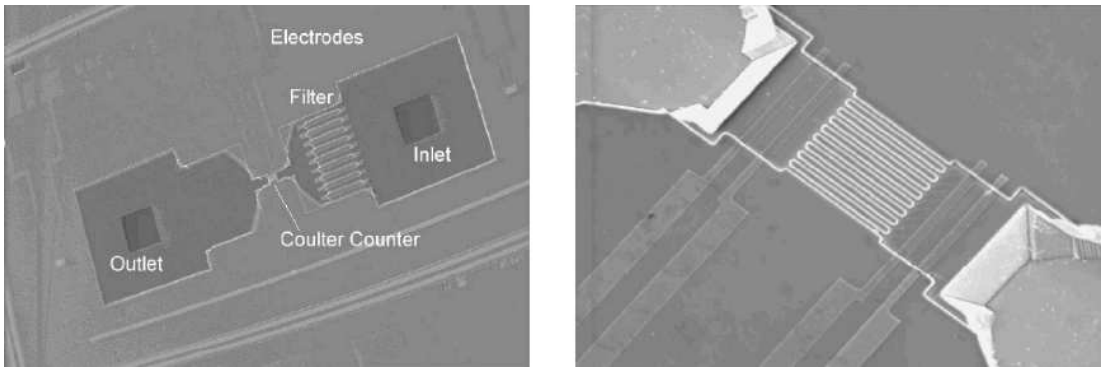

(a) (b)

FIGURE 1.2: Images of the Coulter counter reported by Koch et al. [1]. (a) Whole device: the integrated pre-filter structure is located next to the inlet, on the right, while Coulter detection region is at the centre. (b) Close-up view of the detection region with two pairs of electrodes.

they are flowing through the detection region of a microfluidic channel [62, 63, 5, 64]. For both types of systems the flow is generally controlled by volume displacement [65] or by pressure gradient [66].

An artificial-pore device is the exact translation to micron scale of the traditional Coulter concept described in the previous section: an orifice connects two reservoirs where micro-electrodes are provided to generate a current path through the orifice. One of the first working examples of on-chip artificial-pore based sensing was reported by Larsen et al. which used a simple aperture in a silicon membrane to measure and count somatic cells [59]. Using standard microfabrication techniques, nano-sized apertures can be easily integrated on a chip and artificial-pore devices have found their main application in the detection of individual sub-micron particles. Nano-pore devices are generally fabricated using a silicon substrate bonded to glass [60] or by sealing a polydimethylsiloxane (PDMS) mold to a glass slide Figure 1.3 [2]. By using a nano-pore with around 1μm diameter Saleh and Sohn demonstrated the ability to sense colloids as small as 87 nm diameter and distinguish between sub-microns particles whose diameters differed by less than 10% [67]. The same authors reported detection of unlabeled antibody binding to the surface of latex colloids [68] and of single DNA molecules [2]. The technique was also employed in a multiple-pore device in order to perform multianalyte immunoassays on a single chip [61].

A variation to the standard Coulter design was reported by Tang et al. who proposed locating the electrodes in a plane perpendicular to the fluid flow in order to reduce the length of the sensing orifice and minimize the occurrence of particle coincidence [69].

By contrast with artificial pore devices, microfluidic channels are usually employed to detect and count particles that are several microns in size, such as biological cells

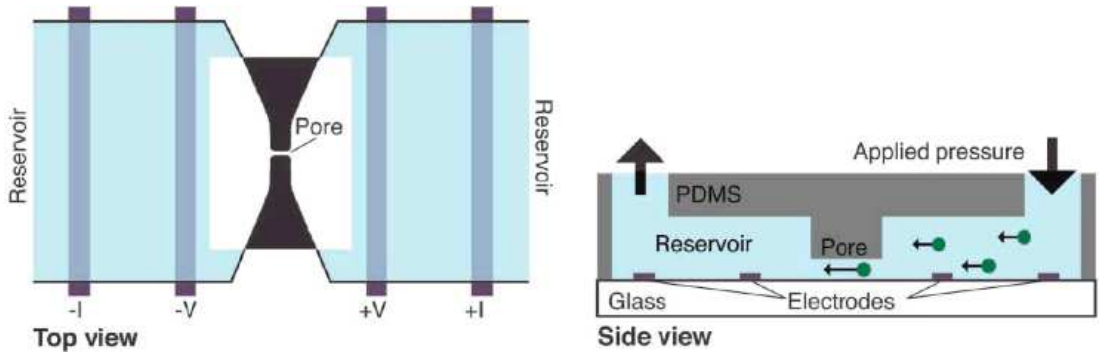

(a) (b)

FIGURE 1.3: Schematic top view (a) and side view (b) of an artificial pore device consisting of a PDMS mold bonded to a glass slide. Two reservoirs are connected via a small pore. A current path is generated through the pore by using microelectrodes located at the bottom of both the reservoirs [2]

[62, 64, 70, 3]. In these devices the detection region is defined by a section of the channel where pairs of microfabricated electrodes are usually arranged in coplanar configurations to generate an electric field. The dimensions of the electrodes are chosen to be comparable to that of the particles in order to achieve a high field line concentration around the particle travelling through the detection region. The channel sizes typically range from 20-30 μm to 100s μm [63]. When the dimension of the channel, and thus of the detection region, is several times bigger than the size of the particles, focussing of the sample is required to ensure that only one particle at a time crosses the detection region and that each particle follows a fixed trajectory within the field. Like in conventional flow cytometry, alignment of the sample particles within the detection region is normally achieved by hydrodynamic focussing [63, 71]. These devices have been employed to count and size mixtures of beads [5, 72] and cells [62]. Arrangements of multiple channel networks that can be monitored simultaneously in order to improve the system throughput have also been proposed [64, 70].

One of the disadvantages of using small electrodes for DC or low frequency measuremets is that the measurements are largely affected by the formation of the electrical double layer at the electrode interface. Besides, Faradaic reactions can occur at the metal electrode surface when DC or low voltages are applied. To overcome these problems, Chun et al. developed a flow cytometer where instead of metal electrodes they used pairs of polyelectrolytic salt bridge-based electrodes (PSBE) [3]. The device, shown in Figure 1.4, was able to count and discriminate up to 1000 cells s^{-1} flowing at a velocity of 100 mm s^{-1}.

The sensitivity and specificity of resistive pulse sensing devices are limited by a number of issues. Essentially the lower detection limit is determined by the electrical noise

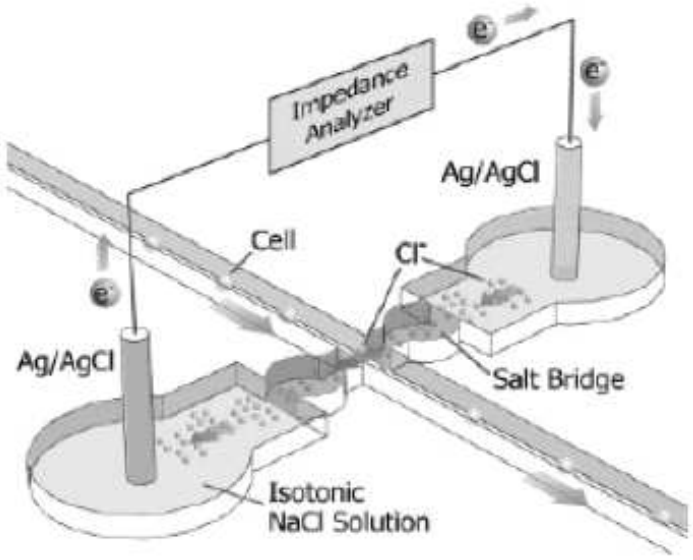

FIGURE 1.4: Microfluidic flow cytometer with pairs of polyelectrolytic salt bridge-based electrodes (PSBE) for DC voltage based detection. DC bias is applied between two Ag/AgCl electrodes connected to the PSBE through an isotonic NaCl solution [3].

associated with the current path through the detection region: when the current displacement corresponding to the transit of a particle causes a pulse that is comparable to the noise level, no detection is possible. In order to improve the signal-to-noise ratio it is necessary to maximize the ratio of particle volume to the volume occupied by the electric field, i.e. the volume fraction. In addition, the spatial location of the particle needs to be controlled accurately within the field. The use of nanopores or small channels is an effective way to maximize the volume fraction and improve the sensitivity of the system. Obviously, this implies a reduction of the size range of detectable particles and a limitation in the ability to analyse heterogeneous samples. Also fabrication of small channels is more difficult and the likelihood of blockages is greatly increased.

In this context, several groups have been devoting their research efforts to enable detection of small particles inside channels that can be easily fabricated by using standard soft-lithography techniques and that are more versatile compared to nano-pores or few micron-wide channels. For example, Li's group reported a sensing scheme to detect and amplify the signal from the translocation of particles that is based on the use of a metal oxide semiconductor field effect transistor (MOSFET) [4]. By monitoring the drain current drops of a MOSFET connected to the fluidic channel (see Figure 1.5 for details) they could differentiate between 4, 6 and 9.86 μm beads and reach a detection limit of 2 μm. The same group also reported detection of 2, 1 and 0.520 μm beads using a symmetric mirror-channel configuration connected to a differential amplifier [46]. In

both cases they used a relative small sensing channel with a cross section measuring 16 x 30 μm^2.

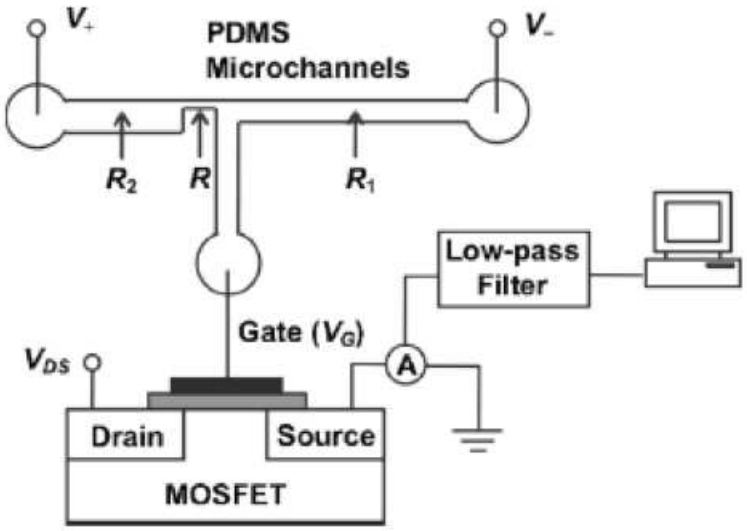

FIGURE 1.5: Schematic of sensing scheme for particle detection proposed by Xu et al. [4]. The gate of a commercial MOSFET is connected to the end of the sensing part of the microfluidic channel. The potential modulation corresponding to the passage of a particle is sensed by monitoring the MOSFET drain current.

An alternative method of increasing the sensitivity whilst maintaining a relatively large channel dimensions is to focus particles into the sensing region with the use of a sheath flow that is made of a less conducting liquid than that of the sample, such as pure water [63]. This way the sheath flow serves to concentrate the electric field lines into the sensing volume without restricting the geometry of the device. Moreover, the width of the sample stream can be dynamically adjusted by varying the relative flow-rates at the sample/sheath inlets.

When sample focussing is achieved both vertically and horizontally along the channel axes [73, 74], the size of the detection area can be precisely adjusted to the size of the particles, thus reaching an optimal sensitivity of the system. The first example of micro-Coulter counter with adjustable aperture was reported by Vellekoop's group in 2004 [5]. A schematic of the device is shown in Figure 1.6 and the working principle can be explained as follow. The sample is introduced from the bottom into a wide channel filled with the sheath liquid so that simultaneous horizontal and vertical sample confinement is obtained. Lateral control ports are also provided for the removal or addition of sheath liquid and to for a finer adjustment of the sample width. The sensing part is located downstream the focussing region and it consist of two pairs of coplanar electrodes.

By using distilled water as the sheath flow, the authors estimated a theoretical increase in sensitivity by a factor of 50 times. However, no quantitative data were reported. More

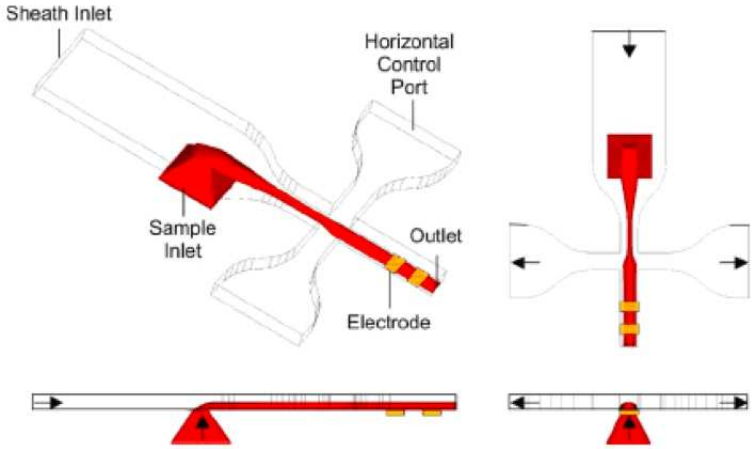

FIGURE 1.6: Micro-Coulter device reported by Nieuwenhuis et al. [5]. The sample is introduced from the bottom (sample inlet) into a wide channel filled with the sheath liquid. Horizontal control ports allow for the removal or addition of sheath liquid and for a finer adjustment of the sample width. The aperture of the device can be controlled in two dimensions by varying the relative flow-rates at the inlets allowing for simultaneous horizontal and vertical sample confinement. The sensing part is located downstream the focussing region and it consist of two pairs of coplanar electrodes.

recently, micro-Coulter devices with adjustable aperture were used to measure mixture of 6 μm and 20 μm beads [72] and to detect yeast cells [62]. However, although a two-dimensional adjustable aperture can improve the flexibility of the system, the devices presented so far suffer from a lack of accuracy, because detection in two-dimensional focussing devices was limited by the use of coplanar electrodes arrangements. These coplanar electrode arrangements give a highly divergent field compared to opposing electrode configurations [75]. The impedance signal from a particle travelling through the detection volume is therefore critically dependent on the height of the particle in the channel, or the distance from the electrodes. This leads to an increase in the dispersion of the signal amplitude distribution, making the result more uncertain and therefore compromising the discrimination of similar size particles.

1.4 Micro-impedance cytometry

In describing the Coulter method it was pointed out that Coulter counters, and their miniaturised counterpart, are generally employed for DC or low frequency analysis, thus their application essentially focuses on cell sizing and sample concentration analysis. As the polarisation response of a cell passing through an electric field region is frequency dependent, measurements taken at multiple frequencies allow for the determination of

different characteristics of the cells under investigation, similarly to that obtained in traditional impedance spectroscopy [76, 77].

The first example of single cell electric impedance spectroscopy performed in a microflow system was reported by Ayliffe et al. in 1999 [78]. The device was based on a glass-polymer microfluidic chip with integrated electrodes fabricated in the channel walls. Spectra over a frequency range from 100 kHz to 2MHz were obtained for a variety of PBS (Phosphate Buffer Saline) solutions at different concentrations and for single human polymorphonuclear leukocytes and teleost fish erythrocytes in suspension. Measurements at multiple frequencies within a bandwidth of 10 MHz were performed by Fuller et al. [79] which investigated different parameters of human peripheral blood granulocytes such as radius, membrane capacitance and cytoplasm conductivity. Measurements on DNA content of eukaryotic cells were reported by Sohn et al [80]. By applying 1 kHz frequency voltage, these authors claimed the ability of differentiating between the DNA content characteristic of a specific stage of the cell-cycle. However, it can be argued that low frequency measurements of intact cells are dominated by the high capacitive response of their membrane and no information relative to the cell internal properties can be obtained. Gawad et al. developed a microflow cytometer with a coplanar electrodes configuration for differential impedance measurements [6]. A schematic of the device illustrating the working principle is shown in Figure 1.7. In this design one pair of electrodes is used for sensing the current change induced by the passage of the particle whilst the other one provides the reference. The authors demonstrated the ability to perform simultaneous measurements at multiple frequencies ranging from 100 kHz to 15 MHz, and to differentiate subpopulations in mixed samples of different sized beads or cell types at a rate of 100 cell s^{-1}.

A coplanar electrode configuration was also employed by Morgan et al. [81] which implemented simultaneous electrical and optical detection in a system for single particles high speed analysis. The same system was employed by Benazzi et al. for the discrimination of different species of marine algae [82]. A microfluidic device with planar electrode pairs for high frequency measurements of cells was reported in [83], where a signal at 8.7 MHz and was employed to detect infections of red blood cells suspended in low conductivity buffer.

An improved version of their earlier device was proposed by Gawad et al. which replaced the coplanar electrodes with two pairs of opposing electrodes located on both top and bottom faces of the channel [7]. A picture of the device and a schematic illustrating the channel cross-section are reported in Figure 1.8. The channel was made of polyimide on a glass substrate and had a cross-section measuring 20 x 40 μm^2.

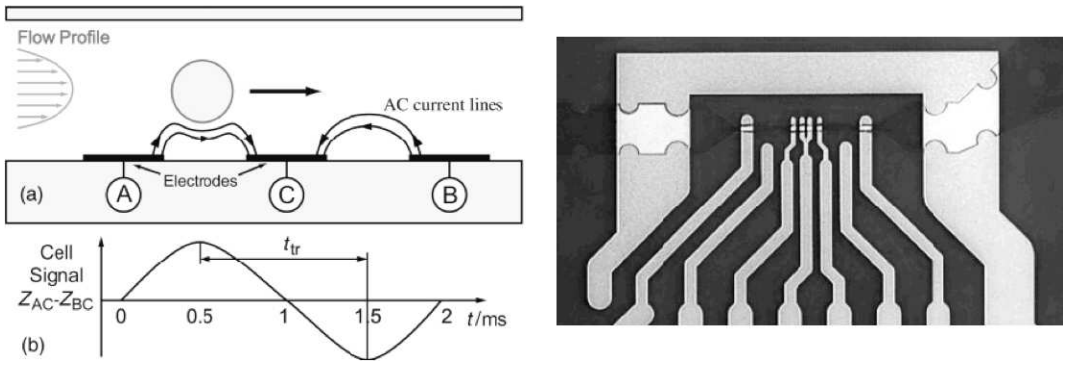

(a) (b)

FIGURE 1.7: Differential impedance measurement scheme reported by Gawad et al. [6]. (a) Schematic showing the transit of a particle through the detection region. Two pairs of electrodes are employed for the differential impedance measurement: one pair is used for sensing the current change caused by the particle whilst the other pair provides the reference. Thus, a positive peak and a negative peak separated by the particle transit time are obtained for each detected particle. (b) View of the device detection region.

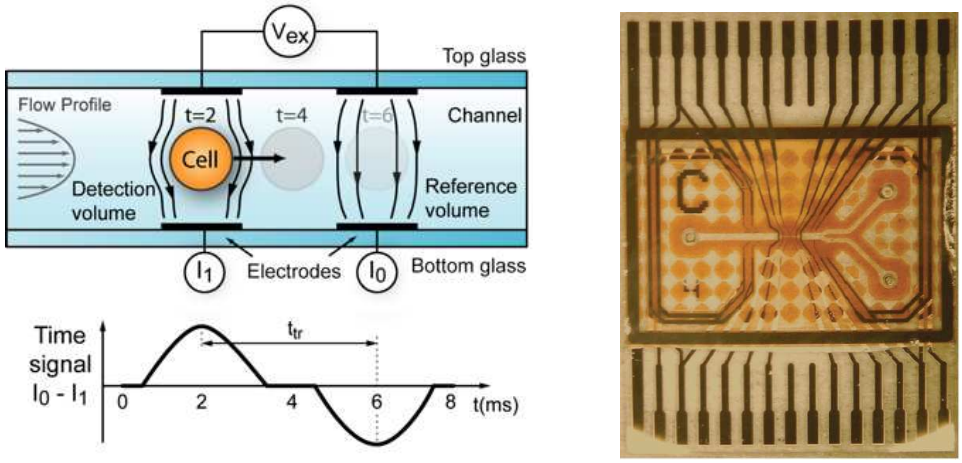

FIGURE 1.8: (left) Impedance flow cytometer with opposing electrode configuration. An AC signal applied to the top electrodes generates an electric field inside the two detection volumes defined by the two electrode pairs. Particles are suspended in an electrolyte and flow through the electrodes, causing a change on the impedance of the detection volumes. This impedance change is measured using a differential scheme: one detection volume measures the impedance of the particle and the other volume is used as a reference. Thus, for each particle crossing the detection region, a positive peak and a negative peak separated by the particle transit time (t_{tr}) are recorded. (right) Picture of the device [7]

The system was capable of differentiating between polystyrene beads and red blood cells and between red blood cells and fixed red blood cells based on the opacity spectra obtained with measurements at 602 kHz and 10 MHz. The phase signal obtained for the same frequencies enabled discrimination of red blood cells and ghosts [84]. A major advance in micro-impedance based blood analysis was recently reported by Holmes et al.

[8] who performed analysis and differentiation of white blood cells using a microfluidic impedance cytometer. They showed that it was possible to clearly identify and count T-lymphocytes, monocytes and neutrophils according to both membrane capacitance and size. Figure1.9 (a) shows the measured impedance magnitude of the three types of cells together with the best fit obtained by PSpice simulations. The data shows that in the frequency range 500 kHz to 3 MHz the different types of cells are characterised by a different impedance magnitude, making discrimination possible. A scatter plot showing clear impedance-based discrimination of the three cell populations is reported in Figure 1.9 (b). The results obtained were comparable to the ones from standard hematology techniques.

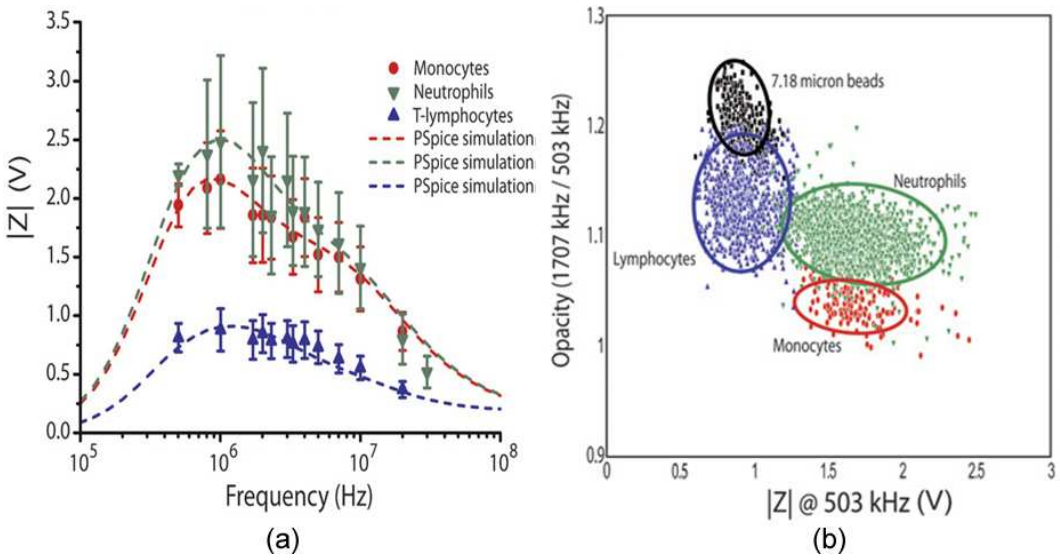

FIGURE 1.9: Differentiation of white blood cells using a microfluidic impedance cytometer with two pair of opposing electrodes reported by Holmes et al. [8]. (a) Experimental data showing the frequency-dependence of the impedance magnitude for purified populations of T-lynphocytes, monocytes and neutrophils. Each data points contains 1500 recorded events, the dashed lines show the best fit PSpice circuit simulations. (b) Scatter plot showing opacity vs low frequency impedance magnitude of the three leukocyte subpopulations (7.18 μm beads were added as a reference).

One of the limitations of conventional impedance measurements is that in order to obtain broad spectra it is necessary to acquire impedance signals at several frequency values. This can be done either by performing a signal sweep over a range of frequencies, which may result in long analysis time, or by probing multiple frequencies at the same time, which implies a more complicated implementation of the system. A novel impedance spectroscopy technique for high speed single particle analysis was reported by Sun et al. [85]. The method is based on the use of maximum length sequence analysis to detect 512 frequency values simultaneously over a range from 1 kHz to 500 kHz was employed to characterise single particles and red blood cells in suspension.

1.5 Impedance analysis of trapped cells

The micro-impedance devices reviewed so far are examples of continuous flow systems, in which single cells are analysed at high speed while they flow through the sensing region of a microchannel. This type of systems is not suitable when analysis over time, such as monitoring of the cell properties in response to a specific active substance is required. To address this problem, microfluidic devices capable of capturing individual cells and performing multiplexed single cells assay have been developed. Generally, these devices consist of a microfluidic channel where arrays of physical hydrodynamic trapping structures are provided to immobilise individual cells; the impedance signal from each trapped cell is then recorded using microelectrodes usually integrated within the traps. Impedance spectroscopy of single HeLa cells was performed by Jang et al. [86] using a pillar microsctructure to immobilize cells flowing in a microchannel. Real time measurements of volume changes in Madin-Darby Canine Kidney (MDCK) epithelial cells in response to hypotonic stimulations were reported in [87]. Malleo et al. [9] developed a system where pairs of adjacent traps were used to perform continuous differential impedance analysis. The concept is shown in Figure 1.10, which illustrates the micro-channel with the pairs of traps and cells in place. In each pair of traps, the trap occupied by the cell is used to perform the measurement, while the empty trap is the reference to normalize the recorded data and make the measurement robust to local changes in temperature, pH, or conductivity. The device was employed to measure the transient effects of a surfactant and a pore-forming toxin on captured HeLa cells.

One of the advantages offered by these systems is that the impedance measurements can be correlated to the data obtained with the simultaneous optical inspection of the cells under study. This technology is mainly limited by the fact that in order to achieve a high throughput, it is necessary to build a high number of traps and, as a result, to increase the complexity of the data acquisition.

1.6 Dielectrophoresis and Electrorotation

AC electrokinetic techniques, especially dielectrophoresis (DEP) and electrorotation (ROT) among the others, have been widely investigated as alternatives to impedance spectroscopy for non-invasive and label-free characterisation of single particles.

While impedance spectroscopy relies on the direct measurement of a signal variations resulting from a perturbation of the electric field, dielectrophoresis and electrorotation based analysis consists of measuring the frequency dependent motion (translation and rotation respectively) of single particles in suspension under the action of inhomogeneous

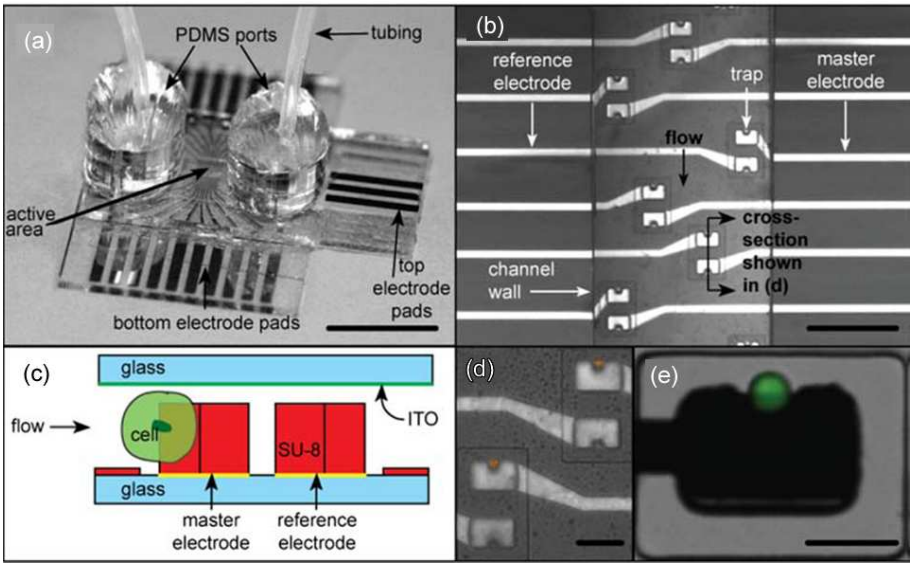

FIGURE 1.10: (a) Image of the device for continuous differential impedance spectroscopy. (b) Photograph of the channel where each pair of traps is connected to a pair of microelectrodes for differential measurements. Correct functioning of the system is ensured by the fact that cells are captured only inside the master traps, while the reference traps, located downstream, stays empty. (c) Schematic cross section of the hydrodynamic trap. (d) Close up view showing trapping of 15 μm beads and (e) HeLa cells [9].

and rotating electric fields [12]. The electric field is generally applied using customised microelectrode arrangements and when its characteristics are known together with the dielectric properties of the suspending medium, it is possible to deduce important information on the properties of the particle, such as conductivity or permittivity. Since the publication of the first example of electrorotation of a single cell reported by Arnold and Zimmermann in 1982 [88], ROT techniques have been employed in the study of a broad variety of microscopic objects, ranging from single living cells to spores, seeds and synthetic materials [89, 90, 91, 92]

For example Gimsa et al. demonstrated the measurement of the dielectric properties of human red blood cells in the frequency range from 2 kHz to 200 MHz at physiological ion concentrations [90] and furthermore showed that they could follow changes of dielectric properties on individual red blood cells after nystatin application [89]. By monitoring shifts in the cellular dielectrophoretic crossover frequencies of promyelocytic HL-60 cells following treatment with genistein, Wang et al. were able to deduce changes in membrane capacitance and conductivity [93]. Chan et al. measured the dielectric properties of trophoblast cells and mixed peripheral blood mononuclear cells using dielectrophoretic crossover and single cell electrorotation methods [91]. Gascoyne and co-workers measured the dielectric characteristics of the four main leukocyte subpopulations by electrorotation over the frequency range 1 kHz to 120 MHz [92]. Mean specific

membrane capacitance values were calculated from the electrorotation by fitting the data to a single-shell dielectric model. Electrorotation has also been used successfully to separate cancerous cells from populations of healthy cells: Becker et al. used electrorotation measurements to demonstrate that the dielectric properties of the metastatic human breast cancer cell line MDA231 were significantly different from those of erythrocytes and T lymphocytes [94]. Cheng et al. separated the metastatic human cervical carcinoma cell line (HeLa cells) from normal human peripheral cells by using inhomogeneous AC field to create the conditions for dielectrophoretic separation of cells [95].

Even if both DEP and ROT techniques have been successfully employed to provide useful and precise information on particle dielectric properties, there are some important disadvantages compared to single cell impedance spectroscopy. First of all, as the rotation rate of the particle in ROT and the direction of the translation in DEP experiments have to be recorded at different frequency values, extensive post-processing and video analysis have to be performed in order to evaluate the data, making it impossible to perform real-time spectroscopic analysis. It is also a highly time consuming procedure. In addition, AC electrokinetic experiments usually need to be done in low conductivity solution in order to reduce electrolysis and Joule heating effects. The suspension in non physiological solution can cause cellular changes and thus affect the response of live cells, limiting the use of the technique for measuring sensitive biological system and medically relevant samples.

1.7 Fluorescence based micro-flow cytometry

In flow cytometry, suspended cells flowing within a capillary tube are focussed into a single-file stream by hydrodynamic focussing and then directed at high speed to a focussed laser beam. For each individual cell flowing past the laser beam, light scattering at different angles and fluorescence emission at multiple wavelengths are collected through a series of optical systems and processed in order to determine a variety of morphological and biochemical properties of the particles [96]. Thanks to the advances in precision technology and to the availability of highly selective fluorescence labelling techniques, flow cytrometry has been subjected to an impressive development in the last 30 years. With the ability to measure up to ten parameters from each cell and with a throughput of 40.000 cells s^{-1}, flow cytometers became an indispensable analytical tool in the field of cell biology, diagnostic, immunology and environmental monitoring. In addition, some flow cytometers allow for the separation and sorting of cells based on preset parameters such as fluorescence intensity (fluorescence activated cell sorter, FACS) at a sorting rate of 10.000 cells s^{-1}.

Although conventional flow cytometers provide rapid and reliable analysis, the systems are bulky and complex and require trained personnel to be operated. Moreover, large sample volumes and time-consuming sample preparation are needed for the analysis.

With the advent of lab-on-a-chip technologies, many research groups have devoted their efforts towards the miniaturisation of these expensive and complex instruments. Over the last few years, numerous optical detection based microsystems have been shown in the literature [97, 98]. Comprehensive reviews on the development of micro-flow cytometry can be found in [99, 100, 101]. These systems make use of a variety of optical detection devices, including commercially available instruments, such as microscopes or photomultipliers (PMTs) [98], or integrated miniaturised components, such as lenses or waveguides [97]. For example, McClain et al [102] reported the detection of fluorescently labelled E. coli at rates up to 85 cells s^{-1}. The device consisted of a microfluidic network to electrokinetically transported and focussed the cells into single streams; the detection of single cells was performed using a microscope coupled to a photomultiplier tube. Assay of protein expression and apoptosis in human primary cells using a microfluidic network with an incorporated a staining step was reported in [103]. Wolf et al described a high-throughput microfluidic device with incorporated cell culturing chamber and waveguides for optical detection [104] .

In spite of the number of optical based flocytometers reported so far, integration of expensive lenses and detectors remains the major limit for the development and commercialisation of cost-effective point-of-care micro-flow cytometry devices. A further drawback of optical based detection compared to label-free techniques, is that although fluorescent markers allow very accurate detection down to the molecular level, they generally require incubation procedures and thus longer sample preparation times. Besides, cell tagging may alter some of the properties of interest. This is especially true when non-surface markers are used for the analysis. In this case, a membrane permeabilisation step is required for the marker to reach the specific target, which may affect further analysis performed on the cell.

1.8 Conclusions and thesis outline

Impedance-based detection is a simple and well established technique for the identification of the properties of particles in suspension in a non-invasive and label-free way. In recent years, lab-on-a-chip technologies have been developed to enable single cell impedance detection and a wide range of impedance-based microfluidic devices have been reported. Potential applications of micro-impedance cytometry involve many fields of medicine and diagnostic, food industry, chemistry and biology. Despite the number

of contributions and the achievements of this field, micro-impedance cytometry still suffers from a lack of sensitivity and specificity compared to traditional flow cytometry, that limits the potential commercialization of microfluidic impedance devices. While impedance measurements of beads and cells are well established, discrimination between particles with very similar sizes or detection of small sized particles, such as bacteria, still represents a challenging task.

A number of issues limit the sensitivity and specificity of these microfluidic systems. Fundamentally the sensitivity is governed by the ratio of particle volume to the volume occupied by the electric field, defined as the volume fraction occupied by the particle, which should be maximised. In addition, the spatial location of each particle needs to be controlled accurately within the field. It is also important to ensure that only one particle at a time enters the detection region. Therefore, an efficient and accurate method for focussing particles into the centre of the electric field is important. One way to improve the sensitivity of the system is to reduce the dimensions of the channel. Typically for cell analysis, channels that are 20 μm to 30 μm in width and height are used. In order to measure smaller objects such as bacteria, the channel dimensions and electrode width should be reduced, for example to 5 μm, but this makes fabrication more difficult and greatly increases the likelihood of blockage of the channel. In general, the detection of sub-micron particles is performed using nanopores with typical sizes ranging from several hundreds of nanometers to few microns [44, 45, 52, 68, 2, 46].

One method that has been reported to increase the sensitivity whilst maintaining a relatively large channel dimensions is to focus particles into the sensing region with the use of a sheath flow that is made of a less conducting liquid such as pure water. In this case, the sheath flow serves to concentrate the electric field lines into the sensing volume without restricting the geometry of the device. Several examples of micro-impedance devices where the sample is sheathed with a less conductive liquid are reviewed in this chapter. In these systems, coplanar electrode configurations are normally used to detect the particles. This electrode arrangement gives a highly divergent electric field compared to opposing electrode configurations. The impedance signal from a particle travelling through the detection volume is therefore critically dependent on the height of the particle in the channel, i.e. the distance from the electrodes. This causes an increase in the dispersion of the signal amplitude distribution, making discrimination of similarly sized particles impossible. Despite efforts to develop a sensitive and reliable micro-impedance system for analysis of particles of around 1 μm in size, to date no effective solution has been shown.

The aim of this work is to develop a micro-impedance cytometer with an improved sensitivity that allows for accurate and reliable discrimination of particles but without sacrificing the ease of fabrication and operation. The device consists of a microfluidic

channel where two pairs of microfabricated electrodes are provided to perform differential measurements of single particles in suspension at high speed. Different electrode configurations and different techniques for focussing the sample within the detection region of the device are investigated in order to improve the sensitivity of the system without reducing the dimensions of the microfluidic channel. One of the objective is to show that it is possible to perform quantitative measurements and discriminate between particles that differ from less than one micron in diameter, and that bacteria can be easily distinguished from similar sized particle within a relatively large channel. Furthermore, I want to demonstrate that besides detection, discrimination and counting, micro-impedance cytometry is a suitable and reliable technique to investigate and determine the unknown dielectric properties of the particles under study.

Chapter two is a review of electrostatic and bio-dielectric theory covering the fundamental concepts that form the background for the work presented in this thesis. Design and fabrication of the device, a description of the experimental set up and procedures, including data acquisition and analysis, are reported in chapter three. In chapter four, the performances of the micro-impedance cytometer that is objective of this thesis are investigated. Finite element analysis of different electrode geometries and different hydrodynamic focusing techniques are performed and compared to experimental data. Measurement results on detection of small particles and bacteria are presented in chapter five. In chapter six, experimental results on the application of micro-impedance cytometry to the study and analysis of the dielectric properties of polyelectrolyte microcapsules are reported. Finally, concluding remarks on the achievements of this work and suggestions for future work are presented in chapter seven.

Chapter 2

Dielectrics and polarisation

This chapter outlines the principles of the theory behind the polarisation of isotropic dielectric materials and their interaction with the applied electric field, in the specific context of impedance spectroscopy of biological cell suspensions.

2.1 Material dielectric properties

Every material has a specific set of electrical characteristics that are dependent on its dielectric properties and that affect the response of the material to an applied electric field. A conductor is a material that contains free charges. When a conductor is placed in a static electric field, a surface charge density is established from the movement of the free charges cancelling, as a consequence, the field inside the bulk material. In contrast, a dielectric material is a material that has only bound charges and no mobile carriers, and has the ability to store energy when an electric field is applied. When a perfect dielectric, a material that has no conductivity, is placed in an external electric field no net current flows and the induced polarisation of the bound charges reduces the field inside the material.

2.1.1 Permanent and induced dipoles

A dipole consists of two equal charges q of opposite sign separated by a distance d. An atom with its electrons at a distance from the positive nucleus does not necessarily form a net dipole, as the electric centre may correspond to that of the nucleus. However, every such atom is polarisable under the action of an external electric field: the external electric field moves positive and negative charges in opposite directions, dipoles are

induced and the material is polarised. In addition, materials can contain molecules that form permanent dipoles independent of the application of an electric field (polar dielectrics). Permanent dipoles are also influenced by an externally applied electric field. Water is an example of polar material. Water molecules are in fact asymmetric molecules and the difference between the position of the centre of positive and negative charges gives rise to a dipole moment.

When a dipole is placed under the action of an applied electric field it experiences a net force (Figure 2.1(a)) that can be written as:

$$\mathbf{F} = q\mathbf{E}(\mathbf{r} + \mathbf{d}) - q\mathbf{E}(\mathbf{r}) \tag{2.1}$$

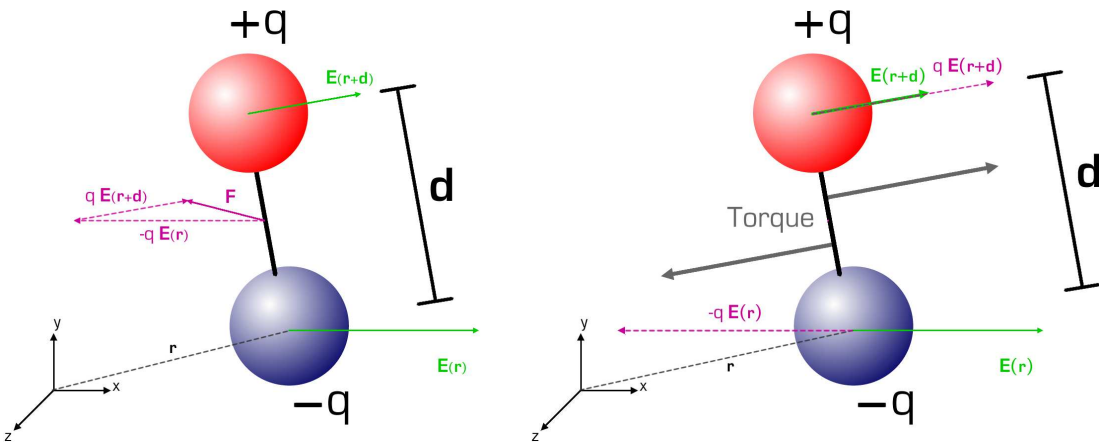

FIGURE 2.1: (a) Force experienced by a dipole under the action of an applied electric field. (b) Torque acting on a dipole placed in a homogeneous electric field.

The expansion of the expression of the net force as Taylor series gives the infinitesimal dipole approximation [105]:

$$\mathbf{F}_{dipole} = q\mathbf{d} \cdot \nabla\mathbf{E} = \mathbf{p} \cdot \nabla\mathbf{E} \tag{2.2}$$

where the quantity

$$\mathbf{p} = q\mathbf{d} \tag{2.3}$$

is known as the electrical dipole moment, and is a vector directed from the negative to the positive charge.

A net force is obtained only if the gradient of the electric field is non-zero, i.e. the electric field is non-uniform.

When the same dipole is placed in a homogenous electric field, it experiences a net electrostatic torque that makes the dipole to align with the field Figure 2.1(b). The

torque is given by

$$\mathbf{O} = \frac{\mathbf{d}}{2} \times q\mathbf{E} + \frac{-\mathbf{d}}{2} \times (-q\mathbf{E}) \tag{2.4}$$

and it can also be expressed in terms of the dipole moment:

$$\mathbf{O} = q\mathbf{d} \times \mathbf{E} = \mathbf{p} \times \mathbf{E} \tag{2.5}$$

The dipole alignment is opposed by random thermal agitation and polarisation is a net effect of a constantly changing charge distribution.

Polarisation **P** is the electrical dipole moment per unit volume. For isotropic material **P** has the same direction as the electric field vector **E**:

$$\mathbf{P} = \mathbf{D} - \epsilon_0\mathbf{E} = (\epsilon_r - 1)\epsilon_0\mathbf{E} = \chi\epsilon_0\mathbf{E} \tag{2.6}$$

Where **D** the electric flux density (or displacement) and its divergence is equal to the free volume charge density. ϵ_0 is the permittivity of free space and it has a value of 8.854x10^{-12} F m^{-1}, ϵ_r is the relative permittivity of the material. χ = ϵ_r - 1 is the electric susceptibility of a material and is a macroscopical parameter related to the polarisability α [12].

A material subjected to an electric field may experience different polarisation effects that contribute to its overall permittivity. A basic description of the principal of polarisation processes is as follows.

2.1.2 Polarisation mechanisms

When a material polarises under the action of an electric field, an additional electric field in the opposite inverse direction is superimposed on the original one; this is where the term dielectric comes from. Materials exhibiting dielectric properties are characterised by their relative permittivity or dielectric constant, which can take values between 1 (for vacuum) and 78 (for water).

There are three basic types of polarisation mechanisms that can occur in a homogeneous dielectric material in reaction to an applied electric field: electronic, atomic and orientational polarisation [105, 12, 30]. Each mechanism is centred around its characteristic frequency that is the reciprocal of the characteristic time, i.e the time that take to the system to adjust to a new equilibrium under external stimuli. If the frequency of the applied electric field is below the characteristic frequency, the system has enough time

to adjust to a new equilibrium and the polarisation is fully established. Above the characteristic frequency the oscillation of the electric field is too fast and no polarisation of the material takes place.

Electronic polarisation occurs in all materials, polar and non-polar. It consists of a small transition of the electronic cloud with respect to the nucleus, when an electric field is applied. Displacement of electrons is very fast and the characteristic frequency of the process is of the order of 10^{15} Hz. In atomic polarisation, instead of a shift of the electronic cloud, a displacement of positive ions with respect to negative ions from their equilibrium position in a molecule takes place. This process is typical in crystal and occurs in the frequency range above 10^{12} Hz.

Orientational polarisation occurs in polar materials and is due to the alignment of the permanent dipoles with the applied electric field. The characteristic frequency of this process is very sensitive to temperature effects, as a temperature increment corresponds to a higher thermal agitation and a consequent reduction of the alignment.

In addition, if the dielectric is heterogeneous, an additional polarisation mechanisms takes place: interfacial polarisations, also know as Maxwell- Wagner polarisation. Interfacial polarisation occurs when the motion of migrating charges is impeded due to the heterogeneous nature of the material under investigation. When an electric field is applied, charges tend to accumulate at discontinuities between the different dielectrics, forming a charge layer. The characteristic frequency of this process and the material polarisability depends on the geometry and properties of the various phases present.

As interfacial polarisation is a mechanism of central interest in the contest of this work, it will be described in more detail in section 2.1.5

The total polarisability of the material is the sum of the different polarisation mechanisms. Assuming all the polarisation mechanisms to be independent, the total polarisability of a dielectric material is:

$$\alpha = \alpha_e + \alpha_a + \alpha_o + \alpha_i \tag{2.7}$$

where α_e, α_a, α_o and α_i are the electronic, atomic, orientational and interfacial polarisability respectively. The frequency response of the different polarization mechanisms is described in Figure 2.2.

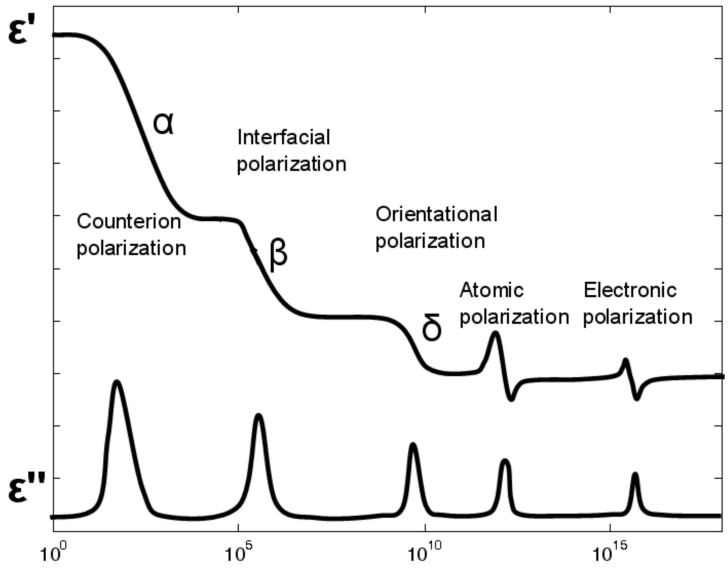

FIGURE 2.2: Diagram illustrating the frequency response of the different polarization mechanisms. Each polarization mechanism has a characteristic frequency. As the frequency increases, the slower mechanism drops-off, leaving only the faster mechanisms to contribute to the dielectric storage (ϵ'). The loss factor (ϵ'') peaks at the characteristic frequencies.

2.1.3 Relative and complex permittivity

Permittivity characterises the ability of a material to store charge and is a measure of the amount of the dipole moment density induced by an electric field. When a voltage V is applied to the plates of an ideal parallel plate capacitor in vacuum, the plates build up a charge Q equal to

$$Q = CV \tag{2.8}$$

where the capacitance C is dependent on the plate surface area A and the distance between the plates d according to the relation:

$$C = \epsilon_0 \frac{A}{d} \tag{2.9}$$

where ϵ_0 is the permittivity of vacuum. If a sinusoidal AC voltage with an angular frequency ω is applied to the plates, the impedance Z of the capacitor is given by

$$Z = \frac{1}{i\omega C} \tag{2.10}$$

where $i = \sqrt{-1}$, is the imaginary unit.

When a perfect dielectric material, i.e. a perfect insulator, is placed between the plates of the capacitor as shown in Figure 2.3(a), it increases the storage capacity of the capacitor by neutralising charges at the electrodes, as surface charges of opposite value are induced on both sides of the dielectric. The capacitance, in this case, changes to

$$C = \epsilon_0 \epsilon_r \frac{A}{d} \tag{2.11}$$

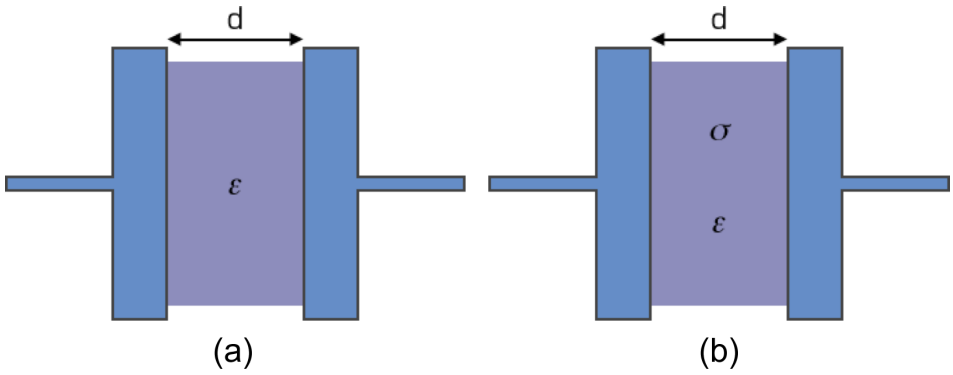

FIGURE 2.3: Diagram showing a parallel plate capacitor filled with a dielectric material: (a) when the material is a perfect dielectric, no current path is generated between the armatures and the storage capacity is increased by a factor equal to ϵ_0. (b) If the dielectric is non-ideal, the free ions cause a current flow between the two electrodes. This behaviour can be described adding a resistor in parallel with the capacitor.

In reality, a perfect dielectric does not represent an accurate model for complex biologic materials, as conductive properties of materials are not taken into account.

Now let us assume that the dielectric material placed between the plates of the capacitor of Figure 2.3(b) is non-ideal. When a voltage is applied to the capacitor, a current path is originated from ion movement and acts like a parallel resistor which actually discharges the ideal capacitor.

The complex admittance Y of the capacitor filled with a non-ideal dielectric can be defined as

$$Y = G + i\omega C = \frac{A}{d}(\sigma + i\omega\epsilon_0\epsilon_r) \tag{2.12}$$

where G is the conductance of the material and is given by

$$G = \sigma \frac{A}{d} \tag{2.13}$$

And C is the capacity of a loss-free dielectric (equation (2.9)).

In order to incorporate dielectric losses and the frequency dependent response of the dielectric to the field, it is convenient to define the permittivity as a complex quantity:

$$\epsilon = \epsilon_r \epsilon_0 - i\frac{\sigma}{\omega} = \epsilon' - i\epsilon'' \tag{2.14}$$

The real part of the permittivity is a measure of how much energy from an external electric field is stored in the material and is at 90° phase shift from the driving field. The imaginary part of the permittivity is in-phase and is a measure of how dissipative or lossy the material is to an external electric field.

In the same manner, the complex conductivity of a material is:

$$\sigma = \sigma + i\omega\epsilon_r\epsilon_0 = \sigma' + i\sigma'' \tag{2.15}$$

Taking into account the frequency dependence, equation (2.12) can be rewritten as:

$$Y = \frac{A}{d}(\sigma + i\omega\epsilon_0\epsilon_r) = i\omega C = i\omega\frac{A}{d}\epsilon = i\omega\frac{A}{d}(\epsilon' - i\epsilon'') \tag{2.16}$$

The loss angle δ is defined as the ratio of the imaginary part of the dielectric constant and the real part:

$$\tan\delta = \frac{\epsilon''}{\epsilon'} \tag{2.17}$$

and is zero for non-lossy insulators.

2.1.4 Relaxation and dispersion

Polarisation and displacement of charges in a material do not occur instantaneously. There is a limit in the speed with which a dipole can orient within a time varying electric field and it depends on the physical size of the dipole moment. The time required by the dipole to respond to a change of the electric field, after the application of an excitation signal, and relax to the new equilibrium, is the *relaxation time*. If the frequency of the applied electric field is low enough so that all charges have the necessary time to change their position and follow the field, polarisation is maximum. When the frequency of the electric field approaches the relaxation frequency, the period of time that the dipole moment has to follow the field is not enough for the polarisation to fully establish. As a result, with increasing frequency the real part of the permittivity, and thus the energy storage, is reduced and energy dissipation starts taking place.

As previously introduced, the energy dissipated in the system is related to the imaginary part of the permittivity (ϵ'') and reaches its maximum at the relaxation frequency. At lower frequencies the polarisation rate is small and therefore the energy dissipated is minimal. Above the relaxation frequency, both ϵ' and ϵ'' drop off as the electric field is too fast to influence the dipole rotation and the orientational polarisation (typically the slowest polarisation mechanism) disappears, resulting in minimal energy dissipation.

For a material that exhibits a single relaxation process with a single characteristic time constant τ (*Debye single dispersion*) the corresponding frequency dependent complex permittivity can be expressed as:

$$\epsilon = \epsilon_0 \left(\epsilon_\infty + \frac{\epsilon_s - \epsilon_\infty}{1 + i\omega\tau} \right) - i\frac{\sigma_s}{\omega} \tag{2.18}$$

where ϵ_s is the value of permittivity for a static driving field, ϵ_∞ represents the permittivity at infinite frequency, and σ_s is the ionic conductivity.

Separating equation (2.14) into real and imaginary part, we obtain:

$$\epsilon' = \epsilon_0 \left(\epsilon_\infty + \frac{\epsilon_s - \epsilon_\infty}{1 + (\omega\tau)^2} \right) \tag{2.19}$$

$$\epsilon'' = \epsilon_0 \left(\frac{(\epsilon_s - \epsilon_\infty)\omega\tau}{1 + (\omega\tau)^2} \right) + \frac{\sigma_s}{\omega} \tag{2.20}$$

The characteristic response in complex permittivity as a function of frequency of a Debye single dispersion is shown in Figure 2.4. It can be observed that the real part of the permittivity is characterised by two different frequency-independent levels and a transition zone around the relaxation frequency. The imaginary part shows a peak at the characteristic relaxation frequency ($f = 1/(2\pi\tau)$). Note that the contribution to the DC loss which is given by the ionic conductivity was subtracted.

An alternative way of representing the complex permittivity is plotting the loss factor ϵ'' versus the permittivity real part ϵ' in a complex plane with the frequency as the independent parameter (Cole-Cole plot, Figure 2.5). The plot consists of a semicircle with the centre lying on the axis $\epsilon''= 0$ and radius equal to the maximum imaginary part of the dielectric constant:

$$\epsilon''_{max} = \epsilon_0 \left(\frac{\epsilon_s - \epsilon_\infty}{2} \right) \tag{2.21}$$

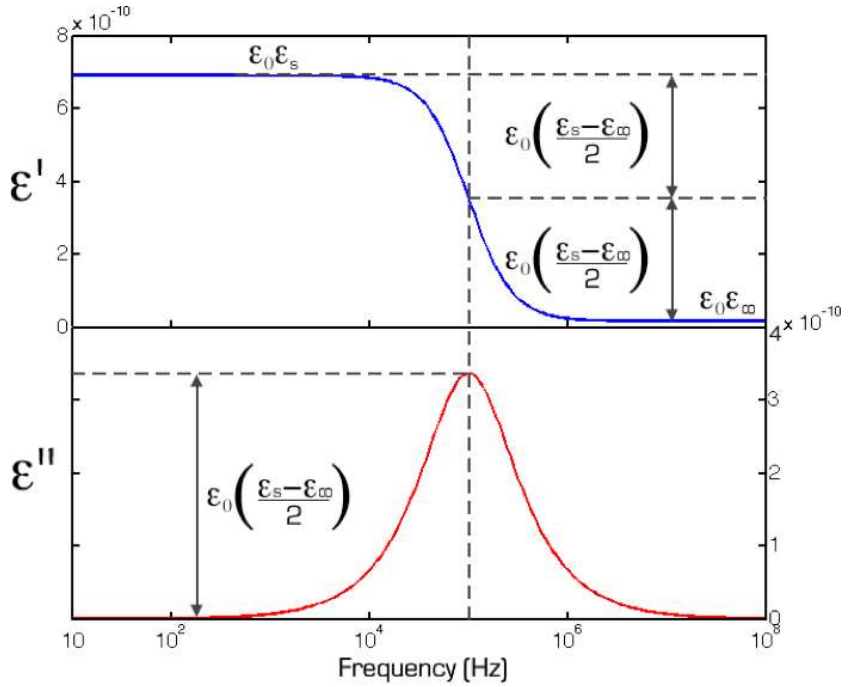

FIGURE 2.4: Complex permittivity plot showing a Debye single relaxation process. ϵ' is constant above and below the relaxation with the transition occurring near the relaxation frequency (10 KHz). ϵ'' is small above and below relaxation and peaks in the transition region at the relaxation frequency. Contribution of the DC loss is not shown.

The frequency moves counter clockwise on the curve and the peak of the loss factor occurs at $1/\tau$.

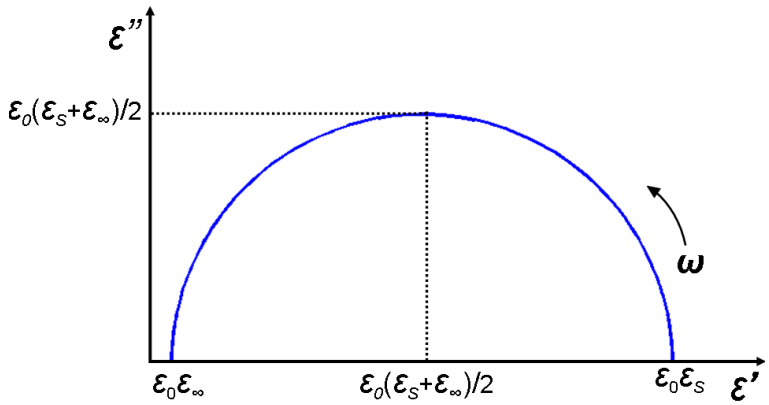

FIGURE 2.5: Cole-Cole representation of the complex permittivity for the Debye single relaxation process of Figure 2.4

In real dielectric materials the dispersion is generally the result of more than one relaxation process. In order to take into account all the contributions from the different

relaxations, the expression of the complex permittivity becomes [106]:

$$\epsilon = \epsilon_0 \left(\epsilon_\infty + \frac{\epsilon_s - \epsilon_\infty}{1 + i\omega\tau^{(1-\beta)}} \right) - i\frac{\sigma_s}{\omega} \tag{2.22}$$

where τ is now the average relaxation time. The term β is a parameter measuring the spread of the relaxation times and ranges between 0 and 1. β equals 0 when a single dispersion mechanism is present and tends to 1 for an infinite number of relaxation processes [107].

The complex permittivity plots and the Cole-Cole plots for multiple relaxation processes are reported in Figure 2.6(a) and Figure 2.6(b) respectively. It can be observed how for increasing values of β the profile of the permittivity decreases and the loss peaks stretch over a wider frequency range (Figure 2.6(a)). The Cole-Cole representation of a material with multiple relaxation frequencies consist of an arc of a circle with the centre lying below the horizontal axis (Figure 2.6(b)). The depression of the arc increases with increasing values of β.

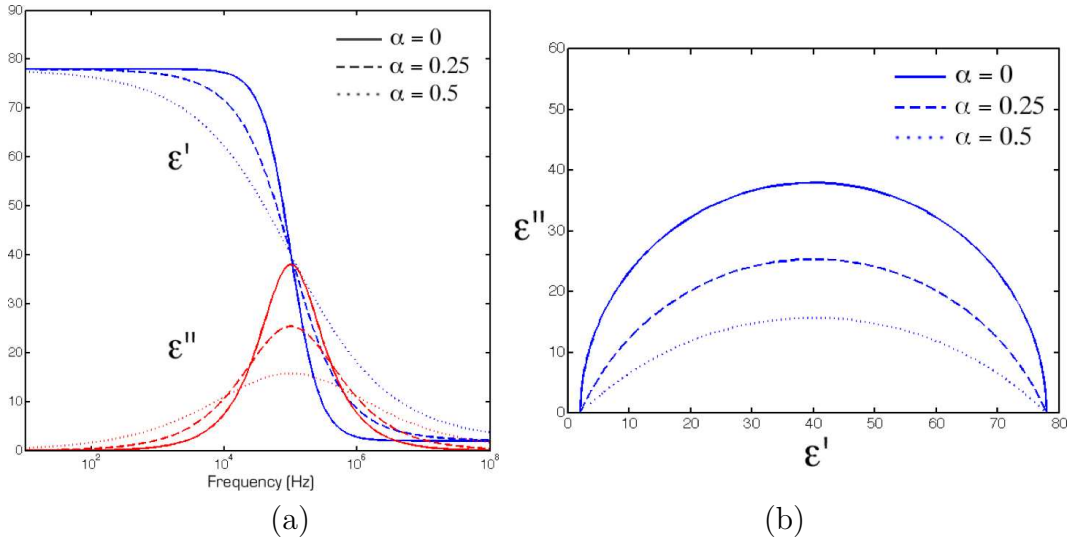

(a) (b)

FIGURE 2.6: Complex permittivity plot for multiple relaxation processes characterised by $\beta = 0, 0.25, 0.5$. (a) Frequency response of the real and imaginary part of the complex permittivity. (b) Cole-Cole plots of the complex permittivity.

2.1.5 Maxwell-Wagner interfacial polarisation and effective dipole moment

As previously introduced, interfacial polarization is due to charge accumulation at interfaces in an inhomogeneous medium. A simple example of Maxwell-Wagner interfacial

polarization is given by a parallel plate capacitor containing two layers of real dielectrics with different electrical proprieties as shown in Figure 2.7. The parameters characterizing the two dielectrics are the permittivities ϵ_1 and ϵ_2, the conductivities σ_1 and σ_2, and the thickness of each slab d_1 and d_2, with $d = d_1 + d_2$. Each slab of dielectric can be modeled using the equivalent circuit of equation (2.10). The combination of the two equivalent circuits can be rewritten as a single capacitance with a complex permittivity, which represents the properties of an equivalent dielectric medium.

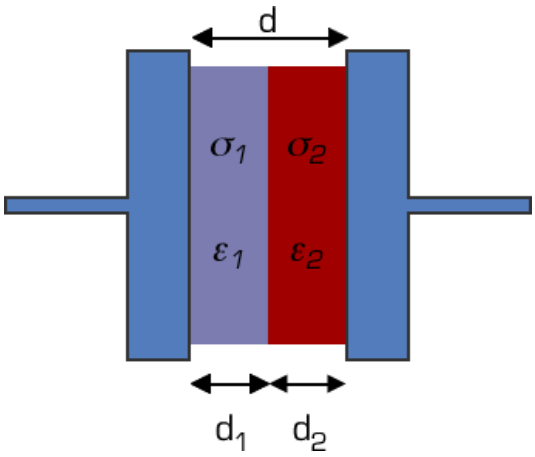

FIGURE 2.7: Parallel plate capacitor including two layers of materials characterized by different dielectric properties ϵ and σ.

The complex permittivity of the equivalent medium can be expressed in the same form as equation (2.19) and equation (2.20), where ϵ_∞, ϵ_s, τ and σ_s have now the following expressions [105]:

$$\epsilon_\infty = \frac{d\epsilon_1\epsilon_2}{d_1\epsilon_2 + d_2\epsilon_1}, \tag{2.23a}$$

$$\epsilon_s = \frac{d(d_1\epsilon_1\sigma_2^2 + d_2\epsilon_2\sigma_1^2)}{(d_1\sigma_2 + d_2\sigma_1)^2}, \tag{2.23b}$$

$$\tau = \frac{\epsilon_0(d_1\epsilon_2 + d_2\epsilon_1)}{d_1\sigma_2 + d_2\sigma_1}, \tag{2.23c}$$

$$\sigma_s = \frac{d\sigma_1\sigma_2}{d_1\sigma_2 + d_2\sigma_1}. \tag{2.23d}$$

Similarly to a capacitor with two slabs of different dielectric materials, a system consisting of a dielectric particle suspended in a dielectric medium can be seen as an inhomogeneous material with a discontinuity given by the particle/liquid interface. When such a system is subjected to an electric field it experiences a charge redistribution resulting in an induced dipole across the particle. The induced dipole moment is related to the

complex dielectric properties of both particle and suspending medium; this relationship is described by the effective complex polarisability of the particle with respect to its suspending medium. In the case of a homogeneous dielectric sphere it is defined as [105]:

$$\alpha = 3\epsilon_m \left(\frac{\epsilon_p - \epsilon_m}{\epsilon_p + \epsilon_m} \right) \tag{2.24}$$

where ϵ_p and ϵ_m are the complex permettivities of the particle and the medium respectively. Now, the effective dipole moment of a spherical particle of volume v suspended in a liquid can be expressed in term of α as [12]:

$$\mathbf{P_{eff}} = v\alpha\mathbf{E} \tag{2.25}$$

This expression for the dipole moment is correct assuming the radius of the particle small compared to the characteristic length the electric field non- uniformity. The expression between brackets in eq. 2.24 is known as the Clausius-Mossotti factor (CM):

$$f_{CM} = \frac{\epsilon_p - \epsilon_m}{\epsilon_p + 2\epsilon_m} \tag{2.26}$$

It is a complex variable reflecting the frequency dependence of the effective polarisability of the system, i.e. the frequency dependence of the effective capacitance and conductivity of the particle with respect to the suspending medium. It ranges between the theoretical values 1 and -$\frac{1}{2}$ for the real part, and $\pm$ 3/4 for the imaginary part. By changing the electric field frequency, the CM factor can experience a transition from a positive value to a negative value.

Separating real and imaginary parts, the CM factor can be expressed as:

$$\Re\left[f_{CM}\right] = \frac{\epsilon_p - \epsilon_m}{\epsilon_p + 2\epsilon_m} + \frac{\left(\frac{\sigma_p - \sigma_m}{\sigma_p + 2\sigma_m}\right) - \left(\frac{\epsilon_p - \epsilon_m}{\epsilon_p + 2\epsilon_m}\right)}{1 + \omega^2\tau_{MW}^2} \tag{2.27}$$

$$\Im\left[f_{CM}\right] = \frac{\left(\frac{\epsilon_p - \epsilon_m}{\epsilon_p + 2\epsilon_m} - \frac{\sigma_p - \sigma_m}{\sigma_p + 2\sigma_m}\right)\omega\tau_{MW}}{1 + \omega^2\tau_{MW}^2} \tag{2.28}$$

where $\Re$ and $\Im$ indicate the real and imaginary part respectively and τ_{MW} is the Maxwell-Wagner relaxation time constant:

$$\tau_{MW} = \frac{\epsilon_p + 2\epsilon_m}{\sigma_p + 2\sigma_m} \tag{2.29}$$

From the analysis of eq. 2.27, it can be seen that the low frequency limiting value of the CM factor is defined by the conductivities of the particle and suspending medium, while the high frequency limiting value is dominated by the particle and suspending medium permittivities.

The real and imaginary part of the complex Clausius-Mossotti factor for the specific case of a spherical polystyrene particle suspended in media with different conductivities ($\epsilon_p << \epsilon_m$ and $\sigma_p >> \sigma_m$) for frequencies ranging from 100 kHz to 1 GHz are shown in Figure 2.8. The magnitude of the real part decreases with increasing conductivity of the medium and that positive values occur only for low conductivity suspending media. In the case of high conductivity solutions, such as phosphate saline buffer (PBS, $\sigma = 1.6$ S/m) is used as the suspending medium, the real part of the CM factor remains negative for all frequencies. In the same way, the highest magnitude peak of the imaginary part is obtained for the lowest conductivity, but for these values of the simulated parameters no transition to positive values can be observed. As mentioned above, this change in magnitude and polarity of the CM factor is the manifestation of the frequency dependence that characterises the response of suspended particles to the action of an electric filed, which will discussed in more details in the following section.

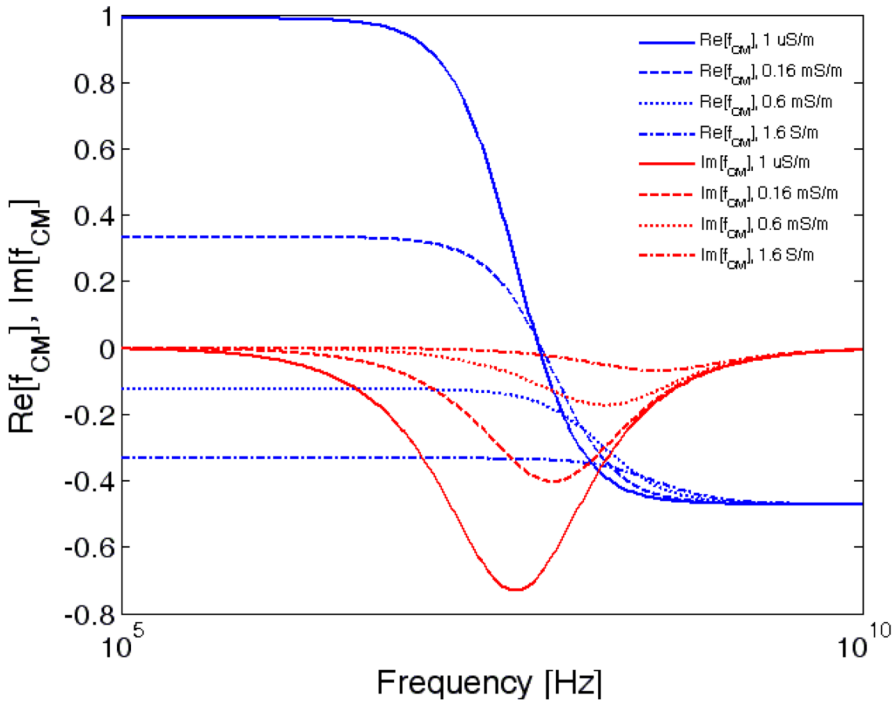

FIGURE 2.8: Frequency dependence of the real and imaginary parts of the Clausius-Mossotti factor for a polystyrene sphere suspended in different conductivity media. The following parameters were used: media: $\epsilon_m = 78\ \epsilon_0$; $\sigma_m =$ 0.001, 0.16, 0.6, 1.6 S/m; beads: $\epsilon_p = 3\epsilon_0$; $\sigma_p = 0.4$ S/m.

2.2 AC Electrokinetics

AC electrokinetics is the study of the movement of polarisable particles in non-uniform AC electric fields [12]. It includes a variety of phenomena such as electrophoresis, electroosmosis, dielectrophoresis, electrorotation, etc., all arising from the interaction of the applied electric field with the particles and the suspending fluid.

2.2.1 Dielectrophoresis

Dielectrophoresis (DEP) is the movement of non-charged dielectric particles in an inhomogeneous electric field [105, 108, 12, 94].

When a uniform electric field is applied, a neutral particle become polarised and an induced dipole arises across the particle. The induced dipole is aligned with the field and its direction is different according to the polarisability of the particle with respect to that of the field (Figure 2.9 and Figure 2.10). If the particle polarisability is higher than that of the suspending medium, the number of charges produced at the interface between the particle and the liquid is higher inside the particle and the induced dipole points in the direction of the field, Figure 2.9(a). If the particle is less polarisable than the suspending medium, more charges are produced outside the particle and the net dipole points in the direction against the field, Figure 2.9(b). In both cases, the net translation force results to be zero and no net movement will be experienced by the particle. Figure 2.10(a) and (b) show the numerical simulations of the electric field distribution for the two cases described in Figure 2.9(a) and (b) respectively. The surface plot shows the magnitude of the electric field and the streamlines show the direction of the electric field vectors

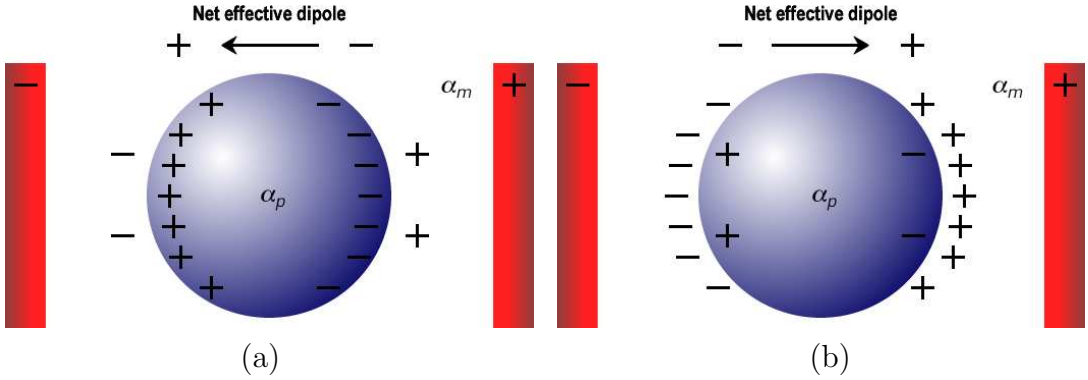

FIGURE 2.9: Uncharged particle exposed to a uniform electric field. (a) the polarisability of the particle is higher than that of the medium. (b) the polarisability of the particle is lower than that of the medium.

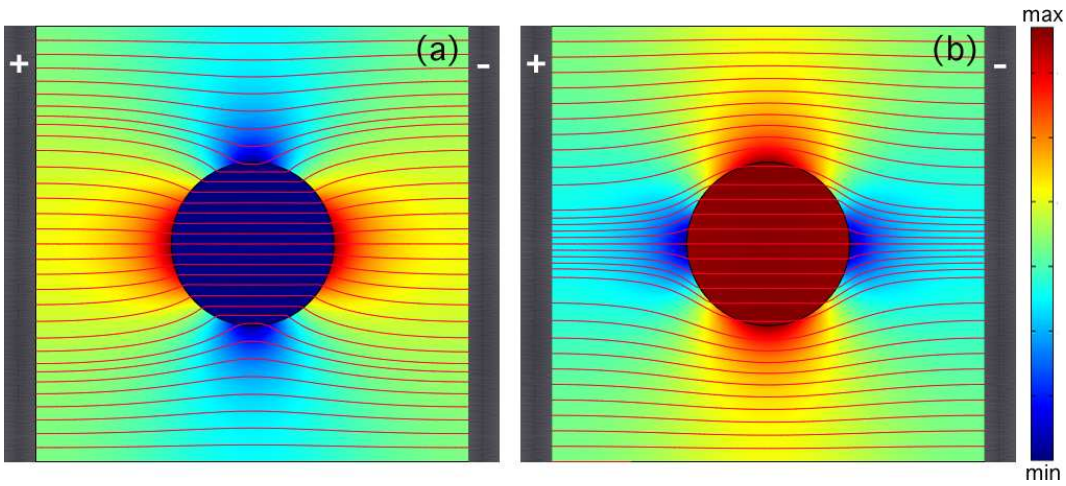

FIGURE 2.10: Numerical simulations showing the electric field distribution around a particle when a uniform electric field is applied. The surface plots indicate the intensity of the field, whereas the lines indicate the field direction. (a) If the polarisability of the particle is higher than that of the medium (i.e. a conducting particle in an insulating medium or a particle with high permitivity in a medium with low permitivity), the number of charges accumulated at the interface is higher inside the particle than in the medium. As a result, the electric field lines bend towards the particle and the magnitude of the field inside the particle is nearly zero. (b) The polarisability of the particle is lower than that of the medium and the field inside the particle is similar to that outside.

When the particle is placed in a non-uniform electric field the situation is different. Again the particle polarises and the charges redistribute in order to have equal amounts of oppositely charged ions facing the oppositely charged electrodes (Figure 2.11). However, as the field is non- uniform, there is an imbalance of forces acting on the induced dipole at opposite ends of the particle (Figure 2.12). The resultant translation force is now different from zero, causing the particle movement.

The direction of the movement is related to the particle polarisability. When the particle is more polarisable than the suspending medium, the dipole has the same direction of the field and the particle experience positive dielectrophoresis (pDEP), moving towords the region of higher electric field intensity. When the particle is less polarisable than the electric field, the particle experiences negative dielectrophoresis (nDEP) and the movement occurs in the opposite direction

The behaviour of a particle in an inhomogeneous electric field depends not only on the particle and suspending medium electric properties, but also on the frequency of the applied field. Particles may therefore experience a force towards a high electric field region at a certain frequency and experience a force in the opposite direction at a different frequency.

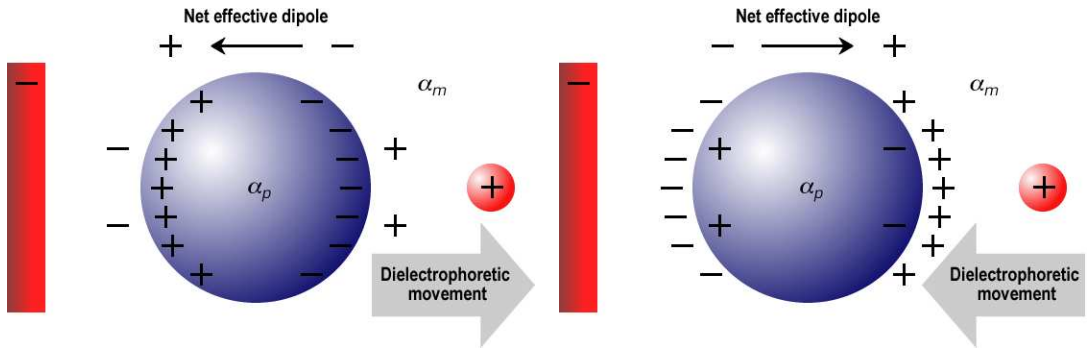

(a) (b)

FIGURE 2.11: The polarisability of the particle is higher than that of the medium. (b) the polarisability of the particle is lower than that of the medium.

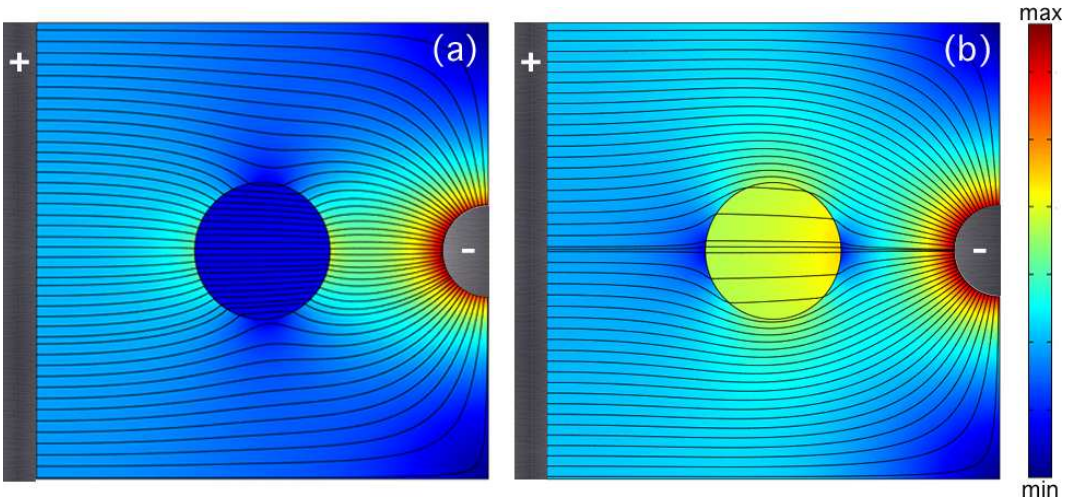

FIGURE 2.12: Numerical simulations showing the electric field distribution around a particle when a non-uniform electric field is applied. The surface plots indicate the intensity of the field, whereas the lines indicate the field direction. (a) The polarisability of the particle is higher than that of the medium. (b) The polarisability of the particle is lower than that of the medium.

The expression for the time average dielectric force acting on a particle of radius a, suspended in a medium of permittivityϵ_m is given by [105, 12],

$$F = \pi \epsilon_m a^3 Re[f_{CM}] \nabla |\mathbf{E}|^2 \tag{2.30}$$

where $\nabla\ |\mathbf{E}|^2$ is the gradient of the square of the electric field.

The expression of the Clausius-Mossotti factor has been introduced in section 2.1.5. It is a complex quantity related to the dielectric properties of the particle and the medium, and to the frequency of the applied field. It describes the dependence of the magnitude of the polarisability, and therefore the effective dipole moment of the particle, on the

frequency of the electric filed. Variations in this factor give rise to a DEP force that is frequency dependent and unique to each particle type.

In particular, for a given particle, there is a frequency at which no DEP forces are present, i.e. the frequency at which the real part of the Clausius-Mossotti factor equals zero. This frequency point is called crossover frequency and is easily observable experimentally. Theoretically can be calculated as:

$$f_{cross} = \frac{1}{2\pi}\sqrt{\frac{(\sigma_m - \sigma_p)(\sigma_p + 2\sigma_m)}{(\epsilon_p - \epsilon_m)(\epsilon_p + 2\epsilon_m)}} = \frac{1}{\sqrt{2\pi}}\sqrt{\frac{\sigma_m - \sigma_p}{\epsilon_p - \epsilon_m} f_{MW}} \tag{2.31}$$

with

$$f_{MW} = \frac{1}{2\pi\tau_{MW}} \tag{2.32}$$

where f_{cross} is the crossover frequency, f_{MW} is the Maxwell-Wagner relaxation frequency, and τ_{MW} is the Maxwell-Wagner time constant.

The measurement of the crossover frequency as a function of the conductivity of the suspending medium is more practicable than direct measurement of the exerted DEP force and provides information on the dielectric properties of the suspended particle. For a biological cell modelled as a shelled-sphere, the crossover frequency can be written as:

$$f_{cross} = \frac{\sqrt{2}}{8\pi R C_{mem}}\sqrt{(4\sigma_m - RG_{mem})^2 - 9R^2G_{mem}^2} \tag{2.33}$$

where R is the radius of the cell and C_{mem} and G_{mem} are the specific capacitance and conductance of the membrane [91, 109].

2.2.2 Electrorotation

When a particle suspended in a liquid is exposed to a rotating electric field it will experience a torque. A dipole is induced in the particle and each time the electric field changes direction, the dipole must realign with the field, causing the particle rotation.

As the polarisation process is not immediate, the dipole will need a finite time to become aligned with the field. As a result, the dipole will lag the external field and a frequency dependent external torque will exist.

The time-averaged torque is given by [12]:

$$\mathbf{A_{rot}} = -4\pi\epsilon_m a^3 \; \mathrm{Il}\left[\frac{\epsilon_p - \epsilon_m}{\epsilon_p + 2\epsilon_m}\right] |\mathbf{E}|^2 \tag{2.34}$$

Where a is the particle radius, $\mathbf{E}$ the electric field, ϵ_p and ϵ_m the complex permittivity of the particle and medium respectively, and Il indicates the imaginary part. The torque is zero when the phase angle between the polarisation vector and the field is zero, it is maximum when the phase angle is $\pm$ 90°. If the induced dipole lags behind the field, i.e. the charge relaxation time constant of the particle is smaller than that of the medium ($\tau_p = \epsilon_p/\sigma_p < \tau_m = \epsilon_m/\sigma_m$) the rotation follows the field (co-rotation); this happens for negative values of the imaginary part of the Clausius-Mossotti factor. If the dipole leads the field, i.e. $\tau_p > \tau_m$, the rotation is opposite to the field (anti-rotation). In this case the imaginary part takes only positive values. The electrorotation spectrum of a particle can be measured indirectly measuring the angular velocity of the suspended particle, given by

$$R_{rot}(\omega) = -\frac{\epsilon_m \; \mathrm{Il}[f_{CM}]|\mathbf{E}|^2}{2\eta} K \tag{2.35}$$

where $R_{ROT}(\omega)$ is the rotation rate, η the viscosity and K a scaling factor introduced to compensate the uncertainties of the actual values of the electric field and the viscosity.

2.3 Dielectric models in biology

Interfacial polarization process plays a very important role in biology, as biomaterials are inhomogeneous dielectrics. Cell suspensions are inhomogeneous dielectric particles placed in a dielectric fluid or in an electrolyte. A conductive dielectric particle suspended in a liquid experiences Maxwell-Wagner interfacial polarization at the particle/liquid interface, inducing a dipole moment on the particle. The interaction of an applied electric field and the induced dipole is at the basis of AC electrokinetics.

2.3.1 The shell model for biological particles

A biological cell is a heterogeneous system that consists of the plasma membrane and the cytoplasm. The plasma membrane has low conductivity. Assuming the cytoplasm to be a homogeneous phase, a biological cell can be modelled as a conductive sphere covered with an insulating thin shell [110, 111, 112]. A schematic of a single-shell modelled

particle is shown in figure 2.13. The particle consists of a core with permittivity ϵ_3 and conductivity σ_3, covered by a shell with permittivity ϵ_2 and conductivity σ_2, suspended in a medium of permittivity ϵ_1 and conductivity σ_1.

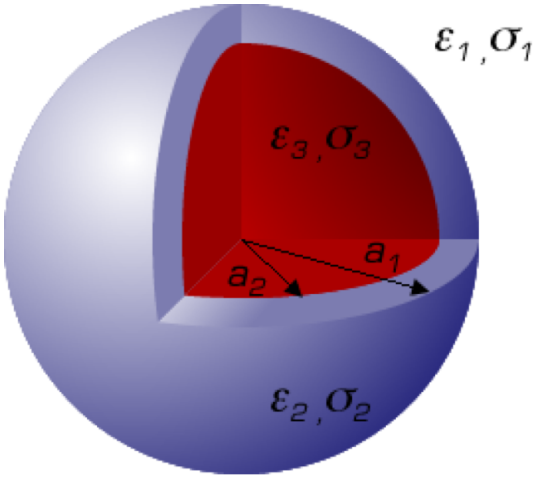

FIGURE 2.13: Schematic of a spherical particle with a single shell.

The polarisability and the dipole moment for this system can be written as [105]:

$$\alpha = 3\epsilon_1 f_{CM,23} = 3\epsilon_1 \left(\frac{\epsilon_{23} - \epsilon_1}{\epsilon_{23} + 2\epsilon_1} \right) \tag{2.36}$$

$$\mathbf{p} = 4\pi\epsilon_1 f_{CM,23} \alpha_1^3 \mathbf{E} \tag{2.37}$$

where the particle complex ϵ_{23} permittivity is given by:

$$\epsilon_{23} = \epsilon_2 \frac{\gamma_{12}^3 + 2\left(\frac{\epsilon_3 - \epsilon_2}{\epsilon_3 + 2\epsilon_2}\right)}{\gamma_{12}^3 - \left(\frac{\epsilon_3 - \epsilon_2}{\epsilon_3 + 2\epsilon_2}\right)} \tag{2.38}$$

Where the factor $\gamma_{12} = \frac{\alpha_1}{\alpha_2}$

This model can be extended to multiple shells using the same equation (2.32) for each shell. The number of relaxation is equal to the number of interfaces in the model. An illustration of the Clausius-Mosotti factor as a function of frequency for different conducting solutions (0.1 M, 10 mM, 1 mM, 0.1 mM PBS solutions) for a single-shell modelled particle is showed in Figure 2.14.

Since the membrane acts as an interface to both the interior of the cell and the medium outside, two relaxations appear on the spectrum. Note how the magnitude of the factor vanishes with increasing the conductivity of the solution.

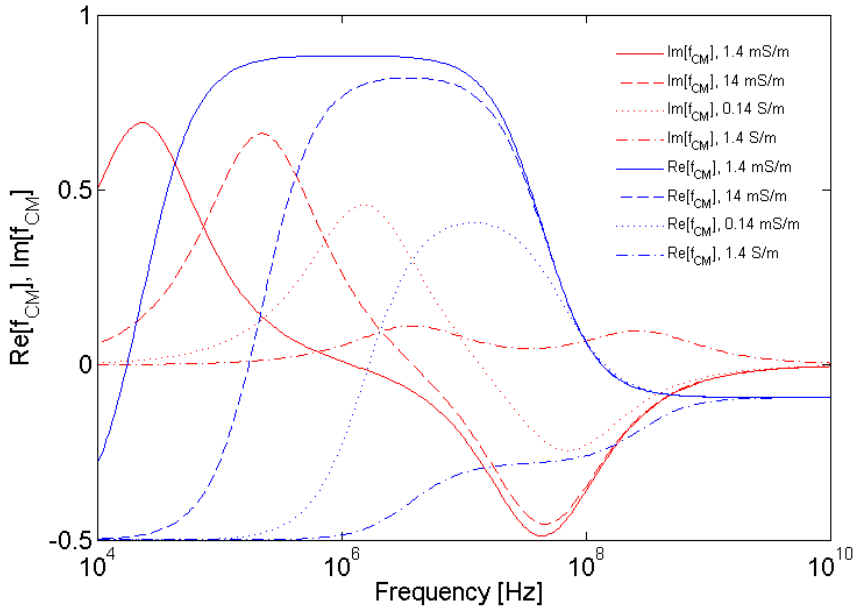

FIGURE 2.14: Frequency dependence of the real and imaginary parts of the Clausius-Mossotti factor for a single-shell sphere in suspending medium of different conductivities: $\sigma_1 = 1.4$ Sm^{-1}, 0.14 Sm^{-1}, 0.014 Sm^{-1}, 0.0014 Sm^{-1}. Other parameters are: $\sigma_2 = 1\text{x}10^{-8}$ Sm^{-1}, $\sigma_3 = 0.5$ Sm^{-1}, $\epsilon_1 = 78\ \epsilon_0$, $\epsilon_2 = 10\ \epsilon_0$, $\epsilon_3 = 60\ \epsilon_0$, a1= $2\text{x}10^{-6}$ m, a1-a2= 10^{-9} m.

2.4 Impedance spectroscopy

In impedance spectroscopy, the impedance of a system is obtained as a function of the frequency measuring the response of the system to an applied excitation signal. Normally, a small AC voltage swept over a range of frequencies is applied and the electrical current response measured. The complex impedance is then calculated as

$$Z(i\omega) = \frac{V(i\omega)}{I(i\omega)} \tag{2.39}$$

where V(iω) is the applied voltage and I(iω) the measured current. As the impedance is a complex quantity, it can be expressed separating the real and imaginary parts:

$$Z(i\omega) = Z_{re}(i\omega) + Z_{im}(i\omega) \tag{2.40}$$

or calculating the magnitude and the phase angle:

$$|Z(i\omega)| = \sqrt{Z_{re}(i\omega)^2 + Z_{im}(i\omega)^2} \tag{2.41}$$

$$\angle Z(i\omega) = \arctan \frac{Z_{re}(i\omega)}{Z_{im}(i\omega)} \tag{2.42}$$

From the measured impedance spectrum the dielectric properties of a system can be derived.

2.4.1 Maxwell's mixture theory

The impedance of a dilute suspension of particles subjected to a uniform electric field can be described in terms of individual particle dielectric properties by the Maxwell's mixture theory [113]. According to this theory, the equivalent complex permittivity of a mixture of particles and suspending medium is given by [113]

$$\epsilon_{mix} = \epsilon_m \frac{1 + 2\Phi f_{CM}}{1 - \Phi f_{CM}} \tag{2.43}$$

where ϵ_m is the permittivity of the medium, Φ is the volume fraction, defined as the ratio of the particle volume to the detection volume, and f_{CM} is the Clausius-Mossotti factor. The complex impedance of the system can now be defined as

$$Z_{mix} = \frac{1}{i\omega C_{mix}} \tag{2.44}$$

where C_{mix} is the complex capacitance of the system. Considering an ideal parallel plate electrode geometry, with electrode area A and gap g, the impedance of the mixture can be rewritten as

$$Z_{mix} = \frac{1}{i\omega \epsilon_{mix} G_f} \tag{2.45}$$

where G_f is the geometric cell constant of the system, which for an ideal parallel plate electrode system is A/g. When the system is not ideal and the electric field is not uniform, the effect of the fringing field is taken into account by modifying the geometric cell constant that becomes $G_f = kl$, where l is the length of the electrode and k is a correction factor, describing the fringing field. k is derived analytically using the Schwarz-Christoffel mapping [114].

An example of the impedance spectra of single shelled particle obtained with the mixture equation for varying values of the membrane permittivity and conductivity is shown in Figure 2.15 and Figure 2.16. For the specific calculated parameters (see Figure 2.15

and Figure 2.16 for details), the membrane relaxation process takes place around 500 kHz. The characteristic time of this process is dominated by the dielectric properties of the membrane, in particular the capacitance. An increment of the membrane relative permittivity results in a higher value of the capacitance. As a consequence, a longer time is required for the relaxation to take place and in the frequency domain this corresponds to a shift towards the low frequency values (Figure 2.15). An increment of the membrane conductivity leads to a lower value of the membrane resistance, and a consequent drop of the impedance magnitude. This effect can be observed only at frequency lower than 1 MHz, at higher frequency the membrane is effectively short circuited and does not affect the magnitude of the impedance (Figure 2.15). One of the limitation of the mixture theory is that it provides a good approximation of the average dielectric properties of the cells only if the volume fraction is small ($\Phi << 1$) and the electric field is uniform.

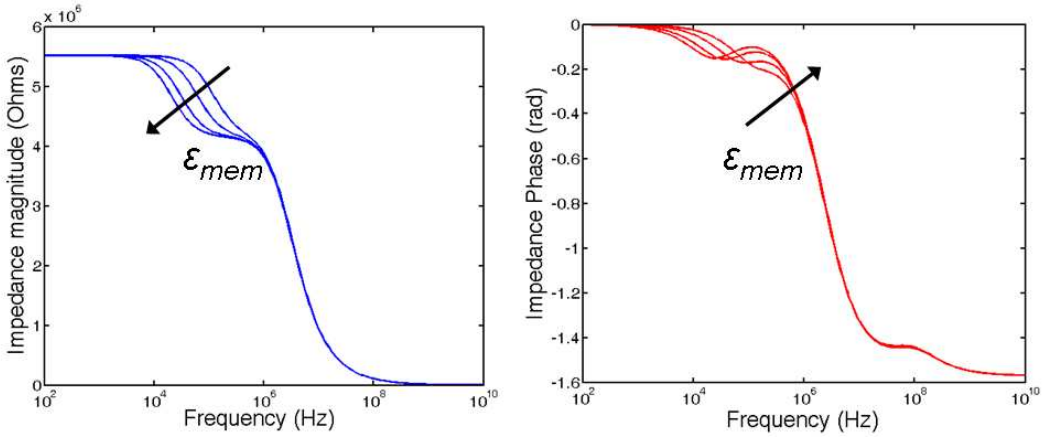

FIGURE 2.15: Impedance magnitude and phase angle spectra of a suspended shell covered particle when the membrane permittivity ϵ_2 varies between 10 and 70. Other parameters are: $\sigma_1 = 1\text{x}10^{-2}$ Sm^{-1}, $\sigma_2 = 1\text{x}10^{-9}$ Sm^{-1}, $\sigma_3 = 1$ Sm^{-1}, $\epsilon_1 = 78 \cdot \epsilon_0$, $\epsilon_3 = 50 \cdot \epsilon_0$, a1= $5\text{x}10^{-6}$ m, a1-a2= $20\text{x}10^{-9}$ m. The arrows show the direction of increasing values of ϵ_2.

2.4.1.1 Equivalent electric circuit model for a single shelled particle

An equivalent electric circuit to describe the behaviour of a single shelled particle was first proposed by Foster and Schwan [10] and consists of a series and parallel arrangement of capacitors and resistors shown in Figure 2.17.

For excitation frequencies lower than the membrane characteristic frequency there are no current paths through the inside of the cell (right side of the circuit). At higher frequencies the membrane capacitance is shorted and the current gradually enters the cytoplasm (left side of the circuit).

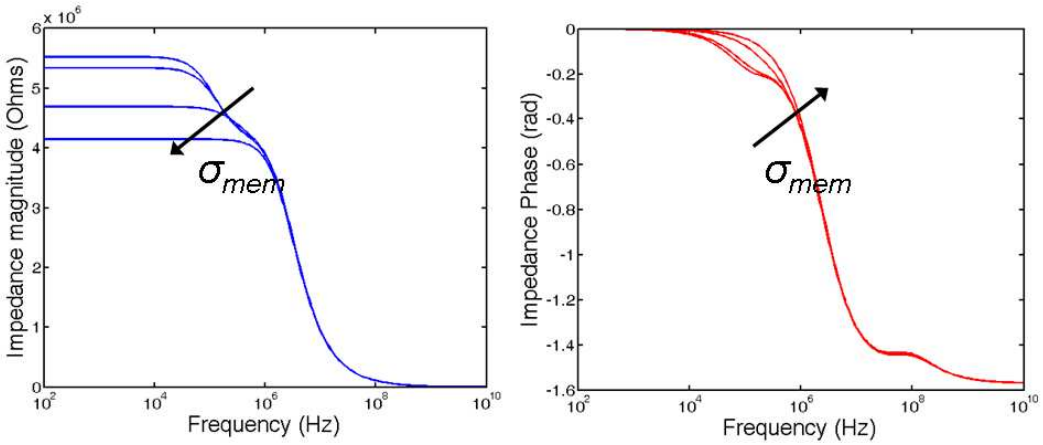

FIGURE 2.16: Impedance magnitude and phase angle spectra of a suspended shell covered particle when the membrane conductivity σ_2 varies between $1e^{-9}$ and 1 S/m. Other parameters are: σ_1 = 1x10^{-2} Sm^{-1}, σ_2 = 1x10^{-9} Sm^{-1}, σ_3 = 1 Sm^{-1}, ϵ_1 =78·ϵ_0, ϵ_3 = 50·ϵ_0, a1= 5x10^{-6} m, a1-a2= 20x10^{-9} m. The arrows show the direction of increasing values of σ_2.

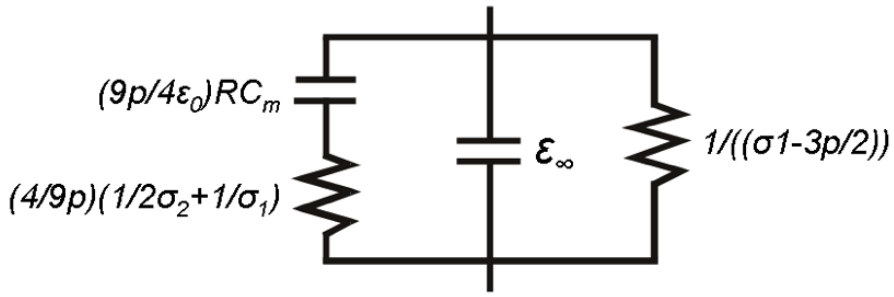

FIGURE 2.17: Equivalent electric circuit of a cell The parameters σ_1 and σ_2 are the conductivity of the suspending medium and cytoplasm respectively, C_m is the membrane capacitance, R the cell radius and p the volume fraction [10].

A more accurate representation of a cell in suspension between two facing electrodes of a microfluidic device is reported in Figure 2.18(a). The properties of the cell and suspending medium are still represented by a combination of resistors and capacitors: R_m and C_m are the resistance and capacitance of the medium, R_{mem} and C_{mem} the resistance and capacitance of the cell membrane, and R_i the resistance of the cytoplasm. This model takes also into account the effect of the electrical double layer that influences the measurement for frequencies below 1 MHz and is modelled as a series of a capacitor C_{DL} and a resistor R_{DL}. Assuming the double layer purely capacitive and neglecting the membrane resistance, the circuit can be simplified as shown in Figure 2.18(b).

The values of the components are expressed as follows [11]:

$$R_m = \frac{1}{\sigma_m(1 - 3\Phi/2)lk} \tag{2.46}$$

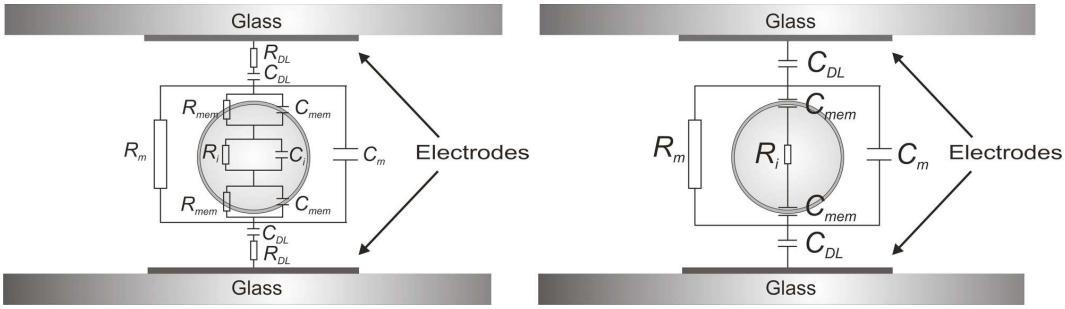

FIGURE 2.18: (a) Schematic representation of a cell suspended between two facing electrodes in a microfluidic channel and its electrical equivalent circuit. (b) Simplified circuit model (see text for further details) [11]

$$C_m = \epsilon_\infty lk \tag{2.47}$$

$$C_{mem} = \frac{9\Phi R C_{mem,0}}{\sigma_m(1 - 3\Phi/2)lk)} \tag{2.48}$$

$$R_i = \frac{4\left(\frac{1}{2\sigma_m} + \frac{1}{\sigma_i}\right)}{9\Phi kl} \tag{2.49}$$

$$C_{mem,0} = \frac{\epsilon_{mem}}{d} \tag{2.50}$$

$$\epsilon_\infty = \frac{2\epsilon_m + \epsilon_i - 2\Phi(\epsilon_m - \epsilon_i)}{2\epsilon_m + \epsilon_i + \Phi(\epsilon_m - \epsilon_i)} \tag{2.51}$$

$$\Phi = \frac{4}{3}\pi R^3 \frac{1}{wlh} \tag{2.52}$$

where $C_{mem,0}$ is the specific membrane capacitance (capacitance per unit area) and ϵ_∞ is the permittivity at infinite frequeny. w is the width of the channel, h the height and l the length of the electrode. d is the membrane thickness and k is the correction factor that takes into account the fringing field.

The impedance of the mixture (particle suspended in the medium) is given by

$$Z_{mix} = \frac{R_m(1 + jwR_iC_{mem})}{jwR_mC_{mem} + (1 + jwR_iC_{mem})(1 + jwR_mC_m)} \tag{2.53}$$

2.4.1.2 Equivalent circuit model for a homogeneous polymer particle

Figure 2.19 shows the equivalent circuit model for a homogeneous polymer particle suspended between a pair of facing electrodes within a microfluidic channel. The bead is modelled as a resistor (R_b) and capacitor (C_b) in parallel. Similarly to the case of the cell, the model includes the resistance and the capacitance of the suspending medium (R_m and C_m, respectively) and the double layer capacitance (C_{DL}).

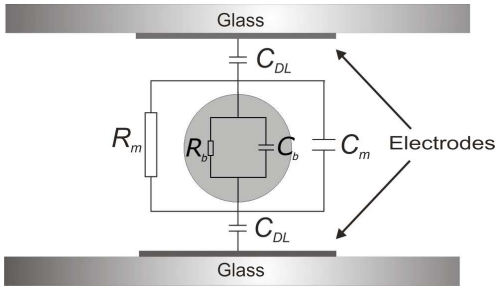

FIGURE 2.19: ECM polymer bead

The values of the electrical components are given by [115],

$$R_m = \frac{1}{\sigma_0 lk} \tag{2.54}$$

$$C_m = \epsilon_\infty lk \tag{2.55}$$

$$R_b = \frac{\tau}{C_b} \tag{2.56}$$

$$C_b = \Delta\epsilon lk \tag{2.57}$$

Where ϵ_∞ is the limiting high frequency permittivity and σ_0 is the limiting low frequency conductivity. $\Delta\epsilon$ is the magnitude of the dielectric dispersion and τ is the relaxation time constant of the Maxwell-Wagner interfacial polarization at the interface between the bead and the suspending medium.

And the expression of the impedance of the mixture becomes,

$$Z_{mix} = \frac{R_m R_b}{R_m + R_b + jwR_m R_b(C_m + C_b)} \tag{2.58}$$

2.4.2 The electrical double layer

In order to perform impedance measurements and manipulate biological particles in microfluidic channels, it is necessary that the electrodes are in contact with the sample suspending solution.

When an electrode is immersed in an ionic solution, charges from the electrolyte opposite in sign to the charges present on the surface of the electrode (counter-ions) accumulate at the electrode/electrolyte interface to provide a localized condition of electroneutrality, while ions with like charges (co-ions) are repelled. This accumulation of charges consisting of two layers (one on the electrode and the other in the solution) is known as the electrical double layer (EDL) and its effect on the system is analogous to the action of a capacitor.

The importance of the EDL has led to numerous studies over the years; several theoretical models have been developed to describe the behaviour of the EDL and the voltage drop across it [116], but the elaboration of a model to provide a complete characterisation is still under discussion [117, 118, 119, 120, 121].

A universally accepted representation of the EDL is the Gouy-Chapman-Stern model described in Figure 2.20 [12]. In this model the EDL is divided in two regions: the diffuse layer (DL) and the Stern layer (SL). The DL is the region where non-bound counter-ions from the solution accumulate, and for this reason it is characterised by a higher density of counter-ions than co- ions. The SL is located between the DL and the electrode surface and consists of a compact layer of tightly bound counter-ions. The SL is further divided in two regions: the inner Helmholtz plane (iHp), consisting of dehydrated ions adsorbed to the surface, and the outer Helmholtz plane (oHp), characterised by the presence of bound hydrated counter-ions.

The change in the electric potential across the double layer is also illustrated in Figure 2.20. The electric potential ϕ_m, virtually constant throughout the metallic phase, linearly increases to ϕ_i across the inner layer of the SL, due to the presence of the adsorbed co-ions, and then decays linearly to ϕ_d at the oHp. In the DL, the potential falls exponentially to the value $\frac{\phi_0}{e}$ that is reached at a distance given by the Debye length λ_d:

$$\lambda_d = \sqrt{\frac{\epsilon_r \epsilon_0 k_B T}{2cz^2 q_e^2}} \tag{2.59}$$

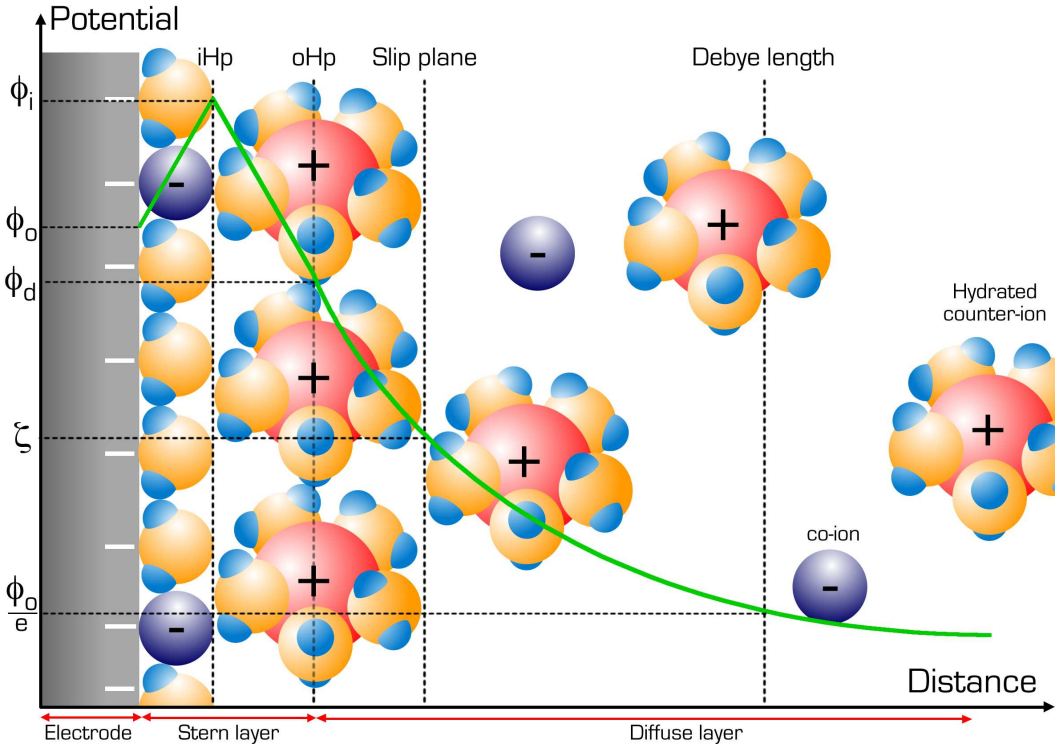

FIGURE 2.20: Schematic representation of the electrical double layer (EDL): next to the solid surface, counterions are adsorbed to the surface. Further out, dehydrated ions, hindered in their mobility are present. Together with the adsorbed ions they form the Stern layer. Further out a diffuse layer of counterions: this is measured as a concentration-dependent capacitance. The bulk of the solution is made of hydrated ions and counterions. The green line shows the potential profile of the EDL formed at the electrode surface: the linear decrease across the Stern layer is followed by an exponential drop across the diffuse layer.

where k_B is the Boltzmann constant, T is the temperature, c is the concentration of ions in the electrolyte bulk, z is the ion valence (for a symmetrical electrolyte) and q_e is the charge of the electron.

There is a conventionally introduced slipping plane that separates the mobile fluid of the DL from the fluid that remains attached to the surface. The electric potential at this plane is known as the zeta potential ζ, which can be measured experimentally and used to estimate the degree of double layer charge.

When an electrical potential is applied across the double layer, the charges react over time in a way similar to a capacitor. Because of the high impedance from the capacitor C_{DL},when a low frequency voltage is applied, most of the voltage signal is dropped across the EDL, resulting in low sensitivity measurements. With increasing frequencies, the effect of the capacitor diminishes and the voltage signal is fully applied to the solution. In terms of equivalent circuit model, the behaviour of the EDL at the electrode/electrolyte

interface can be described as shown in Figure 2.21. The bulk fluid is modeled as a resistor R_m in parallel with a capacitor C_m, and the double layers as a series of a capacitor and resistor. In some cases this model is further simplified to only a capacitor for the double layer. This can be done considering that the double layer primarily stores charge and the current flows only when the double layer is changing.

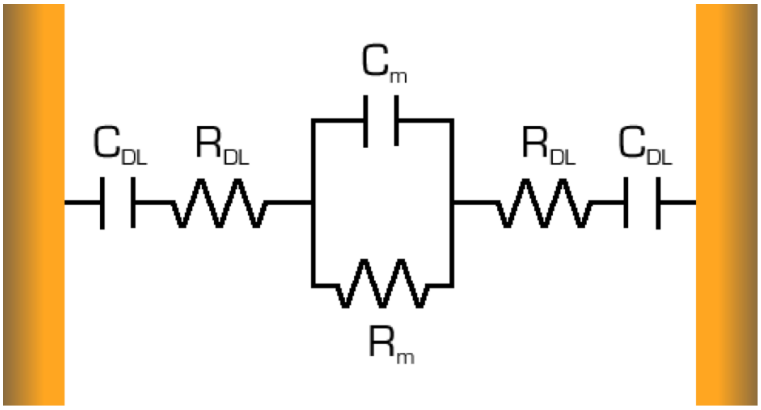

FIGURE 2.21: Equivalent circuit model for the electrode/electrolyte interface: taking into account the effect of the EDL. The bulk fluid is modeled as a resistor Rm in parallel with a capacitor C_m, and the double layers as a series of a capacitor and resistor.

A more general description is given by modelling the EDL as a Constant Phase Angle (CPA) element with impedance Z_{DL} is given by

$$Z_{DL} = \frac{R_{DL}}{(i\omega R_{DL} C_{DL})^{\beta}} \qquad 0 < \beta < 1 \tag{2.60}$$

where when $\beta = 0$, the model is reduced to a pure resistor, whilst $\beta = 1$ gives a perfect capacitor.

2.5 DLVO theory

The DLVO theory, named after Deriaguin and Landau, Verwey and Overbeek, describes the effects of two counteracting forces arising from the interaction of charged surfaces in solution, such us suspended particles: the attractive force of the van der Waals interaction and repulsive force between electric double layers formed at the surfaces/liquid interfaces. In this section, the van der Waals and the double layer forces are briefly described and some insights into the stability and instability of particles in solution are presented.

2.5.1 Van der Waals force

The van der Waals force is the total effect of the action of three different forces: dipole-dipole force, dipole-induced dipole force, and dispersion force. Firstly, dipole-dipole force arises from the interaction between two molecules with permanent dipole moment, i.e. water molecules. Dipole-induced dipole forces are due to the interaction of a polar and a non-polar molecule. In this case, the electric field of the permanent dipole induces a dipole moment in a near by non-polar molecule. Finally, the dispersion force is due to random fluctuations in the electron distribution around atoms and molecules. These fluctuations lead to the formation of momentary dipoles which average zero over time. However, an induced dipole is formed by the interaction between several atoms and an attractive force between the atoms created. Dispersion force is always present.

The potential energy of interaction between two atoms is of the form [12]:

$$U(r) = -C\frac{1}{r^6} \tag{2.61}$$

where the constant C depends on the atom properties and r is the distance to the atom. The total interaction energy between large particles or surfaces can be calculated by adding the interaction energy for all the atoms forming the particles/surfaces. Expressions of the van der Waals interactions energy for important cases are presented in table 2.1. For convenience, the Hamaker constant $A = \pi^2 C n_1 n_2$ is defined, where n is the atom density of the particle or surface [18].

Atom and atom	Sphere and flat surface	Sphere and sphere	Two flat surfaces
$U(r) = -C\frac{1}{r^6}$	$U(r) = -\frac{AR}{6r}$	$U(r) = -\frac{AR_1R_2}{6r(R_1+R_2)}\frac{1}{r}$	$U(r) = -\frac{A}{12\pi}\frac{1}{r^2}$

TABLE 2.1: Van der Waals interaction energy between particles with different shapes [18].

2.5.2 Double layer force and total interaction

When two particles in solution, surrounded by a double layer come together, even if the number of counterions between the two particles remains constant (in order to guarantee neutrality of the layers), compression of the double layers leads to a higher concentration of ions close to the particle surface. This gives rise to an osmotic pressure between the mid-plane between the two surfaces and the outside of the surfaces which tries to move the two surfaces apart. The expression of this repulsive energy can be obtained from

the expression of the work done in bringing the particles together. The repulsive energy per unit area between two planar surfaces is defined as [18]:

$$U_{EDF}(r) = \frac{64nk_BT\gamma^2}{\kappa}e^{-\kappa r} \tag{2.62}$$

where $\gamma = \tanh\left(\frac{zq_e\phi_0}{4k_BT}\right)$, q_e is the electron change, ϕ_0 is the potential on the surface, n is the valence of the ion, k_B is the Boltzmann constant and κ is the Debye length. The total interaction energy considering the van der Waals attraction energy and the double layer repulsive interaction is [12]:

$$U_T(r) = U(r) + U_{EDF}(r) \tag{2.63}$$

The total interaction energy, defined in equation (2.63), plays a key role in the stability or instability of suspension of particles and can be analyzed in terms of the particle distance, the electrolyte concentration and surface charge density. A typical example of the total interaction energy is shown in Figure 2.22 for different values of electrolyte concentration. When the two surfaces are very close or far apart the van der Waals force dominates and the total force is attractive, independent of the electrolyte concentration or the surface charge. The van der Waals force also dominates in the case of zero surface charge ($U_{EDF}(r)$ is switched off) and the interaction always results in attraction (red curve). In this case the suspension becomes unstable and the particles form agglomerates. In contrast, for high surface charge or low electrolyte concentration $U_{EDF}(r)$ becomes large, the surfaces repeal each other and the suspension is stable. If the surface charge decreases or the electrolyte concentration increases, a minimum in the potential appears and in this case the suspension can remain stable (blue curve). Decreasing the surface charge or increasing the electrolyte concentration further, pushes the curve towards the attractive potential leading again to aggregations (black curve). This particular curve corresponds to a point call critical coagulation concentration.

2.6 Summary

In this chapter the basic theory that describes the behaviour of suspended particles under the action of an applied AC electric field has been presented. The polarization mechanisms and the forces arising from the interaction of an induced dipole with the applied field have been introduced. It has been pointed out how the differences in the dielectric polarisability of particles and the frequency dependence of their dielectric response are

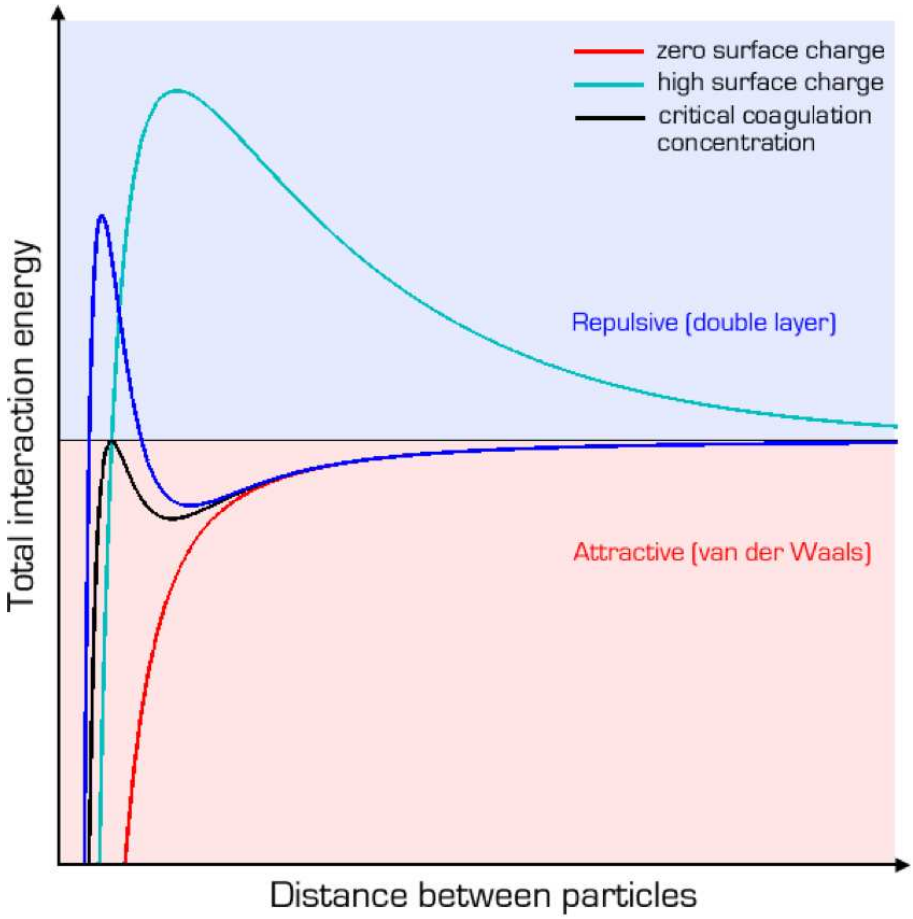

FIGURE 2.22: Total interaction energy as a function of distance for various values of surface charge [12].

at the origin of the electrical manipulation and separation using AC electrokinetic techniques. As the dielectric properties of suspended particles are strictly related to their morphology and structural architecture, the measurement of the dielectric response to a specific applied frequency signal provides useful information on the particle structure and characteristics, which is at the basis of impedance spectroscopy.

In the next chapter, the design and development of an impedance based microfluidic system, capable of detecting and distinguishing dielectric properties of single particles in suspension will be presented.

Chapter 3

Design considerations and experimental procedure

3.1 Introduction

As introduced in the previous chapters, in electrical impedance spectroscopy, the dielectric properties of a system are measured as a function of the frequency of applied AC potentials. In micro-impedance cytometry, this concept is applied to the analysis of single particles suspended in an electrolyte solution flowing through the detection region within a microchannel. Generally, the detection region of an impedance-based microfluidic cytometer consists of a portion of the channel where an electric field is generated using microfabricated electrodes. The microfabricated electrodes are normally integrated into the channel walls, and they can be arranged in different configurations. Different types of microelectrode configurations were reviewed in chapter one, and they can be grouped in two main categories: coplanar electrode configurations and parallel facing electrode configurations. Importantly, it was pointed out that, for a given geometry (electrode width and length), the parallel facing electrode design is more sensitive than the coplanar electrode design.

The working principle of parallel facing electrode configuration is explained in Figure 3.1, where a schematic image of the channel cross-section is presented. Two pairs of overlapping electrodes are positioned on the top and bottom surfaces of the channel, defining two detection volumes. The channel is filled with an electrolyte solution (particle suspending medium). An AC signal (either single frequency or multiple frequency signal) is applied continuously to the top excitation electrodes. The applied signal generates an electric field within the channel and a current path. A suspended particle travelling along

the channel successively passes through the two detection volumes altering the electric field and, as a result, modifying the magnitude of the current. The current change is measured in differential mode: while the particle flows through the electrodes, one pair is used for sensing the change, whilst the other pair provides the reference. Thus, for each particle crossing the detection region, a positive peak and a negative peak separated by the particle transit time (time taken by a particle to travel from one pair of electrodes to the other) are recorded. When no particles are present in the channel, both detection volumes are occupied by the medium only, and no signal is recorded.

The aim of this thesis is to develop a micro-impedance cytometer where a parallel facing electrode configuration is employed for rapid and effective detection and identification of single particles in suspension. In this context, the building of an experimental setup that allows for an easy and reproducible operation of the system is of primary importance to ensure reliability of the measurement results. The complete system is complex and includes: a fluid control setup, an electronic detection system for impedance measurements, a free space optical setup for simultaneous fluorescence detection, and an interface which connects the micro device to the rest of the system.

In this chapter, the design of the microfluidic device and the development of the experimental setup are presented. The beginning of the chapter will illustrate the mask design and the fabrication process of the impedance device. The next section will focus on the experimental setup, including sample focussing, principles of optical and electrical detection, data acquisition and analysis. Sample preparation will not be explained here, details will be given in the following chapters together with the experimental results.

3.2 Design and fabrication process

In this section, the mask design and the clean room process for the fabrication of microfluidic channels with integrated electrodes are described. The micro-impedance chip consist of a microfluidic channel with two pair of electrodes located on both top and bottom faces of the channel. The chip is fabricated from glass and the electrodes are made of platinum. Similar micro-impedance devices are extensively used in our group and where also reported by Renaud's group [7, 84, 122]. Differently from the previously reported devices, the devices developed in this work have multiple inlets which enable hydrodynamic focusing of the sample and a wide (200 μm) channel that makes the system more robust against clogging. Furthermore, novel electrodes configurations for improved impedance detection have been developed.

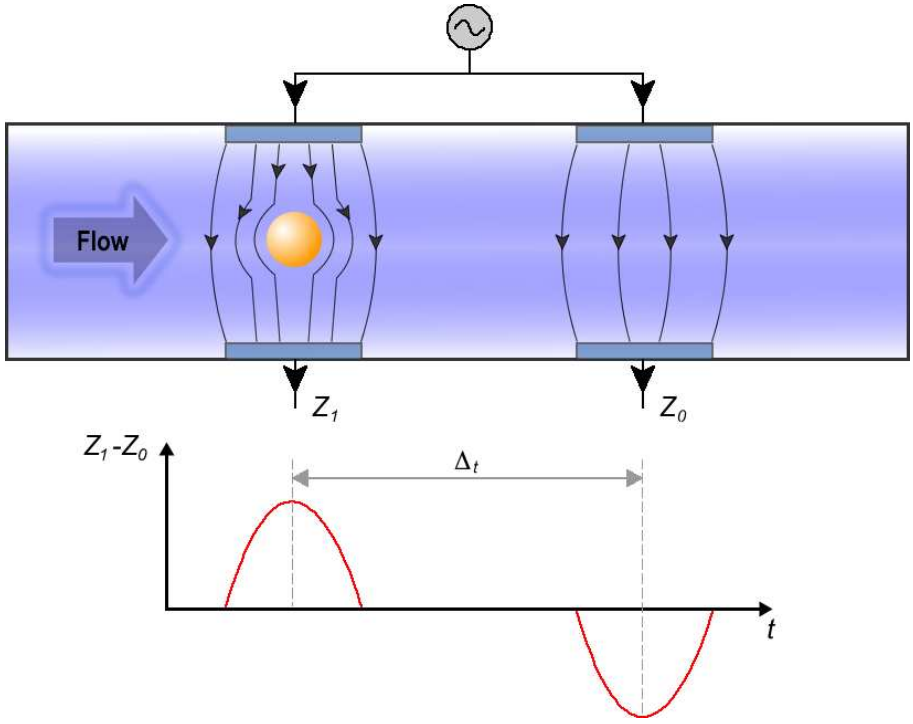

FIGURE 3.1: Schematic diagram showing the channel cross-section of the microfluidic impedance cytometer with parallel facing electrodes. An AC signal applied to the top electrodes generates an electric field inside the two detection volumes defined by the two electrode pairs. Particles are suspended in an electrolyte and flow through the electrodes, causing a change on the impedance of the detection volumes. This impedance change is measured using a differential scheme: one detection volume measures the impedance of the particle and the other volume is used as a reference. Thus, for each particle crossing the detection region, a positive peak and a negative peak separated by the particle transit time (Δt) are recorded.

3.2.1 Mask design

Two masks were designed: a light-field mask for the fabrication of the electrodes using lift-off technique, and a dark-field mask to pattern the negative laminate that defines the microfluid path. The drawing of the masks was done using CleWin (WieWeb). A detailed view of the masks, showing the design of a single chip, is reported in Figure 3.2. Figure 3.2(a) shows the electrodes and their different functions. The electrodes for impedance measurements are located in the centre of the device (pin numbers 7 and 10) and are shielded by a pair of large electrodes that during the experiment are connected to ground (pin numbers 5 and 12). Other electrode structures are provided to enable optional DEP focussing of the sample (2-5) and DEP sorting (13-15).

The structure of the microfluidic channel is Figure 3.2. Each chip has three inlets and two outlets. The channel is 12 mm long, 200 μm wide and 30 μm high. This channel is much wider than the typical size of biological cells, which are of high interest and

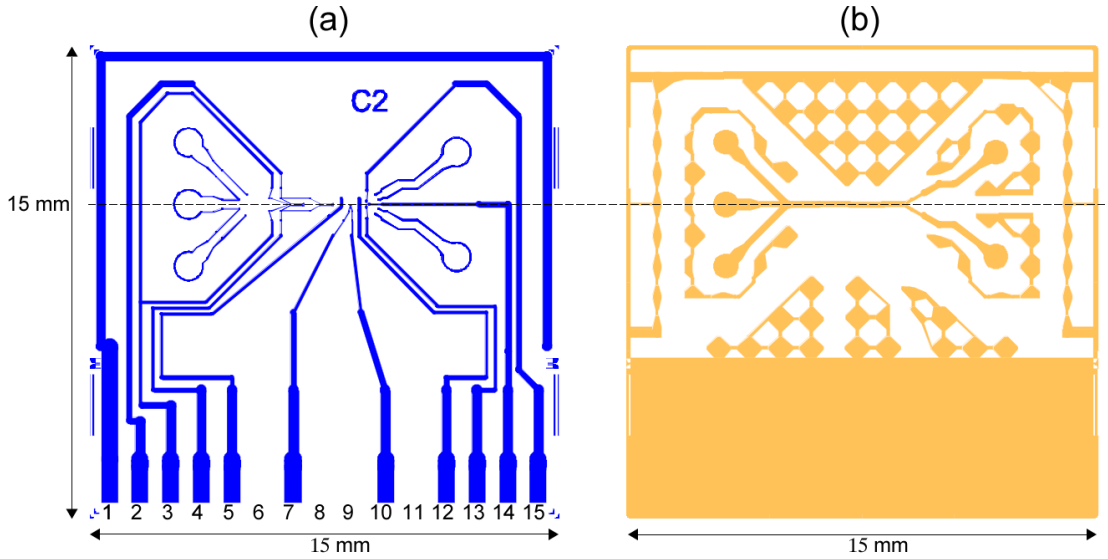

FIGURE 3.2: Details of the masks used for (a) fabrication of the electrodes, and (b) fabrication of the microfluidic channel.

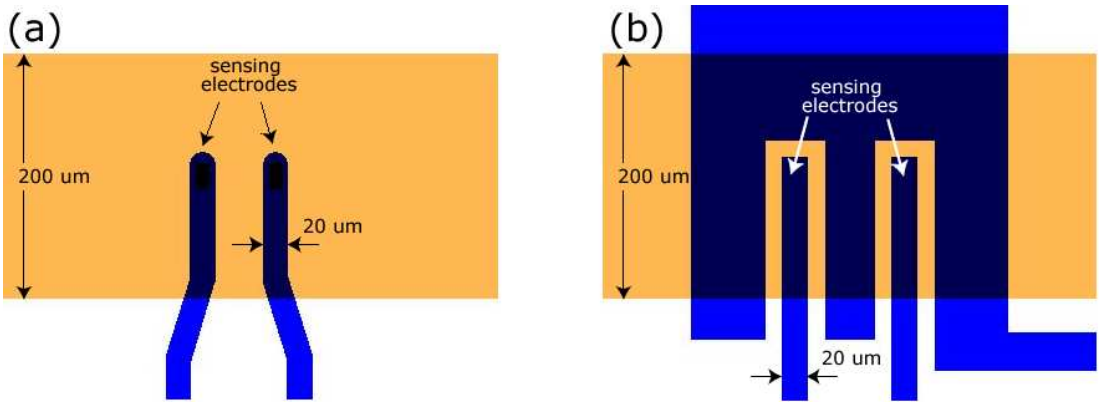

FIGURE 3.3: Close-up view of the two different configurations of sensing electrodes. (a) Overlapping electrodes configurations, the electrodes are 120 μm long and 20 μm wide and extend part-way across the channel. (b) Plate electrode configuration, in this case the sensing electrode consists of two stripes 120 μm long and 20 μm wide surrounding by a large guard electrode.

common targets for impedance measurements. The requirement in terms of size is that the channel is big enough to easily accommodate the biggest particles present in the sample. Thus, a micro-channel that measures 40 μm is big enough to accommodate biological cells. However, working with channels that are similar in size to the particles under study increases the chances of channel blockage while working with wider channels increases the lifetime of the device and makes the system easier to operate.

A metal path along the channel walls in correspondence of the inlets and outlets is provided to increase the pressure during bonding of the devices, to ensure a better bonding result and reduce likelihood of leakages from the channel. Figure 3.3 is a close-up view of the two different configurations of sensing electrodes developed in this thesis.

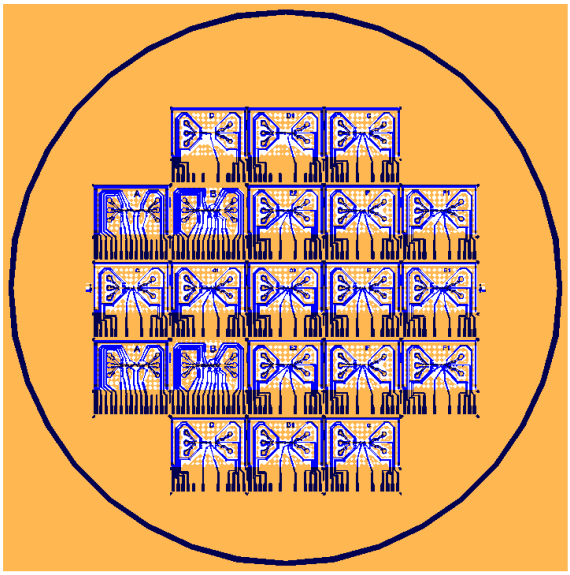

FIGURE 3.4: Image of the microfluidic (orange) and electrode (blue) mask used for fabrication of the devices.

A detailed description of the features of these electrodes and their working principle will be given in chapter 4. In both cases, the electrodes are 20 μm wide. This size was chosen because for accurate impedance measurements the electrodes have to be of sizes similar to the particle under study and working examples of devices using the same size of electrodes have been reported [8, 7, 84]. The complete electrode and microfluidic masks are shown in Figure 3.4 where the two layers are superimposed and aligned. A wafer includes 21 chips. Each chip corresponds to half of a final device; full devices are obtained by bonding two identical wafers. The chips are designed following an axial symmetry along the channel length (see Figure 3.2), so that the electrodes overlap each other in the channel when the two half-devices are bonded; this is shown in Figure 3.5. A half device measured 15x15 mm^2. When bonded, two facing chips overlap over an area of 10x15 mm^2 and the electrode contacts are accessible from the sides of the chip. The final size of a bonded device is 20x15 mm^2.

3.2.2 Fabrication process

Fabrication of the devices was carried out by Andrew Whitton at the Center of Micro-Nano Technology (CMI), EPFL (Lausanne, CH). Glass wafers with a diameter of 100 mm and a thickness of 700 μm (CMI-EPFL, Lausanne) were chosen as the substrate for microfabrication of the devices. The different steps of the fabrication process are schematically reported in Figure 3.6. The first deposited layer consisted of a thin metal film structure patterned by lift-off. Before metal deposition, a first layer of LOR5A and a second layer of SI813 were spun and patterned. The sputtered electrode material was

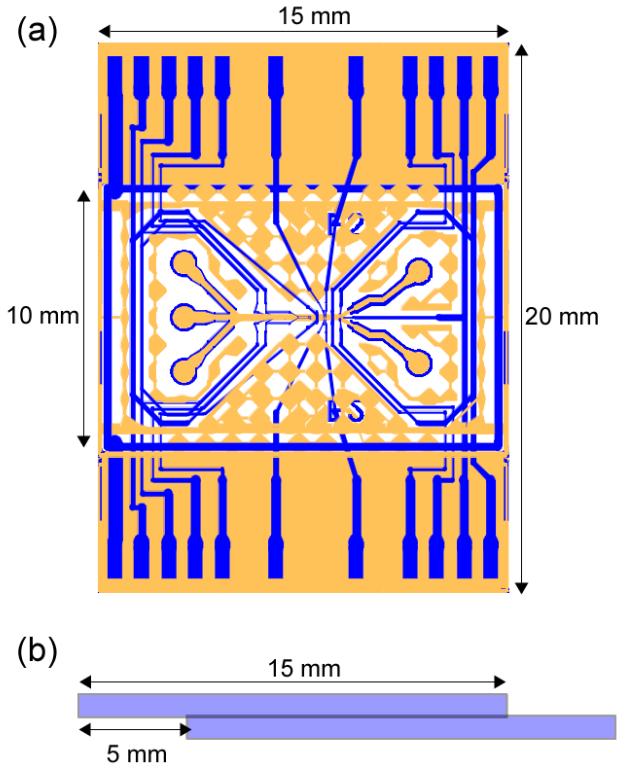

FIGURE 3.5: (a) Schematic image of a device obtained by bonding two facing halves. (b) The top half is flipped and bonded to the bottom half so that they overlap in the central part of the device.

titanium (20 nm), as the adhesion layer, followed by platinum (200 nm) as the active electrode material. Lift-off was carried out in ultrasonic bath using Remover 1165 as the solvent (Figure 3.6 (1)). The microfluidic structures were defined by laminating the substrates with patterned electrodes with a 20 μm thick dry film resist (Ordyl SY320, Elga Europe). The lamination process was performed at 100 °C with 20 kg of pressure and at 0.8m/min. The sample was then exposed under UV light with a dose equal to 194 mJcm^{-2}. The laminate was developed using BMR developer C-3 in ultrasonic bath for 20 s (Figure 3.6 (2)). The alignment and bonding of the two facing wafers was performed with a bond aligner (EVG520, EV Group) under a force of 2500 N and by ramping the temperature to 150 °C for a bake of 30 minutes, and next to 200 °C in N_2 for a bake of 1 hour (Figure 3.6 (3)). To build the complete devices the two wafers were put face-to-face and bonded, therefore the final height of the channel was defined by the thickness of the two laminate layers. Due to a volume reduction of the laminate which occurrs during the bonding process, a final channel height of ∼30 μm was estimated. Partial chip dicing was performed to separate the devices (Figure 3.6 (4)). Access holes were drilled through the top glass layer. Access holes were drilled through the top glass layer using carbide spade drills (SPADEG-12M1, Drill Service Ltd., UK). Images of the fabricated device are shown in Figure 3.7.

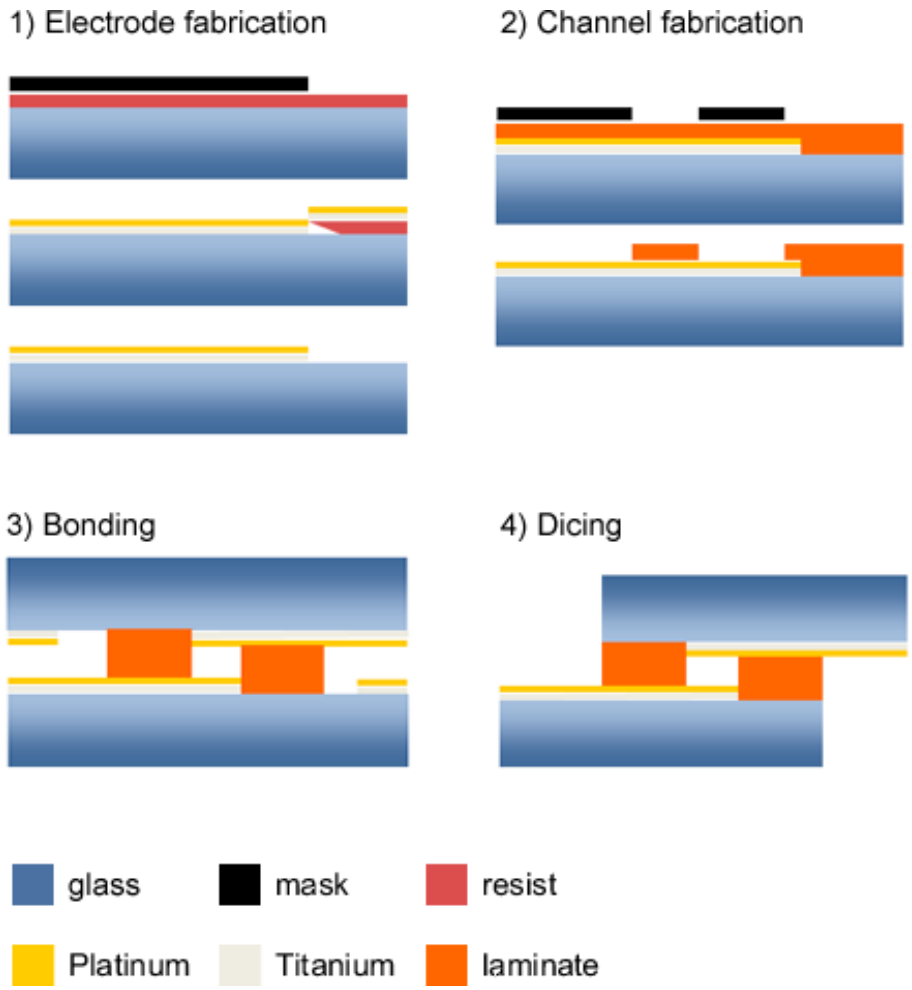

FIGURE 3.6: Chip fabrication process: (1) electrodes definition by photolithography, thin film deposition and lift-off; (2) channels definition by photosensitive dry-resist structuring, (3) chip bonding (4) and dicing. After [13]

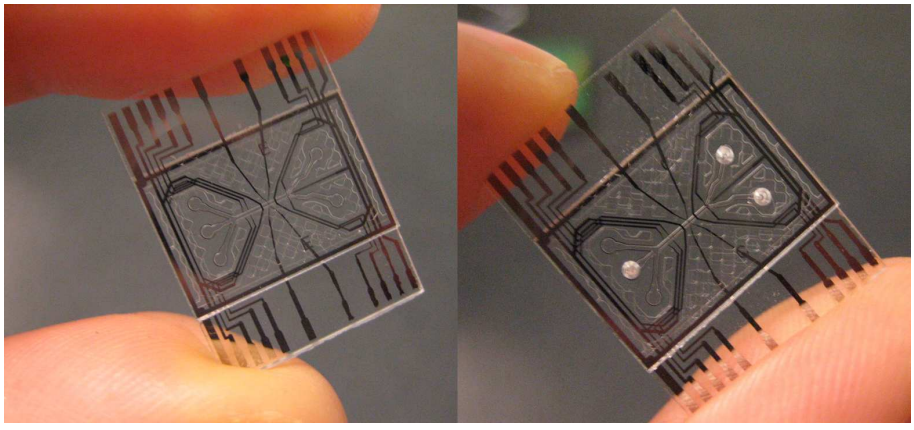

FIGURE 3.7: (left) Image of a fabricated device. (right) Image of a fabricated device with drilled access holes at the two outlets and at one of the inputs.

3.3 Experimental set up

Figure 3.8 is a diagram of the the micro-impedance measurement setup used in this work. The system includes a pneumatic flow control system for precisely controlling the sample flow in the microfluidic chip, electrical system for impedance detection, data acquisition and signal processing. A bench top optical system for fluorescence detection is also included in the system in order to allow simultaneous impedance and fluorescence detection from single particles. Fluorescence detection is not of central interest for this work but it is used to validate the impedance detection results.

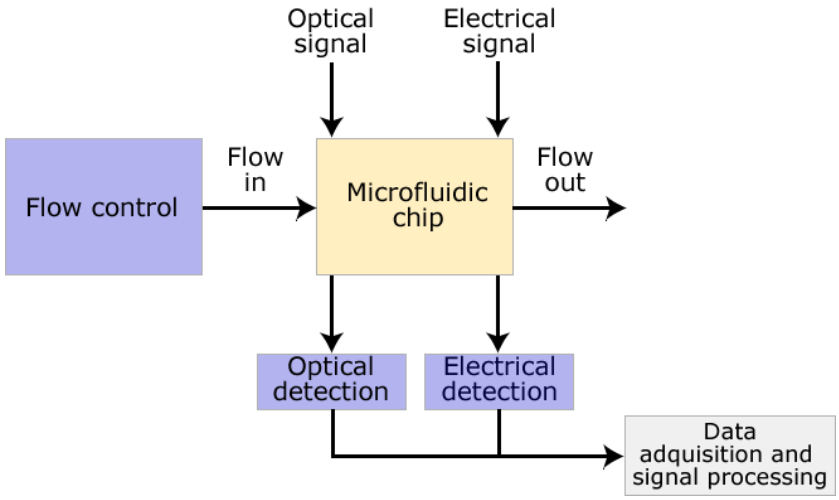

FIGURE 3.8: Diagram of the experimental setup used. The system includes a pneumatic flow control system for precisely controlling the sample flow in the microfluidic chip, optical system for fluorescence detection, electrical system for impedance detection, data acquisition and signal processing.

In the following sections, the experimental setup and procedures are described, including: sample focussing, electrical and fluidic connections, flow control, optical and electrical detection and data acquisition.

3.3.1 Hydrodynamic focussing

The reliability and reproducibility of the results in flow cytometric analysis is strongly affected by the accuracy and efficiency of the confinement of the sample within the detection region of the device [123]. More specifically, it is very important that all the particles follow the same trajectory while flowing through the channel and that only one particle at a time enters the detection region. The most common way to confine the sample within a micro-channel is by one-dimensional (1D) hydrodynamic focussing. The concept is shown in Figure 3.9, which illustrates the micro-channel where the sample flow, supplied from a central inlet, is constrained laterally by two equal streams coming

from the side inlets, and forced into a narrow stream in the centre of the channel. This ensures that the suspended particles are aligned into a single file, and cross the interrogation region (two pairs of micro-electrodes located downstream) one at a time. The width of the sample flow can be dynamically adjusted during the experiment by changing the pressure at the inlets.

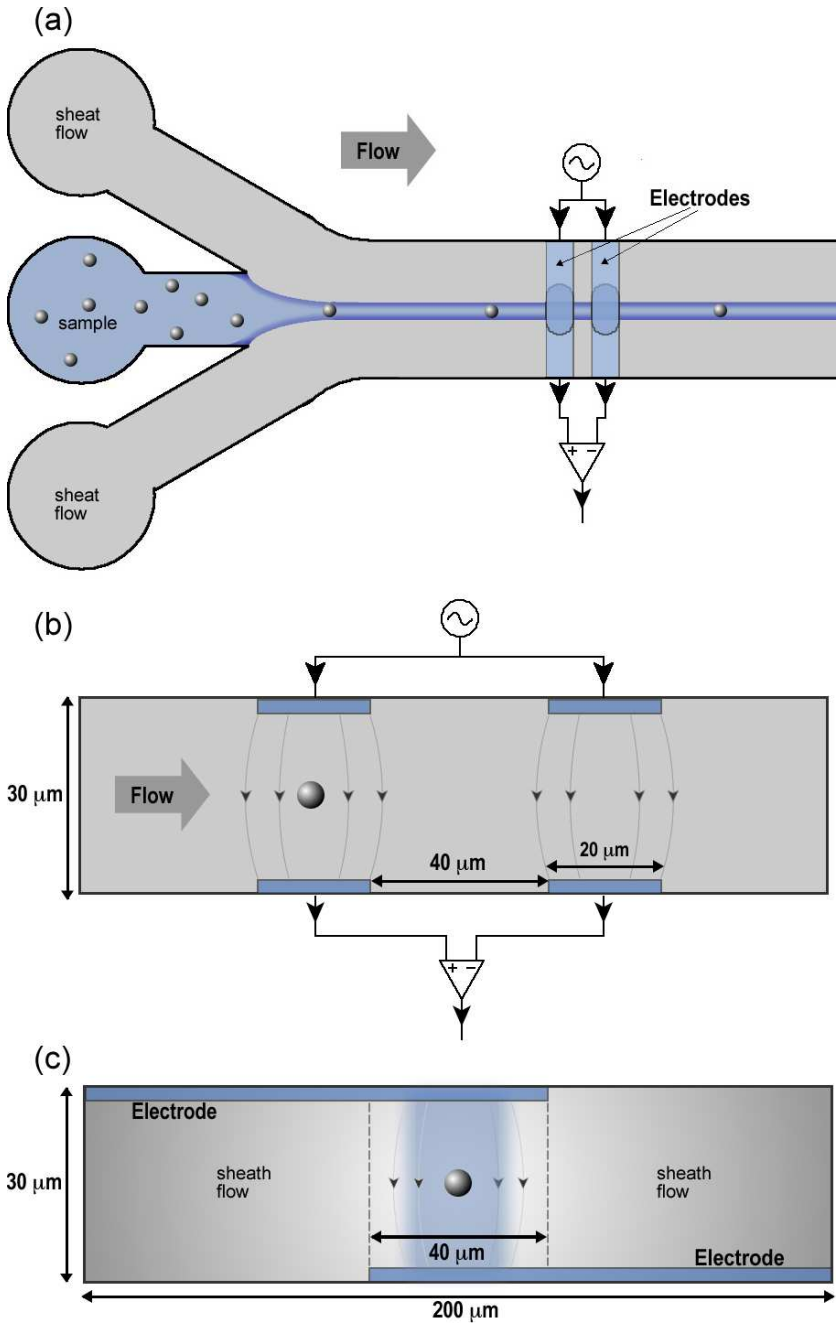

FIGURE 3.9: (a) Top view, (b) side view, and (c) cross-section of the micro-impedance device showing hydrodynamic confinement of the sample inside the detection region.

In a more sophisticated implementation of the hydrodynamic focussing scheme, confinement of the particles is achieved in two dimensions (2D), that is along both the vertical

and horizontal axis of the channel [102, 124, 74, 5, 125, 104]. 2D focussing, commonly used in traditional flow cytrometry, has found wide application in fluorescence-based microflow cytometry. This technique is preferable to 1D focussing because it leads to lower coefficient of variation (CV) in measured fluorescence and scattered light. Differently from their macroscale counterpart that makes use of concentric capillaries to focus the particles right in the centre of the detection region [39], in microflow cytometers particles are normally confined toward the channel surface (top or bottom). Focussing of the sample in the middle of the channel requires more elaborated designs or physical constrictions within the channel [74, 125, 104]. For the specific case of impedance-based microflow cytometry, confinement of the sample toward the channel surface implies the use of coplanar electrode configurations for the detection, which suffers from a lower sensitivity compared to facing electrode configurations [75]. On the other side, 2D focussing of the particles in the centre of the channel does not allow the use of a non-conductive fluid as the sheath flow, as no impedance signal can be detected if the sample flow is surrounded by an insulating fluid.

Particle focussing by negative dielectrophoresis (nDEP) [126, 127] was not taken into consideration as this technique allows for efficient sample confinement only at low flowrates. Besides, nDEP is not compatible with the use of insulating fluid to reduce the size of the detection volume and increase the sensitivity of the system.

For the reasons mentioned above, 1D hydrodynamic focussing was chosen as the technique for confining the sample within the device detection region. Measurements were performed using different fluids with different conductivity values as the sheath flow. These were phosphate buffer saline (PBS, $\sigma = 1.6$ S/m), water ($\sigma = 0.6$ S/m) and oil ($\sigma = 0$ S/m).

3.3.2 Fluidic and electrical connections

During the experiments, the chip was housed in a microfluidic block which provided electrical and fluidic connections to the rest of the system. The block consisted of two parts and schematically shown in Figure 3.10. The bottom part was a brass plate directly screwed to the PCB used for the electrical detection, and with a recess for the positioning and alignment of the chip. The top part was made of PEEK and served as a lid connecting the tubing and the access holes on the chip. A silicon rubber gasket between the chip and the PEEK block ensured good sealing and helped in reducing the mechanical stress on the glass. The tubing connection to the microfluidic block was made through Lee connectors (The Lee Company, USA). Holes were provided in both microfluidic block and circuit board for optical detection and channel inspection during the experiment. The connection between the electrodes on the chip and the PCB were

made using 15 pin spring connectors (1mm pitch, Samtec) that were integrated into the chip holder. The PCB was placed on top of the objective lens of a custom made microscope. The position of the device on top of the objective was adjusted by using a micrometer translation stage (Newport). Images of the PCB and chip holder are shown in Figure 3.11.

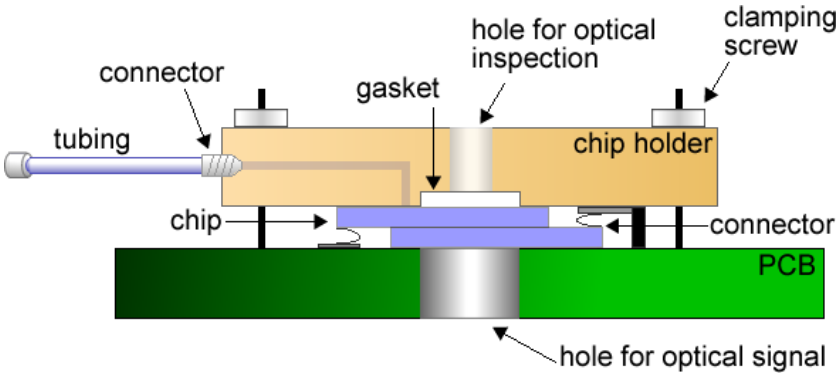

FIGURE 3.10: Schematic of the chip holder for the microfluidic device. A fluidic and electric interface block made of PEEK is mounted on top of the PCB and connects the chip to the pneumatic setup.

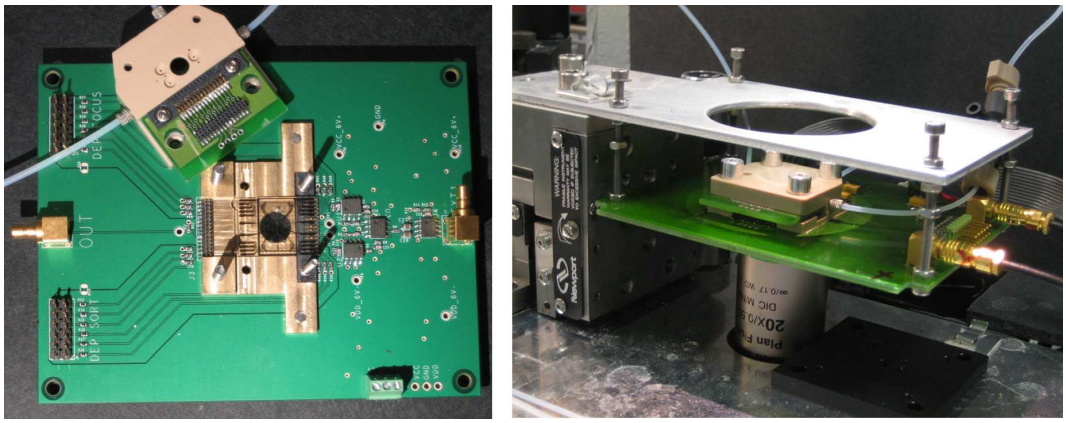

FIGURE 3.11: (left) Picture of the PCB and chip holder before assembling. The chip is positioned in the recess of a brass plate directly screwed to the PCB and secured with the top part of the holder that serves as a lid. Holes in the PCB and holder are provided to allow optical inspection of the channel during the experiments. (right) Picture of the PCB and assembled chip holder placed on top of the objective lens. A metal support is used to fix the PCB to a micrometer translation stage employed for positioning the device on top of the lens.

3.3.3 Pressure driven flow control

There are different techniques to generate and control liquid flow in microfluidic devices. The most commonly used is flow control by volume displacement [65]. This method is

easy to implement, as it simply requires the use of syringe pumps, and allows direct setting of the flow rate, however it becomes very expensive when high precision is required. An alternative technique to control flow in microchannels is electroosmotic pumping [128, 129, 130, 131]. Electro-osmotic flows (EOF) are characterised by a flat velocity profile, which is highly desirable in many microfluidic applications, as the speed of suspended particles is independent from their position. However, this technique requires the use of electrodes, and is strongly affected by the properties of the channel surface and medium. Besides, high voltages are normally used to energize the electrodes, and this might interfere with the detection of impedance signals. Another common way to control the flow is to create a pressure gradient that acting on the fluid reservoir forces the liquid through the channel. In pressure driven flows, the driving pressure is normally generated outside the chip using pressure regulators. The simplest implementation of this technique is to generate a pressure difference by keeping input samples and output collection at different heights. When high stability and precision are required, pressurised sample holders and flow regulators are used for more sophisticated configurations [66, 132, 133].

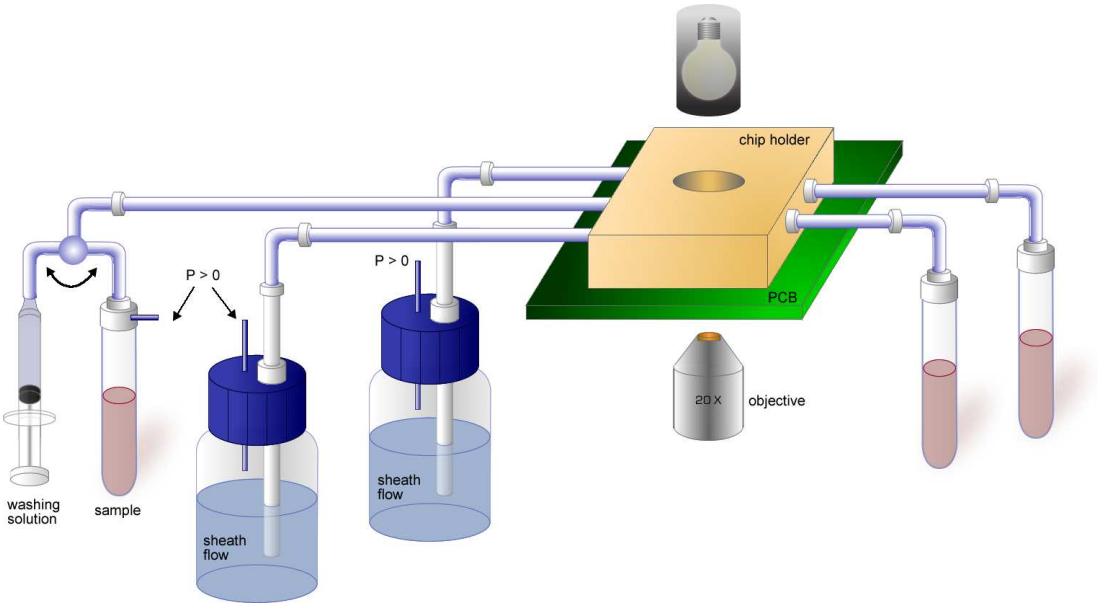

FIGURE 3.12: Schematic of the pneumatic control setup. The containers with the sample and sheath flow are pressurized using high precision pressure regulators. The connection between the microfluidic block holding the chip and the sample containers was made using Teflon tubes. A rotary valve was placed before the sample inlet to select between the sample or washing liquid.

A pressure driven flow control was implemented in this setup as it was found particularly convenient for controlling multiple flows and hydrodynamically focussing the sample. A schematic of pneumatic control setup is shown in Figure 3.12. High precision pressure regulators (10 psi, Marsh-Bellofram) were used to pressurise the containers with the sample and sheath fluid. The channel inlets were controlled independently using three

pressure regulators. This choice increased the complexity of the system but allowed a more flexible control of the fluid pressure. The independent control of the flows was found particularly useful to compensate pressure differences at the inlets that might result from partial occlusion of a channel or fabrication defects. The connection between the microfluidic block holding the chip and the sample containers was made using 1/16" outer diameter Teflon tubes. A rotary valve was placed before the sample inlet to select between the sample or washing liquid.

3.3.4 Optical detection

Fluorescence emission from individual particles was detected using a custom made optical system. The system is shown in Figure 3.13 and was designed to detect fluorescence emission at two different wavelengths simultaneously: 585 ± 30 nm and 670 ± 40 nm. Light from a 532 nm (20 mW solid state) and 633 nm (20 mW HeNe) laser was combined using a dichroic mirror (Chroma Technologies, Rockingham, VT, USA) and expanded using a beam expander consisting of two achromatic lenses. The beam was then coupled to the back of on an infinity corrected objective lens (Plan Fluor x20, NA = 0.7, Nikon). The position of the device was adjusted on top of the objective lens so that the spot formed at the focal plane of the lens resulted in the centre of the channel. Fluorescence emission was collected by the same objective lens and spectrally filtered using dichroic mirrors and bandpass filters (Chroma, Technologies, Rockingham, VT, USA). Collected light was then passed through lenses and pinholes (200 μm, Thorlabs) positioned in front of photomultipliers tubes (H7710-13, Hamamatsu) used for the detection. The gain of the PMTs was adjusted using a power supply (C7169, Hamamatsu) and the signals were amplified using an amplifier (C7319, Hamamatsu). The output signals from the photomultipliers were sampled with a 16-bit acquisition card (NI6034E, National Instruments, USA) and the data captured with software written in LabVIEWTM (National Instrument, USA). A CCD camera (AC254-100-A1, Watec) was used to image the channel detection region during the experiment.

3.3.5 Electrical detection

As introduced at the beginning of this chapter, a particle flowing within the channel of a micro- impedance device is analyzed by measuring the current change that it causes while passing through the detection region of the channel. This current change is measured using a differential scheme whose principles are explained in Figure 3.1. The current change is the consequence of a change in impedance of the detection volume due to the presence of the particle, thus it is directly related to the size, shape and dielectric

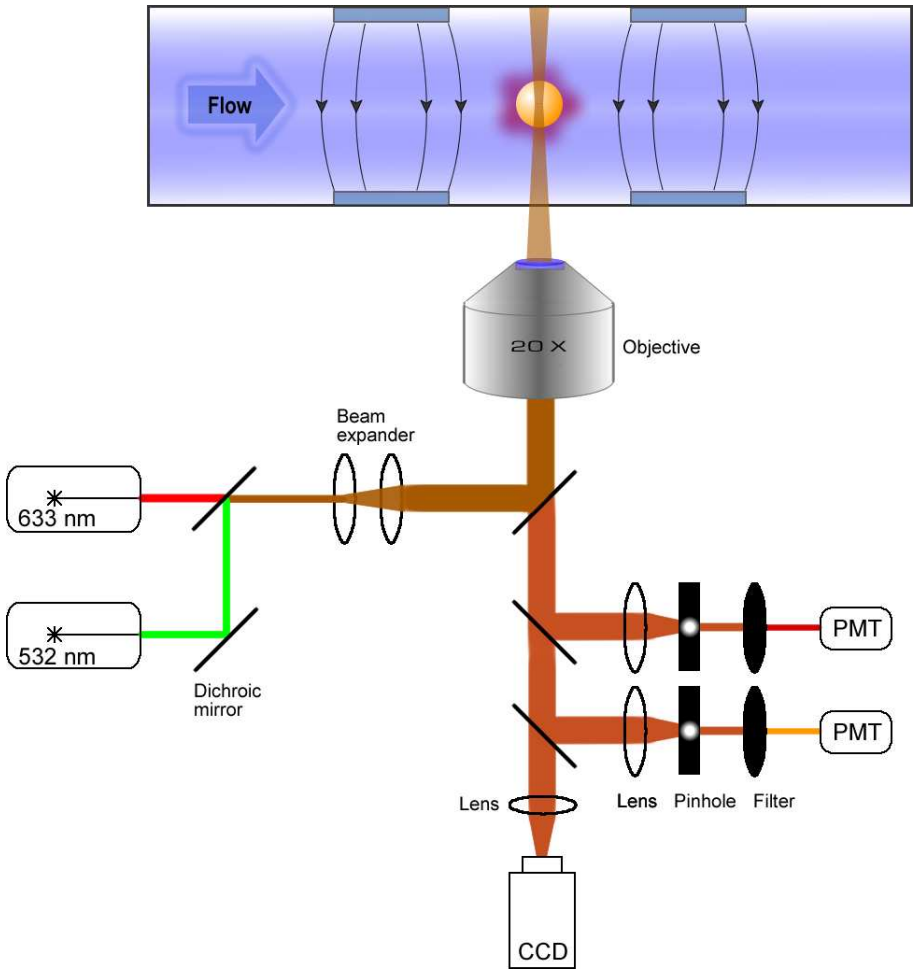

FIGURE 3.13: Details of the optical system for the detection of fluorescence emission at ∼585 nm and 670 nm. Light from a 532 nm and 633 nm laser is combined using a dichroic mirror and expanded using a beam expander consisting of two achromatic lenses. The beam is then coupled to the back of on an infinity corrected objective lens. Fluorescence emission is collected by the same objective lens and spectrally filtered using dichroic mirrors and bandpass filters. Collected light was then passed through lenses and pinholes positioned in front of photomultipliers tubes used for the detection.

properties of the particle. As these properties, and thus the impedance, are frequency dependent, measurements of the current changes at different frequencies provide different information on the properties of the particle under study.

The AC impedance measurement set up is shown in Figure 3.14. An AC signal obtained by mixing two probe frequencies was applied continuously to the top electrodes of the microflow cytometer. The electric current flowing through the two detection volumes was sensed using the bottom electrodes and converted into a voltage signal using a pair of current to voltage converters and amplified. Two RF lock- in amplifiers (SR844 Stanford Research Systems Inc., USA) demodulated the signals, giving the in- phase and out-of-phase signals at the two applied frequencies, whilst rejecting noise at other

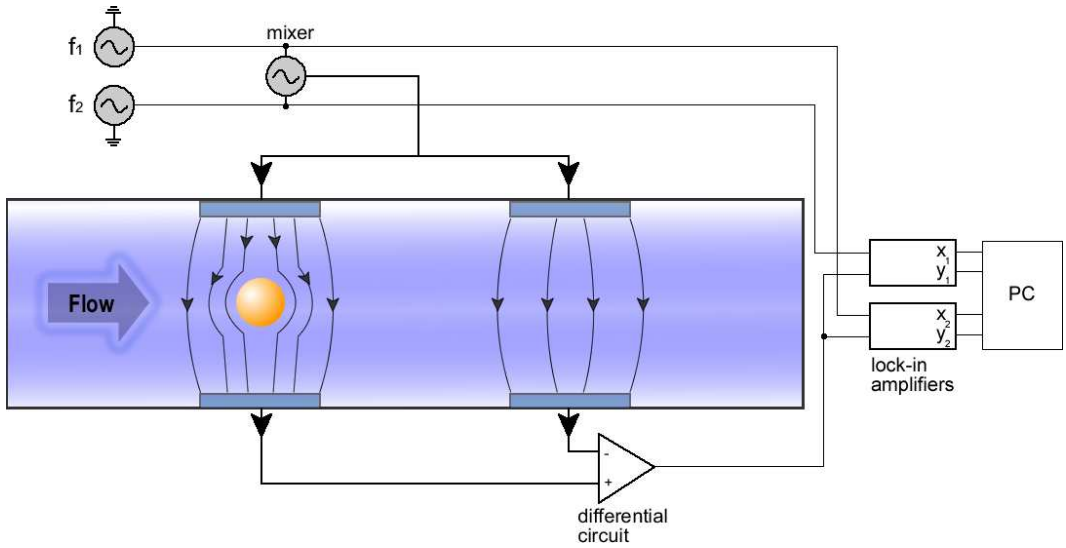

FIGURE 3.14: Schematic layout of the impedance detection system. Two sinusoidal signal at fixed frequencies are mixed and applied to both pairs of detection electrodes. A custom built differential circuit amplifies the signal from the microfluidic chip. Two lock-in amplifiers (one for each frequency) are used to demodulate the signals. The outputs of the lock-in amplifiers (in-phase (X) and out-of-phase (Y) components of the impedance signal at each particular frequency) are sampled using a digital acquisition card.

frequencies. The output signals from the lock-in amplifiers were sampled at 120 kHz with a 16-bit data acquisition card (NI6034E, National Instruments, USA) and then processed to calculate the parameters of interest. As introduced at the beginning of this chapter, a particle flowing within the channel of a micro- impedance device is measured by measuring the current change that it causes while passing through the detection region of the channel. This current change is measured using a differential scheme whose principles were explained in Figure 3.1. The current change is the consequence of a change in impedance of the detection volume due to the presence of the particle, thus it is directly related to the size, shape and dielectric properties of the particle. As these properties, and thus the impedance, are frequency dependent, measurements of the current changes at different frequencies provide different information on the properties of the particle under study.

3.3.5.1 Differential circuit schematic

The detection circuit was developed at Philips Research Laboratories (Cambridge, UK) and is similar to the differential schemed reported by Gawad et al. in [7]. The schematic of the circuit is shown in Figure 3.15. The first stage consists of two auto-balanced-bridge circuits that convert the current response from the input into voltage signals. The

difference of the two voltage signals is performed in the second stage using a differential amplifier and then amplified in the last gain stage.

Simulations of the circuit of Figure 3.15 were performed using PSpice (Orcad Capture, Cadence Inc., USA) in order to study the response of the system to variation of particle properties. A substantial understanding of the system response is of fundamental importance for a correct interpretation of experimental data. In the simulations, the equivalent circuit models (ECM) for a particle (a homogeneous polymer bead or a cell) suspended in the medium and for the medium without particle, both including the electrical double layer, described in sections 2.3.1, were used at the two input channels of the circuit ("Circuit Input" in Figure 3.15) [8]. The schematics of the ECMs for the bead, the cell and the suspending medium without particle are shown in Figure 3.16(a), (b) and (c), respectively. The parameters used to calculate the values of the equivalent circuit components are summarised in table 3.1.

TABLE 3.1: Simulated parameters for the impedance spectra of Figure 3.17

Bead:		
	$D_b = 10\ \mu m$	Diameter
	$\sigma_b = 0.36e^{-3}$ S/m	Conductivity
	$\epsilon_b = 2.5$	Relative permittivity
Cell:		
	$D_c = 10\ \mu m$	Diameter
	d = 20 nm	Membrane thickness
	$C_{mem} = 1.5e^{-3}$ F/m^2	Specific membrane capacitance
	$\sigma_i = 0.56e^{-3}$ S/m	Conductivity of the cytoplasm
	$\epsilon_i = 50$	Relative permittivity of the cytoplasm
Medium and channel:		
	$w = 20\ \mu m$	Width of the electrodes
	$h = 30\ \mu m$	Height of the channel
	$l = 40\ \mu m$	Length of measurement electrodes
	$\sigma_b = 1.6$ S/m	Conductivity
	$\epsilon_b = 78$	Relative permittivity
	$C_{DL} = 50$ pF	Electrical double layer capacitance

In Figure 3.17, the magnitude of the differential impedance signal obtained for the cell and the bead are compared. At low frequency the system is dominated by the double layer capacitance and the two spectra overlap. At frequencies below 1 MHz, the cell membrane acts like a perfect insulator and the cell appears like a solid object, therefore its impedance magnitude is very similar to the impedance magnitude of the bead. In the frequencies between 1 MHz and 10 MHz the impedance of the cell decreases due to the interfacial relaxation of the membrane, while the impedance of the bead stays constant.

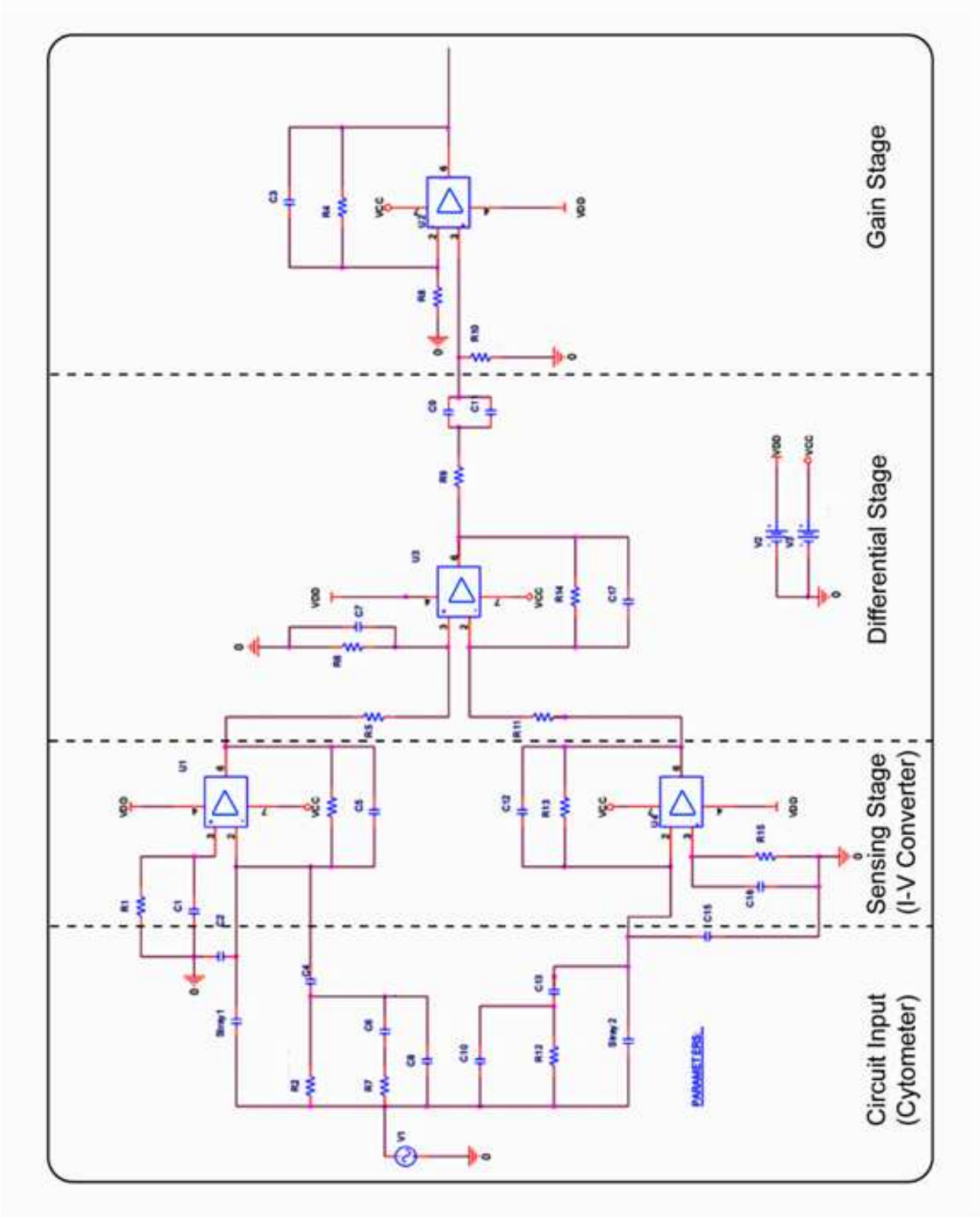

FIGURE 3.15: Orcad Capture schematic of the differential amplification circuit. After [14]

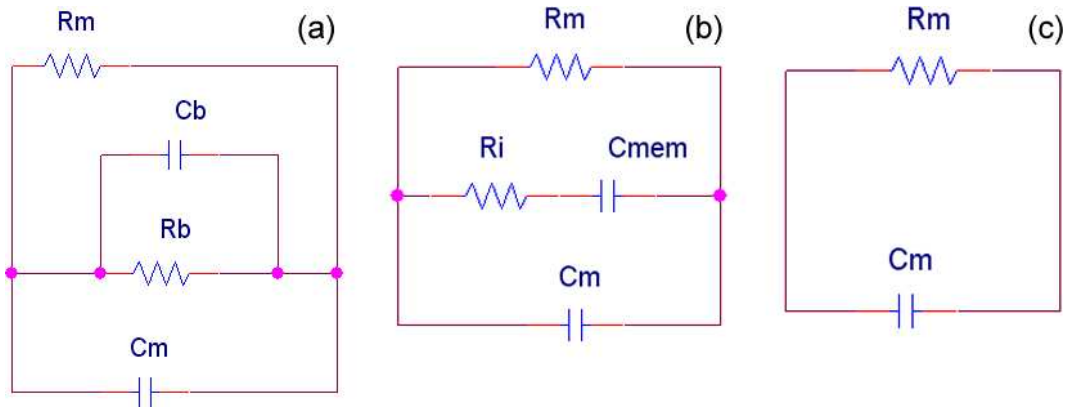

FIGURE 3.16: Equivalent circuit model (ECM) for (a) a homogeneous polymer bead and (b) a cell suspended in the detection volume of the microfluidic channel. (c) ECM of the detection volume filled with the medium only. R_m and C_m are the equivalent resistance and capacitance of the medium respectively. C_b and R_b are the equivalent resistance and capacitance of the bead respectively. Cmem is the equivalent capacitance of the cell membrane, R_i is the equivalent resistance of the cytoplasm.

At higher frequencies the impedance spectrum of the cell is dominated by the dielectric properties of the cytoplasm.

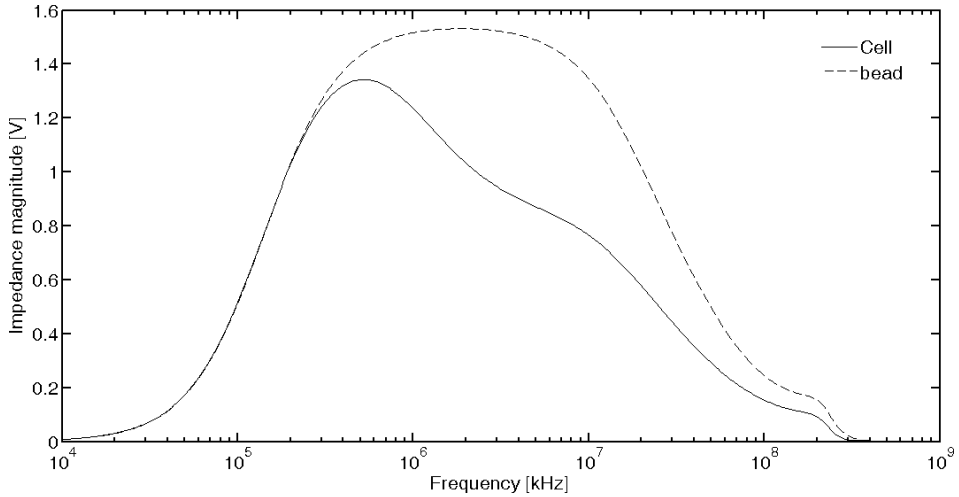

FIGURE 3.17: Impedance magnitude signal for a 10 μm diameter solid bead and a 10 μm diameter cell. At low frequency the system is dominated by the double layer capacitance and the two spectra overlap. At frequencies below 1 MHz, the cell membrane acts like a perfect insulator and the cell appears like a solid object, therefore its impedance magnitude is very similar to the impedance magnitude of the bead. In the frequencies between 1 MHz and 10 MHz the impedance of the cell decreases due to the interfacial relaxation of the membrane, while the impedance of the bead stays constant. At higher frequencies the impedance spectrum of the cell is dominated by the dielectric properties of the cytoplasm.

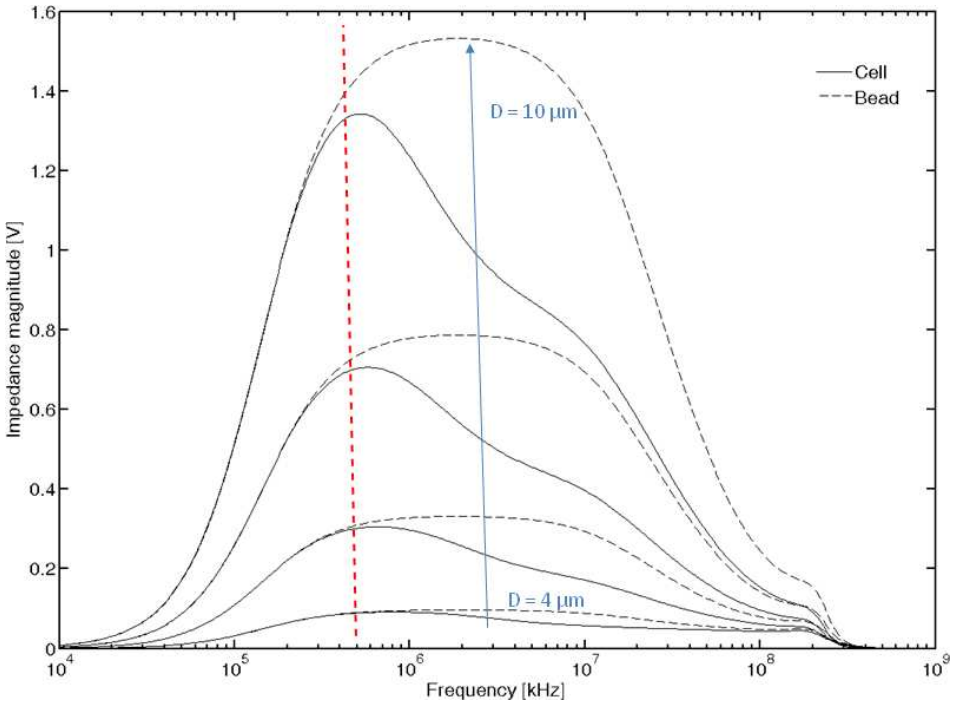

FIGURE 3.18: Variation of the magnitude of the impedance signal due to variation in cell size. Simulated values of the particle diameter were D = 4, 6, 8, 10 μm. The plots show that the magnitude of the impedance is highly affected by the variation in size in the frequency range 100 kHz to 15 MHz, with a maximum amplitude variation between 300 kHz and 3 MHz.

Figure 3.18 shows the magnitude obtained for variations in particle diameter (other simulated parameters were unchanged). The plots show that the magnitude of the impedance is highly affected by the variation in size in the frequency range 100 kHz to 15 MHz, with a maximum amplitude variation between 300 kHz and 3 MHz. The relationship between particle size and impedance magnitude is clearly observed in Figure 3.19, where the magnitude of the impedance at 500 kHz is plotted against the diameter of the particle. The graph shows that as the particle size decreases, there is almost a cubic decrease in magnitude, which tends towards zero for the smallest detectable particle within the detection volume. This curve is a function of the size of the detection volume and for the channel dimensions simulated in this example, the theoretical smallest detectable size is around 4 μm diameter.

The effect of changes in specific membrane capacitance of the cell on the impedance signal is shown in Figure 3.20. The plot shows that the interfacial relaxation of the cell membrane takes place around 3 MHz. The characteristic time of this process is dominated by the membrane capacitance. An increment of the membrane capacitance results in a longer time for the relaxation process to take place, which corresponds in the frequency domain to a shift towards the low frequency values. The same observations were made in section 2.3.1.1 for the modelling of the mixture theory.

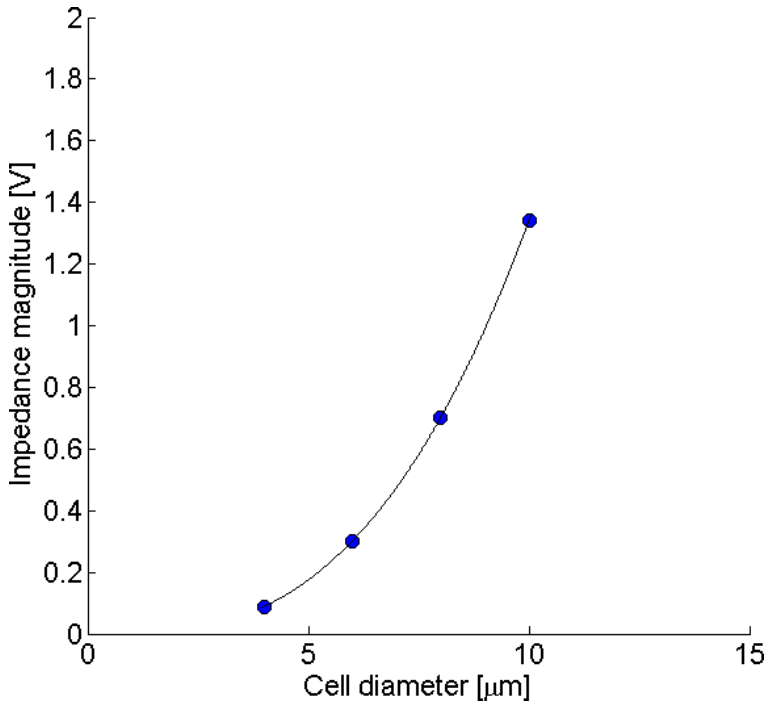

FIGURE 3.19: Plot showing the correlation between the particle size and the magnitude of the impedance signal at 500 kHz. There is almost a cubic decrease in magnitude, which tends towards zero for the smallest detectable particle within the detection volume.

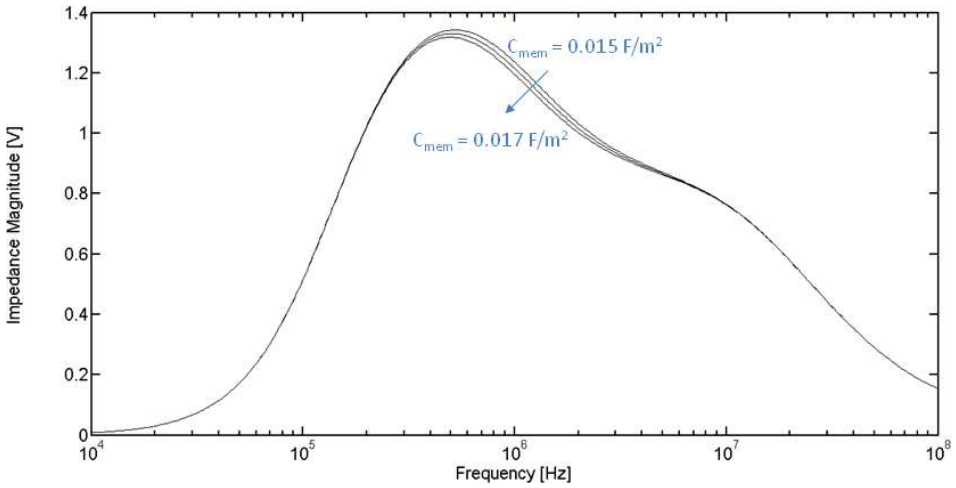

FIGURE 3.20: Plot of the variation of the impedance signal due to changes in specific membrane capacitance of the cell. The plot shows that the interfacial relaxation of the cell membrane takes place around 3 MHz. An increment of the membrane capacitance results in a longer time for the relaxation process to take place, which corresponds in the frequency domain to a shift towards the low frequency values.

Figure 3.21 shows the impedance signal for different values of the cytoplasm conductivity of the cells. The effect of a change in cytoplasm conductivity are observed at frequency higher than 10 MHz. At these frequency values the cell membrane is short circuited,

and the system is dominated by the dielectric properties of the inside of the cell.

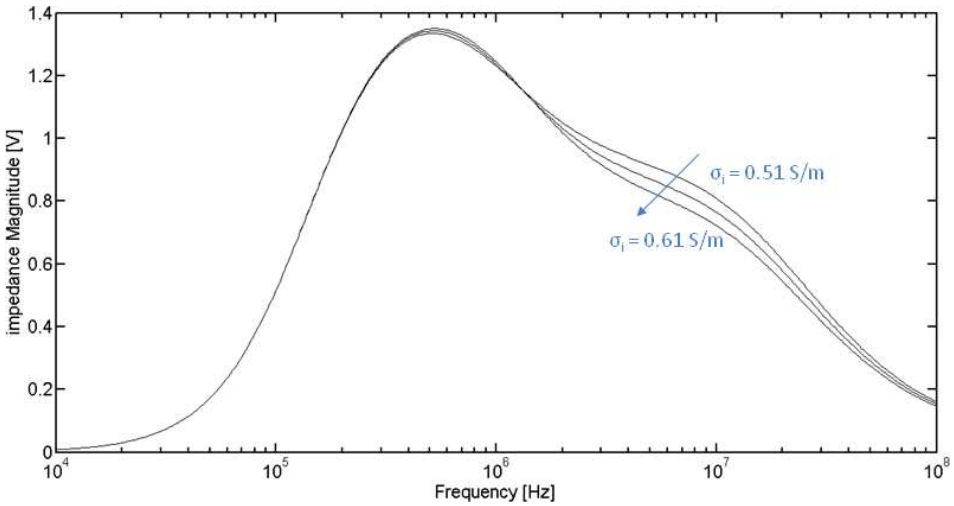

FIGURE 3.21: Plot of the variation of the impedance signal due to changes in cytoplasm conductivity of the cell.

The effect of changes in conductivity of the suspending medium is shown in Figure 3.22. An increase in conductivity corresponds to a reduction of the impedance of the medium within the detection volume, and to a consequent increase of the cell impedance magnitude.

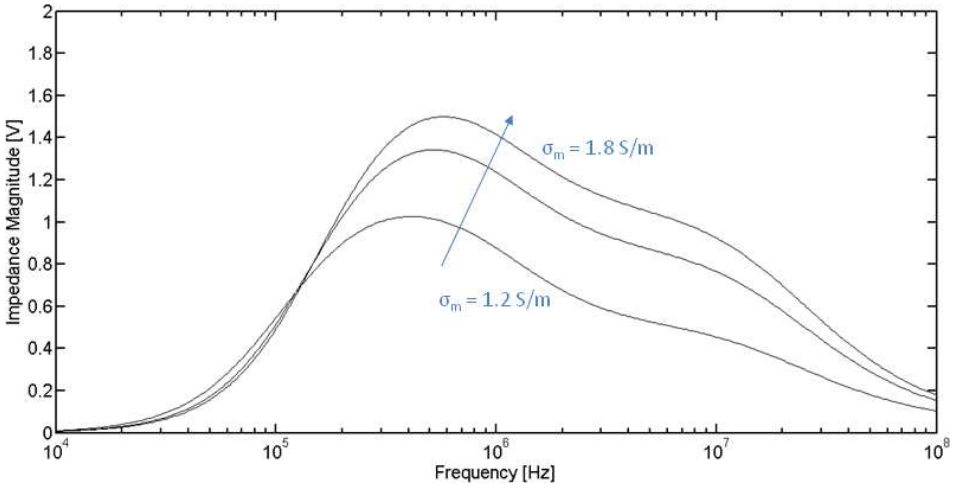

FIGURE 3.22: Variation of the impedance magnitude due to variations in conductivity of the suspending medium.

Figure 3.23 shows variations in impedance magnitude caused by the variation in electrical double layer capacitance. The electrical double layer dominates the system at frequencies below 1 MHz. A higher value of capacitance reduces the voltage drop across the double layer, resulting in the expansion of the spectrum toward the lower frequency and in the increase of the system sensitivity.

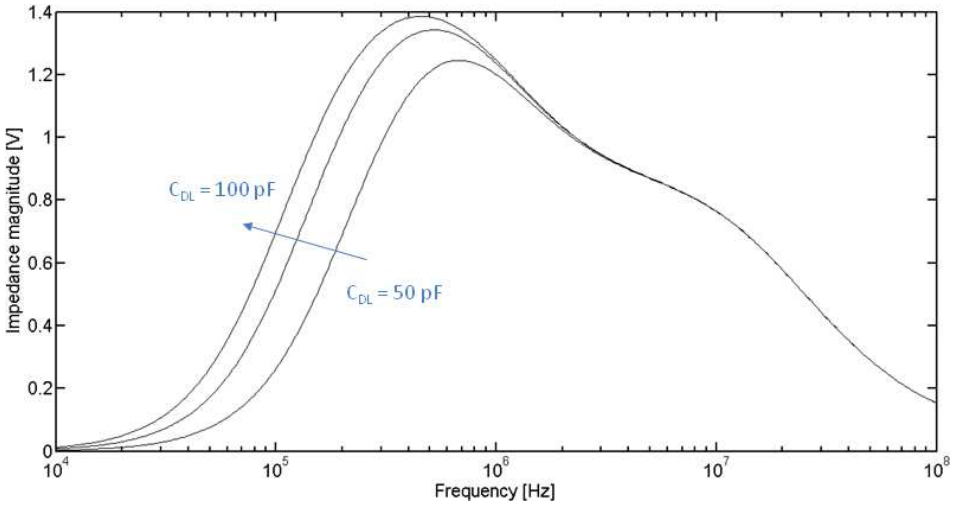

FIGURE 3.23: Variation of the impedance magnitude due to variations in electrical double layer capacitance.

3.3.6 Data acquisition and processing

The output signals from the electrical and optical detection systems were sampled at 120 kHz with a 16- bit data acquisition card (NI6034E, National Instruments, USA) and the data captured and analysed with two pieces of software written in LabVIEW^{TM} (National Instruments, USA) by Christian Reccius (Philips Research Laboratories, Cambridge, UK). The acquisition software allowed the setting of the acquisition parameters of the digital card, such as sample rate, trigger channel and level, and signal range. During the recording, a continuous stream of raw data, including the acquisition timing, was stored in a buffer, and saved in the memory at the end of the acquisition. By setting a threshold voltage on one of the impedance or fluorescence acquisition channels, triggered signals from the raw data stream were plotted in real-time. Once saved, the raw data could also be re-triggered by changing trigger channel and trigger level. The analysis software was used to process the triggered data sets. A number of different parameters such as amplitude, phase, or transit time were computed and plotted. By gating on the different computed parameters, data sub-sets were created and saved for further analysis and statistics.

Figure 3.24 shows an example of signal collected from a single fluorescent (red) 5.49 μm diameter bead when two AC signals (503 kHz and 5 MHz, 1.5 Vpp) were applied simultaneously. The signal was recorded by setting the trigger on the low frequency in-phase impedance signal. The double peak signals correspond to the in-phase and out of phase components of the impedance signal, one for each applied frequency. These signals are followed by a single peak that is the fluorescence signal from the particle (670/40 nm).

Further processing and analysis of the data was performed using code written in MATLAB (Mathworks Inc., Natick, USA).

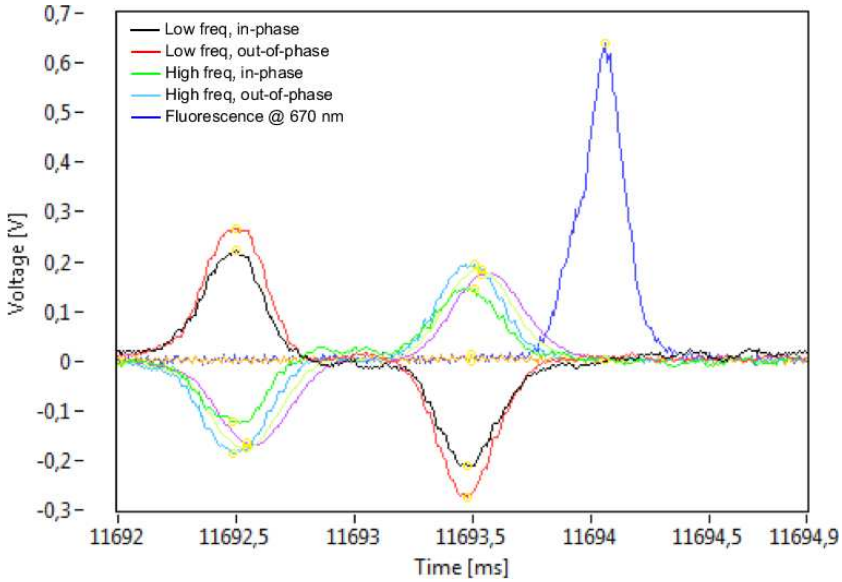

FIGURE 3.24: Example of impedance signals from a 5.49 μm diameter bead detected in the micro flow cytometer. The double peak signals correspond to the real component (in phase) and imaginary component (90° out of phase) of the electrical impedance at each applied frequency. The impedance signal is followed by a single peak showing red (670/40 nm) fluorescence emission.

3.4 Conclusions

In this chapter, the design and development of the micro-impedance cytometer and the experimental procedures used in this work were described. The principles of differential impedance measurements were presented, and a brief description of the mask design and fabrication process were provided. A detailed description of experimental set up and an explanation of the optical and electrical detection techniques, including data acquisition and analysis, were presented.

Chapter 4

Modelling of electrode configurations and impedance measurements

4.1 Introduction

In chapter 1.1, a review of the microfluidic devices for the analysis of the dielectric properties of single particles in suspension that have been developed in recent years was presented. It was pointed out that in these systems, different from traditional Coulter devices, which employ relatively large electrodes, particles flow between pairs of micron-sized planar electrodes that are fabricated within a microfluidic channel, and which define the electric field distribution of the detection region. These devices have been able to discriminate different micron sized objects including beads according to size [6, 81, 85], and cells according to size and membrane properties [80, 84, 8, 134].

The advantage of using electrodes whose dimensions are comparable to the ones of the particles under study is that, the electric field is more concentrated around the cell and, as a result, a higher sensitivity is achieved. Also, scaling the electrodes dimensions reduces the stray capacitance and enables measurements at high frequency. However, a smaller electrode surface area also results in higher impedance of the double layer at the electrode/electrolyte interface, which then dominates the low frequency measurements.

A number of issues limit the sensitivity and specificity of these microfluidic systems. Fundamentally the sensitivity is governed by the ratio of particle volume to the volume occupied by the electric field, defined as the volume fraction occupied by the particle, which should be maximised. In addition, the spatial location of each particle needs

to be controlled accurately within the field. It is also important to ensure that only one particle at a time enters the detection region. Therefore, an efficient and accurate method for focussing particles into the centre of the electric field is important. One way to improve the sensitivity of the system is to reduce the dimensions of the channel. Typically for cell analysis, channels that are 20 μm to 30 μm in width and height are used. In order to measure smaller objects such as bacteria, the channel dimensions and electrode width should be reduced, for example to 5 μm, but this makes fabrication more difficult and greatly increases the likelihood of blockage of the channel. In general, the detection of sub-micron particles is performed using nanopores with typical sizes ranging from several hundreds of nanometers to few microns [44, 45, 52, 68, 2, 46].

In terms of impedance cytometry, it was shown that one way of increasing the sensitivity whilst maintaining a relatively large channel dimensions is to focus particles into the sensing region with the use of a sheath flow that is made of a less conducting liquid such as pure water. This principle is used in Coulter counters; the sheath flow serves to concentrate the electric field lines into the sensing volume without restricting the geometry of the device. Several examples of micro-impedance devices where the sample is sheathed with a less conductive liquid were reviewed in chapter 1.1. In these systems, coplanar electrode configurations are normally used to detect the particles. This electrode arrangement gives a highly divergent electric field compared to opposing electrode configurations. The impedance signal from a particle travelling through the detection volume is therefore critically dependent on the height of the particle in the channel, i.e. the distance from the electrodes. This causes an increase in the dispersion of the signal amplitude distribution, making discrimination of similarly sized particles impossible. Despite efforts to develop a sensitive and reliable micro-impedance system for analysis of particles of around 1 μm in size, to date no effective solution has been shown.

One of the primary aims of this work is to investigate different methods to increase the sensitivity of a micro-impedance system, in order to enable detection of small particles and discrimination between particles with very similar sizes, without sacrificing flexibility, robustness and ease of operation of the device. More specifically, the work is focussed on investigating different sensing electrodes geometries and different techniques to confine the sample within the device detection region.

In the following sections, the three electrode configurations that are introduced in Chapter 3 are described and compared. Numerical simulations of the electrode geometries are performed to evaluate their performances. The effect of focussing the sample using different fluids (PBS; water and oil) is also investigated by numerical analysis. Simulation results are then compared with the experimental data obtained when the impedance was measured using the different configurations and when the sample was focussed using the different fluids.

4.2 Electrode configurations

As previously mentioned, three different parallel facing electrode configurations have been used in this work. The first configuration, named "standard electrode configuration", was previously developed and already presented in several publications [84, 11, 85]. This configuration has been employed for the experimental work that will be presented in chapter 6; here it serves as a reference to evaluate the performance of other two novel configurations: overlapping electrode configuration and plate electrode configuration. These two configurations originate from the idea of implementing a facing electrode arrangement into a wide channel (200 μm) without increasing the detection volume, aiming for a sensitivity that is comparable to that of a smaller channel (40 μm x 30 μm).

4.2.1 Standard electrode configuration

The standard electrode configuration is shown in Figure 4.1. It consists of two pairs of facing electrodes 40 μm long and 20 μm wide located on both top and bottom faces of a channel 40 μm wide and 30 μm high. The two pairs of electrodes define two detection volumes measuring 40 x 20 x 30 μm^3 and with a separation gap of 40 μm. The excitation signal is applied simultaneously to the top electrodes, whilst the bottom pair is used for differential measurement of the impedance.

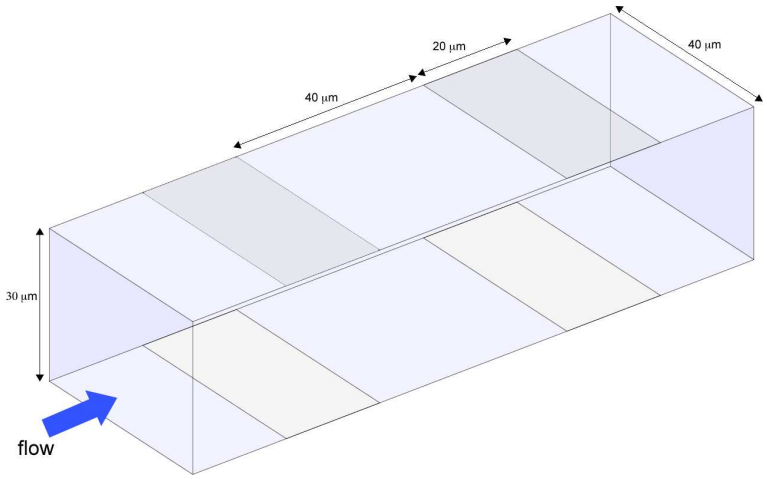

FIGURE 4.1: Standard electrode configuration. Two pairs of electrodes are located on the top and bottom faces of a microchannel 40 μm wide and 30 μm high, to define two detection volumes measuring 40 x 20 x 30 μm^3 and separated by a 40 μm gap

4.2.2 Overlapping electrode configuration

The overlapping electrode configuration is shown in Figure 4.2. It consists of two pairs of opposing electrodes 120 μm long and 20 μm wide, which extend part-way across the channel (200 μm wide and 30 μm high) overlapping in the centre. The overlap region measures 40 μm in length. As the channel height is 30 μm, the electrode pairs define two detection volumes measuring 40 x 20 x 30 μm^3, with a separation of 40 μm. Like in the previous configuration, the top electrodes are used for applying the excitation signal and the bottom electrodes for measuring the impedance.

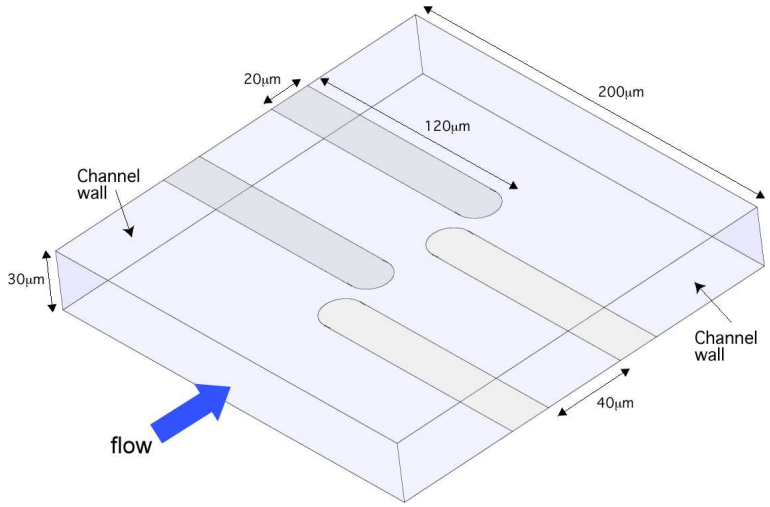

FIGURE 4.2: Overlapping electrode configuration. Two pairs of electrodes 120 μm long and 20 μm wide are located on the top and bottom faces of a channel 200 μm wide and 30 μm high, defining two detection volumes measuring 40 x 20 x 30 μm^3 and separated by a 40 μm gap.

4.2.3 Plate electrode configuration

In this configuration, shown in Figure 4.3, the two top electrodes are replaced by a single plate electrode 120 μm long and 260 μm wide. The bottom electrodes consist of two stripes 120 μm long and 20 μm wide, surrounded by a large guard electrode. The gap between the stripe electrodes and the guard electrode measures 10 μm. The top plate electrode and the bottom electrodes overlap in the centre of the channel. The length of the overlapping region is the same as the previous configuration (40 μm) so that also the volume of the detection regions (40 x 20 x 30 μm^3) is unchanged. The excitation signal is applied to the top plate electrode while, similar to the previous configurations, the bottom pair is used for differential measurements. The reason for using a guard electrode around the sensing electrodes and an excitation electrode that is much larger than the sensing electrodes is that, this way, the curvature of the electric field is reduced,

limiting the fringing field effect and obtaining a more uniform distribution of the field inside the detection region.

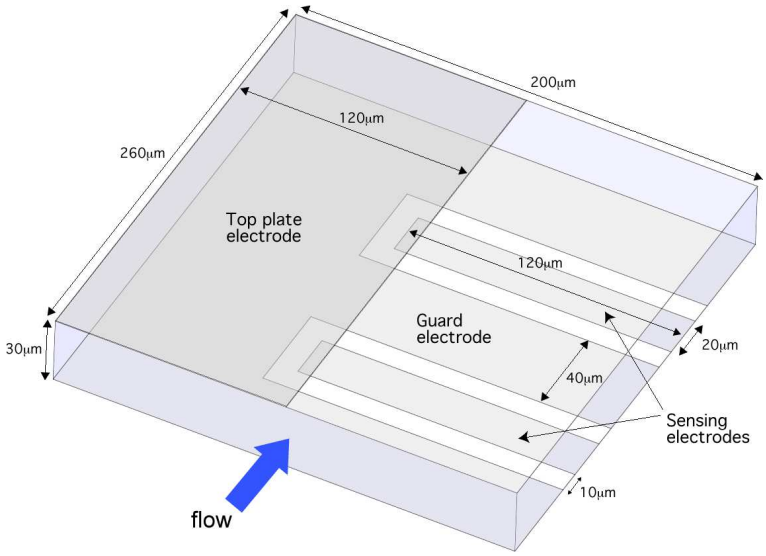

FIGURE 4.3: Plate electrode configuration. A plate electrode 120 μm long and 260 μm wide located on the top face of the channel (200 μm wide and 30 μm high) overlaps with a pair of electrodes 120 μm long and 20 μm wide located on the bottom face of the channel, defining two detection volumes measuring 40 x 20 x 30 μm^3 and separated by a 60 μm gap

4.3 Numerical modelling of electrode configurations

For impedance-based microfluidic systems it is important to determine the electric and dielectric response of the system to an applied voltage. The detected impedance signal strongly depends on the electric field distribution and current flow within the detection volume. Therefore, an accurate map of the electric field distribution in the sensing region of the device is required to evaluate the performances of the system.

The electric field distribution was calculated by numerically solving Maxwell's equations in the quasi-electrostatic approximation, from which the quasi-electrostatic form of Poisson's equation is derived

$$\nabla \cdot \left(\epsilon - \frac{j\sigma}{\omega} \right) \nabla \phi = 0 \tag{4.1}$$

where ϵ is the permittivity, σ is the conductivity, $w = 2\pi f$ is the angular frequency and ϕ is the electric potential.

Numerical solutions to equation (4.1) were obtained using the finite element method (FEM). The FEM is a very general technique to calculate approximate solutions to those boundary-value problems described by partial differential equations. It originated from structural analysis in civil engineering in the early 1950s and has since been generalised for numerical modelling in a wide variety of engineering disciplines, including electrodynamics. The FEM operates by discretising the domain into a mesh of smaller polygonal domains and by solving the original partial differential equations on each domain. Instead of approximating the partial differential equations as in the finite difference method, the FEM approximates their solutions. A detailed description of the FEM is behind the scope of this thesis, a more comprehensive discussion can be found in [135].

FEM simulations were performed using the commercially available package COMSOL Multiphysics 3.4 (COMSOL Inc.). The software package incorporates all the tools required for the FEM modelling process: CAD tools for geometry design, mesh generation tools, several solvers for space matrices, visualisation and post-processing tools. The next section describes the different steps involved in the numerical calculations, and the assumptions and considerations that were made in the model.

4.3.1 Model considerations

For an accurate solution of the electric field distribution within the microfluidic channel, a 3D representation of the channel geometry is required. The computational domain consists of a rectangular box that has the same dimensions as the microfluidic channel. The three configurations described in the previous section were simulated and the simulation domains are shown in Figure 4.4. The coordinate system that will be used through this chapter is also shown in Figure 4.4 and defined as follows: channel width (x), channel length (y) and channel height (z). The central point within the channel is set to (0,0,0) and the flow is in the y direction. The following considerations are valid for the three cases.

The electrodes are defined as portions of the lower and upper faces of the box and they are modelled as perfect conductors. They are considered to be equipotential surfaces with no finite thickness. This assumption can be considered reasonably valid since the thickness of the fabricated electrodes is very small compared to that of the channel. The advantage of modelling the electrodes as infinitely thin is that much fewer elements are needed to obtain an accurate solution. The top and bottom electrodes are set to Dirichlet boundary conditions $\phi = 1$ V and $\phi = 0$ V , respectively. Although the fabricated microfluidic device is provided with two pairs of electrodes (see section 4.2), the model only considers a single set, located in the centre of the channel, since the

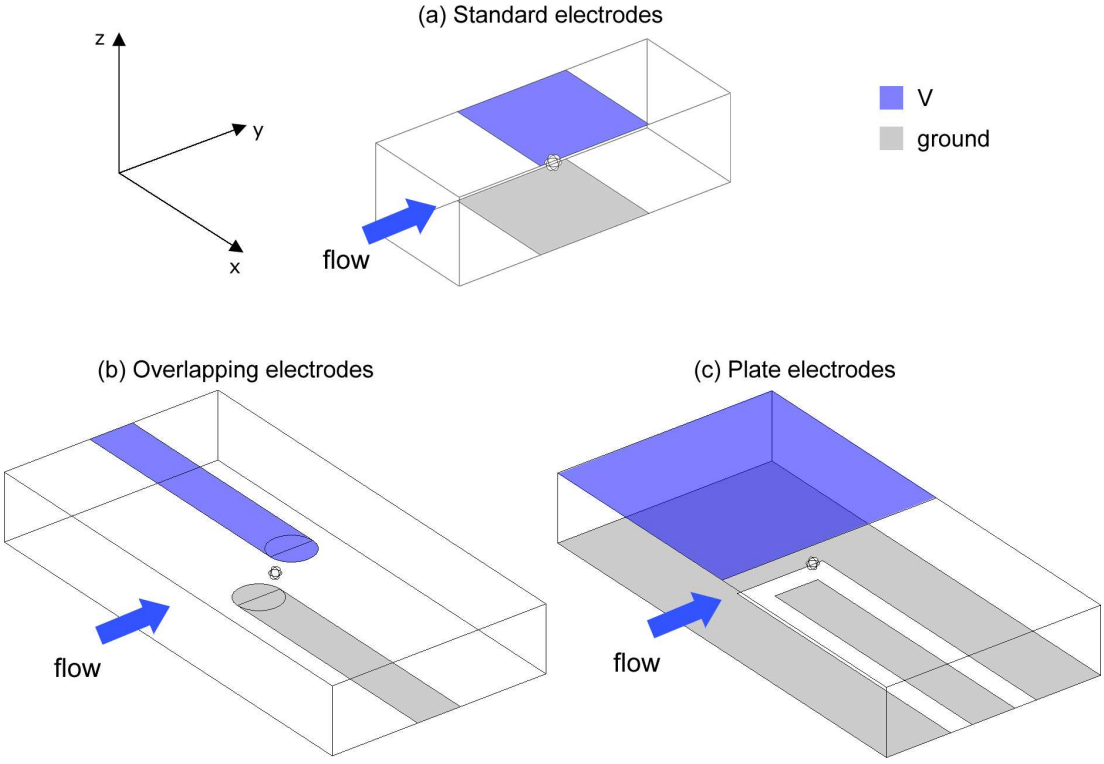

FIGURE 4.4: Schematic of the simulation domains for the three electrode configurations: (a) overlapping electrode configuration, (b) standard electrode configuration, (c) plate electrode configuration. A solid polymer particle of 5 μm diameter located in the centre of the detection region

electrode pairs are sufficiently far away as to have no significant interactions with each other. The channel walls are set to be perfect insulators (Neumann boundary conditions $\frac{\partial \phi}{\partial n} = 0$). In reality the channel is made of glass but, due to the very large difference in conductivity between the fluid and glass, the effect of the glass structure on the solution is negligible for frequency values lower than the charge relaxation frequency of the system (300 MHz in PBS) and therefore glass is not included in the computational domain [136]. Also the channel input and output are considered perfect insulators, as the channel length is set to be large enough so that does not significantly affect the electric field distribution. A solid polymer particle in suspension was modelled as a 5 μm diameter solid sphere with homogeneous dielectric properties, located in the centre of the detection region. Simulations were performed at 500 kHz, other frequencies were not considered since for the range of interest (300 kHz -15 MHz) the magnitude of the impedance signal from an homogeneous particle is almost constant (see section 3.3.5.1). The results presented here are valid for all the frequency range of interest.

The material dielectric properties set for each region of the domain (subdomains properties) are summarised in Table 4.1. The conductivity of water was set to 0.12 S/m to take into account that for the experiments food dye was added to the water in order to

distinguish the sheath flow from the sample stream. Continuity of the normal current is satisfied at all the internal subdomain boundaries.

	PBS	Oil	Water	Particle
ϵ_r	78	10	78	2.5
σ (S/m)	1.6	0	0.12	$0.36\text{x}10^{-3}$

TABLE 4.1: Subdomain parameters used for FEM model of electrode configurations.

By initialising the mesh generation, the computational domain is divided into smaller tetrahedron volumes. The number of mesh elements ultimately determines the computational time and the accuracy of the solution. Several mesh parameters can be adjusted. For the simulations, a denser mesh was used in regions of large variations of the field while a coarser mesh was used where the field is uniform. Mesh convergence tests were carried out in order to optimise the number of elements, minimize numerical errors and avoid unnecessarily long calculations. A typical example of convergence as a function of number of mesh elements is shown in Figure 4.5. For a number of mesh elements greater than 5000000 the calculated impedance converges to a stable value. This convergence test was carried out for a uniform mesh density across the computational domain. For all the simulations presented in this section, the number of mesh elements was selected in order that the error in the calculated impedance value is less than 2%. The solutions were computed using the default GMRES interactive solver.

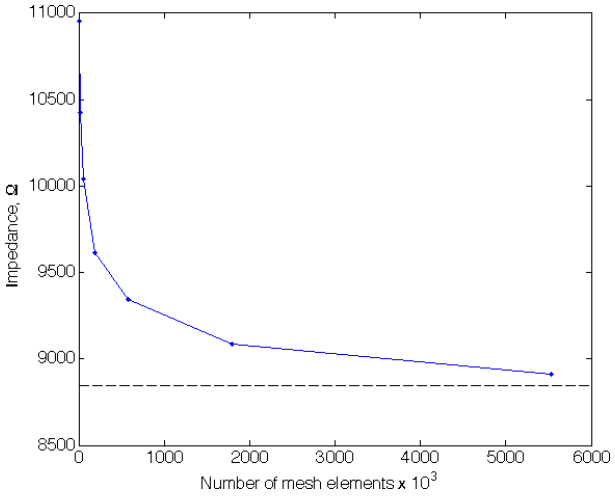

FIGURE 4.5: A typical example of convergence as a function of number of mesh elements.

4.3.2 Modelling results

In the following sections, the results obtained from the simulations of the electrode geometries described above are shown and compared.

4.3.2.1 Standard electrode configuration

The simulation domain for the standard electrode configuration is shown in Figure 4.4 (b). The simulation was performed with the channel filled with buffer solution (PBS; σ = 1.6 S/m and $\epsilon_r = 78$). A 5 μm diameter polymer bead was modelled as a homogeneous sphere located at the centre of the channel. The dielectric properties of the particle are listed in Table 4.1. Figure 4.6(a) shows intensity plots and streamlines of the calculated electric displacement field in a cross section on the xz plane at the centre of the channel (y = 0). A 3D view of the electric displacement streamlines is shown in Figure 4.6(b). For reasons of clarity, streamlines are plotted only on one side of the channel but, due to the symmetry of the problem, the same distribution is obtained on the other side. Both plots shows that the field distribution is uniform within the detection region, while a fringing field effect is clearly observed at the electrode edges, along the channel width.

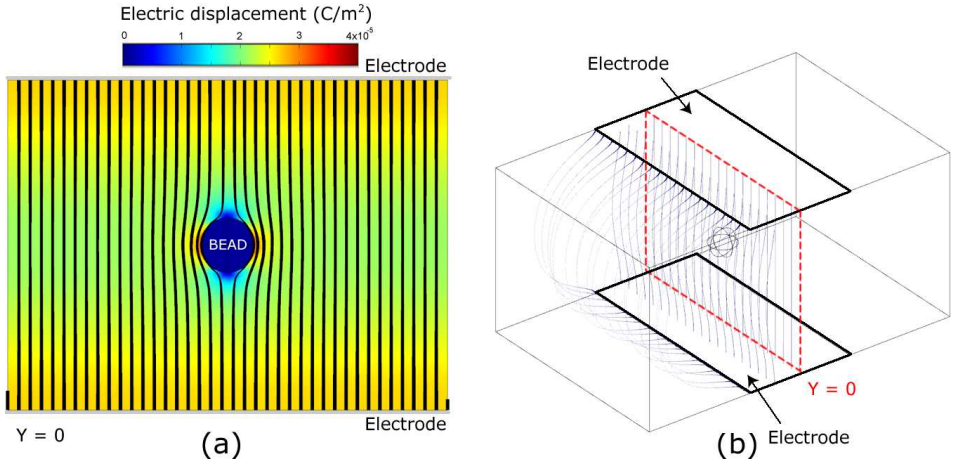

FIGURE 4.6: (a) Intensity plot and streamline of the electric displacement field in the channel cross section on the xz plane (y=0). (b) 3D plot of the electric field displacement streamline. For reasons of clarity, streamlines are plotted only on one side of the channel but, due to the symmetry of the problem, the same distribution is obtained on the other side.

Figure 4.7 is an intensity plot of the current density on a horizontal plane through half of the channel height (z = 0) and it shows that the current density is very uniform at the centre of the channel and drops rapidly away from the sensing region.

4.3.2.2 Overlaping electrodes

In order to investigate the effect of focussing the sample stream and to estimate the increase in sensitivity of the system, three situations were analysed: first with the entire volume filled with buffer solution (σ = 1.6 S/m and $\epsilon_r = 78$), then with buffer occupying a central portion of the channel, equivalent to a sample stream 30 μm wide and 30 μm

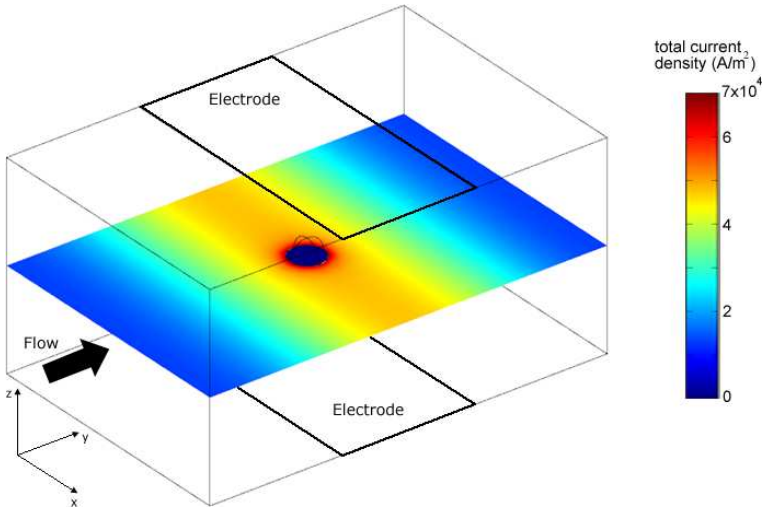

FIGURE 4.7: Calculated current density cross section (z = 0) for standard electrodes. The current density is very uniform at the centre of the channel and drops rapidly away from the sensing region. The blue sphere at the centre of the channel corresponds to the modelled bead.

high, as shown in Figure 4.8. Outside this region there was water (σ = 0.12 S/m and ϵ_r = 78) in one case, and oil (σ = 0 S/m and ϵ_r = 10) in the other case.

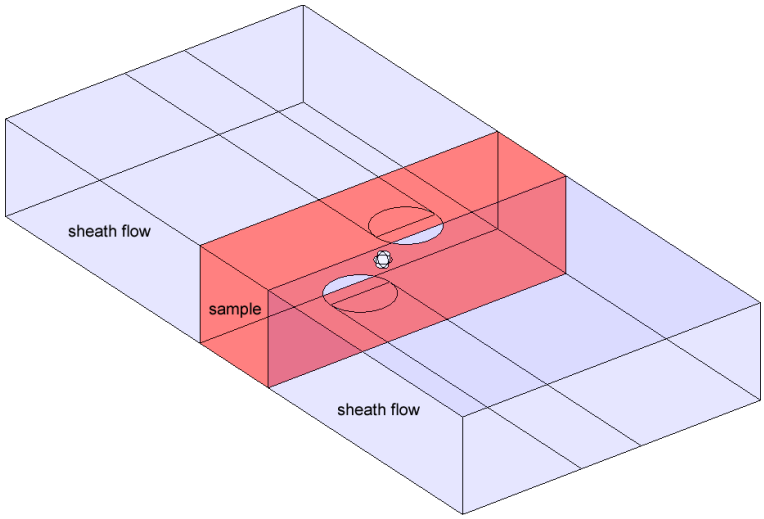

FIGURE 4.8: Schematic showing the simulation domain. The buffer containing the sample particles occupies only the central portion measuring 30 μm in width and 30 μm in height and it is indicated in red. The rest of the channel (in blue) is filled with sheath fluid (PBS, water or oil).

Figure 4.9 shows intensity plots and streamlines of the calculated electric displacement in a cross section at the centre of the channel (on the xz plane at y = 0), for the three simulated cases. For a direct comparison of the three situations, intensity plots are shown using the same scale and in order to define a scale that was suitable for the three different situations, the points of high field intensity were removed from the plots (white areas located at the electrode edges in Figure 4.9(a) and (b)) . When the channel is filled

with buffer (Figure 4.9(a)) or buffer and water (Figure 4.9(b)), the electric displacement is divergent and occupies a large portion of the channel cross section; however a more uniform distribution of the field magnitude is observed for the case of sample focussing with water. When the channel is filled with buffer and oil (Figure 4.9(c)), the field is confined to the centre of the channel and extends very little into the oil regions. The field distribution is analogous to the one obtained for the standard configuration. The intensity of the displacement field around the particle is very similar in the three cases (green regions around the particle), as the sample fluid was the same in all three simulations.

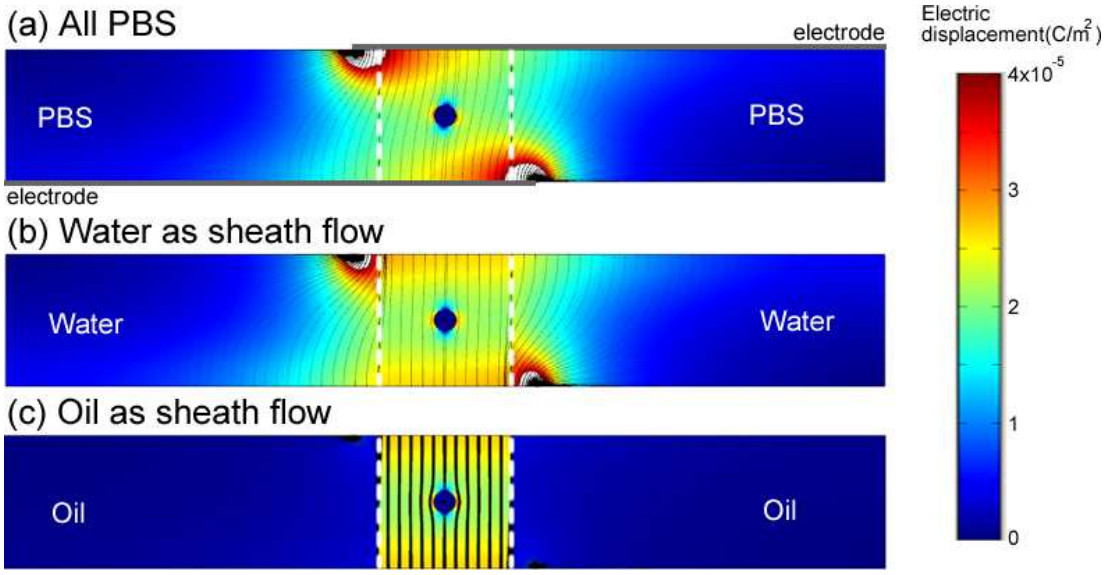

FIGURE 4.9: Cross section (y=0) and stream lines of the calculated electric displacement at the centre of the channel for overlapping electrodes when PBS, oil and water are used as sheath flow. The central sample stream (between dashed lines) is PBS. A polymer bead is located at the centre of the sample stream. Lines indicating the location of the electrodes are shown for the PBS case.

A clear indication of the distribution of the electric displacement within the channel is given in Figure 4.10, where 3D streamline plots are shown. In these plots, the thickness of the lines is proportional to the field strength. However, a direct comparison of the field magnitude between the three cases is not possible as, for simplicity, a different scale was applied for the stream lines in the three plots. Similar to what observed before, it is shown that when PBS or water are used as the focussing fluid, the field is divergent and occupies a large volume of the channel. When the sample is confined using a low permittivity material (oil), the field is effectively confined to the central part of the channel, and does not extend along the channel width (x direction) where oil is present. The fringing effect is present only along the y direction, within the portion of the channel occupied by the sample, and a more homogeneous field distribution is observed.

Plots of the current density on a horizontal cross section of the channel are shown in Figure 4.11. When the device is filled with buffer, the current path is divergent and occupies a large region, resulting in a big sensing volume. When the sample is focussed with a low conductivity fluid, the current density is tightly confined to the high conductivity region occupied by the sample stream, creating a much smaller sensing volume, and increasing the sensitivity of the system.

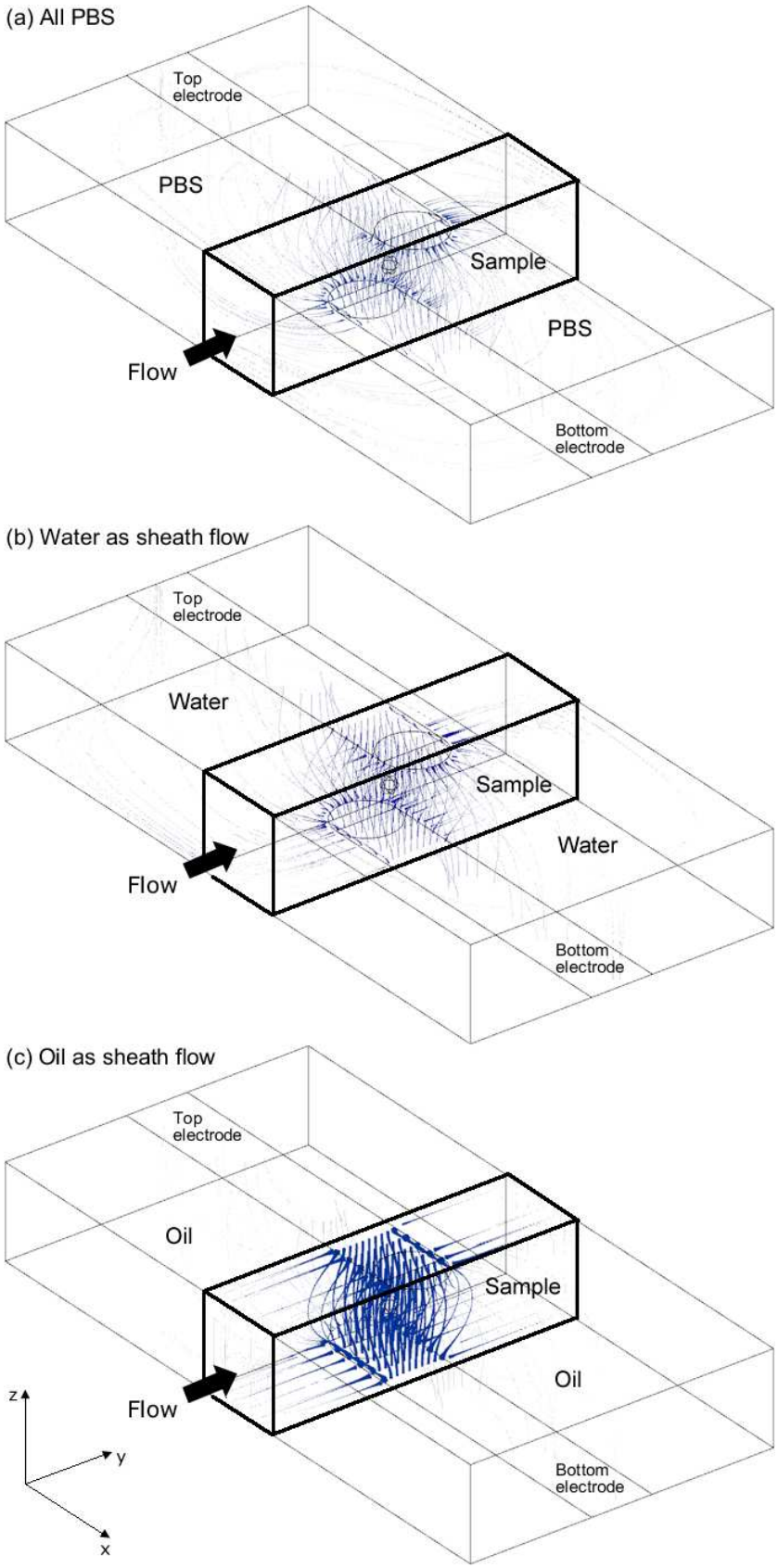

FIGURE 4.10: Stream lines of the calculated electric displacement when PBS, oil and water were the sheath fluids.

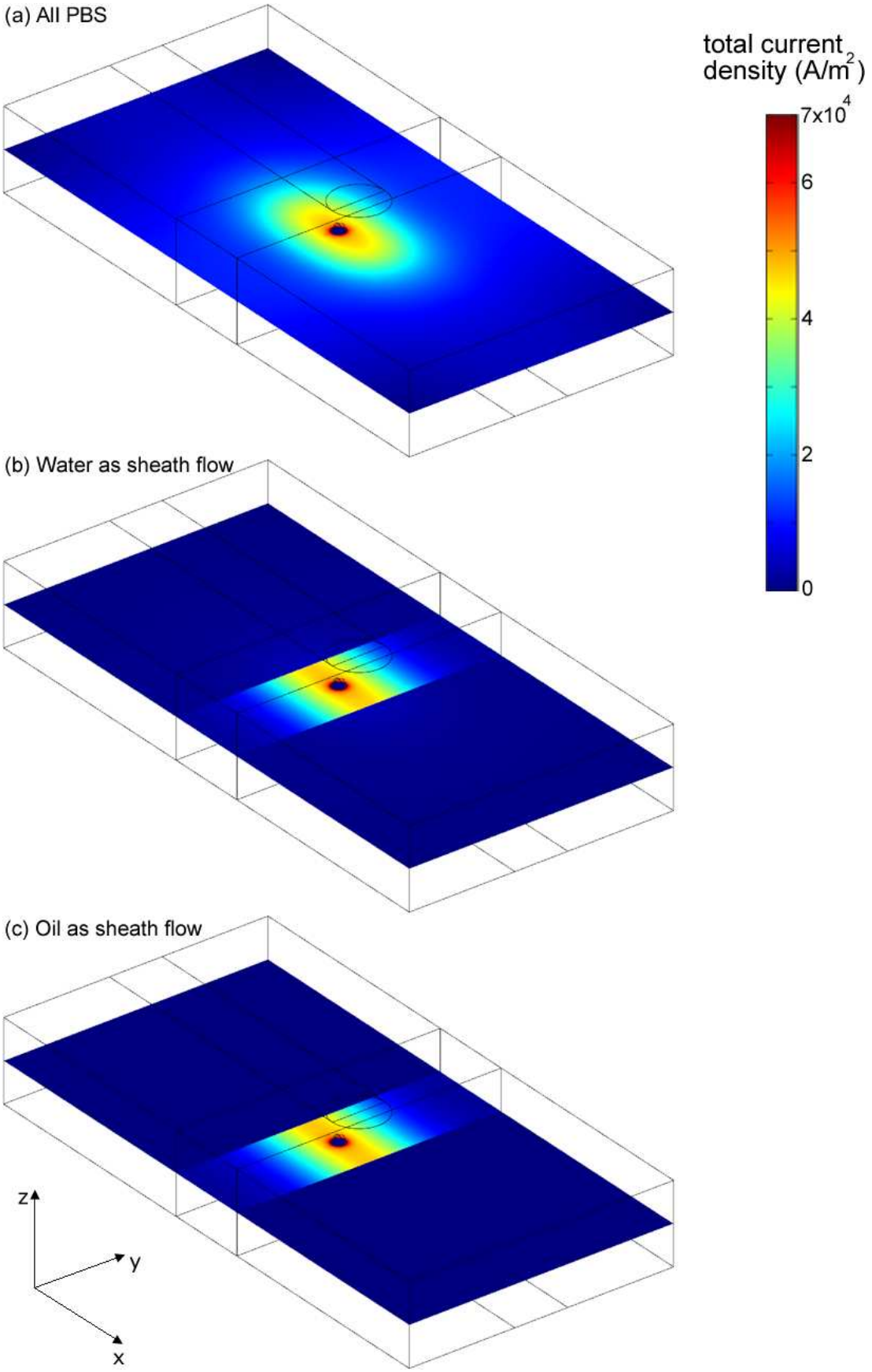

FIGURE 4.11: Calculated current density cross sections in the middle of the channel (z = 0) for overlapping electrodes with different focussing fluids, as shown in Figure 4.10.

4.3.2.3 Plate electrode configuration

In the previous section, it was shown that the use of a low conductivity fluid to hydrodynamically focus the sample stream results in a more homogeneous distribution of the field, a more effective confinement of the current path and, as a consequence, a smaller effective detection volume. In alternative to the use of low conductivity sheath flows, a similar result can be obtained by optimising the geometry of the electrodes. The use of a big excitation electrode and a guard plate around the sensing electrode (Figure 4.4 (c)) acts on the field distribution in a similar way to the insulating sheath fluid, except that the reduction of the field curvature is more effective. In fact, for the overlapping electrode configuration confinement is possible only along the electrode width (sample/sheath-flow interface), in this configuration the guarding plate surrounds three sides of the sensing electrode.

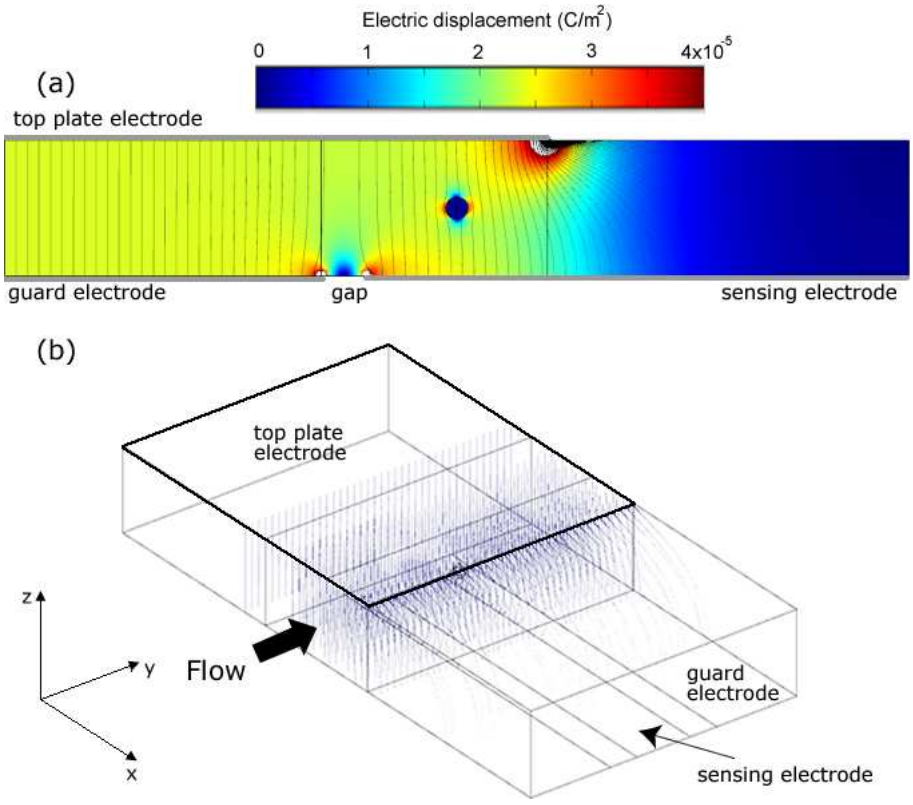

FIGURE 4.12: (a) Intensity plot and streamline of the electric displacement field in the channel cross section (y=0). (b) 3D plot of the electric field displacement streamline. For the sake of simplicity, only some of the streamlines between the top plate and the bottom guard electrode are shown. The whole channel is filled with PBS and a spherical particle is located in the middle of the channel.

The results of the simulation of this electrode configuration are shown in Figure 4.12. Figure 4.12(a) shows the intensity and the streamlines of the electric displacement in a channel cross section (y = 0). A 3D view of the electric displacement streamlines is

given in Figure 4.12(b). Again, for the sake of simplicity, only some of the streamlines between the top plate and the bottom guard electrode are shown. These plots show that there is almost no curvature of the field along the guarded edges of the electrode, and the distribution of the field is similar to the distribution obtained for the oil focussing (Figure 4.9(c)).

Figure 4.13 is an intensity plot of the current density on a horizontal plane in the channel. The current density is very homogeneous in the portion of volume underneath the plate electrode. As expected, due to the increased dimension of the excitation electrode and the presence of the guarding electrode, the total amount of current flowing within the channel is higher, but this does not affect the size of the detection volume, that is defined by the current flow between the top plate and the sensing electrodes only. The current flow outside the overlapping region does not contribute to the measurements.

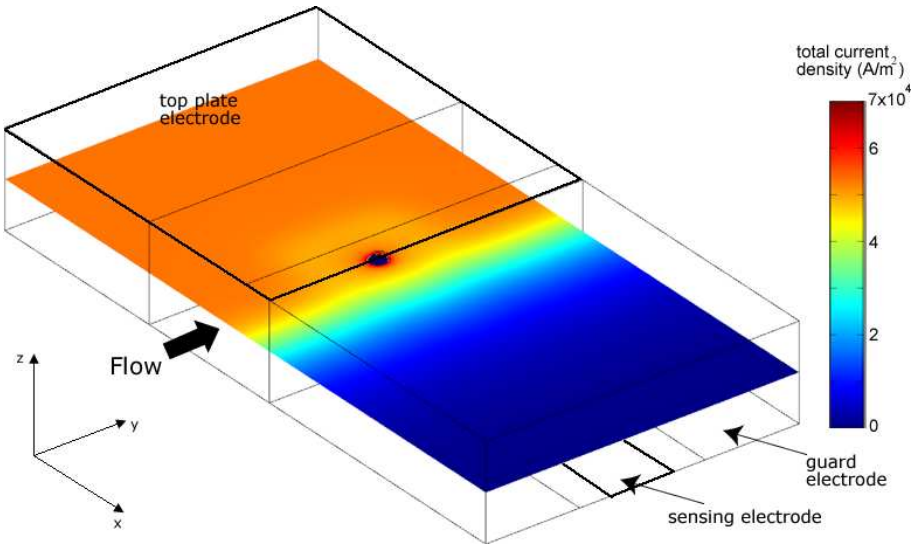

FIGURE 4.13: Intensity plot of the total current density on a horizontal plane (z=0) within the channel for the plate electrode configuration. The whole channel is filled with PBS and a spherical particle is located in the middle of the channel.

4.3.2.4 Impedance calculation

In order to obtain a quantitative estimation of the performances of the electrode configurations and an evaluation of the effects of the sample focussing, the measurement sensitivity, defined as the relative change in the impedance of the sensing volume due to the presence of a particle,

$$S = \frac{|Z_{mix}| - |Z_{ref}|}{|Z_{ref}|} \tag{4.2}$$

was calculated.

The magnitude of the impedance of the detection volume containing the particle in suspension was obtained from the simulation results of the previous section. To obtain the value of the impedance of the reference volume (suspending medium without particle), another set of simulations which did not include the bead, were performed. In both cases (detection volume with medium and particle, or medium only), the impedance was calculated by integration of the current density across the sensing electrode area. The results are summarised in table 4.2, where the magnitude of impedance of the sensing volume containing the medium only ($|Z|$ no particle), the magnitude of the impedance due to the presence of the particle ($|Z|$ with particle), their difference (ΔZ), and the sensitivity (S) are shown. The same data is shown in the histogram plots of figure Figure 4.14.

Electrode configuration - Focusing fluid	$\|Z\|$ with particle (Ω)	$\|Z\|$ no particle (Ω)	$\Delta\|Z\|$ (Ω)	S (x10^{-4})
Overlapping - PBS	9413	9402	11.46	12.2
Overlapping - Water	18942	18895	46.64	24.6
Overlapping - Oil	20937	20880	57.25	27.4
Plate - PBS	15872	15839	32.59	20.8
Standard - PBS	15645	15612	32.48	20.5

TABLE 4.2: Calculated impedance values and sensitivity for different electrode configurations and focussing techniques.

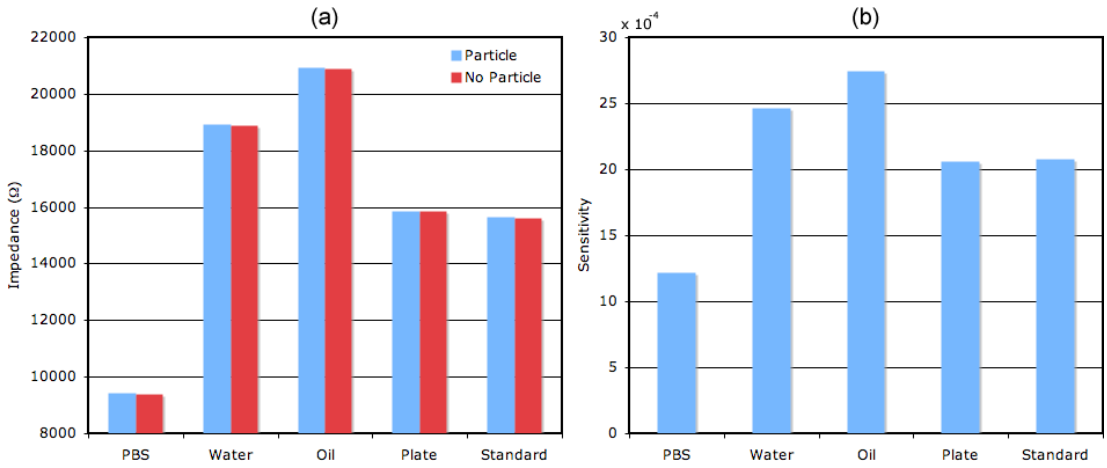

FIGURE 4.14: Calculated change in the impedance due to the presence of a particle in the detection volume. (a) Comparison between the impedance of the detection volume filled with medium and the impedance of the detection volume with medium and particle. (b) Calculated sensitivity.

As expected, the overlapping electrode configuration with PBS as the focussing flow gives the lowest sensitivity: 12.2x10^{-4}, compared to 20.5x10^{-4} for the standard configuration. This is due to the fact that in this case, the detection volume is very large. The sensitivity

of the overlapping electrode configuration significantly increases when a low conductivity medium is used as the sheath fluid: $S = 24.6\text{x}10^{-4}$ when the sample is focussed using water and $S = 27.4\text{x}10^{-4}$ when the sample is focussed using oil. Confining the sample using an insulating liquid is equivalent to performing the measurement with a smaller channel. In the simulations, the width of the focussed sample stream was set equal to 30 μm, narrower than the channel of the standard configuration (40 μm). For this reason, the standard configuration has a lower sensitivity. In addition to the improvement in sensitivity, the insulating fluid also reduces the fringing field at the electrodes edges. Finally, an increase in sensitivity is also observed for the plate electrode configuration, resulting in an impedance change and sensitivity very similar to that obtained with standard electrodes.

In order to validate the simulation results, the impedance of the channel with the standard electrode configuration was calculated analytically using the Maxwell's mixture theory. The calculations were performed for the case in which a 5 μm diameter polymer bead was suspended in the detection volume (impedance of the mixture) and for the case in which the channel was filled with buffer solution only (reference volume). The impedance of the mixture (Z_{mix}) was calculated using equation (2.45) reported in section 2.4.1. The impedance of the channel filled with the medium (Z_{ref}) was calculated using the same relation where the complex permittivity of the medium (ϵ_m) was used instead of ϵ_{mix}. The detection volume was defined by the width and length of the electrodes and the height of the channel which, for the standard electrode configuration, measured 20, 40 and 30 μm, respectively. The parameters of the medium and polymer particle were set to the same values used in the FEM simulation and are listed in table 4.1. The geometric constant G_f was determined using conformal mapping [114], and was equal to 44.268 μm for the geometrical parameters of the chip. The values obtained at a frequency of 500 kHz were $\text{Z}_{mix} = 14180\ \Omega$ and $\text{Z}_{ref} = 14120\ \Omega$. These values can be considered in good agreement with the ones obtained by FEM analysis of the standard configuration (last row of table 4.2).

4.3.2.5 Effect of particle misalignment on device sensitivity

In impedance measurements, it is very important that all the particles follow the same trajectory while flowing through the device detection region. In this section, the effect of the displacement of the particle position from the centre of the channel is studied.

Simulations of the overlapping electrode configuration, when the channel was filled with PBS, were performed for different displacements of a 5 μm diameter particle, from the centre of the channel along the channel width. The position of the particle was varied

with lateral steps of 5 μm, up to a maximum lateral displacement of 20 μm, in both directions from the centre.

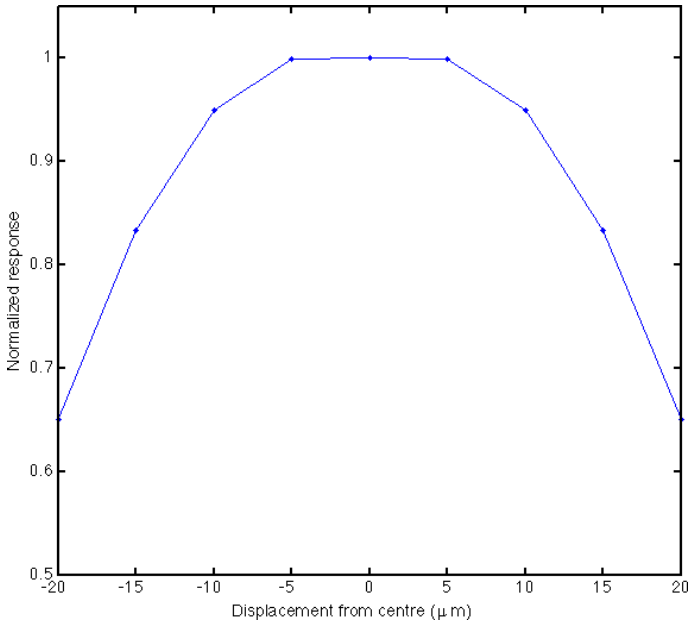

FIGURE 4.15: Effect of the particle displacement from the centre of the channel on the sensitivity of the device.

Figure 4.15 shows the sensitivity calculated for the different displacements, normalized to the sensitivity at the centre of the channel. Small displacements ($\pm$5 μm) from the centre do not affect the sensitivity of the device due to the homogeneity of the field in this region. However, if the particle crosses the detection region more than 10 μm away from the centre, the sensitivity begins to drop rapidly. In terms of measurement results, a particle that crosses the detection volume away from the centre of channel is detected by the system as a smaller particle located in the centre. This has two main consequences: first, an increase in coefficient of variation (CV) in size of the measured particles, then a strong limitation of the capability of discriminating between particles with very similar size. For this reason, it is of fundamental importance to accurately control the width of the sample stream and its position within the channel during the experiments.

4.4 Impedance measurements

The numerical calculations shown in the previous section showed that the sensitivity of the micro-impedance cytometer can be significantly improved by focussing the sample with a low conductivity fluid or using an improved electrode design. In this section, the performances of the electrode configurations and focussing techniques are tested by

measuring the impedance of two types of polymer beads with similar sizes (4.62 μm and 5.49 μm). These two beads differ in less than 1 μm in diameter and therefore where chosen to test the sensitivity of the system.

4.4.1 Experimental procedure

Polystyrene (PS) particles with a certified mean diameter of 4.62 $\pm$ 0.09 μm and quoted coefficient of variation (CV) of 1.5 %, were purchased from microparticles GmbH. Fluorescent (633/760 nm) carboxylate-modified polystyrene beads (Bangs Laboratories Inc. USA) with a mean diameter of 5.49 $\pm$ 0.48 μm and quoted CV of 5 % were obtained from Molecular Probes. The beads were washed three times and re-suspended after sonication in PBS (σ = 1.6 S/m). A mixture of the two types of beads in a ratio of approximately 2:1 (4.62 μm:5.49 μm) with a final concentration of 300 particles/μl was prepared. Impedance and fluorescence emission were measured simultaneously using the experimental setup described in section 3.3. Impedance was measured using AC signals at frequencies between 503 kHz and 15 MHz and amplitude of 2.5 V. Fluorescence emission from the red beads was measured at 670 $\pm$ 40 nm. The overlapping configuration was tested using different sheath flows (PBS; Hexandiol and water). For the plate electrode configuration, measurements were performed focussing the sample with PBS. To control the position and width of the sample stream within the channel, red food dye was added to the sheath flow when this was PBS or water. When the sheath flow was Hexandiol, in order to improve the wettability of the channel, the channel was coated before the experiment with bovine serum albumin (BSA) by flowing 5 % solution of BSA in PBS through the device for 1 hour. 1 % Tween 20 was added to the Hexandiol to reduce the surface tension at the oil/sample interface. Flow was controlled using the pneumatic method described in section 3.3.1. For all the experiments, the sample flow rate was adjusted to give a sample stream width of 30 μm and a particle transit time (through the measurement region) was between 0.6 and 1.2 ms, which corresponds to a flow velocity between 50 and 100 mm/s. For each experiment the number of events ranged from 1000 to 3000.

4.4.2 Results

4.4.2.1 Overlapping electrode configuration and hydrodynamic focussing with PBS

Figure 4.15 shows scatter plots of the impedance of a mixture of 4.62 μm and 5.49 μm diameter beads. In both plots the data points are colour-coded according to the

fluorescence signal acquired from the 5.49 μm. In figure 4.15 (a), the impedance is displayed as opacity ($|Z|_{15MHz}$ / $|Z|_{503kHz}$) vs magnitude of the low frequency impedance ($|Z|_{503kHz}$). Opacity is the ratio of the high frequency to the low frequency signal and provides information on the difference in particle resistivity at high and low frequency [56]. As the beads have homogeneous dielectric properties and their impedance response is almost constant in the frequency range 500 kHz to 15 MHz, the opacity is close to 1.

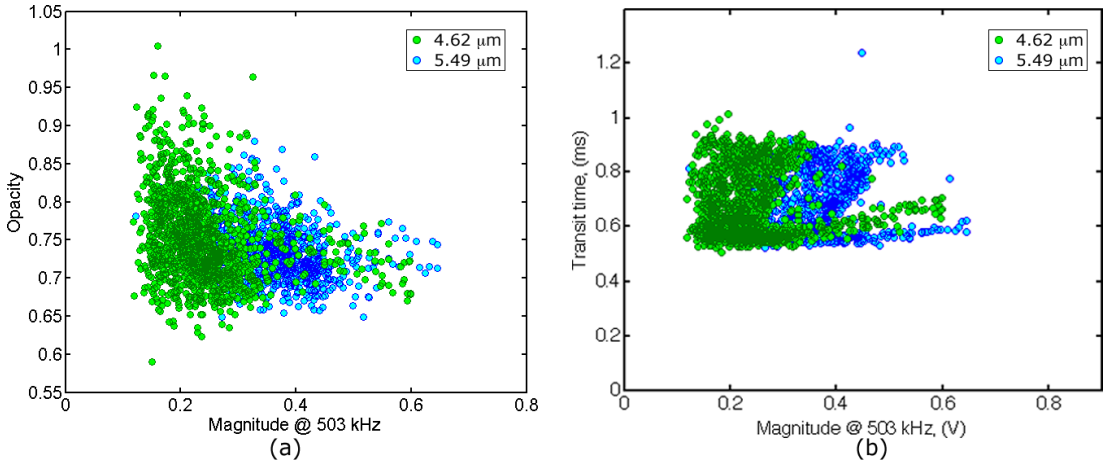

FIGURE 4.16: Overlapping electrodes focussing with PBS. (a) Scatter plot of opacity against magnitude at low frequency (503 kHz) for a mixture of 4.62 μm and 5.49 μm diameter beads. (b) Scatter plot of transit time against magnitude at low frequency (503 kHz) for a mixture of 4.62 μm and 5.49 μm diameter beads. Both plots are colour-coded based on the fluorescence emission recorded from the 5.49 μm beads.

Figure 4.15 (b) is a scatter plot of the particle transit time (through the detection region) against the impedance at 503 kHz. The transit times are uniformly distributed for the two types of particles. The elongation towards higher values of the impedance magnitude that is observed in both distributions might be caused by a small number of doublets crossing the detection region. Both figures show that two populations can be identified but there is not clear separation between them. This is more evident in Figure 4.16, where an intensity plot together with the histograms of the low-frequency impedance magnitude and opacity of the same data of Figure 4.15 (a) is shown. The 4.62 μm bead population is located around a mean value of the low-frequency magnitude of around 0.25 V and is almost twice the size of the 5.49 μm population which has an average impedance magnitude of about 0.4 V.

In order to estimate the number of particles in each distribution, the histogram of the impedance magnitude (503 kHz) was fitted to a linear combination of two Gaussian distribution. The Gaussian fit was performed on the impedance data without bias and is shown in figure 4.17 (b). From the fit, the mean amplitude values (μ), the CVs and the percentages (%) were calculated. The same analysis was also performed with

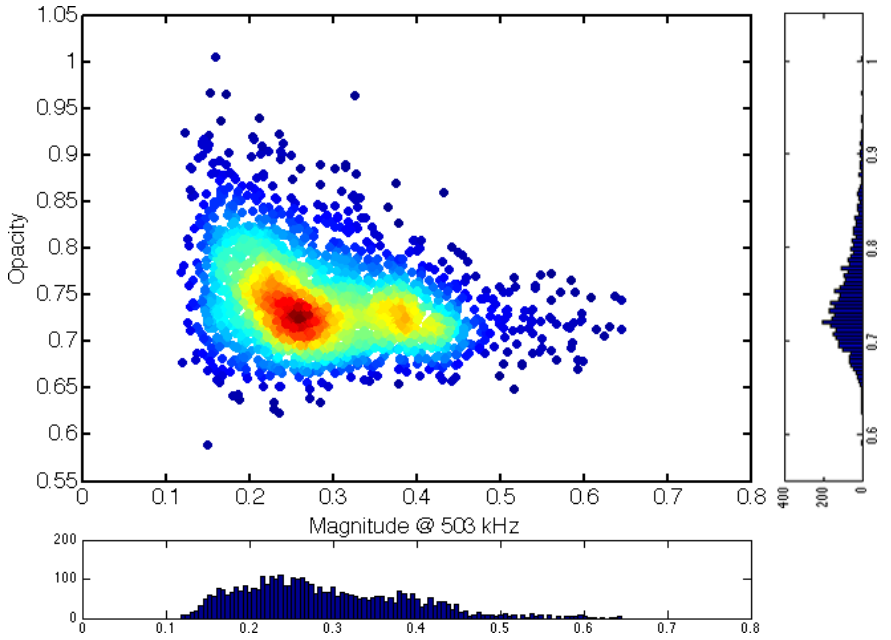

FIGURE 4.17: Overlapping electrodes focussing with PBS. Intensity plot of opacity against magnitude at low frequency (503 kHz) for a mixture of 4.62 μm and 5.49 μm diameter beads. Histograms of the impedance magnitude at 503 kHz and opacity of the same data are also shown.

particles identified from their fluorescence signal rather than impedance. These data are summarised in table 4.3.

One dimensional Gaussian fitting allows for fitting the data along one axis and cannot provide accurate information when the populations have an irregular shape, i.e. when they cannot be separated with a straight line perpendicular to the axis. However, Gaussian fit in two dimensions would not add further information as there is not difference in the population opacities. A more accurate way of analyzing the experimental data is by plotting an intensity distribution to visually identify the populations. Then a manual gating can be performed by enclosing the populations with irregular polygons. A code for the manual gating of the populations similar to the one normally used in traditional flow cytometry was written in MATLAB. The intensity plot with manual gating of the two populations is shown in Figure 4.18(a). The results obtained from the analysis of the gated population are shown in table 4.4 where data obtained from analysis of the fluorescence emission are compared.

The population percentages shown in table 4.3 and table 4.4 are in good agreement with the ratio of the sample mixture, however a discrepancy between the values determined when the analysis was performed on data triggered on impedance or data triggered on fluorescence signals is observed. The number of 4.62 μm beads obtained from impedance-based analysis is higher than one from fluorescence detection. A deviation in the values of the mean magnitudes is also observed. However, the analysis performed on gated

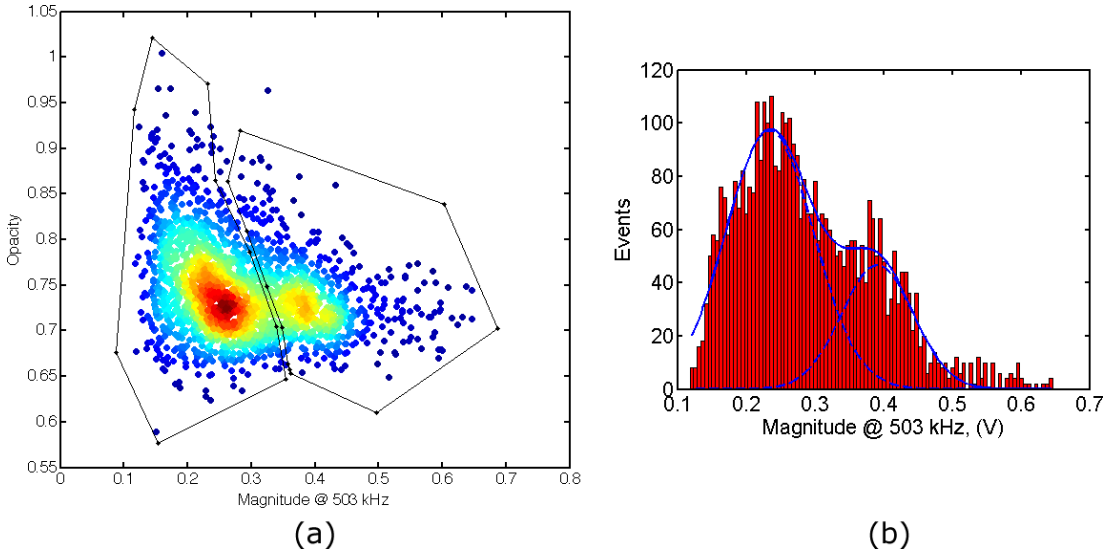

FIGURE 4.18: Overlapping electrodes focussing with PBS. (a) Intensity plot of opacity against magnitude at low frequency (503 kHz) for a mixture of 4.62 μm and 5.49 μm diameter beads where gating of the populations is shown. (b) Histograms of the impedance amplitudes for the mixture of beads measured at 503 kHz fitted to a Gaussian distribution with two peaks.

populations is more effective than the Gaussian fit, as the values obtained are closer to the ones given by analysis of the fluorescence signals. The difference in percentages and mean amplitudes is due to the overlap of the two populations, indicating that when the sample is focussed using PBS, impedance-based discrimination of particles that are very similar in size is possible, but is less accurate than fluorescence detection.

	1D Gaussian			**Fluorescence**		
	μ (V)	CV	%	μ (V)	CV	%
4.62 μm beads	0.23	11 %	69.29	0.24	31 %	60.82
5.49 μm beads	0.39	43 %	30.71	0.36	23 %	39.18

TABLE 4.3: Mean amplitude (μ), coefficient of variation (CV) and % determined from the fitted Gaussian distributions for data triggered on impedance. The same information is shown for analysis of data triggered on fluorescence signal. Measurements were performed using the overlapping electrode configuration and PBS focussing.

4.4.2.2 Overlapping electrode configuration hydrodynamic focussing with oil

The impedance for the mixture of beads measured when the sample was sheathed with oil is shown in figure 4.18. In figure 4.18 (a) the data is plotted as opacity against impedance magnitude at 503 kHz, and is colour-coded based on the fluorescence emission from the 5.49 μm beads. Figure 4.18 (b) shows the particle transit time against

	Impedance			Fluorescence		
	μ (V)	CV	%	μ (V)	CV	%
4.62 μm beads	0.23	21.8 %	66.21	0.24	31 %	60.82
5.49 μm beads	0.40	16.5 %	33.79	0.36	23 %	39.18

TABLE 4.4: Mean amplitude (μ), coefficient of variation (CV) and % determined from the 2D population gating for data triggered on impedance. The same information is shown for analysis of data triggered on fluorescence signal. Measurements were performed using the overlapping electrode configuration and PBS focussing.

impedance magnitude at 503 kHz. Two populations are clearly delineated, showing that discrimination based on the impedance signal from the beads is possible. From both figures it is observed that the spread of the distributions is higher than the one found when PBS was used as the sheath flow. This is probably due to the elongation of the parabolic profile of the sample stream, and a consequent spread in particle transit time, which occurs when the sample is confined using a fluid with different viscosity. However, this wide spread in transit time does not affect the discrimination between the two populations. Figure 4.19 shows the intensity plot and corresponding histograms of the impedance data of Figure 4.18 (a).

The intensity plot showing population gating is shown in Figure 4.20. The data obtained from the analysis of gated populations and fluorescence signals are summarised in table 4.5, where it is shown that both techniques give very similar results.

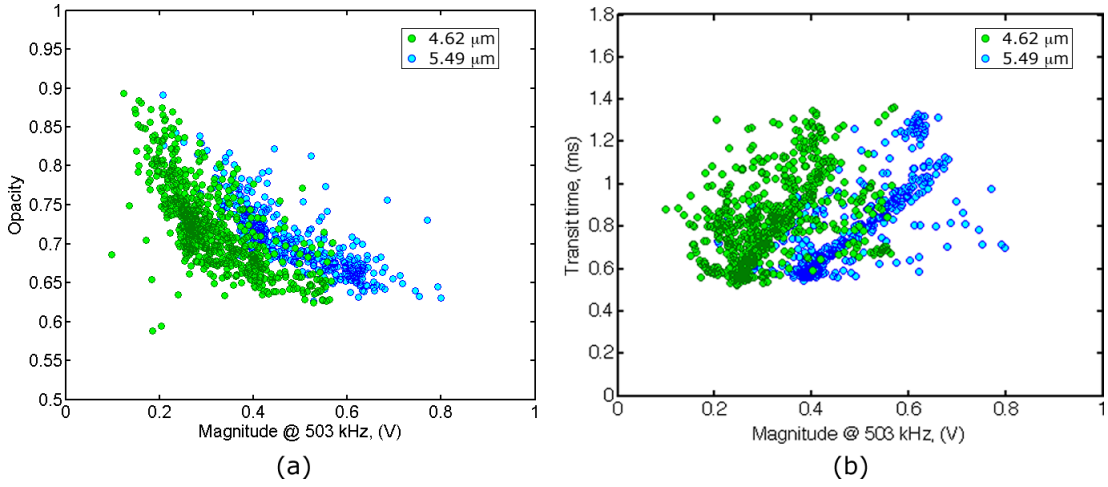

FIGURE 4.19: Overlapping electrodes focussing with oil. (a) Scatter plot of opacity against magnitude at low frequency (503 kHz) for a mixture of 4.62 μm and 5.49 μm diameter beads. (b) Scatter plot of transit time against magnitude at low frequency (503 kHz) for a mixture of 4.62 μm and 5.49 μm diameter beads. Both plots are colour-coded based on the fluorescence emission recorded from the 5.49 μm beads.

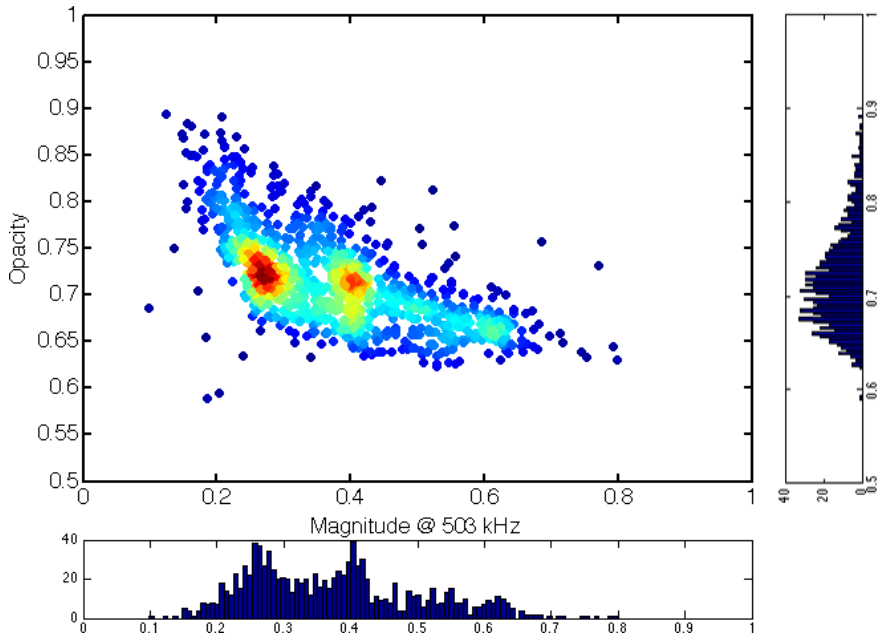

FIGURE 4.20: Overlapping electrodes focussing with oil. Intensity plot of opacity against magnitude at low frequency (503 kHz) for a mixture of 4.62 μm and 5.49 μm diameter beads. Histograms of the impedance magnitude at 503 kHz and opacity of the same data are also shown.

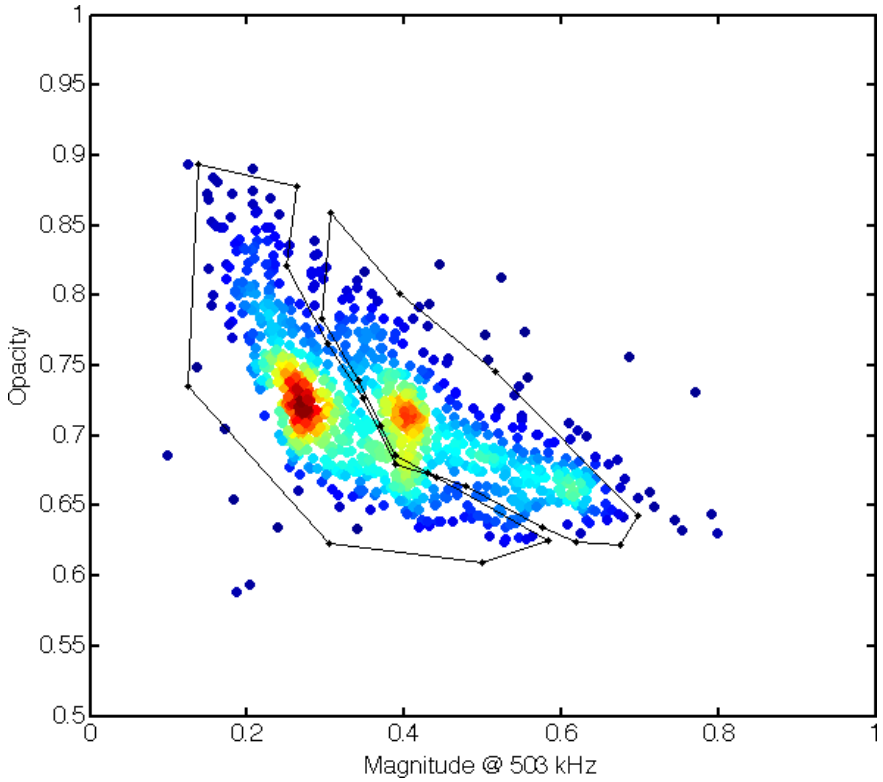

FIGURE 4.21: Overlapping electrodes focussing with oil. (a) Intensity plot of opacity against magnitude at low frequency (503 kHz) for a mixture of 4.62 μm and 5.49 μm diameter beads where gating of the populations is shown.

	Impedance			**Fluorescence**		
	μ (V)	CV	%	μ (V)	CV	%
4.62 μm beads	0.29	26.5 %	59.34	0.32	29 %	63.7
5.49 μm beads	0.46	19.9 %	40.66	0.48	23 %	36.3

TABLE 4.5: Mean amplitude (μ), coefficient of variation (CV) and % determined from the 2D population gating for data triggered on impedance. The same information is shown for analysis of data triggered on fluorescence signal. Measurements were performed using the overlapping electrode configuration and oil focussing.

4.4.2.3 Overlapping electrode configuration and hydrodynamic focussing with water

The good performance of the overlapping electrode configuration and hydrodynamic focussing with water predicted by numerical analysis, was not achieved experimentally. The opacity of the mixture of beads plotted against the impedance magnitude at 503 kHz is shown in Figure 4.22. The figure shows that each population of beads generates two distributions: one distribution (right hand side) consisting of peak signals that have the usual shape observed in impedance measurements (see figure 3.22). The other

distribution (left hand side) is obtained from deformed signals similar to the one shown in Figure 4.23. The reason for noise in the measurement may be ion diffusion from the high conductivity buffer of the sample, to the low conductivity liquid of the sheath flow. Impedance measurements for different widths of sample stream were carried out. The problem persisted until the width of the sample stream increased to 80 μm, i.e. when the PBS/water interface was moved far away from the overlapping region, where around the electrode tips the magnitude of the electric field reaches its maximum. For widths of sample equal or higher than 80 μm, the deformed peak signals disappeared, but no discrimination between the two population was possible, as all the events merged into a single distribution. These experiments showed that the overlapping configuration is not suitable for measurements when the sample is focussed using a low conductivity liquid. A facing electrode configuration in which the electrode pairs extend for the whole channel width, instead of electrodes overlapping in the centre of the channel, could have solved the problem, as in this case the PBS/water interface would not be exposed to the high electric field regions around the electrode tips.

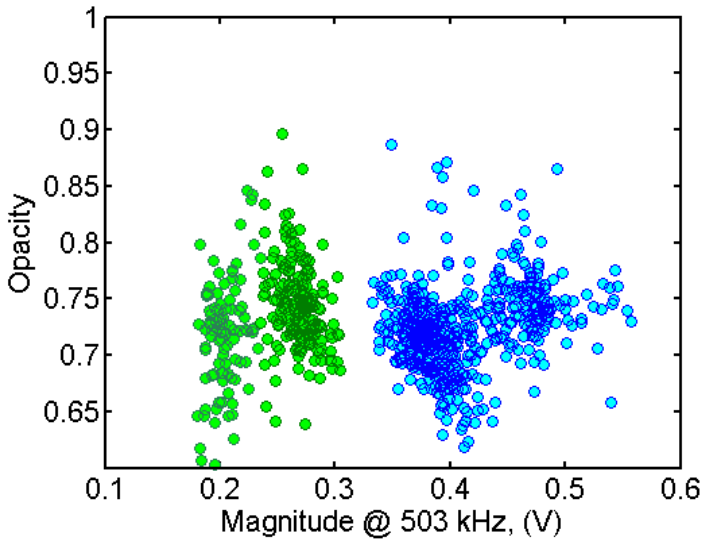

FIGURE 4.22: Experimental results, overlapping electrodes and water focussing. Scatter plot of opacity against magnitude at low frequency (503 kHz) for a mixture of 4.62 μm and 5.49 μm diameter beads. Each bead population forms two distributions.

4.4.2.4 Plate electrode configuration and hydrodynamic focussing with PBS

Experimental results for the measurement of the mixture of beads with the plate electrode configuration and PBS hydrodynamic focussing are shown in Figure 4.24, where the opacity (Figure 4.24 (a)) and the particle transit time (Figure 4.24 (b)), are plotted

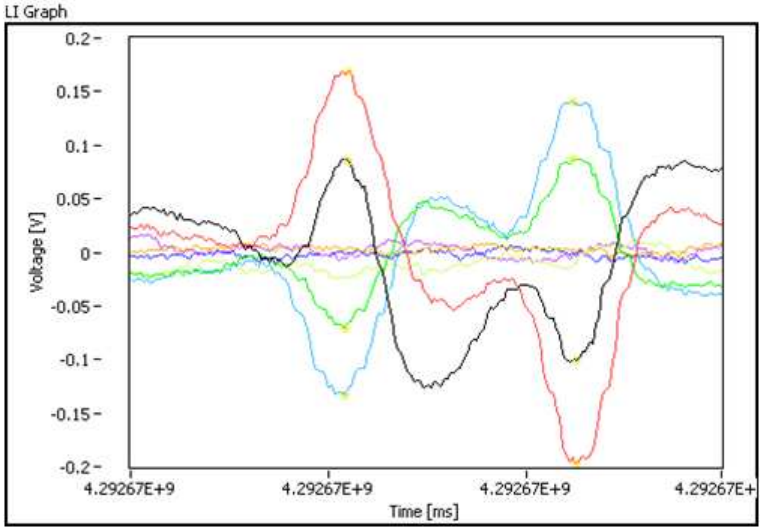

FIGURE 4.23: Typical deformed peak signal recorded during impedance measurements where water was used as the sheath flow.

against the magnitude at 503 kHz. Similarly to the case of oil focussing, two populations can be clearly distinguished. The impedance magnitude is lower than the one obtained with oil focussing, but the two populations are more uniformly distributed. The transit time is tightly distributed and is lower than in the other cases, as in this configuration the distance between the two sensing electrodes is higher. Figure 4.25 shows the intensity plot of the opacity against the low-frequency magnitude and corresponding histograms of the number of events. The intensity plot with the population gating is shown in Figure 4.26. The values of mean amplitudes for the two populations, the CVs and the percentages obtained from the analysis of the gated populations are shown in table 4.6. The same data obtained form analysis of the fluorescence signals is also shown in table 4.6. Good agreement between the results given by the two detection techniques is observed.

	Impedance			**Fluorescence**		
	μ (V)	CV	%	μ (V)	CV	%
4.62 μm beads	0.25	12.0 %	61.81	0.26	16 %	60.75
5.49 μm beads	0.40	11.5 %	38.19	0.40	12.6 %	39.25

TABLE 4.6: Mean amplitude (μ), coefficient of variation (CV) and % determined from 2D population gating for data triggered on impedance. The same information is shown for analysis of data triggered on fluorescence signal. Measurements were performed using the plate electrode configuration and PBS focussing.

4.4.2.5 Comparison of results

The experimental results from impedance measurements of the mixture of 4.62 μm and 5.49 μm beads are summarised in Figure 4.27, where data on the two electrode

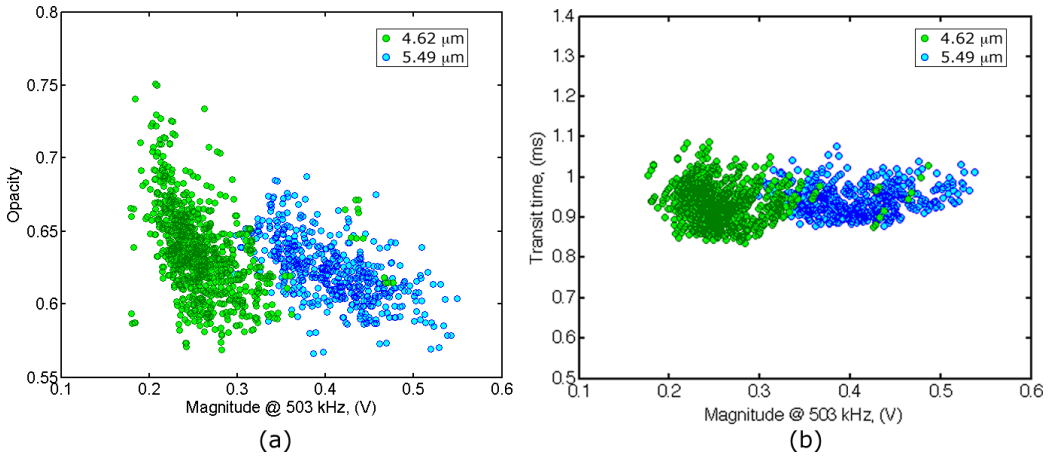

FIGURE 4.24: Plate electrode focussing with PBS. (a) Scatter plot of opacity against magnitude at low frequency (503 kHz) for a mixture of 4.62 μm and 5.49 μm diameter beads. (b) Scatter plot of transit time against magnitude at low frequency (503 kHz) for a mixture of 4.62 μm and 5.49 μm diameter beads.

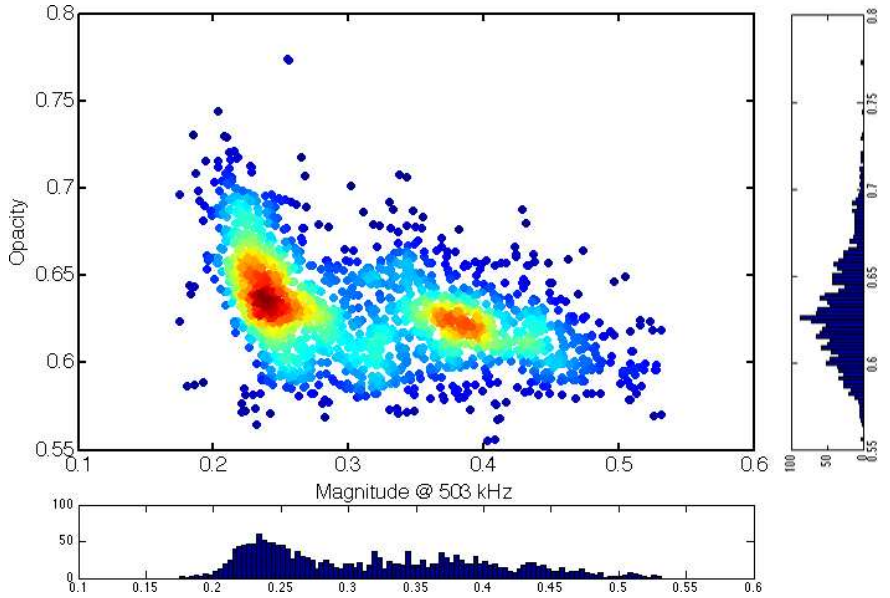

FIGURE 4.25: Plate electrode focussing with PBS. Intensity plot of opacity against magnitude at low frequency (503 kHz) for a mixture of 4.62 μm and 5.49 μm diameter beads. Histograms of the impedance magnitude at 503 kHz and opacity of the same data are also shown.

configurations and different sheath fluids are compared. Figure 4.27 (a) shows the mean amplitudes of the low frequency (503 kHz) impedance signal for 4.62 μm beads obtained, Figure 4.27 (b) shows the same data for 5.49 μm beads. In both plots, the values obtained from the analysis of data triggered on impedance or fluorescence signals are compared. The mean impedance amplitude for 5.49 μm beads measured using the standard configuration electrode was provided by Dr David Holmes and added to the plot of Figure 4.27 (b) for comparison.

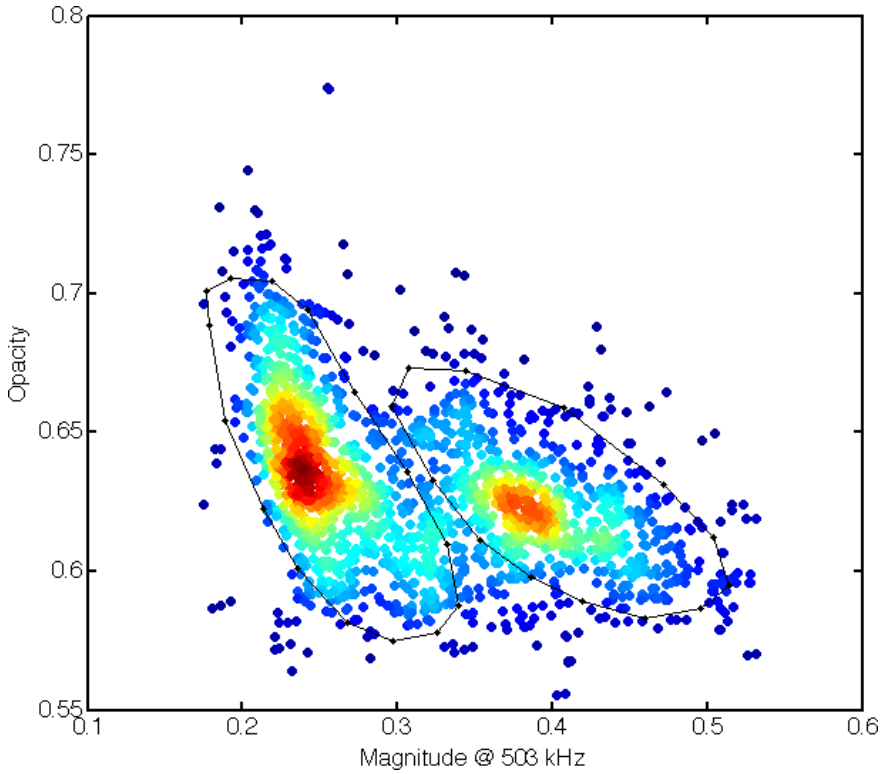

FIGURE 4.26: Plate electrode focussing with PBS. (a) Intensity plot of opacity against magnitude at low frequency (503 kHz) for a mixture of 4.62 μm and 5.49 μm diameter beads where gating of the populations is shown.

For both particle sizes, the impedance magnitude is maximum when the sample was focused using oil. Compared to PBS focussing that gives the lowest magnitude, oil focussing gives an increase in signal magnitude of 26 % and 15 % for the 4.62 μm and 5.49 μm beads, respectively. Oil focussing also provides better results than the standard electrode configuration, which uses a narrower channel.

When the sample was focussed using PBS, the mean amplitude of the 4.62 μm bead population obtained by impedance detection was lower than the one given by fluorescence detection, but the opposite result was obtained for the 5.49 μm beads. The reason of this inconsistency is the big overlap of the two populations when using PBS focusing, which means that it is impossible to separate of the two populations.

The smallest difference between the results obtained when the analysis was performed on data triggered on the impedance or fluorescence signal is obtained for the plate electrode configuration with PBS focussing, and is due to the good separation and the tight distributions of the data.

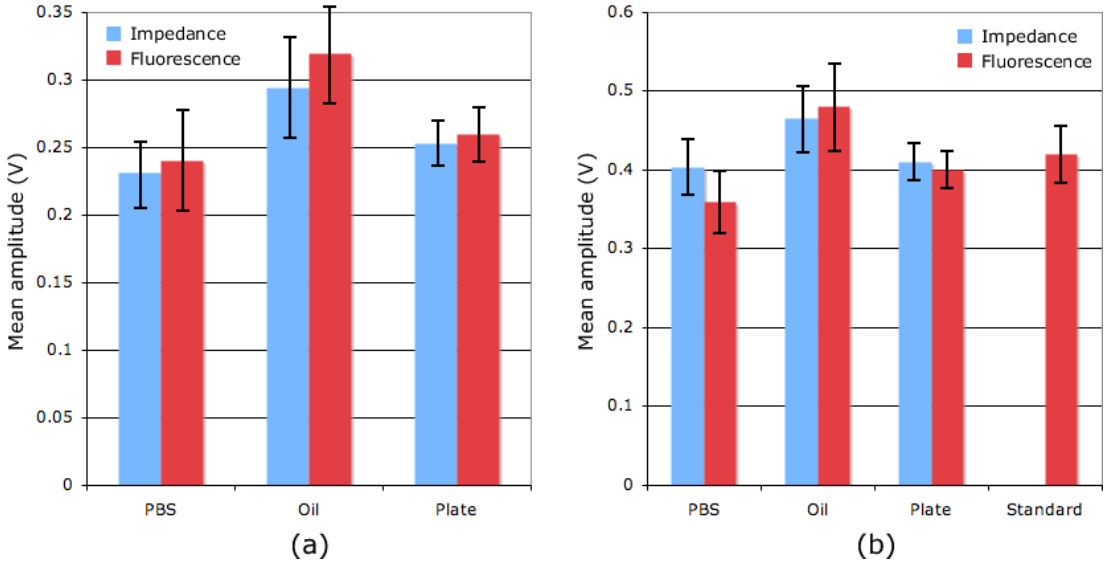

FIGURE 4.27: Experimental results from impedance measurements of a mixture of 4.62 μm and 5.49 μm diameter beads obtained from the analysis of data triggered on impedance or fluorescence signal. (a) Mean amplitude of the low frequency (503 kHz) impedance signal for 4.62 μm beads. (b) Mean amplitude of the low frequency (503 kHz) impedance signal for beads 5.49 μm diameter. (c) Difference in mean value obtained for 4.62 μm and 5.49 μm diameter beads with data triggered on impedance.

4.4.2.6 Effect of particle displacement on the impedance measurements

The effect of the displacement of the sample stream on the signal amplitude was investigated by measuring the impedance of a suspension of 5.49 μm beads. Measurements were performed using the overlapping electrode configuration and hydrodynamic focussing with PBS. The sample stream had a constant width of 20 μm and was shifted from the centre of the channel by adjusting the flow rate of the lateral streams. The results obtained for different displacements of the sample stream are shown in Figure 4.28, where the magnitude of the impedance at 503 kHz is plotted against the distance from the centre. The plot shows that the signal magnitude is significantly affected by the position of the particle within the detection region, and displacement of the sample stream might lead to errors in particle sizing as predicted from numerical calculations (section 4.3.2.5). Figure 4.29 compares the experimental and numerical results for the normalized response. For positive values of displacement the experimental results agree very well with the numerical simulations. For negative values of displacement the signal obtained experimental was somehow lower than numerically predicted and it drops rapidly for displacements larger than 5 μm.

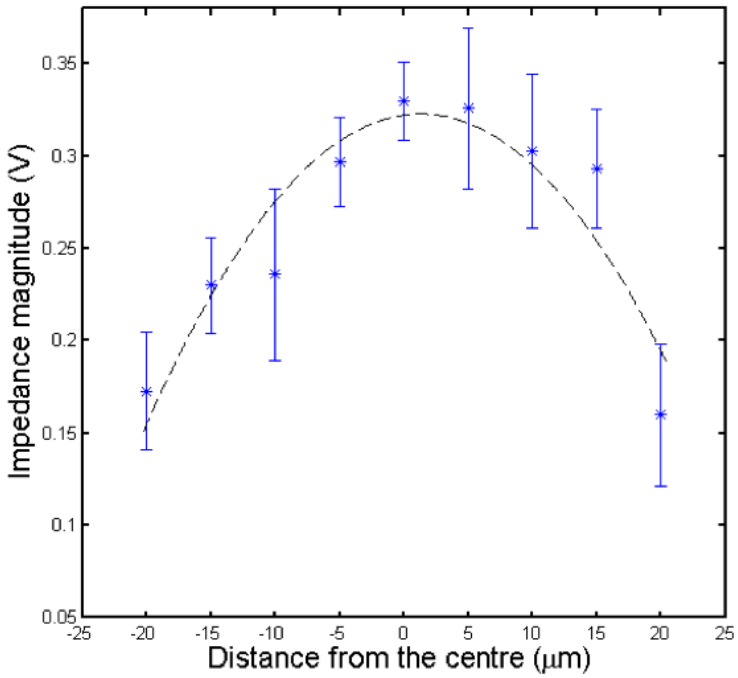

FIGURE 4.28: Effect of the shift of a 20 μm wide sample stream from the centre of the channel on the magnitude of the impedance signal for a suspension of 5.49 μm beads.

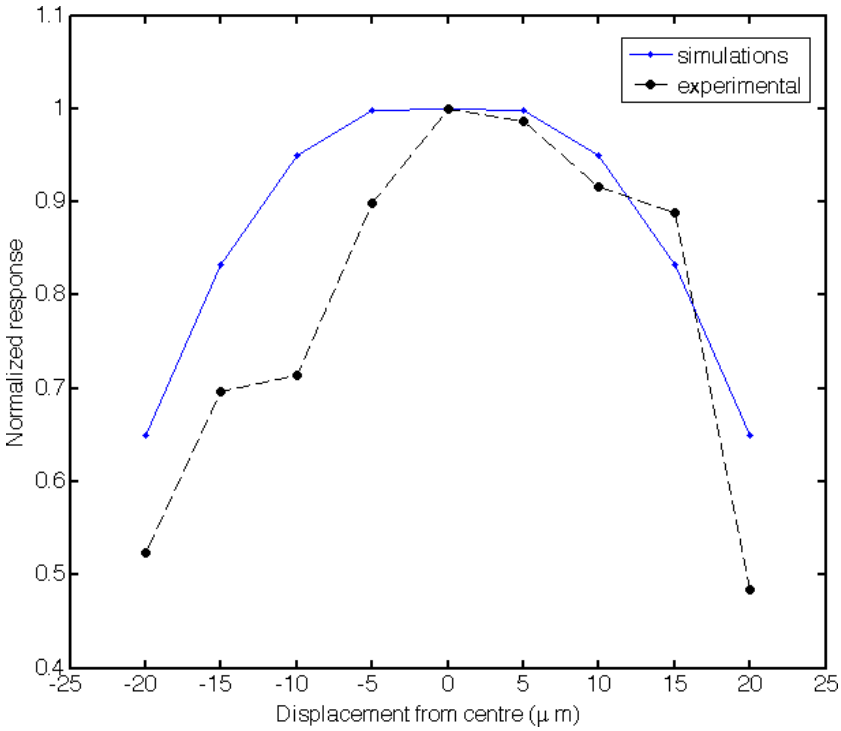

FIGURE 4.29: Comparison between the normalised experimental results and the simulation results.

4.5 Conclusions

In this chapter, three different facing electrode configurations for micro-impedance cytometry were presented and compared. Numerical simulations of the electrode geometries were carried out to evaluate their performances. The effect of focussing the sample using different fluids was also studied by numerical analysis. Simulation results were compared with the experimental data obtained from impedance measurements of a mixture of 4.62 μm and 5.49 μm beads performed using the different geometries and focussing techniques. The results showed that the sensitivity of the system can be significantly improved when the sample is focussed using an insulating fluid, obtaining a clear discrimination between the two populations of beads.

Chapter 5

Detection and discrimination of bacteria and micro-particles

5.1 Introduction

The ability of detecting single bacteria and micro-particles is of fundamental importance in many applications related to the field of biology, medicine and pharmaceutical industry. Detection of sub-microns particles is normally performed using nanopores, with sizes ranging from hundreds of nanometers to few microns. The system operates like a Coulter counter, where an electrical current passing through the channel is modulated by the presence of a particle in the channel. In chapter 1, few examples showing the employment of this technique to detect colloids [44, 45], viruses [52], antibodies [68], and single molecules [2] were reported.

In terms of impedance cytometry, it was shown in the previous chapter that the sensitivity of the system increased remarkably when the sample was sheathed by an insulating fluid of oil. The system sensitivity can be further increased by constraining the sample in a narrower stream. In this chapter, results on the detection and discrimination of small polymer beads (1 μm and 2 μm diameter) and *Escherichia coli* (*E. coli*), using the overlapping electrode configuration and hydrodynamic focusing with oil are reported.

5.2 Experimental procedure

Carboxylate-modified polystyrene beads were purchased from Molecular Probes. They were fluorescent, orange (540/560 nm) and (red 633/760 nm) with a mean diameter of

1 μm and 2 μm respectively, and a quoted coefficient of variation (CV) between 1% and 5%. The beads were washed three times and re-suspended after sonication in PBS (conductivity = 1.6 S/m).

E. coli is a Gram negative bacterium that is commonly found in the lower intestine of endotherm organisms. *E. coli* cells are rod-shaped, about 2 μm long and 0.5 μm in diameter, with a cell volume of 0.6 - 0.7 μm^3. Their structure consist of an outer and inner membranes separated by the periplasmic space surrounding the cytoplasm [137]. Frozen stock of *E. coli* strain BL21(DE3) expressing Ds Red protein (558/583 nm) was provided by Dr. Peter L. Roach (University of Southampton). The bacteria were inoculated into 10 ml of sterile 2YT broth (Sigma-Aldrich) containing ampicillin (100 mg/ml) and cultured overnight under aerobic conditions at 37°C with shaking (180 rpm) [138]. A fresh *E. coli* culture was started by inoculating 1 ml of the overnight culture into 100 ml of sterile 2YT contaning ampicillin (100 mg/ml). Culturing conditions were kept the same. The growth was monitored by measuring the optical density (OD) of cells at 600 nm with a spectrometer (Cary 100, Varian). Expression of DS Red protein was induced by the addition of 1 mM IPTG (Isopropyl β-D-1-thiogalactopyranoside, Melford) when OD_{600} reached 0.6. *E. coli* was washed and re-suspended in PBS in order to arrest cell growth and to maintain a constant concentration during the experiment.

Two different samples were prepared for the measurements: a mixture of 1 μm and 2 μm beads, and a mixture of 2 μm beads and bacteria. For both samples, the mixture was in a ratio of 1:1 with a final concentration of 300 particles/μl (3 x 10^5 cfu per ml).

Conventional flow cytometric analysis of the samples was carried out as described in section **??**. The 1μm and 2 μm diameter beads were sized using dynamic light scatter (DLS). For DLS measurements, the beads were suspended in PBS at a concentration of 3000 particles/μl.

The insulating sheath flow was Hexandiol (Sigma-Aldrich) containing 1% Tween 20 as the sheath flow. In order to improve the wettability of the channel, the channel was coated with bovine serum albumin (BSA) by flowing a 5% solution of BSA in PBS through the device for 1 hour. The sample flow rate was adjusted to give a sample stream width of 12 μm and a particle transit time (through the measurement region) of $\sim$2 ms. Flow was controlled using pneumatic methods as described in section 3.2.3. Impedance was measured using AC signals at frequencies between 503 kHz and 5 MHz and amplitudes ranging from 3.5 Vpp to 5 Vpp. For each experiment the number of events ranged from 3000 to 5000.

5.2.1 Results and discussion

Figure 5.1, shows an example of a typical impedance signal from a 1 μm diameter polystyrene bead with two AC signals (503 kHz and 5 MHz, 5 Vpp) applied simultaneously. The double peak signals correspond to the in phase and out of phase components of the impedance signal, one for each applied frequency. These signals are followed by a single peak that is the fluorescence signal from the particle (585 nm for the 1 μm bead).

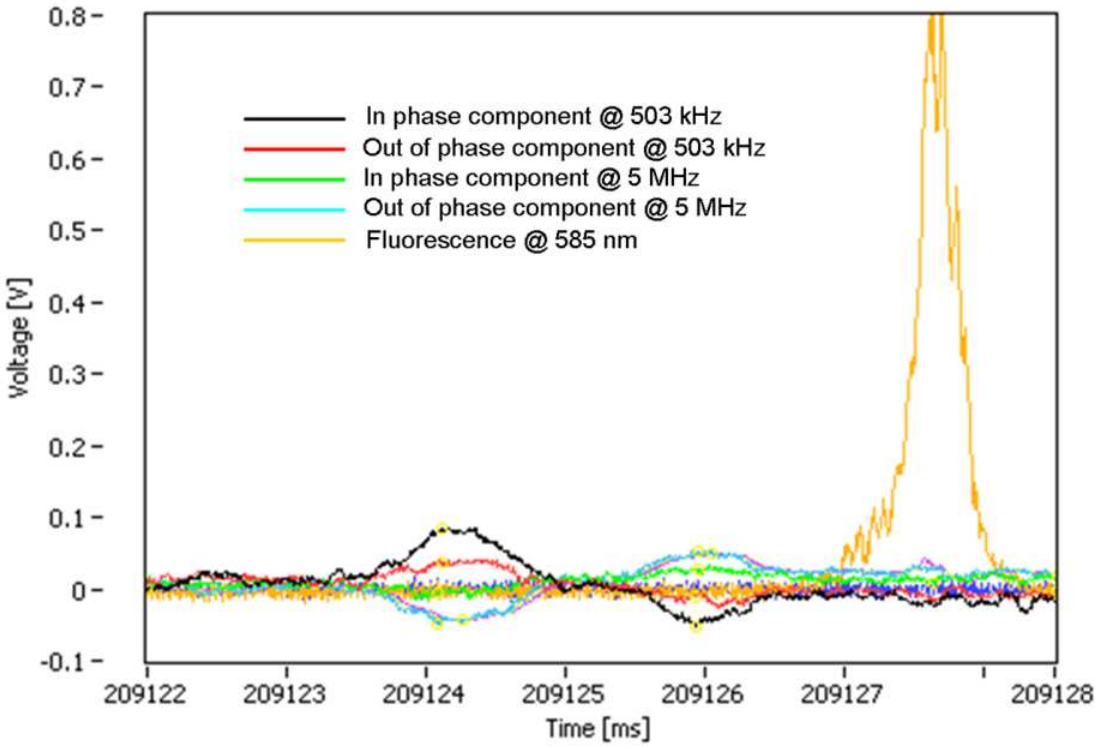

FIGURE 5.1: Typical impedance signals from an individual 1 μm bead detected in the micro flow cytometer. The real component (in phase) and imaginary component (90° out of phase) of the electrical impedance at each applied frequency are shown. Orange (585/40 nm) fluorescence emission from the bead is also shown.

Scatter plots of the impedance (peak signals from Figure 5.1) for mixtures of beads and *E. coli* are shown in Figure 5.2 and Figure 5.3. Figure 5.2(a) shows data for a (nominal) 1:1 mix of 1 μm and 2 μm beads; figure 5(a) shows similar data for a 1:1 mix of 2 μm beads and *E. coli*. The data is plotted as transit time vs magnitude of the impedance at 503 kHz, triggered from the low frequency in-phase impedance signal. The data are colour-coded according to the fluorescence signal (acquired simultaneously) from the particles. Both figures show that impedance can discriminate between the two different populations.

In conventional micro-impedance cytometry, the transit times for the particles are distributed owing to the variable position occupied by the particle in the laminar flow.

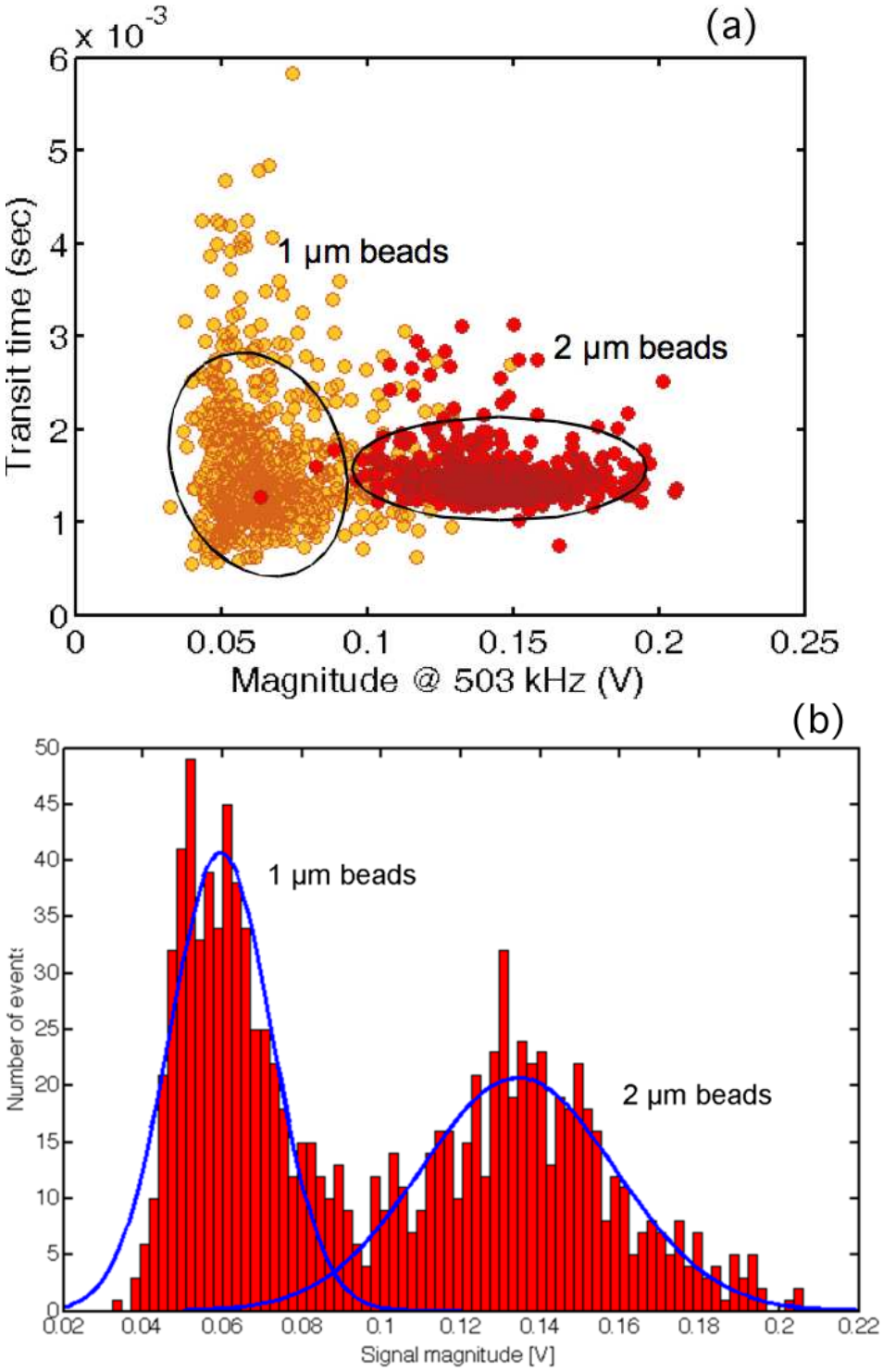

FIGURE 5.2: (a)Scatter plot of particle transit time against magnitude of the low frequency (503 kHz) impedance for a mixture of 1 μm and 2 μm diameter polystyrene beads. The plot is colour coded based on the fluorescence measured from each bead. (b) Histograms of the impedance amplitudes for the mixtures of 1 μm and 2 μm diameter polystyrene beads measured at 503 kHz.

Figure 5.2 and Figure 5.3 show that with the oil focussing, the transit times for all the particles are almost the same, implying that all the particles travel through the detection

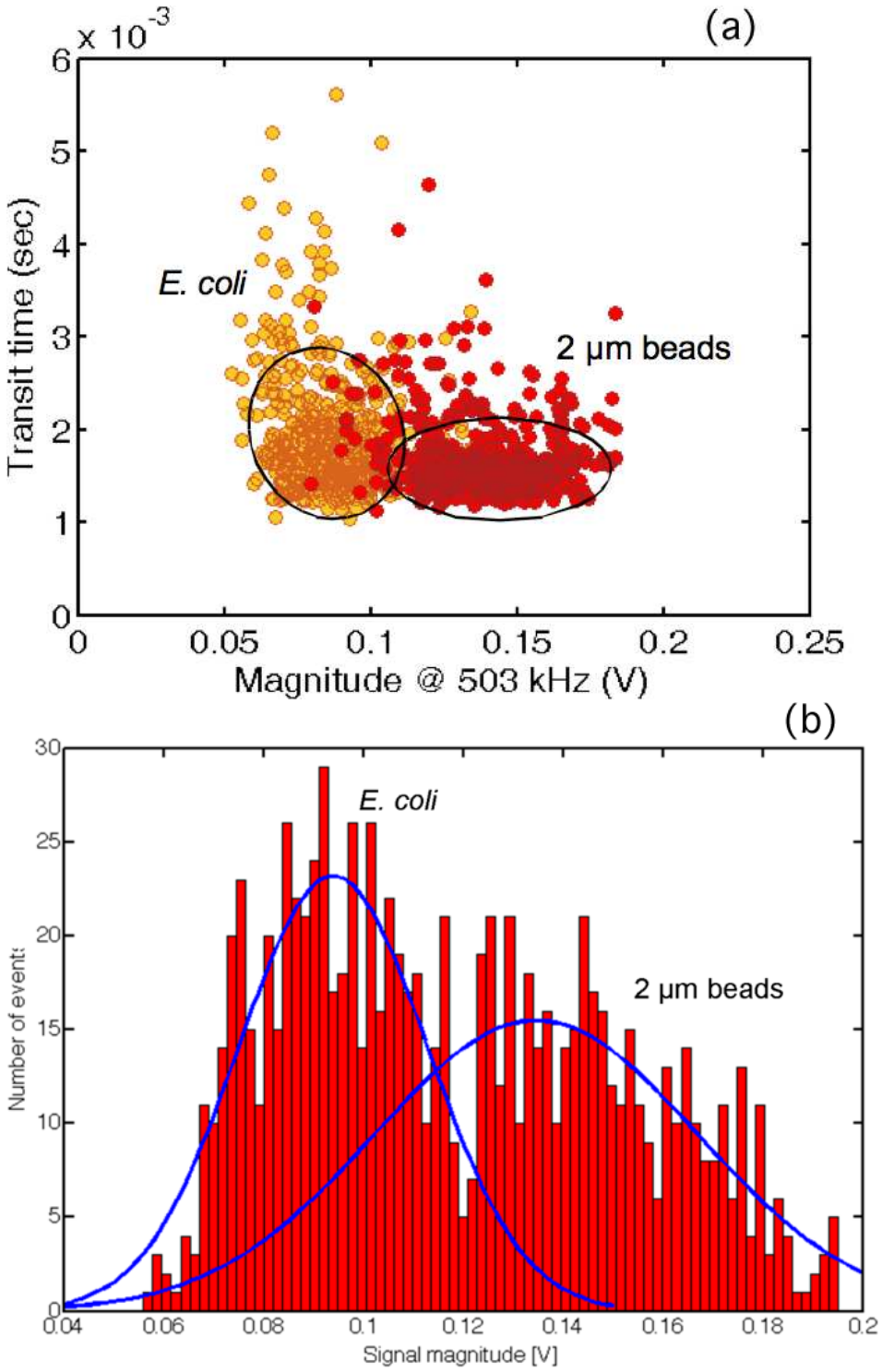

FIGURE 5.3: (a) Scatter plot of particle transit time against magnitude of the low frequency impedance for a mixture of *E. coli* and 2 μm diameter polystyrene beads. The plot is colour coded based on the fluorescence measured from each particle. (b) Histograms of the impedance amplitudes for the mixtures of *E. coli* and 2 μm diameter polystyrene beads measured at 503 kHz.

region with the same velocity and by implication occupy the same height in the channel. This is in contrast with the observation in the previous chapter, where a big spread in

transit time was obtained for the measurements of beads ($\sim 5\mu$m) hydrodynamical focussed using oil, and it can be explain considering that small particles are less subjected to the inertial migration away from the channel centre[1] [140].

From the average of the recorded transit times, a mean particle velocity of ∼38 mm/sec was obtained for the mixture of 1 μm and 2 μm beads, and ∼32 mm/sec for the mixture of 2 μm beads and *E. coli*; giving a flow rate of approximately 0.8 μl/min and 0.7 μl/min, respectively. The volume of sample analysed during the experiments is obtained by multiplying the flow rate by the length of the measurement (19 min for the mixture of beads, and 17 min for the mixture of beads and *E. coli*). Dividing the number of events by the sample volume, shows that for both samples the concentration of particles was 10% lower than the one calculated from the stock solutions. Although this is not a deviation, the discrepancy could be due to an error in the calculation of the cross-sectional area of the channel (and the volumetric flow rate) due to the unknown shape of the meniscus formed at the oil/buffer (assumed to be a square cross section in the calculations).

Figure 5.2(b) and Figure 5.3(b) show histograms of the number of events plotted against the magnitude of the impedance (at 503 kHz). The histograms were fitted to Gaussian distributions. For the bead mixture (Figure 5.2), two clearly separated distributions are obtained. For *E. coli* and 2 μm bead mixture, the fits produce less well defined populations. The 2 μm bead distribution overlaps into the *E. coli* population, probably due to the wide spread in size of *E. coli*. The organism is typically 2 μm long, and 0.5 μm wide so that orientation effects may also influence the impedance signal. These Gaussian fits were performed on the complete impedance data sets without bias. However, Figure 5.3 shows that the *E. coli* population is clearly delineated from the bead population when the fluorescence signal is considered.

From these fits, the number of particles in each distribution was estimated. The same analysis was also performed with particles identified from their fluorescence signal rather than impedance. This data, together with CVs is summarised in table 5.1. The particle

[1] Particles in a flow experience both shear and normal stresses over their surfaces yielding parallel (drag) forces and perpendicular (lift) forces to the flow direction. Therefore, particles flowing in undisturbed streamlines can migrate to equilibrium positions across the channel. For example, in [139] it was observed that randomly dispersed particles migrated to an annulus located between the centre and the wall of a centimeter diameter pipe. More recently, the phenomenon was observer in a micrometer scale square channel in which particles migrated to four symmetric equilibrium positions close to the faces of the channel [140]. The lateral displacement velocity for particles near the centre of the channel is proportional to the particle diameter and Reynolds number, as $v_p = \frac{v_{max}^2 r^3}{3\pi v D_h} f_c(R_c, x_c)$ where v_{max} is the maximum channel velocity, v is the kinematic viscosity, r is the particle radius, D_h is the hydraulic diameter defined as $2wI/(w+l)$, (where w and l are the channel's width and height) and $f_c(R_c, x_c)$ is a lift coefficient that is a function of the particle Reynolds number and position (f_c equals zero when the equilibrium position is reached). The particle Reynolds number is $R_c = \frac{v_{max} D_h}{v}$.

size distribution and fluorescence intensity distribution was also measured by conventional flow cytometry (FACS) and Dynamic Light Scattering (DLS). FACS analysis of the particles was carried out using a FACSAria (Becton Dickson) fitted with two lasers: 488 nm solid state (20 mW, Coherent® Sapphire^{TM}) and a 633 nm HeNe (20 nm, JDS Uniphase^{TM}). FACSFlow sheath fluid (Becton Dickson) was used and samples were forced at a pressure of 70 psi through a 70 μm nozzle. The instrument was controlled by a PC running FACSDiVa^{TM} software (Becton Dickson). FACS sizes particles from the forward scattered light intensity, but the 1 μm and 2 μm beads were too small to be measurer. However, the ratios of particles in the two populations were measured by triggering on the fluorescence signals. The results obtained from the FACS analysis of the two samples are shown in Figure 5.4, where fluorescence emission at 780/60 nm is plotted against fluorescence emission at 575/26 nm. Figure 5.4(a) shows data for the mix of 1 μm and 2 μm beads; Figure 5.4(b) shows data for the mix of 2 μm beads and E. coli. The relative percentages of particles (measured by FACS and micro-cytometer) are in good agreement. Examination of the CV of fluorescence intensity shows that the particles have quite a wide distribution in fluorescence, but the CV from both the FACS and the micro-cytometer are similar. This data, together with the CVs for the fluorescence signals is summarised in table 5.1.

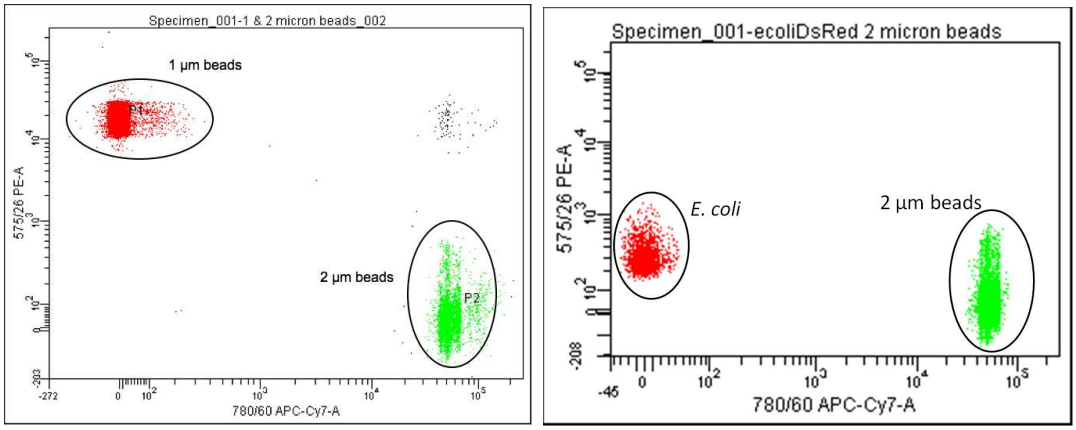

(a) (b)

FIGURE 5.4: FACS analysis of the two samples showing fluorescence emission at 780/60 nm against fluorescence emission at 576/26 nm. (a) Data obtained from the same samples of Figure 5.2(a). (b) Data obtained from the same sample of Figure 5.3(a).

Dynamic Light Scattering, also known as Photon Correlation Spectroscopy (PCS), measures Brownian motion and relates this to the size of the particles. It does this by illuminating the particles with a laser and analysing the intensity fluctuations in the scattered light. DLS measurements were performed using a Zetasizer Nano ZS (Malvern Instruments) equipped with a 633 nm laser and capable of sizing particles ranging from

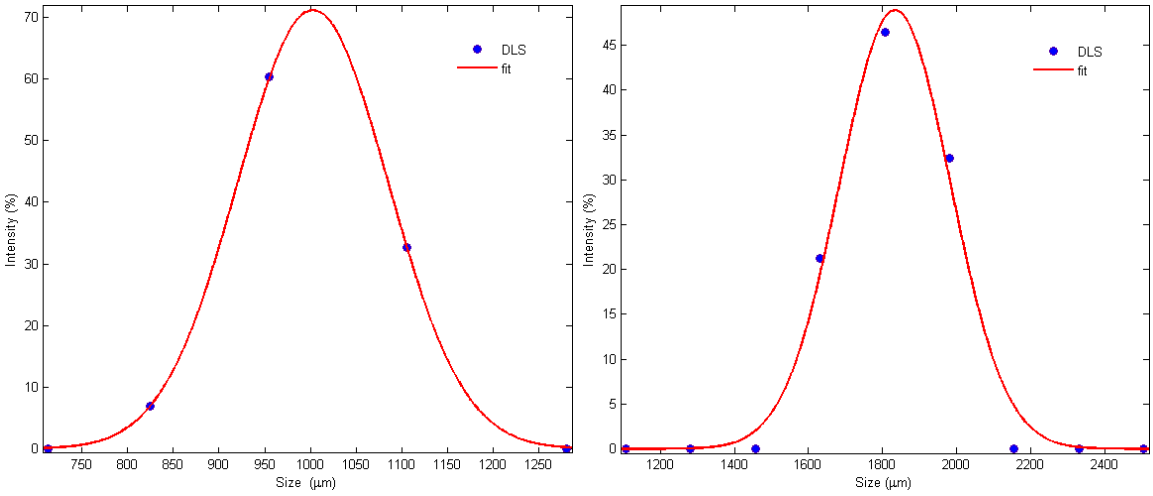

FIGURE 5.5: Results obtained from DLS measurement of the (a) 1 μm beads and (b) 2 μm beads The continuous line shows the Gaussian fit of the experimental data.

0.6 nm to 6 μm in diameter. The intensity based particle size distributions (PSD) obtained from DLS measurement of the 1 μm and 2 μm beads are shown in Figure 5.5. According to these distributions, the average size for the suspension of 1 μm beads is 1.003 μm (Figure 5.5(a)), while the average size for the suspension of 2 μm bead is of 1.834 μm (Figure 5.5(b)). The CVs of the distributions were calculated from the Gaussian fit (shown in the figures) of the recorded data, and are reported in table 5.1. The size CV obtained from DLS is slightly higher than the manufacturer quoted values, but lower than the 500 kHz impedance CV. This apparent discrepancy is explained as follows.

To a first approximation, the magnitude of the low frequency impedance can be considered proportional to particle volume [141]. A calculation showing the relationship between particle size and impedance magnitude was reported in section 3.2.5.1, where the correlation between the particle size and the magnitude of the impedance signal at 500 kHz obtained from the full electrical circuit analysis of the system was shown. As previously explained, the electrical model used in the circuit analysis included the electrical characteristic of the microfluidic chip, the electrical double layer, the properties of the particles and the amplifier circuit components. The same circuit analysis was performed here with the settings used in this experiment. The result is shown in Figure 5.6, where the relationship between particle size and impedance magnitude is plotted. Similar to what observed in section 3.2.5.1, the graph shows that as the particle size decreases, there is almost a cubic decrease in impedance magnitude, tending towards zero for a 0.5 μm diameter particle. The data points obtained from circuit

analysis were fitted to a cubic polynomial; the fit is shown in the figure. The measured impedance signals are also plotted on the figure.

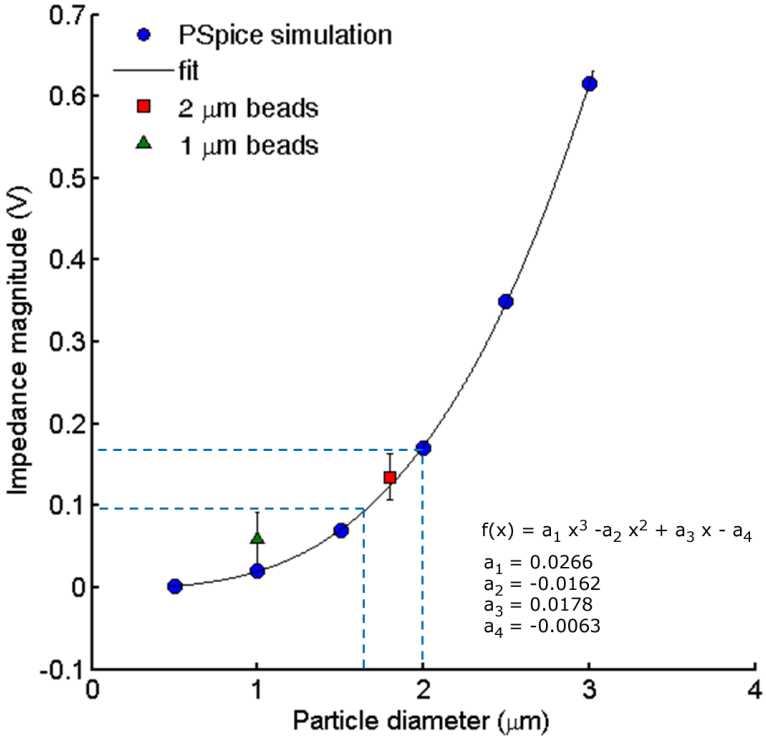

FIGURE 5.6: Size-dependent impedance magnitude signal obtained from the PSpice full circuit analysis of the micro-impedance system. The simulations were performed for a detection volume measuring 12 μm x 20 μm x 30 μm, with an applied voltage of 5 Vpp at a frequency of 503 kHz. The bead permittivity was 2.5 ϵ_0 and surface conductivity 1.2 nS, with PBS suspending medium. The double layer capacitance was 50 pF.

The measured value for the 2 μm particle is plotted considering a true size of 1.8 μm and it corresponds closely to the fitted curve, but the impedance for the 1 μm particle is higher than calculated. Again, this difference might be due to an error in the cross-sectional area, and thus in the volume fraction, calculations. From this circuit analysis, the equivalence between particle diameter and low frequency electrical impedance (dotted line) can be obtained. This information was used to calculate the equivalent size CV from the impedance data; listed in table 5.1 as "calculated CV in size". These size CVs are very close to the DLS data and the manufacturer's data for the latex particles. The CV in size for the E.coli was also estimated from the impedance data, showing that the bacteria have a reasonably tight distribution, as expected since they are in stationary phase.

	Impedance (Micro flow-cytometer)				**Fluorescence (Micro flow-cytometer)**			**Fluorescence (FACS)**		**DLS**	**Manufacturer's data**
	μ (V)	CV	Corresponding CV in size	%	μ (V)	CV	%	CV	%	CV	CV
1 μm beads	0.060	22%	8%	54.3	0.060	22%	57.8	28.8%	60	8%	5%
2 μm beads	0.134	19%	6%	45.7	0.140	14%	42.2	17.1%	40	8%	5%

	Impedance (Micro flow-cytometer)				**Fluorescence (Micro flow-cytometer)**			**Fluorescence (FACS)**		**DLS**	**Manufacturer's data**
	μ (V)	CV	Corresponding CV in size	%	μ (V)	CV	%	CV	%	CV	CV
E. coli	0.094	20%	6%	55.2	0.091	19%	52.4	50.1%	53	-	-
2 μm beads	0.135	23%	7.5%	44.8	0.147	16%	47.6	21.2%	47	8%	5%

TABLE 5.1: Summary data for mixture of beads (figure 4) and beads and *E. coli* (figure 5). Table shows mean amplitude (μ), coefficient of variation (CV), and % determined from the fitted Gaussian distributions for data triggered on impedance or fluorescence signals. For comparison, the % population and CV obtained from flow cytometry (FACS) fluorescence data is shown, together with the size CV of the beads, obtained from Dynamic Light Scatter (DLS).

5.3 Conclusions

Hydrodynamic focussing of the sample using an insulating sheath flow was shown to significantly increase the sensitivity of the micro-impedance cytometer whilst maintaining large channel dimensions which do not block. Assuming that the PBS sample is sheathed with oil with vertical walls, the volume ratio of particle to sensing volume is estimated to be 0.007 %. Measurements of the low frequency (503 kHz) impedance from single particles was used to discriminate between 1 μm and 2 μm diameter beads and E. coli and 2 μm beads. Accurate detection and identification of the particles was confirmed by simultaneously measuring the fluorescence emission. The distribution in size and fluorescence (CV) is found to be in good agreement with data obtained with standard commercially available instruments (FACS and DLS).

Chapter 6

Polyelectrolyte microcapsules

6.1 Introduction

Recent years have seen a growing interest in the development of systems for controlled encapsulation and release of active substances. Possible applications include many fields such as material and polymer chemistry, catalysis, cosmetics, food industry, biosensing, and in particular drug delivery.

Scientists are focusing on the development of carriers for therapeutic molecules [65]. They are looking for systems able to reach and affect only pathological cells, in order to reduce the total drug concentration and to improve specificity, limiting the side-effects and preserving healthy tissues. This requires intelligent carrier systems with the ability to initially enclose the active substances, protect them from extracellular enzymes, and then release them at the target location where they can be effective given the presence of certain conditions.

During the last decade a large variety of micro-and nanocarriers based either on solid micro and nanoparticles, as well as liposomes or polymeric micelles have been developed to serve this purpose [142, 143, 144].

In the late nineties, a novel approach to fabricating micro- and submicrometer sized capsules from polyelectrolyte molecules was introduced [145]. The capsules are formed by "Layer-by-Layer" adsorption of polyelectrolytes onto sacrificial colloidal substrates. The method offers the possibility of employing a great variety of substances as core materials and shell constituents. What makes polyelectrolyte microcapsules a very attractive system is the opportunity of tailoring the properties of the capsule walls and combining different functions in one carrier. Thanks to the high sensitivity of the capsule

walls to variations in external conditions, it is possible to reversibly change the capsule permeability by changing the properties of the suspending medium, switching between an "open and "close state of the carrier, which allows for encapsulation and subsequent release of the desired substances (Figure 6.1)

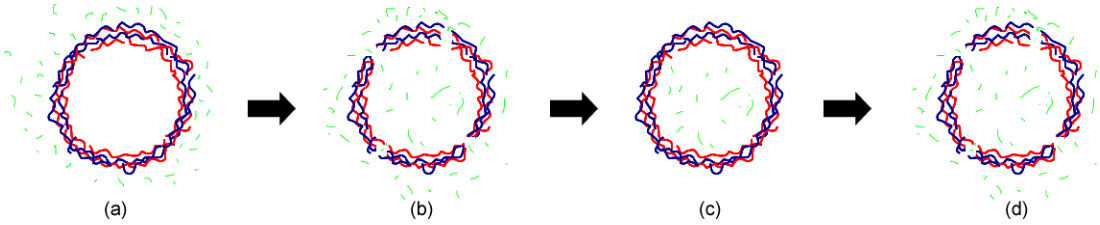

FIGURE 6.1: Schematic representing macromolecule encapsulation principle. Pores are reversibly created in the capsule walls varying the solvent polarity, salt concentration or pH of the suspending medium to allow inward diffusion of macromolecules (a, b). The pores are then closed and the loaded substance trapped inside the capsules by dispersing the capsules in the original medium (c). The encapsulated substance can subsequently be released changing again the properties of the suspending medium (d).(After from [15]).

The aim of this work is to investigate and characterise the properties of polyelectrolyte microcapsule by micro-impedance spectroscopy. Measurements of single capsules could provide a quantitative understanding of their characteristics and open the way to the development of new assembly and detection tools, increasing interest in a topic that has already gained much attention from the industry.

This chapter gives an introduction to the Layer-by-Layer technique as well as a review of different microcapsule types. Microcapsule preparation and characterisation by confocal spectroscopy is presented. The dielectric properties of the capsule and their response to changes in pH of the suspending medium is investigated by micro-impedance spectroscopy. The results obtained from complete circuit analysis is performed to determine the properties of single capsule in suspension and the results obtained are presented and discussed.

6.2 Layer-by-Layer deposition

The "Layer-by-Layer (LbL)" self-assembly method is one of the most recently investigated molecular assembly techniques. It consists of alternating adsorption of oppositely charged polyelectrolytes in aqueous solution and it is based on the electrostatic attraction between electrolyte groups.

Studies of electrostatic self-assemblies (ESA) by alternating adsorption of oppositely charged polyions were first proposed by Iler in 1966 [146] but the major contribution to

the field was given by Decher et al. when, in the 1990s, he developed a practical method for multilayer assembly, first using anionic and cationic bipolar amphiphiles [147] and then extending the technique to polyelectrolytes [148].

The process, which has received strong interest due to its extreme simplicity, is shown in Figure 6.2 and is described as follows. A solid substrate with positively charged planar surface is immersed in a solution containing an anionic polyelectrolyte and a layer of polyanion is absorbed (step 1). The adsorption is carried out at a relatively high concentration of polyelectrolyte and for this reason a number of ionic groups remains exposed at the interface with the solution, causing surface charge reversal. After the first layer adsorption, the substrate is washed in pure water (step 2). The adsorption of the second layer is carried out by immersing the substrate in a solution containing a cationic polyelectrolyte (step 3), followed by a second washing step (step 4). Again, after absorption, the surface charge of the substrate is reversed. Cyclic repetition of these four steps leads to the formation of multilayer structures.

Surface charge reversal upon deposition of layers is the only critical factor for successful deposition and plays a key role in the self-regulation of the adsorbed layers. The repulsion of equivalently charged molecules is, in fact, the cause of the restriction of each adsorption step to a single layer, on top of which only oppositely charged molecules can be absorbed.

The main advantage offered by LbL deposition compared to other traditional methods, like Langmuir-Blodgett (LB) techniques, is that no special equipment is required and there are no limitations to the choice of substrate size and topology. Moreover, no covalent bonds are formed, therefore the quality of the multilayer film does not depend on the yield of chemical reactions, which represents the main limitation for assembly techniques based on covalent chemistry [149, 150].

The thickness of the film can be tuned in the nm range by the number of deposition cycles, chemical composition and preparation conditions [16]. A variety of materials, such as a synthetic polyelectrolytes, biopolymers (proteins and nucleic acids), lipids, inorganic particles, and multivalent dyes can be used to fabricate multilayer film assembly.

Since film cohesion mainly depends on electrostatic interactions the structure is stable against desorption. At the same time, as ion pair interactions are weak, the structure can be modified by changing the conditions during the fabrication and subsequent treatment. Therefore, it has been reported that the thickness of the film can be varied, and the structure rearranged by changing pH [151, 152] ionic strength [153, 154], humidity [155] and temperature [156] depending on the actual film composition.

The adsorption process is independent of the shape of the substrate and for this reason LbL technology can be also used for multilayer assembly on the surface of colloidal particles and the fabrication of polyelectrolyte microcapsules.

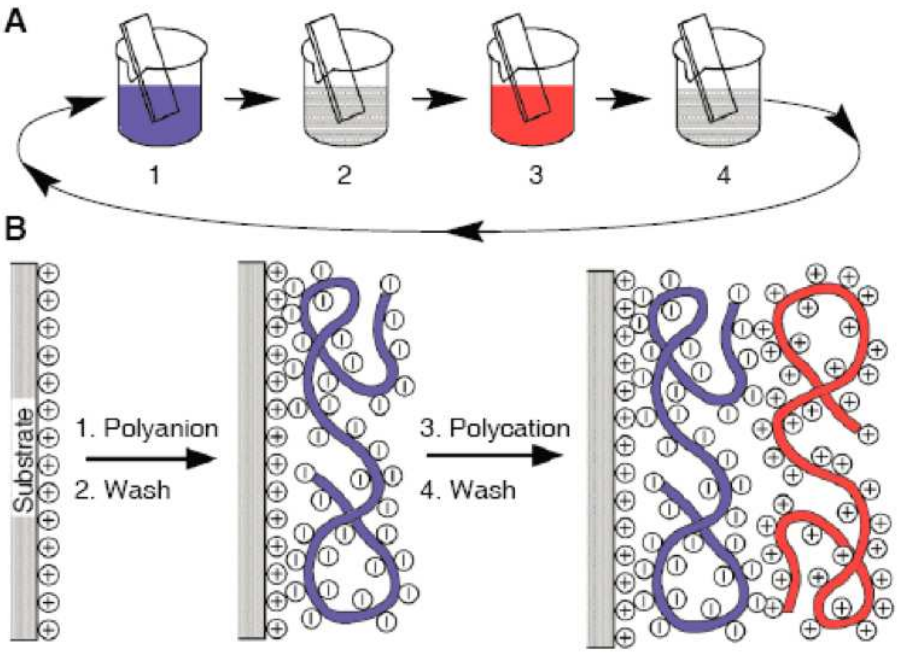

FIGURE 6.2: Schematic representation of L-b-L polyelectrolyte deposition on a flat substrate. A) Steps 1 and 3 represent the adsorption of respectively a polyanion and polycation, steps 3 and 4 are washing steps. B) Simplified representation of the first two adsorption steps on a positively charged substrate, after [16].

6.2.1 Polyelectrolyte microcapsules

Polyelectrolyte microcapsules were first introduced by Mohwald's group in 1998 [145, 157, 158]. They are obtained from LbL deposition on the surface of colloidal particles used as a template, followed by template dissolution. A schematic illustration of the capsule assembly process is shown in Figure 6.3 [158].

The process is the same as that followed for multilayer film assembly on planar substrates: oppositely charged polyelectrolytes are consecutively adsorbed on the surface of a template, with the difference that the template is then removed by dissolution or calcination at the end to form a hollow capsule.

As already mentioned, capsules and multilayer in general are very sensitive to the external conditions, so change in pH [159], ionic strength [160], temperature [161], or solvent [162] leads to the change of their structure and, as a result, to different permeability.

The response of the capsules to the environment strongly depends on the composition of the shell, i.e. polyelectrolytes employed, adsorption conditions and number of layers, but also the choice of core material plays a determinant role on the final capsule characteristics. A variety of cores have been used as templates; they can be generally classified in three groups: organic [163], inorganic [159, 164], and biological cells [165].

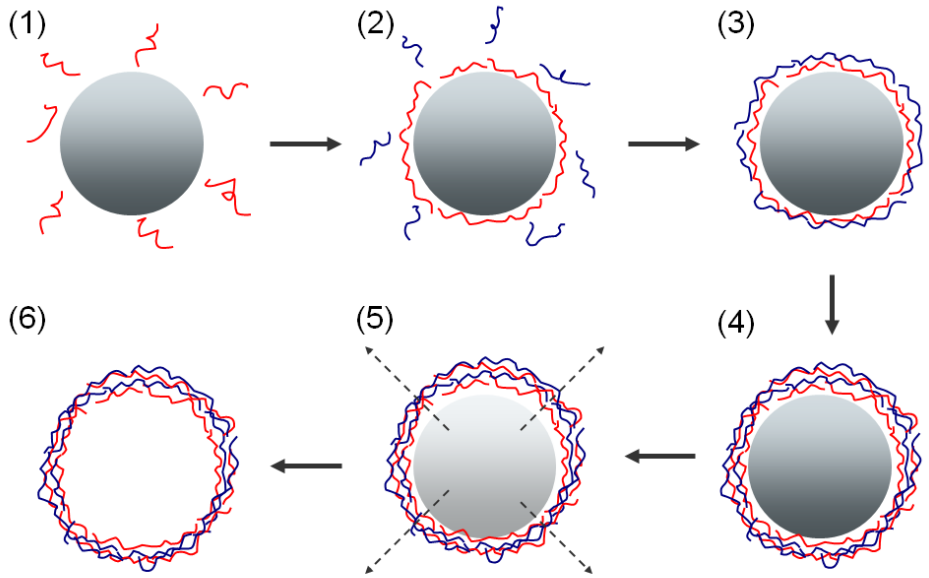

FIGURE 6.3: Consecutive adsorption of positively and negatively charged polyelectrolytes onto negatively charged colloid particles (14), followed by core dissolution (5,6). After [17].

Organic cores, like melamine formaldehyde (MF) or polystyrene (PS) cores, are obtained through a well-established process of synthesis and they are characterised by very good monodispersity. For these reasons they have been the most widely studied templates for capsule preparation. Organic cores can be dissolved at low pH (MF cores) or in organic solvents like tetrahydrofuran (PS cores). The main drawback during core dissolution is the difficulty in removing the oligomers that tend to stick to the capsule interior. Moreover, oligomer formation leads to high osmotic pressure in the inner volume, with consequent swelling and stretching of the polyelectrolyte shell and rupture of the capsule, in particular when MF-cores are used.

Carbonate particles ($CaCO_3$, $CdCO_3$ and $MnCO_3$) and silica particles (SiO_2) are examples of inorganic cores. They can be either soluble in acidic or basic conditions or in an organic solvent. Due to the low molecular weight of the ions, complete dissolution of the inorganic core can be easily achieved without any mechanical stress on the shell structure, even if a high number of layers is deposited. As a consequence, these

capsules are characterised by a permeability coefficient significantly lower than organic-template capsules. However, when silica particles are used as a template, hydrofluoric acid solution is required for core dissolution, making the use of this type of core less practical.

PE microcapsules have been also fabricated by LbL deposition on fixed erythrocytes. The core dissolution was achieved by oxidation with sodium hypochlorite (NaOCl) solution. Limitations in the use of these templates are related to the restricted number of suitable PEs that can be used [165].

A variety of PEs have been used as shell constituents of hollow polyelectrolyte capsules, including synthetic polyelectrolytes, natural polymers such as polysaccharides, polypeptides, lipids and multivalent dyes. One of the most frequently used PE combination is poly(styrene sulfonate) (PSS) and poly(allylamine hydrochloride) (PAH). This PEs pair was previously used for planar multilayer film assembly and has been investigated by several groups. PAH/PSS-based capsules are responsive to the pH variation of the environment, which causes the reversible formation of pores in the shell.

The reversible pore formation on PSS/PAH-based capsules has been used for the encapsulation of high molecular weight compounds such as FITC-dextrans (FITC = fluorescein isothiocyanate) [166] and Rhodamine-labelled PSS [167]. Reversible changes in PAH/PSS capsule permeability induced by varying the salt concentration has also been reported [168, 169]. It was shown that at high salt concentration (10-2 M) macromolecules with a molecular weight up to 70 kDa could be encapsulated, while at lower concentrations the walls were closed. In this case the higher permeability was not due to the formation of pores, but to the increased distance between the polyelectrolyte layers caused by the partial shielding of the charges on the polyelectrolytes.

Incorporation of gold or silver nanoparticles in the PAH/PSS polyelectrolyte shell allowed for the fabrication of infrared (IR)-light sensitive capsules, enabling remote release of encapsulated macromolecules [170, 171]. As absorption properties of metal nanoparticles can be adjusted choosing particle material and size, a selective remote activation of differently doped capsules was achieved. Incorporation of positively charged gold coated cobalt nanoparticles (Co@Au) or colloidal magnetic nanoparticles, such as iron oxide (Fe_3O_4), makes the capsules addressable by a magnetic field was also reported [172].

6.3 Complete equivalent circuit model for a single microcapsule in suspension

The electrical response of a microcapsule in suspension between the facing electrodes of the microchannel detection area can be studied in terms of its equivalent circuit model (ECM). The ECM for a single-shelled biological particle was discussed in section 2.4.1.1 where, assuming a very high membrane resistance and ignoring the cytoplasmic capacitance, the cell was simply modelled by a capacitor in series with a resistor. However, this model is not suitable to describe the behaviour of a microcapsule as the resistance of the capsule shell and the capacitance of the inside cannot be ignored.

To take into account the effect of the membrane conductivity and the internal properties, a complete ECM for single shelled particle in suspension was developed by Tao Sun and is shown in Figure 6.4. The capsule is modelled as a capacitor C_{sh} in parallel with a resistor R_{sh} representing the shell, and a series combination of a capacitor C_i and a resistor R_i representing the capsule inside. The capacitor C_m and the resistor R_m represent the properties of the suspending medium, while the double layer is modelled as the capacitor C_{DL}.

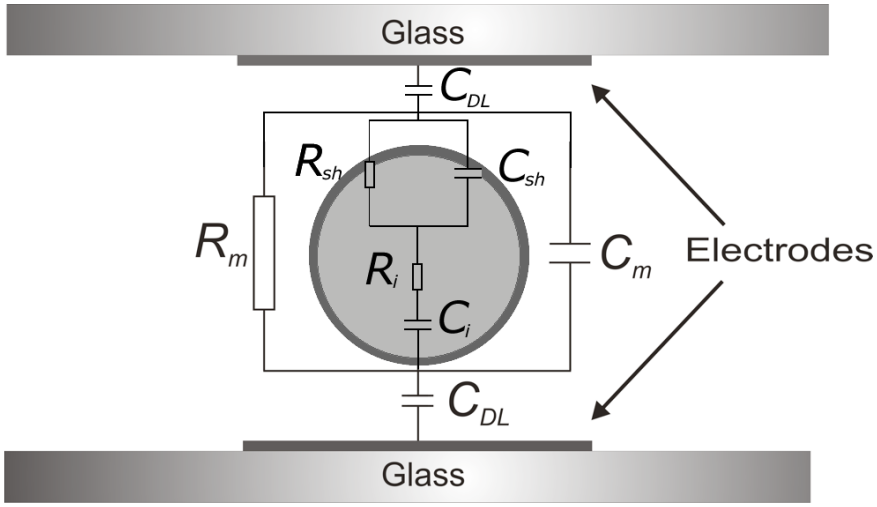

FIGURE 6.4: Equivalent circuit model for a microcapsule suspended between the measurement electrodes. R_m, R_{sh} and R_i are the resistance of the suspending medium, capsule shell and capsule interior respectively; C_m, C_{sh} and C_i are the capacitance of the suspending medium, capsule shell and capsule interior respectively. The electrical double layer is modelled by the capacitor C_{DL}

The dielectric properties of a single-shelled particle are described by the well known Maxwells mixture equation, presented in section 2.4.1. The relation between the dielectric response of the system and the electrical components of the circuit can be obtained by applying Laplace and Fourier transforms to the mixture equation, as reported in

[141]. This method allows for an expression of the complex equivalent permittivity of the system linking time and frequency domains, from which the expressions of the electrical components are derived. According to [141], the mixture equation can be rewritten in the form:

$$\epsilon_{mix} = \frac{\epsilon_m a_1}{b_1} + \frac{k_2\tau_1}{1+i\omega\tau_1} + \frac{k_3\tau_2}{1+i\omega\ tau_2} + \frac{k_1}{i\omega} \tag{6.1}$$

where

$$\epsilon_\infty = \frac{\epsilon_m a_1}{b_1} \tag{6.2}$$

$$\sigma_0 = k_1 \tag{6.3}$$

$$\Delta\epsilon_1 = k_2\tau_1 \tag{6.4}$$

$$\Delta\epsilon_2 = k_3\tau_2 \tag{6.5}$$

$$\tau_1 = \frac{2b_1}{b2 - \sqrt{b_2^2 - 4b_1b_3}} \tag{6.6}$$

$$\tau_2 = \frac{2b_1}{b2 + \sqrt{b_2^2 - 4b_1b_3}} \tag{6.7}$$

The coefficients a_1, b_1, b_2, b_3, k_1, k_2, k_3 are described in [100].

Equation (6.2), represents the limiting high frequency permittivity of the system and is related to the instantaneous response of the complex permittivity in the time domain. When an excitation signal is applied, the response of the system is determined by its charge accumulation, which is dominated by the permittivity of the suspending medium ϵ_m. Equation (6.3) and equation (6.4) give the magnitude of the dielectric dispersions characterised by the time constants τ_1 and τ_1, respectively. $\Delta\epsilon_1$ represents the lower frequency dispersion and is related to the polarisation of the membrane. The dispersion $\Delta\epsilon_2$ occurs at higher frequency values for which the membrane is short-circuited and is related to the interfacial polarisation of the particle interior and exterior. Equation (6.5)

gives the limiting low frequency conductivity and is related to steady-state response of the system which is governed by ionic conduction in the suspending medium.

Considering that the circuit elements of the suspended shelled particles are in parallel with the suspending medium, the impedance of the circuit can be written as:

$$Z_{cir} = \frac{1}{\left(sC_m + \frac{1}{R_m}\right) + \frac{1}{Z_p}} \tag{6.8}$$

where Z_p is the impedance of the particle. Derivation of the expressions of the electrical components is as follow. From the equation of the mixture theory

$$Z_{mix} = \frac{1}{i\omega\epsilon_{mix}G_f} \tag{6.9}$$

replace $j\omega$ with s and substitute in equation equation (6.1) to give:

$$Z_{mix} = \frac{1}{s\left(\epsilon_\infty \frac{\sigma_0}{s} + \frac{\Delta\epsilon_1}{1+s\tau_1} + \frac{\Delta\epsilon_2}{1+s\tau_2}\right)G_f} \tag{6.10}$$

Mapping the corresponding terms in equation (6.9) and equation (6.9) gives:

$$R_m = \frac{1}{\sigma_0 G_f} \tag{6.11}$$

$$C_m = \epsilon_\infty G_f \tag{6.12}$$

$$Z_p = \frac{\tau_1\tau_2 s^2 + (\tau_1+\tau_2)s + 1}{\left[(\tau_1\Delta\epsilon_2 + \tau_2\Delta\epsilon_1)s^2 + (\Delta\epsilon_1 + \Delta\epsilon_2)s\right]G_f} \tag{6.13}$$

According to equation (6.13), the complete circuit of a shelled particle is given by a parallel combination of a resistor and a capacitor, representing the shell, and a series of a resistor and capacitor for the inside. In terms of circuit components, the impedance of the particle can be written as:

$$Z_p = \frac{R_{sh}R_iC_{sh}C_is^2 + (R_{sh}C_i + R_{sh}C_{sh} + R_iC_i)s + 1}{R_{sh}C_{sh}C_is^2 + C_is} \tag{6.14}$$

where the values of the electrical components are:

$$R_{sh} = \frac{1}{G_f}\left[\frac{\tau_1+\tau_2}{\Delta\epsilon_1+\Delta\epsilon_2} - \frac{1}{k_2+k_3} - \frac{\tau_1\tau_2(k_2+k_3)}{(\Delta\epsilon_1+\Delta\epsilon_2)^2}\right] \tag{6.15}$$

$$C_{sh} = \frac{\tau_1\tau_2(k_2+k_3)}{(\Delta\epsilon_1+\Delta\epsilon_2)R_{sh}} \tag{6.16}$$

$$R_i = \frac{1}{(k_2+k_3)G_f} \tag{6.17}$$

$$C_i = (\Delta\epsilon_1+\Delta\epsilon_2)G_f \tag{6.18}$$

To demonstrate the difference between the simplified circuit model of section 2.4.1.1 and the complete circuit model for single-shell particles in suspension, calculations of a typical cell in suspension with different values of membrane (shell) conductivity and cytoplasm (inner permittivity), using both mixture theory and the circuit models where performed. The parameters are as follows: R = 5 μm, d = 5 nm, ϵ_m = 78 ϵ_0, σ_m = 1.6 Sm^{-1}, ϵ_{sh} = 11.3 ϵ_0, σ_{sh} = 1 x 10^{-8} Sm^{-1}, ϵ_i = 60 ϵ_0, σ_i = 0.6 Sm^{-1}, with volume fraction ϕ = 0.1 and G_f = 1 m. The results are shown in Figure 6.5. Figure 6.5(a) and (b) show the magnitude of the impedance and the phase for different values of σ_{sh}, respectively. For low values of σ_{sh} (1 x 10^{-8}), the difference between the simplified circuit model and the Maxwell's mixture theory is visible, while the complete circuit model agrees perfectly with mixture theory. When σ_{sh} increases the difference between the simplified circuit model and the full circuit model is more evident. Figure 6.5(c) and (d) show the magnitude of impedance and phase for different values of ϵ_i, respectively. The spectra are plotted over the frequency range from 100 kHz to 100 MHz as the inner properties of the particle influence the response at high frequencies (> 1 MHz). From these figures it is observed that a change in inner permittivity produces a small change in impedance magnitude and phase which can be observed only above 20 MHz.

6.4 Capsule preparation

6.4.1 Materials

Poly(sodium 4-styrenesulfonate) (PSS, MW=70000), poly(allylaminehydrochloride) (PAH, MW=70000), sodium chloride, Rhodamine B, and tetrahydrofuran (THF) were purchased from Sigma-Aldrich and used without further purification. Polystyrene beads with an average diameter of 10.25 ± 0.09 μm were provided by Microparticles GmbH

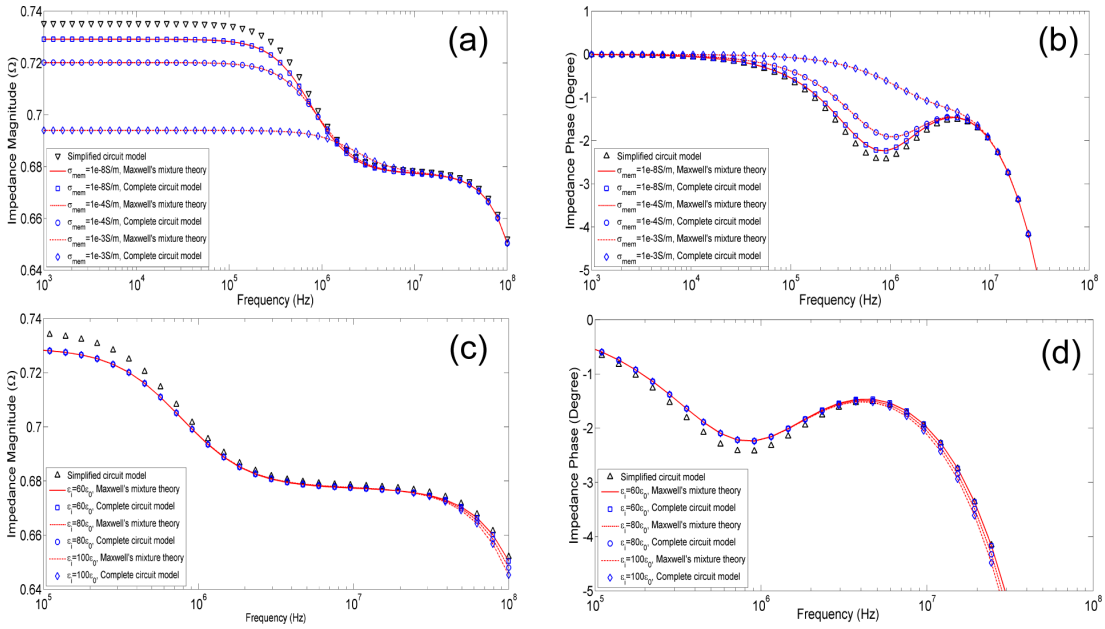

FIGURE 6.5: Comparison of Maxwell's mixture theory and complete circuit model for different values of shell conductivity (a) and (b), and for different values of inner permittivity (c) and (d).

(Berlin, Germany). The water was purified before use in a three-stage Millipore Milli-Q Plus 185 purification system.

6.4.2 PAH/PSS capsule assembly

Hollow capsules were obtained by assembling PAH/PSS multilayers on the surface of 10.25 μm PS particles from 2 mg ml^{-1} PSS and PAH solutions in 0.5 M NaCl. The samples were prepared using 2 ml Eppendorf test tubes; an initial amount of 300 μl of particles (10 wt.- % aqueous dispersion) was placed in each tube. Before starting the assembly process, the particles were washed five times with water and ultrasonic agitated for a few seconds between each washing step. After the last washing step, the supernatant was removed and 1800 μL of polyelectrolyte solution added to start the film deposition. As the PS particles were negatively charged, the layer deposition started from adsorption of a positive polyelectrolyte solution, which in this case was PAH. The polyelectrolytes were adsorbed for 12 minutes under gentle shaking, followed by a centrifugation step (4000 rpm, 2 minutes) to separate the particles from the solution. The remaining polyelectrolyte solution was removed with a pipette and the tube filled with water. After dispersing the particles by shaking, the suspension was centrifuged again for 2 minutes at 4000 rpm and the supernatant removed. The washing step was carried out twice for each deposited layer.

10.25 μm particles were used to prepare two sets of capsules: one set coated with 6 bi-layers (6 PAH layers alternated to 6 PSS layers) and the other one with 9 bi-layers (9 PAH layers alternated to 9 PSS layers). For simplicity, the samples are named below $(PS\text{-}10)_6$ and $(PS\text{-}10)_9$, respectively. After completing the multilayer structure, the sacrificial cores were dissolved by re-suspending the particles in tetrahydrofuran (THF). The solvent was removed after 4 hours by centrifugation at 1000 rpm for 10 minutes. To obtain the final hollow microcapsules, the particles were treated with THF two more times for 2 hours; the dissolution process was then followed by multiple washing with water. After core dissolution, the capsule shells were labelled by adding 1 ml of 1 μM Rhodamine B dye solution to 1ml of capsule water suspension. The capsules were exposed to the dye solution for 20 minutes and then stored in pure water.

For the experiments, capsules were suspended in PBS ($\sigma = 1.6$ S/m, pH = 7). To study the response to pH variations, capsule suspensions in buffer solutions with a conductivity of 1.6 S/m and pH ranging form $\sim$8 to 12 were also prepared. The pH and conductivity of the buffer solutions were adjusted by adding different amounts of 1 M potassium hydroxide (KOH) and water to PBS. The measured pH values of the solutions were: 7.8, 8.92, 10.07, 10.56 and 11.53.

6.5 Capsule characterisation by confocal microscopy

Images of the polyelectrolyte capsules in solution were obtained by confocal microscopy. Confocal microscopy was performed using a Zeiss LSM 5 Exciter system (Carl Zeiss MicroImaging GmbH) equipped with the following lasers: diode laser (405 nm; 25 mW), Ar laser (458, 488, 514 nm; 25 mW), HeNe laser (543 nm;1 mW), HeNe laser (633 nm; 5 mW). Images were taken using the following objective lenses: 20x/0.50, 40x/0.75 Ph2, 40x/1.3 oil immersion, 63x/1.4 oil immersion. Processing of the images was done using ZEN software (Carl Zeiss MicroImaging GmbH). The PE multilayers were visualized by incorporating dye (Rhodamine B) during capsule preparation. The size of the capsules was determined from the average of the measurement of thirty individual capsules of each type.

Typical confocal fluorescence images of a $(PS\text{-}10)_6$ and a $(PS\text{-}10)_9$ capsule are shown in figure 6.5 (a) and figure 6.5 (b), respectively. The average diameters obtained from the measurements were 10.38 $\pm$ 0.24 μm for the $(PS\text{-}10)_6$ capsules and 10.78 $\pm$ 0.18 μm for the $(PS\text{-}10)_9$ capsules. Similar values were obtained from the measurement of both types of capsule suspended in water, implying that re-suspension in PBS did not alter

the shell structure. From a survey of the numerous examples on the synthesis of similar capsules reported in the literature, the shell thickness was estimated to be 24 nm for the 12 layer capsules and 36 nm the 18 layer capsules [173, 174, 175, 176, 177].

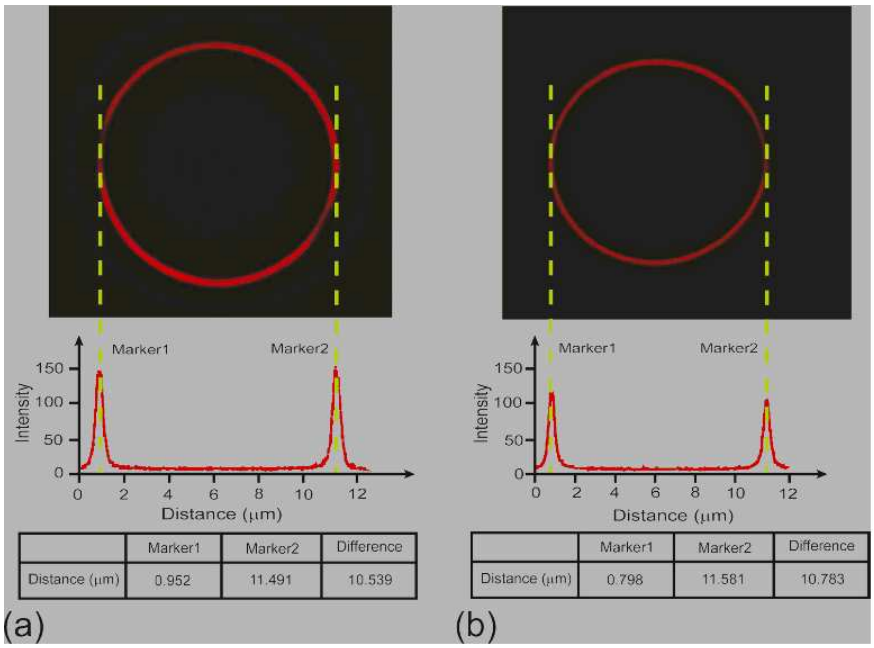

FIGURE 6.6: Confocal images of fluorescently labelled polyelectrolyte microcapsules in different pH solutions. (top) Six bi-layers and (bottom) nine bi-layers, templated on 10.25 μm diameter cores.

The response of $(PS\text{-}10)_6$ and $(PS\text{-}10)_9$ capsules to changes in the pH of the suspending medium is shown in Figure 6.7, where confocal images of the capsules suspended in the different buffer solutions are shown. After a significant initial swelling that occurred immediately after re-suspension, the capsules started to shrink. The total duration of the process (swelling and then shrinking) lasted only few minutes, after which the capsules reached their final size. For pH values higher than 7.8, the final size of the capsules was smaller than the initial one. For both types of capsules, the change in size was more significant for pH higher than 10. The final sizes of the capsules after relaxation as a function of the pH are presented in Figure 6.8. The diameter was measured 30 minutes after re-suspension in the different buffer solutions, to ensure that all the capsules reached a stable rearrangement. For pH = 11.53, the 12 layer capsules shrunk to 8.01 $\pm$ 18 μm diameter, while the final average diameter for the 18 layer capsules was 7.78 $\pm$ 0.19 μm.

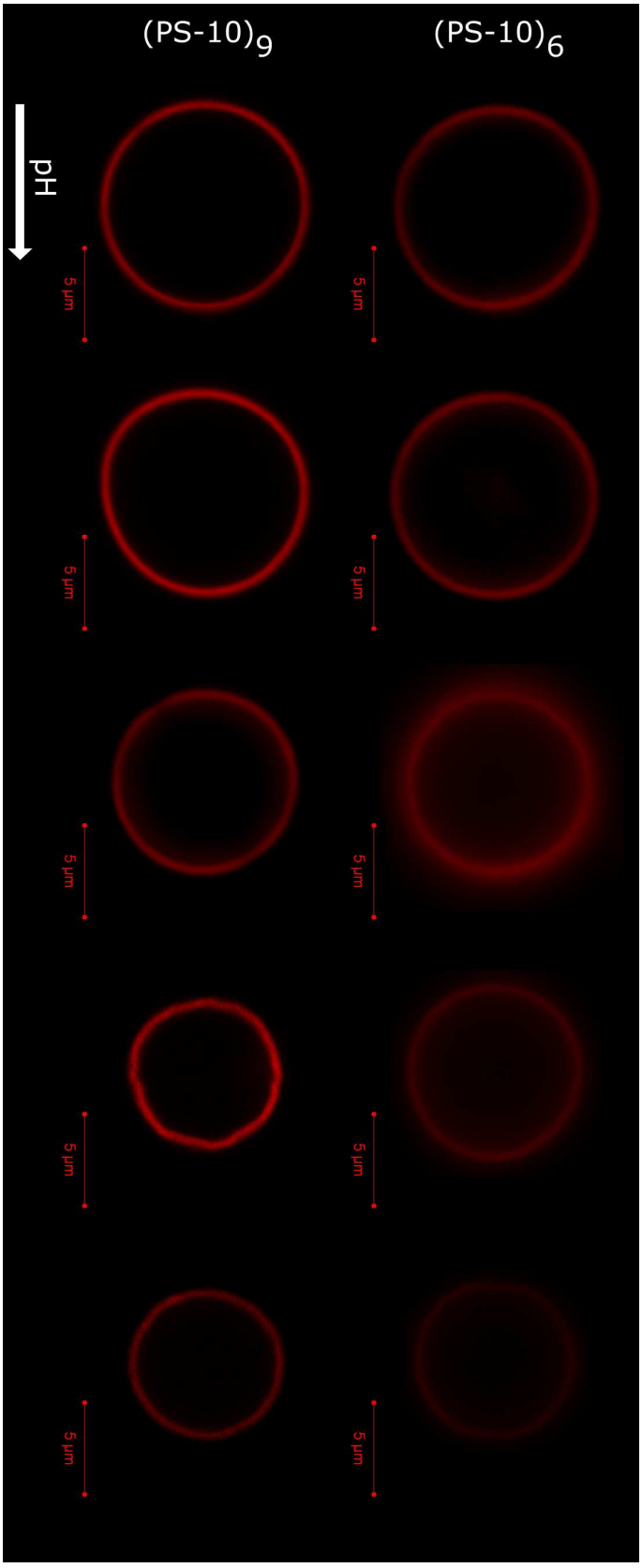

FIGURE 6.7: Confocal images of fluorescently labelled polyelectrolyte microcapsules with (a) six bi-layers and (b) nine bi-layers, templated on 10.25 μm diameter cores.

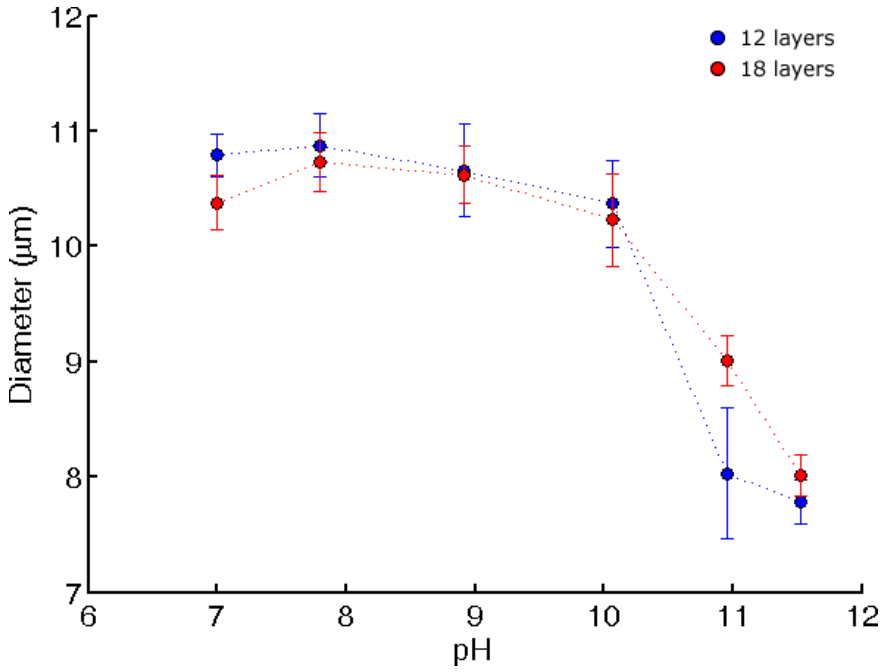

FIGURE 6.8: Diameter of 12 layer and 18 layer capsules as a function of the pH of the suspending buffer solution.

The initial swelling observed immediately after re-suspension of the capsules in high pH buffers could be due to electrostatic repulsion between the accumulated excess of negative charges: while PSS is a strong polyanion, PAH is a weak polycation and its charge density varies with the acidity of the suspending solution. For values of pH higher than 10, the majority of the ammonium groups of PAH become deprotonated and the charge density of the polymer decreases [178, 159]. As a consequence, many charges of the PAH/PSS structure are not compensated. The remaining charges are mainly negative charges from PSS that repel each other, causing the swelling of the multilayer structure. However, as the pH is not high enough to cause the total deprotonation of PAH, the remaining charges enable a reorganization of the polymeric structure towards a thermodynamically more stable and closed rearrangement, which leads to shrinking of the multilayer. The relaxation of the capsules after swelling depended not only on the pH of the solution, but also on the ionic strength. The influence of the ionic strength on the response of PAH/PSS capsules that were exposed to solutions with the same pH has been reported elsewhere [178, 179, 180, 160]. In [178], Dejugnat et al observed the complete dissolution of PAH/PSS capsules templated on PS cores after 30 minutes of re-suspension in pH above 11. However, no dissolution occurred when the capsules were exposed to buffer solutions with the same pH but with higher ionic strength [178]. The buffer solutions used here were based on PBS, which has multiple charged species. The presence of the ions in the solutions caused a screening effect which reduced the Debye length and compressed the capsules, leading to the structure relaxation. Even if the capsules suspended in high pH did not dissolve and did not change in size after several

days, inspection of the samples in both bright field and confocal mode showed lower definition and contrast of the capsule structure, indicating that before relaxing to their final size, the capsules might have experienced partial dissolution of the PE multilayer. This is observed also in Figure 6.7, where the shells of capsules suspended at high pH have a less defined structure.

From Figure 6.8, it is observed that the change in size is similar for both types of capsules, independent of the number of deposited layers. Capsules with a different number of layers that shrunk to similar sizes when exposed to ionic solutions were reported in [160]. During the relaxation process, rearrangement of the structure is opposed by the elastic resistance of the multilayer. Capsules with a high number of layers were more rigid than the thin ones, but the rigidity can be reduced by the screening effect of the ions in the solutions [178, 180].

6.6 Characterisation of PE microcapsules by impedance measurements

The system for single-particle electrical impedance spectroscopy and simultaneous fluorescence detection was described in chapter 3. The measurements were performed using a microfluidic chip with a channel measuring 40 μm in width and 30 μm in height with the standard electrode configuration described in section 4.2.1. A mixture of $(PS\text{-}10)_6$ and $(PS\text{-}10)_9$ capsules and 6.2 μm latex beads (Molecular Probes) was suspended in PBS in a ratio of 2:2:1. The latex beads were added to the mixture to provide a reference during the measurements. The final concentration of the mixture was 500 particles/μl. The sample was pumped through the microchannel and the flow rate was adjusted to obtain a particle transit time (through the detection region) of $\sim$ 1 ms. Measurements were carried out using a population-averaged frequency sweep technique with two AC signals applied simultaneously to the excitation electrodes. The applied frequency signals ranged from 300 kHz to 20 MHz with amplitude of 2.5 Vpp. The reference frequency was kept at a constant value of 503 kHz, while the probe frequency was varied.

Figure 6.9 shows the average value of the impedance magnitude for the three different particles measured at six discrete frequencies. Approximately 2000 events were recorded at each frequency. The dots show the mean value of the impedance data, while the bar gives the standard deviation in that population at the corresponding frequency. The highest magnitude of the impedance was obtained for the 18 layer capsules at nearly all the frequencies, while the 12 layer capsules had the lowest impedance magnitude. At frequency value below 500 kHz, the impedance of the particles is dominated by electrical

double layer formed on the electrodes. At higher frequencies, the properties of the shell dominate the system. For frequencies higher than 20 MHz the system is dominated by the parasitic capacitances in the electrical circuit.

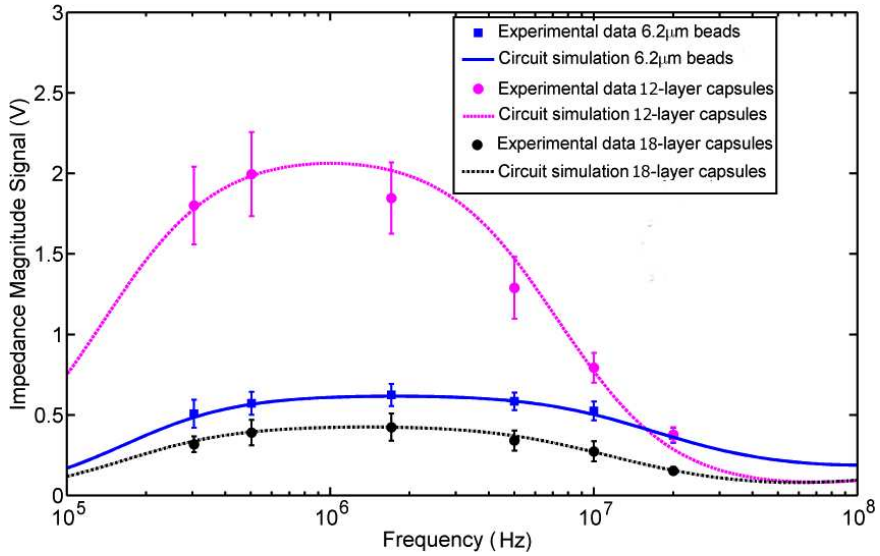

FIGURE 6.9: Experimental data showing the magnitude of the impedance vs the frequency for 12 layer and 18 layer PE capsules and 6.2 μm latex beads. The curves show the best fit PSpice circuit simulation, based on the complete circuit model to estimate the relative permittivity and conductivity in the capsule shell.

Analysis of the data was performed using the complete equivalent circuit model. The geometric constant G_f was determined using conformal mapping [114] and was equal to 64.97 μm for the geometrical parameters of the chip. Simulations of the circuit shown in section 3.3.5.1 were performed using PSpice. The simulated model included the transfer functions of the active components of the circuit (obtained from the manufacturer) and the full ECM for a capsule. The microcapsule diameters and the shell thicknesses reported in the previous section where used in order to model capsules. The value of the electrical double layer (100 pF) and stray capacitance (0.5 pF) were estimated from the fitting of the impedance data for the beads. The bead permittivity was 2.5 ϵ_0 and conductivity 0.36 mS/m [181]. The dielectric properties of the capsule interior were set equal to those of the suspending medium (ϵ = 78 ϵ_0, σ = 1.6 S/m), since the PE multilayer is permeable to ions and the capsule were suspended in PBS for a period of time long enough to allow complete ion diffusion. The permittivity and conductivity of the shell were estimated from the best PSpice fits (shown in Figure 6.9). According to these fits, a shell permittivity of 50 was determined. This value is reasonable as a large amount of water is present in PE multilayers [182] and it is in agreement with data reported in [183]. The conductivity of the capsule shell was found to be 28 $\pm$ 6 mS/m for the $(PS\text{-}10)_6$ capsules and 3.3 $\pm$ 1.7 mS/m for the $(PS\text{-}10)_9$ capsules. The lower conductivity of the capsules with a higher number of layers leads to a higher impedance magnitude. The deposition of a higher number of layers causes a reduction of the pores

in the PE structure. The result is in agreement with what reported in [165], where a decrease in capsule permeability due to an increase in number of deposited layers was observed by electrorotation measurements.

Figure 6.10 is a scatter plot showing the opacity (ratio of the impedance at 5 MHz to the impedance at 503 kHz) against the impedance magnitude at 503 kHz. The three populations can be clearly distinguished. The position of the impedance data for each population in the scatter plot was confirmed by separate measurements of samples containing only one type of particle. The plot shows a number of recorded events equal to 730 for the $(PS\text{-}10)_9$ capsules, 851 for the $(PS\text{-}10)_6$ capsules and 463 for the 6.2 μm beads, which is in agreement with the ratio of the mixture. The wide distribution in impedance magnitude for the $(PS\text{-}10)_9$ capsules might be due to damages or deformation of the multilayer structure.

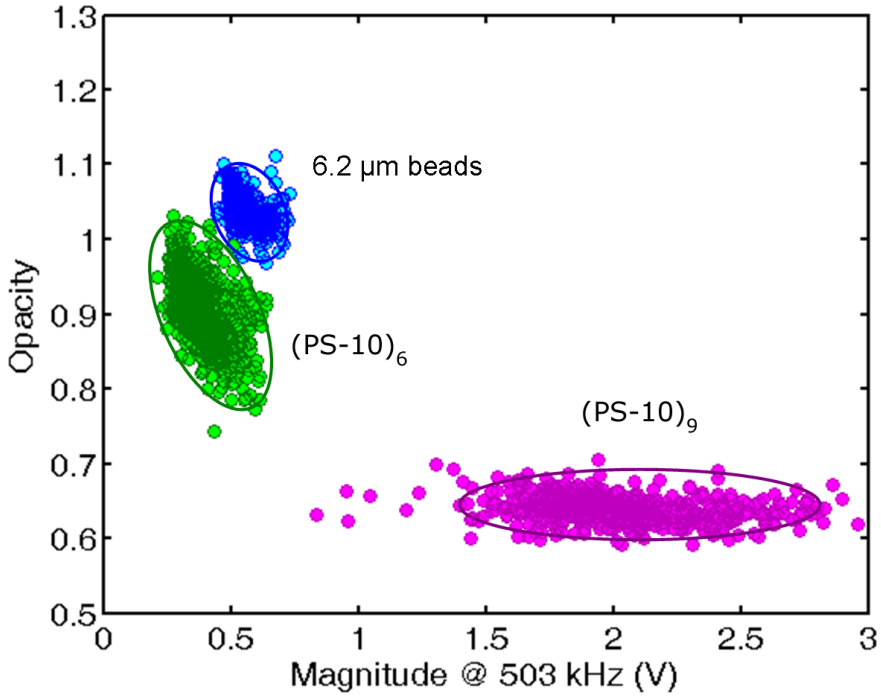

FIGURE 6.10: Scatter plot of opacity ($|Z|$ @ 5 MHz/ $|Z|$@ 503 kHz) against low frequency impedance magnitude ($|Z|$ @ 503 kHz).

6.7 Impedance spectroscopy of pH-responsive microcapsules

Impedance measurements of $(PS\text{-}10)_6$ and $(PS\text{-}10)_9$ microcapsules were performed in order to investigate their changes in dielectric properties and sizes as a response to variation in the pH of the suspending solution. A mixture of the two types of capsules

was suspended in buffer solutions with pH ranging from 7 to 11.5 and conductivity 1.6 S/m. 6.2 μm diameter latex beads were added to the mixture to provide a reference during the measurements. The ratio of the mixture was 2:2:1 $(PS\text{-}10)_6$:$(PS\text{-}10)_9$:beads) and the final concentration of 500 particles/μl. The measurements were carried out using the same system and with the same settings described in the previous section.

Figure 6.11 shows scatter plots of the opacity ($|Z|$@5MHz/$|Z|$@503kHz) against the impedance magnitude at 503 kHz for the sample mixture at different pHs. Three population can be clearly distinguished only for pH between 7 and 10. For values of the pH higher than 10, the capsule populations merged into a single distribution which did not allow for the discrimination of the two types of particles. In all the plots, the position and the distribution of the beads did not vary, as the dielectric properties of the beads are not responsive to changes in pH, whereas the capsules' electrical properties showed a marked variation with pH. For increasing values of pH, the $(PS\text{-}10)_6$ capsules showed a decrease in opacity and a shift towards lower values of the impedance magnitude at 503 kHz. The change was more evident for the $(PS\text{-}10)_9$ capsules, which showed a substantial decrease in the low-frequency impedance magnitude and a simultaneous shift towards higher opacity. For both types of capsules, a general increase in distribution for increasing values of pH was observed. The position of each population in the scatter plots was confirmed by separate measurements of pure samples. For each pH value, around 2000 events were recorded. In all the plots, the number of recorded events is in good agreement with the ratio of the sample mixture apart from the case of pH equal to 11.53, where the number of detected beads was lower than the one expected. Even if the samples were agitated before running the experiments, this difference might be due to the faster sedimentation time of the beads compared to that of capsules. For pH = 10.07, $(PS\text{-}10)_9$ capsules were distributed in two separate populations that differed in the low-frequency impedance magnitude. One population distributed around an average low-frequency magnitude of 0.6 V, while the mean amplitude of the second population was around 1 V. The same behaviour for pH = 10.07 was confirmed by several runs of fresh samples containing only $(PS\text{-}10)_9$ capsules. A reason for this could be relaxation to a different size of some of the capsules or even damage of the shell structure during capsule re-suspension. The fact that a similar behaviour was not observed at different values of pH might indicate that pH = 10.07 represents a critical value for the equilibrium of the forces involved during rearrangement of the polymeric network following capsule re-suspension. This is supported by the fact that drastic changes in capsule final sizes were observed only for pH higher than 10, while changes for pH below 10 were less relevant. However, no apparent damages or large size distributions emerged from optical inspection of the pH = 10.07 samples.

Figure 6.12 shows the average values of the impedance magnitude for the two different

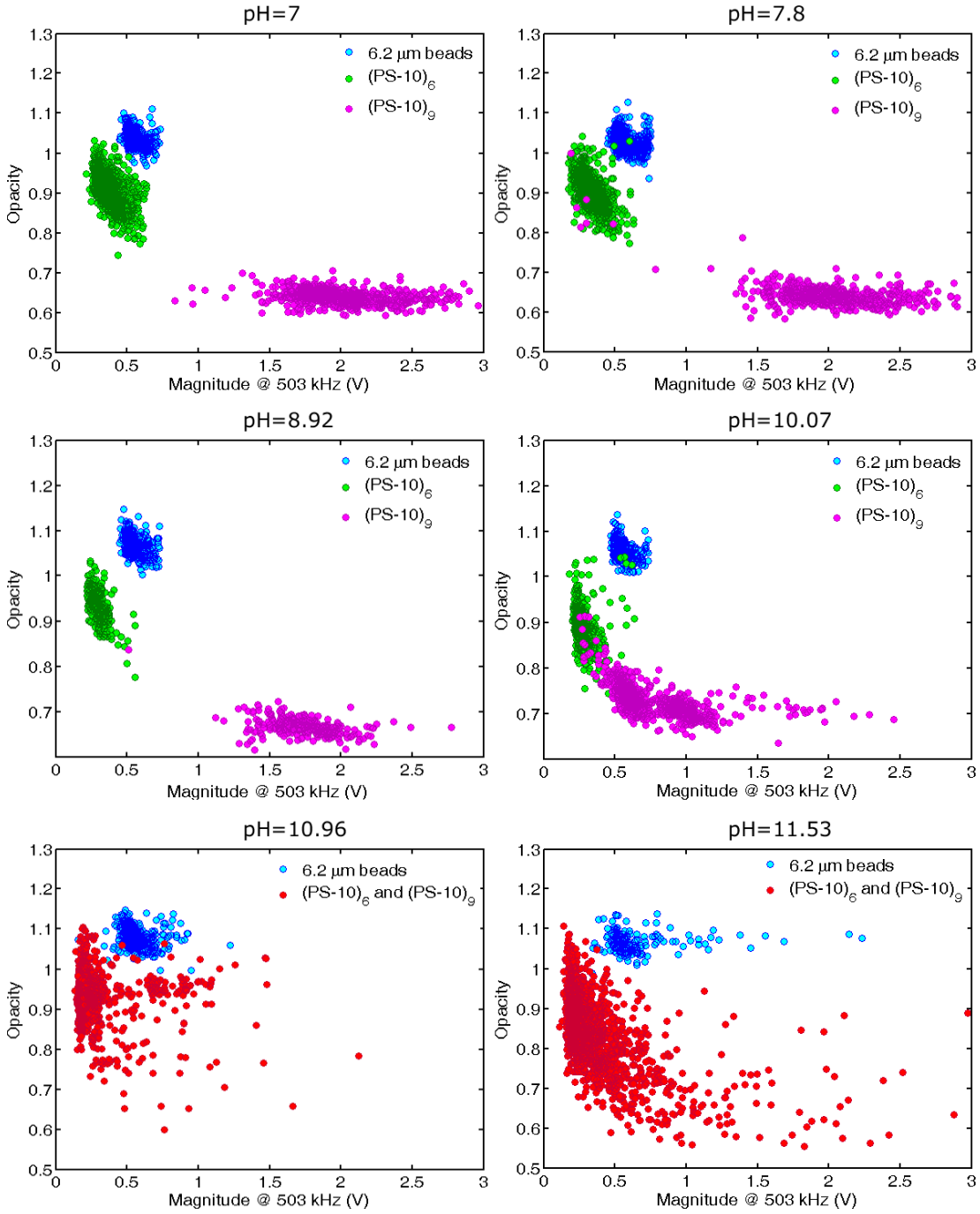

FIGURE 6.11: Scatter plots of the opacity ($|Z|$@5MHz/$|Z|$@503kHz) vs the low-frequency impedance signal for a mixture of $(PS\text{-}10)_6$ and $(PS\text{-}10)_9$ capsules and 6.2 μm beads for different pH of the suspending medium.

capsules and beads measured at different pH, while Figure 6.13 shows the average signal magnitude at 5 MHz for the three different particles as a function of pH. The particle impedance spectra for pH = 11.53 are not reported as discrimination between capsules and beads at this pH value was possible only at 5 MHz and 20 MHz. Both figures show that the impedance magnitude of the beads is constant, as the dielectric properties of the beads did not change and the conductivity of the suspending medium was the same

for the different buffer solutions. Similarly to that observed from the analysis of the opacity scatter plots, the $(PS\text{-}10)_9$ capsules show a large change in signal magnitude with pH, while for the $(PS\text{-}10)_6$ capsules this change is less evident. For pH = 10.96 the spectra of the two type of capsules almost overlap, implying that the different capsules have very similar properties at this pH value.

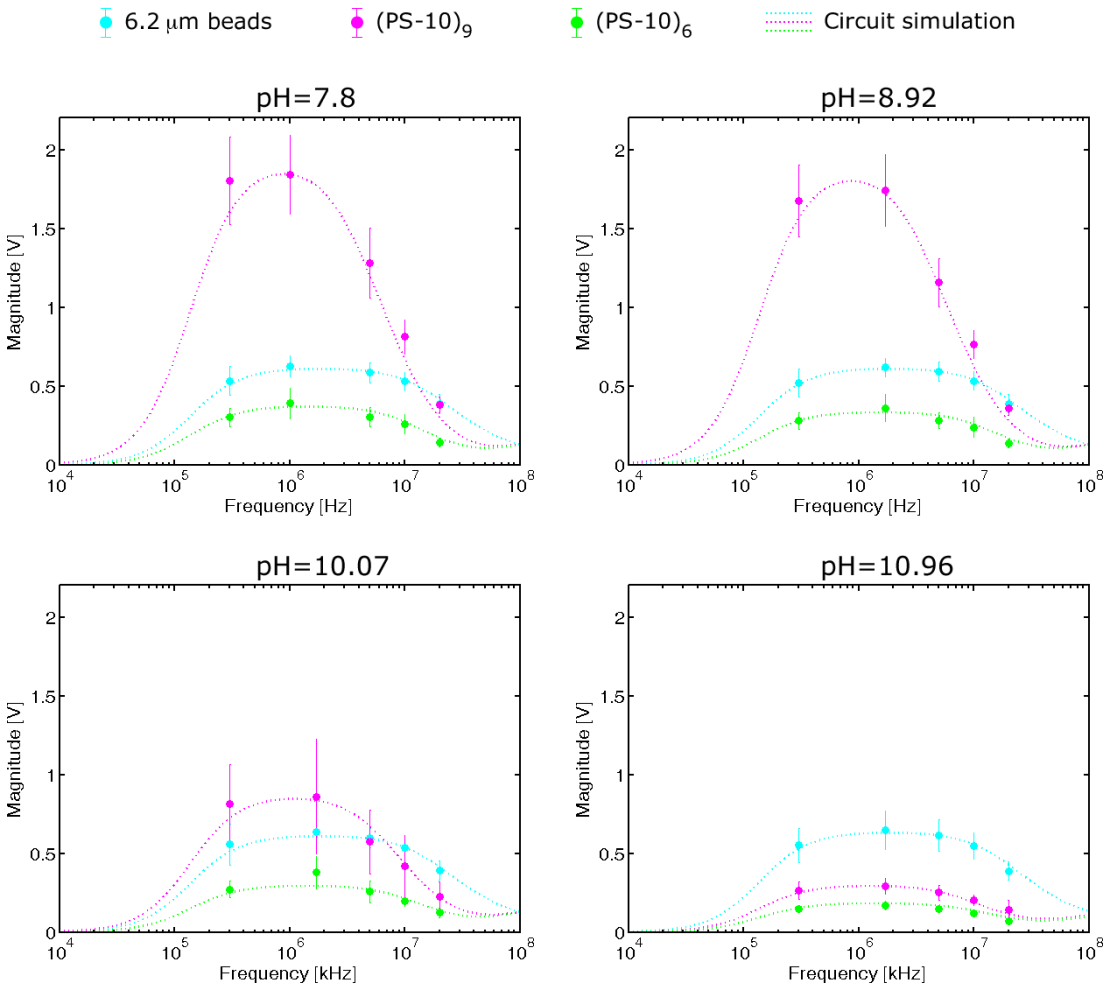

FIGURE 6.12: Experimental data showing the magnitude of the impedance vs frequency for $(PS\text{-}10)_6$ and $(PS\text{-}10)_9$ capsules and 6.2 μm beads for different pH of the suspending solution. The data were fitted to curves obtained from PSpice circuit simulations including the full ECM of the particle in suspension.

The changes in dielectric properties of the capsules exposed to different pH values was investigated by circuit analysis of the system including the full circuit model of a single capsule in suspension. For the simulations, the geometric constant G_f and the double layer and stray capacitances were set to the same values used in the previous section. The validity of these values was confirmed by the excellent fits obtained for the beads (dotted blue lines in Figure 6.12) at each pH. The average diameters obtained by confocal microscopy of the suspensions in different pH (Figure 6.8) were used to model the

capsules. However, precise information on the shell thickness was not available. Assuming that the capsules did not undergo any partial dissolution of the PE layers before relaxing to their final state, a constant volume of the capsule shell is expected. Thus, a decrease in capsule diameter corresponds to an increase in shell thickness given by the relation [180]:

$$h_s = \frac{r_0^2 h_0}{r_s^2} \tag{6.19}$$

where h_s and r_s are the final shell thickness and final radius of the capsule after relaxation respectively, and h_0 and r_0 are the shell thickness and radius before capsule re-suspension. If partial dissolution of the shell occurred, the final thickness of the capsule walls is unknown. However, due to the high conductivity and permittivity of the shell, the PSpice simulation results were not considerably affected by changes in shell thickness, and a decrease in thickness down to a value that was a third of the initial thickness did not alter substantially the fits of the data. This effect was within the error margins given by the standard deviation of the measured capsule diameters.

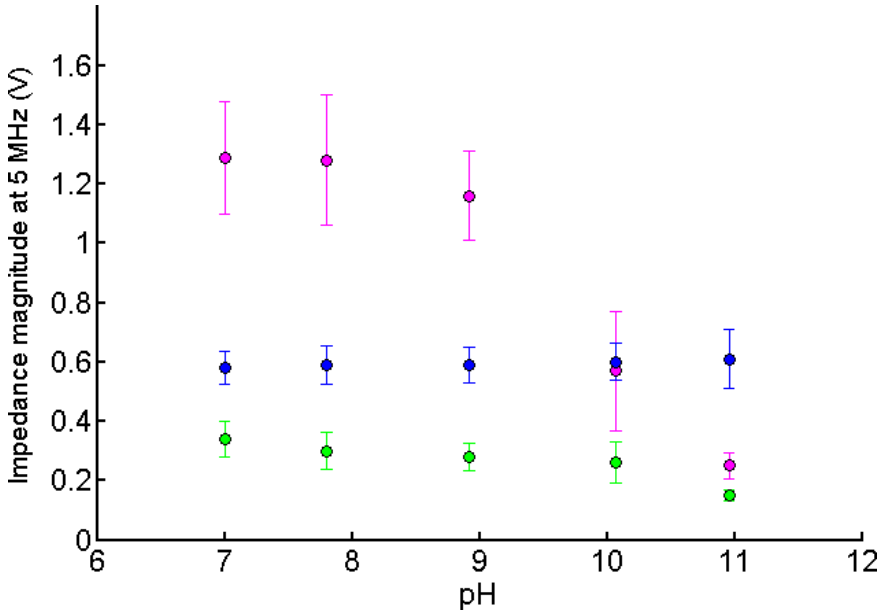

FIGURE 6.13: Variation of the impedance magnitude at 5 MHz of the $(PS\text{-}10)_6$ (green) and $(PS\text{-}10)_9$ (pink) capsules and beads (blue) in response to changes in pH of the suspending medium.

The shell conductivity and permittivity values obtained from the best fits of the impedance data of Figure 6.12 are summarised in table 6.1 The values obtained from the measurements at pH = 7 of the previous section are also shown in the table. A small increase in conductivity is observed for both capsules types at pH = 7.8 and pH = 8.92. This could correspond to a small increment of the number of pores in the PE multilayer caused

by the slight increase in capsule size. The properties of the $(PS\text{-}10)_6$ capsules did not change even for pH = 10.07, while the $(PS\text{-}10)_9$ capsules showed a drop in impedance magnitude which corresponds to a considerable increment in the shell conductivity. For both types of capsules, the best fit was obtained for a value of permittivity equal to 60, however the fit of the data for the $(PS\text{-}10)_9$ capsules cannot be considered very reliable due to the large distribution of the data obtained at this pH value. At pH = 10.96, both types of capsules experienced a substantial drop in impedance magnitude, and the conductivities of the shells for $(PS\text{-}10)_6$ and $(PS\text{-}10)_9$ capsules were found to be 55 ± 3.2 and 29 ± 7.4 mS/m, respectively. An increase in shell conductivity supports the hypothesis of partial dissolution of the multilayer structure during re-suspension in high pH. Partial disassembly of the PE layers would lead to a shell structure which presents an increased number of pores, resulting in a more "electrical transparent" object. Partial dissolution of the PE network could also cause defects in the capsule walls that would explain the large data distribution obtained for high values of pH.

pH		7	7.8	8.92	10.07	10.96
$\mathbf{(PS\text{-}10)_6}$	σ **(mS/ m)**	28 ± 6	35 ± 5	33 ± 4	33 ± 6	55 ± 3.2
	ϵ_r	50	50	50	60	60
$\mathbf{(PS\text{-}10)_9}$	σ **(mS/ m)**	3.3 ± 1.7	4 ± 2.1	3.3 ± 2.2	16 ± 3.7	29 ± 7.4
	ϵ_r	50	50	50	60	60

TABLE 6.1: Shell conductivity and permittivity values for the two types of capsules suspended in different pH. The values were obtained from the PSpice fits of the data of Figure 6.12.

6.8 Conclusions

PE microcapsules with six and nine deposited bi-layers were synthesised and characterised by confocal microscopy. The dielectric properties of the capsules were measured using a micro-impedance cytometer. The values of the capsule dielectric parameters were obtained from circuit analysis of the system including the full equivalent circuit model of a single capsule in suspension. The circuit analysis gave a relative permittivity of the shell of 50 and conductivities of the six- and nine-bi-layer shells of 28 ± 6 and 3.3 ±1.7 mS/m. Impedance spectroscopy was shown to be a very effective technique for the characterisation of the capsules response to changes in pH of the suspending solution. Measurements at six different pH values of the suspending medium were performed. A considerable increase in shell conductivity was obtained for both type of capsules when they were exposed to pH of the suspending medium higher than 10. The conductivities of the six- and nine-bi-layer shells of the capsules suspended in pH = 10.96 were found to be 55 ± 3.2 and 29 ± 7.4 mS/m, respectively. This results implies that during

re-suspension of the capsules in high pH, partial dissolution of the PE shells occurred, leading to the formation of a structure which presented a higher number of pores.

Chapter 7

Conclusions and future work

7.1 Conclusions

Electrical impedance spectroscopy is a non-invasive and label free technique that allows for rapid counting and characterisation of particles in suspension based on their response to applied AC potentials. In recent years, lab-on-a-chip technologies have been developed to enable single-cell impedance detection and a wide range of impedance-based microfluidic devices have been reported. Despite the number of contributions and the achievements of this field, micro-impedance cytometry still suffers from a lack of sensitivity and specificity compared to traditional flow cytometry, which limits the potential commercialization of microfluidic impedance devices. While impedance measurements of beads and cells are well established, discrimination between particles that are very similar in size or detection of small particles (around 1 μm in diameter), such as bacteria, still represents a task.

A number of issues limit the sensitivity and specificity of these microfluidic systems. Primarily, the sensitivity is governed by the dimension of the sample analysis volume. A small volume gives a high sensitivity, but this can lead to practical problems, including fabrication and clogging of the device. In addition, the spatial location of each particle needs to be controlled accurately within the field. Therefore, an efficient and accurate method for focussing the particles in the centre of the electric field is important.

The aim of this work was to develop a micro-impedance cytometer with an improved sensitivity, in order to enable accurate and reliable detection of small particles and discrimination between particles with very similar size, without sacrificing flexibility, robustness and ease of fabrication and operation of the device.

Two novel electrode configurations for the differential measurement of single particles flowing within a wide (200 μm) channel were presented. The performance of the two electrode configurations were investigated by numerical analysis and compared to the performance of a facing electrode configuration implemented into a smaller (40 μm wide) channel. The effect of focussing the sample stream using liquid with different conductivities was also investigated by numerical simulations. Results from the numerical simulations showed that the sensitivity of the system could be improved using an insulating fluid to focus the sample or by optimising the electrode geometry. This result was confirmed by the impedance measurement of a mixture of 4.62 μm and 5.49 μm beads where clear discrimination of the two populations of beads was obtained.

A significant increase the sensitivity of the micro-impedance cytometer whilst maintaining large channel dimensions which do not block was observed and detection at a volume ratio of particle to an estimated sensing volume of 0.007% was demonstrated. Measurements of the low frequency (503 kHz) impedance from single particles was used to discriminate between 1 μm and 2 μm diameter beads and E. coli and 2 μm beads. Accurate detection and identification of the particles was confirmed by simultaneously measurements of the fluorescence emission. The distribution in size and fluorescence (CV) was found to be in good agreement with data obtained from with standard commercially available instruments (FACS and DLS).

Impedance spectroscopy was proven to be a reliable and effective technique to investigate and determine the unknown properties of particles in suspension, such as polyelectrolyte microcapsules. PE microcapsules with six and nine deposited bi-layers were synthesised and characterised by confocal microscopy. The dielectric properties of the capsules were measured using the micro-impedance cytometer. The values of the capsule dielectric parameters were obtained from circuit analysis of the system including the full equivalent circuit model of a single capsule in suspension. Impedance spectroscopy was also used to characterise the capsules response to changes in pH of the suspending solution. Changes in capsules dielectric properties were detected and quantified for six different pH values of the suspending medium.

7.2 Future work

This work demonstrated the development of a micro-impedance cytometer with an improved sensitivity. Quantitative data on the detection and discrimination of single bacterium in suspension were reported for the first time. Detection of bacteria is of fundamental importance for many applications in the field of medicine, biology and food

industry. The impedance cytometr presented here could be employed to further investigate the properties of bacteria and to discriminate between different types of bacteria. Sample focussing with a low conductivity fluid implemented into a smaller channel could also enable detection of sub-microns particles such as large molecules and viruses. The improved sensitivity could allow measurements of synchronised cell populations aimed to monitor the cell cycle. Characterisation of polyelectrolyte microcapsules with different shell components and dielectric properties could be performed; encapsulation and release of active substances could be observed by impedance measurements.

The performance of the system could be further improved by investigating different configurations of the sensing electrodes.

The combination of single cell impedance spectroscopy with other features for sample preparation could allow for the development of portable devices for point-of-care diagnostic or platforms for general cell manipulation and study.

Appendix A

List of Publications

Journal Publications

1. **Characterisation of pH responsive microcapsules by impedance spectroscopy.**
   Catia Bernabini, David Holmes, Gleb Sukhorukov and Hywel Morgan, *Manuscript in preparation.*

2. **Micro-impedance cytometry for detection and analysis of micron-sized particles and bacteria.**
   Catia Bernabini, David Holmes and Hywel Morgan., *Lab on a Chip* **11**, 407, (2011).

3. **Single-Colloidal Particle Impedance Spectroscopy: Complete Equivalent Circuit Analysis of Polyelectrolyte Microcapsules.**
   Tao Sun, Catia Bernabini and Hywel Morgan., *Langmuir*, **26**, 3821, (2010).

4. **Broadband single cell impedance spectroscopy using maximum length sequences: theoretical analysis and practical considerations.**
   Sun, T., Gawad, S., Bernabini, C., Green, N. G. and Morgan, H, *Measurement Science and Technology*, **18**, 2859, (2007).

Conference Publications

1. **Micro-impedance spectroscopy for detection and discrimination of bacteria and microparticles.**
   Bernabini, C., Holmes, D. and Morgan, H., in *Proc Micro Total Analysis Systems*, Jeju, Korea, 2009.

2. **On-Chip Impedance spectroscopy of pH-responsive Polyelectrolyte Microcapsules.**
   Bernabini, C., Holmes, D., Bedard, M., Sukhorukov, G. B. and Morgan, H., in *Proc Micro Total Analysis Systems*, San Diego, USA, 2008.

Bibliography

[1] M. Koch, A. G. R. Evans, and A. Brunnschweiler. Design and fabrication of a micromachined coulter counter. *Journal of Micromechanics and Microengineering*, 9(2):159–161, 1999.

[2] O. A. Saleh and L. L. Sohn. An artificial nanopore for molecular sensing. *Nano Letters*, 3(1):37–38, 2003.

[3] H. G. Chun, T. D. Chung, and H. C. Kim. Cytometry and velocimetry on a microfluidic chip using polyelectrolytic salt bridges. *Analytical Chemistry*, 77(8):2490–2495, 2005.

[4] D. Xu, Y. Kang, M. Sridhar, A. B. Hmelo, L. C. Feldman, D. Li, and D. Li. Wide-spectrum, ultrasensitive fluidic sensors with amplification from both fluidic circuits and metal oxide semiconductor field effect transistors. *Applied Physics Letters*, 91(1):–, 2007.

[5] J. H. Nieuwenhuis, F. Kohl, J. Bastemeijer, P. M. Sarro, and M. J. Vellekoop. Integrated coulter counter based on 2-dimensional liquid aperture control. *Sensors and Actuators B-Chemical*, 102(1):44–50, 2004.

[6] S. Gawad, M. Wuthrich, L. Schild, O. Dubochet, and P. Renaud. Micromachined impedance spectroscopy flow cytometer for cell analysis and sizing. *Lab on a Chip*, 1(1):762 – 82, 2001.

[7] S. Gawad, K. Cheung, U. Seger, A. Bertsch, and P. Renaud. Dielectric spectroscopy in a micromachined flow cytometer: theoretical and practical considerations. *Lab on a Chip*, 4(3):241–251, 2004.

[8] D. Holmes, D. Pettigrew, C. H. Reccius, J. D. Gwyer, C. van Berkel, J. Holloway, D. E. Davies, and H. Morgan. Leukocyte analysis and differentiation using high speed microfluidic single cell impedance cytometry. *Lab on a Chip*, 9(20):2881–2889, 2009.

[9] D. Maello. Continuos differential spectroscopy of single cells. *Microfluid nanofluid*, 1(1):21–22, 2009.

[10] K. R. Foster and H. P. Schwan. Dielectric-properties of tissues and biological-materials - a critical-review. *Critical Reviews in Biomedical Engineering*, 17(1):25–104, 1989.

[11] H. Morgan, T. Sun, D. Holmes, S. Gawad, and N. G. Green. Single cell dielectric spectroscopy. *Journal of Physics D-Applied Physics*, 40(1):61–70, 2007.

[12] H. Morgan and N. G. Green. *AC electrokinetics: colloids and nanoparticles*. Research Studies Press Ltd., Baldock, Hertfordshire, 2002.

[13] U. Seger, S. Gawad, R. Johann, A. Bertsch, and P. Renaud. Cell immersion and cell dipping in microfluidic devices. *Lab on a Chip*, 4(2):148–151, 2004.

[14] S. Tao. *Single cell impedance spectroscopy*. PhD thesis, University of Southampton, 2007.

[15] D. G. Shchukin and G. B. Sukhorukov. Selective yf3 nanoparticle formation in polyelectrolyte capsules as microcontainers for yttrium recovery from aqueous solutions. *Langmuir*, 19(10):4427–4431, 2003.

[16] G. Decher. Fuzzy nanoassemblies: Toward layered polymeric multicomposites. *Science*, 277(5330):1232–1237, 1997.

[17] G. B. Sukhorukov, A. Fery, M. Brumen, and H. Mohwald. Physical chemistry of encapsulation and release. *Physical Chemistry Chemical Physics*, 6(16):4078–4089, 2004.

[18] J. Israelachvili. *Intermolecular and surface forces*. Academic Press, 1992.

[19] R. Hober. Eine methode die elekrishe leitfaehigkeit im innern von zellen messem. *Arch. Ges. Physiol*, 148:189–221, 1910.

[20] R. Hober. Ein zweites verfahren die leitfaehigkeit in innern von zellen ze messem. *Arch. Ges. Physiol*, 148:189–221, 1912.

[21] R. Hober. Messungen der inneren leifaehigkeit von zelen iii. *Arch. Ges. Physiol*, 150:15–45, 1913.

[22] H. Fricke. A mathematical treatment of the electric conductivity of colloids and cell suspensions. *J. Gen. Physiol*, 6:375–384, 1924.

[23] H. Fricke. A mathematical treatment of the electric conductivity and capacity of disperse systems, i. the electric conductivity of a suspensions of homogeneous spheroids. *Phys., Rev*, 24:575–587, 1924.

[24] H. Fricke. A mathematical treatment of the electric conductivity and capacity of disperse systems, ii. the capacity of a suspensions of conducting membrane for a current of low frequency. *Phys., Rev*, 26:678–681, 1925.

[25] H. Fricke and H. J. Curtis. The electric impedance of hemolyzed suspensions of mammalian erythrocytes. *J. Gen. Physiol.*, 18(18):821–836, 1935.

[26] K. S. Cole. Electric impedance of hipponoe eggs. *J. Gen. Physiol.*, 18:877–887, 1935.

[27] K. S. Cole and R. H. Cole. Electric impedance of asteria eggs. *J. Gen. Physiol.*, 19:609–623, 1936.

[28] K. S. Cole and R. H. Cole. Electric impedance of arbacia eggs. *J. Gen. Physiol.*, 19:625–632, 1936.

[29] H. J. Curtis and K. S. Cole. Transverse electric impedance of nitella. *J. Gen. Physiol.*, 21:189–201, 1937.

[30] S. Grimnes and O. G. Martinsen. *Bioimpedance and Bioelectricity Basics*. Academic Press, London, 2000.

[31] R. Pethig and D. B. Kell. The passive electrical-properties of biological-systems - their significance in physiology, biophysics and biotechnology. *Physics in Medicine and Biology*, 32(8):933–970, 1987.

[32] U. Zimmermann, U. Friedrich, H. Mussauer, P. Gessner, K. Hamel, and V. Sukhoruhov. Electromanipulation of mammalian cells: Fundamentals and application. *Ieee Transactions on Plasma Science*, 28(1):72–82, 2000.

[33] K. Asami. Characterization of heterogeneous systems by dielectric spectroscopy. *Progress in Polymer Science*, 27(8):1617–1659, 2002.

[34] M. E. Lidstrom and D. R. Meldrum. Life-on-a-chip. *Nature Reviews Microbiology*, 1(2):158–164, 2003.

[35] D. Di Carlo and L. P. Lee. Dynamic single-cell analysis for quantitative biology. *Analytical Chemistry*, 78(23):7918–7925, 2006.

[36] Coulter, W. H. (US patent 1953).

[37] N. C. Hughes-Jones, I. Norley, J. M. S. Young, and J. M. England. Differential white cell counts by frequency distribution analysis of cell volumes. *J. Clin. Path*, 27:623–625, 1974.

[38] H. Bayley and C. R. Martin. Resistive-pulse sensing - from microbes to molecules. *Chemical Reviews*, 100(7):2575–2594, 2000.

[39] http://www.beckman-coulter.com.

[40] R. Ramon, D. Sawadogo, F. S. Koko, V. Noba, R. Likikouet, G. Gourvellec, I. Viho, L. Mandelbrot, F. Dabis, C. W. Ekra, and P. Msellati. Haematological characteristics and hiv status of pregnant women in abidjan, cote d'ivoire, 1995-96. *Transactions of the Royal Society of Tropical Medicine and Hygiene*, 93(4):419–422, 1999.

[41] I. A. W. Hwa, K. Reimann, P. K. C. Lim, and L. C. Lai. Effects of insulin-like growth factors i and ii on oestrone sulphatase activity in human breast cancer cell lines. *International Journal of Molecular Medicine*, 4(2):175–178, 1999.

[42] A. P. Han, G. Schurmann, G. Mondin, R. A. Bitterli, N. G. Hegelbach, N. F. de Rooij, and U. Staufer. Sensing protein molecules using nanofabricated poresn. *Applied Physics Letters*, 88(9):909–912, 2006.

[43] R. Fan, R. Karnik, M. Yue, D. Y. Li, A. Majumdar, and P. D. Yang. Dna translocation in inorganic nanotubes. *Nano Letters*, 5(9):1633–1637, 2005.

[44] R. W. Deblois and C. P. Bean. Counting and sizing of submicron particles by resistive pulse technique. *Review of Scientific Instruments*, 41(7):909–912, 1970.

[45] R. W. Deblois, C. P. Bean, and R. K. A. Wesley. Electrokinetic measurements with submicron particles and pores by resistive pulse technique. *Journal of Colloid and Interface Science*, 61(2):323–335, 1977.

[46] X. D. Wu, Y. J. Kang, Y. N. Wang, D. Y. Xu, D. Y. Li, and D. Q. Li. Microfluidic differential resistive pulse sensors. *Electrophoresis*, 29(13):2754–2759, 2008.

[47] C. C. Harrell, Y. Choi, L. P. Horne, L. A. Baker, Z. S. Siwy, and C. R. Martin. Resistive-pulse dna detection with a conical nanopore sensor. *Langmuir*, 22(25):10837–10843, 2006.

[48] J. B. Heng, C. Ho, T. Kim, R. Timp, A. Aksimentiev, Y. V. Grinkova, S. Sligar, K. Schulten, and G. Timp. Sizing dna using a nanometer-diameter pore. *Biophysical Journal*, 87(4):2905–2911, 2004.

[49] S. B. Smith, Y. J. Cui, and C. Bustamante. Stretching individual dna molecules with force-measuring laser tweezers. *Abstracts of Papers of the American Chemical Society*, 212:40–41, 1996.

[50] S. M. Bezrukov, I. Vodyanoy, and V. A. Parsegian. Counting polymers moving through a single-ion channel. *Nature*, 370(6487):279–281, 1994.

[51] J. L. Li, M. Gershow, D. Stein, E. Brandin, and J. A. Golovchenko. Dna molecules and configurations in a solid-state nanopore microscope. *Nature Materials*, 2(9):611–615, 2003.

[52] R. W. Deblois and R. K. A. Wesley. Sizes and concentrations of several type-c oncornaviruses and bacteriophage-t2 by resistive-pulse technique. *Journal of Virology*, 23(2):227–233, 1977.

[53] D. E. Swartzendruber, G. L. Travis, and J. C. Martin. Flow cytometric analysis of the effect of 5-bromodeoxyuridine on mouse teratocarcinoma cells. *Cytometry*, 1(3):238–244, 1980.

[54] R. A. Thomas, T. A. Yopp, B. D. Watson, D. H. K. Hindman, B. F. Cameron, S. B. Leif, R. C. Leif, L. Roque, and W. Britt. Combined optical and electronic analysis of cells with amac transducers. *Journal of Histochemistry & Cytochemistry*, 25(7):827–835, 1977.

[55] N. Tokita, T. S. Johnson, R. A. Hoffman, and M. R. Raju. Introduction of cytokinetic perturbations and increased cell-killing of v79 cells by radio-chemotherapy. *Cell and Tissue Kinetics*, 12(6):681–681, 1979.

[56] R. A. Hoffman, T. S. Johnson, and W. B. Britt. Flow cytometric electronic direct-current volume and radiofrequency impedance measurements of single cells and particles. *Cytometry*, 1(6):377–384, 1981.

[57] http://www.sysmex.com.

[58] U. D. Larsen, G. Blankenstein, and J. Branebjerg. Microchip coulter particle counter. *Transducers 97 - 1997 International Conference on Solid-State Sensors and Actuators, Digest of Technical Papers, Vols 1 and 2*, pages 1319–1322?1525, 1997.

[59] U. D. Larsen, H. Norring, and P. Telleman. ? *Micro Total Analysis Systems 2000*, 1(1):103–106, 2000.

[60] O. A. Saleh and L. L. Sohn. A resistive sensing device for biological solutions. *Biophysical Journal*, 80(1):143a–143a, 2001.

[61] A. Carbonaro and L. L. Sohn. A resistive-pulse sensor chip for multianalyte immunoassays. *Lab on a Chip*, 5(10):1155–1160, 2005.

[62] R. Rodriguez-Trujillo, O. Castillo-Fernandez, M. Garrido, M. Arundell, A. Valencia, and G. Gomila. High-speed particle detection in a micro-coulter counter with two-dimensional adjustable aperture. *Biosensors & Bioelectronics*, 24(2):290–296, 2008.

[63] R. Rodriguez-Trujillo, C. A. Mills, J. Samitier, and G. Gomila. Low cost micro-coulter counter with hydrodynamic focusing. *Microfluidics and Nanofluidics*, 3(2):171–176, 2007.

[64] A. V. Jagtiani, J. Zhe, J. Hu, and J. Carletta. Detection and counting of micro-scale particles and pollen using a multi-aperture coulter counter. *Measurement Science & Technology*, 17(7):1706–1714, 2006.

[65] H. A. Stone and S. Kim. Microfluidics: Basic issues, applications, and challenges. *Aiche Journal*, 47(6):1250–1254, 2001.

[66] T. Braschler, L. Metref, R. Zvitov-Marabi, H. van Lintel, N. Demierre, J. Theytaz, and P. Renaud. A simple pneumatic setup for driving microfluidics. *Lab on a Chip*, 7(4):420–422, 2007.

[67] O. A. Saleh and L. L. Sohn. Quantitative sensing of nanoscale colloids using a microchip coulter counter. *Review of Scientific Instruments*, 72(12):4449–4451, 2001.

[68] O. A. Saleh and L. L. Sohn. Direct detection of antibody-antigen binding using an on-chip artificial pore. *Proceedings of the National Academy of Sciences of the United States of America*, 100(3):820–824, 2003.

[69] H. Tang and Y. F. Gao. An impedance microsensor with coplanar electrodes and vertical sensing apertures. *Ieee Sensors Journal*, 5(6):1346–1352, 2005.

[70] J. Zhe, A. Jagtiani, P. Dutta, J. Hu, and J. Carletta. A micromachined high throughput coulter counter for bioparticle detection and counting. *Journal of Micromechanics and Microengineering*, 17(2):304–313, 2007.

[71] S. Kostner and M. J. Vellekoop. On-chip coulter counter with variable aperture using a two layer su-8 process for improved sample focussing, 2008.

[72] R. Scott, P. Sethu, and C. K. Harnett. Three-dimensional hydrodynamic focusing in a microfluidic coulter counter. *Review of Scientific Instruments*, 79(4):–, 2008.

[73] J. H. Nieuwenhuis, J. Bastemeijer, P. M. Sarro, and M. J. Vellekoop. Integrated flow-cells for novel adjustable sheath flows. *Lab on a Chip*, 3(2):56–61, 2003.

[74] C. Simonnet and A. Groisman. Two-dimensional hydrodynamic focusing in a simple microfluidic device. *Applied Physics Letters*, 87(11):–, 2005.

[75] T. Sun, N. G. Green, S. Gawad, and H. Morgan. Analytical electric field and sensitivity analysis for two microfluidic impedance cytometer designs. *Iet Nanobiotechnology*, 1(5):69–79, 2007.

[76] K. Asami, E. Gheorghiu, and T. Yonezawa. Real-time monitoring of yeast cell division by dielectric spectroscopy. *Biophysical Journal*, 76(6):3345–3348, 1999.

[77] Y. Polevaya, I. Ermolina, M. Schlesinger, B. Z. Ginzburg, and Y. Feldman. Time domain dielectric spectroscopy study of human cells - ii. normal and malignant white blood cells. *Biochimica Et Biophysica Acta-Biomembranes*, 1419(2):257–271, 1999.

[78] H. E. Ayliffe, A. B. Frazier, and R. D. Rabbitt. Electric impedance spectroscopy using microchannels with integrated metal electrodes. *Journal of Microelectromechanical Systems*, 8(1):50–57, 1999.

[79] C. K. Fuller, J. Hamilton, H. Ackler, and B. Boser. Microfabricated multifrequency particle impedance characterization system. *Micro Total Analysis Systems 2000*, pages 265–268, 2000.

[80] L. L. Sohn, O. A. Saleh, G. R. Facer, A. J. Beavis, R. S. Allan, and D. A. Notterman. Capacitance cytometry: Measuring biological cells one by one. *Proceedings of the National Academy of Sciences of the United States of America*, 97(20):10687–10690, 2000.

[81] H. Morgan, D. Holmes, and N. G. Green. High speed simultaneous single particle impedance and fluorescence analysis on a chip. *Current Applied Physics*, 6(3):367–370, 2006.

[82] G. Benazzi, D. Holmes, T. Sun, M. C. Mowlem, and H. Morgan. Discrimination and analysis of phytoplankton using a microfluidic cytometer. *Iet Nanobiotechnology*, 1(6):94–101, 2007.

[83] C. Kuttel, E. Nascimento, N. Demierre, T. Silva, T. Braschler, P. Renaud, and A. G. Oliva. Label-free detection of babesia bovis infected red blood cells using impedance spectroscopy on a microfabricated flow cytometer. *Acta Tropica*, 102(1):63–68, 2007.

[84] K. Cheung, S. Gawad, and P. Renaud. Impedance spectroscopy flow cytometry: Parameters for label-free cell differentiation. *Micro Total Analysis Systems 2004, Vol 1*, 4(296):55–57 684, 2005.

[85] T. Sun, D. Holmes, S. Gawad, N. G. Green, and H. Morgan. High speed multi-frequency impedance analysis of single particles in a microfluidic cytometer using maximum length sequences. *Lab on a Chip*, 7(8):1034–1040, 2007.

[86] L. S. Jang and M. H. Wang. Microfluidic device for cell capture and impedance measurement. *Biomedical Microdevices*, 9(5):737–743, 2007.

[87] S. Z. Hua and T. Pennell. A microfluidic chip for real-time studies of the volume of single cells. *Lab on a Chip*, 9(2):251–256, 2009.

[88] W. M. Arnold and U. Zimmermann. Rotation of an isolated cell in a rotating electric-field. *Naturwissenschaften*, 69(6):297–298, 1982.

[89] J. Gimsa, T. Schnelle, G. Zechel, and R. Glaser. Dielectric-spectroscopy of human erythrocytes - investigations under the influence of nystatin. *Biophysical Journal*, 66(4):1244–1253, 1994.

[90] J. Gimsa, T. Muller, T. Schnelle, and G. Fuhr. Dielectric spectroscopy of single human erythrocytes at physiological ionic strength: Dispersion of the cytoplasm. *Biophysical Journal*, 71(1):495–506, 1996.

[91] K. L. Chan, H. Morgan, E. Morgan, I. T. Cameron, and M. R. Thomas. Measurements of the dielectric properties of peripheral blood mononuclear cells and trophoblast cells using ac electrokinetic techniques. *Biochimica Et Biophysica Acta-Molecular Basis of Disease*, 1500(3):313–322, 2000.

[92] J. Yang, Y. Huang, X. J. Wang, X. B. Wang, F. F. Becker, and P. R. C. Gascoyne. Dielectric properties of human leukocyte subpopulations determined by electrorotation as a cell separation criterion. *Biophysical Journal*, 76(6):3307–3314, 1999.

[93] X. J. Wang, F. F. Becker, and P. R. C. Gascoyne. Membrane dielectric changes indicate induced apoptosis in hl-60 cells more sensitively than surface phosphatidylserine expression or dna fragmentation. *Biochimica Et Biophysica Acta-Biomembranes*, 1564(2):412–420, 2002.

[94] F. F. Becker, X. B. Wang, Y. Huang, R. Pethig, J. Vykoukal, and P. R. C. Gascoyne. Separation of human breast-cancer cells from blood by differential dielectric affinity. *Proceedings of the National Academy of Sciences of the United States of America*, 92(3):860–864, 1995.

[95] J. Cheng, E. L. Sheldon, L. Wu, M. J. Heller, and J. P. O'Connell. Isolation of cultured cervical carcinoma cells mixed with peripheral blood cells on a bioelectronic chip. *Analytical Chemistry*, 70(11):2321–2326, 1998.

[96] H. M. Shapiro. Practical flow cytometry. *New York: Wiley-Liss*, 1995.

[97] A. Y. Fu, H. P. Chou, C. Spence, F. H. Arnold, and S. R. Quake. An integrated microfabricated cell sorter. *Analytical Chemistry*, 74(11):2451–2457, 2002.

[98] J. Kruger, K. Singh, A. ONeill, and C. Jackson. Development of a microfluidic device for fluorescence activated cell sorting. *J. Micromech. Microeng*, 12:486–494, 2002.

[99] D. Erickson and D. Li. Integrated microfluidic devices. *Anal Chim Acta*, 507:11–26, 2004.

[100] K. B. Mogensen, H. Klank, and J. P. Kutter. Recent developments in detection for microfluidic systems. *Electrophoresis*, 25:3498–3512, 2004.

[101] D. A. Ateya, J. Erickson, and L. R. Howell. The good, the bad, the tiny: a review of microflow cytometry. *Anal Bioanal Chem*, 7:1827, 2008.

[102] M. A. McClain, C. T. Culbertson, S. C. Jacobson, and J. M. Ramsey. Flow cytometry of escherichia coli on nucrifluidic devices. *Analytical Chemistry*, 73(21):5334–5338, 2001.

[103] S. D. Chan, G. Luedke, M. Valer, and C. Buhlmann. Cytometric analysis of protein expression and apoptosis in human primary cells with a novel microfluidic chip-based system. *Cytometry*, 55:119–125, 2003.

[104] A. Wolff, I. R. Perch-Nielsen, U. D. Larsen, P. Friis, G. Goranovic, C. R. Poulsen, J. P. Kutter, and P. Telleman. Integrating advanced functionality in a microfabricated high-throughput fluorescent-activated cell sorter. *Lab on a Chip*, 3(1):22–27, 2003.

[105] T. B. Jones. *Electromechanics of particles*. Cambridge University Press, Cambridge, 1995.

[106] K. S. Cole and R. H. Cole. Dispersion and absorption in dielectrics i.alternating current characteristics. *Journal of Chemical Physics*, 9(4):341–351, 1941.

[107] S. Havriliak and S. negami. A complex plane representation of dilectric and mechanical relaxation processes in some polymers. *Polymer*, 8(4):161, 1967.

[108] R. Pethig. Dielectric-based biosensors. *Biochemical Society Transactions*, 19(1):21–25, 1991.

[109] P. Gascoyne, R. Pethig, J. Satayavivad, F. F. Becker, and M. Ruchirawat. Dielectrophoretic detection of changes in erythrocyte membranes following malarial infection. *Biochimica Et Biophysica Acta-Biomembranes*, 1323(2):240–252, 1997.

[110] A. Irimajiri, T. Hanai, and A. Inouye. Dielectric theory of multi-stratified shell-model with its application to a lymphoma cell. *Journal of Theoretical Biology*, 78(2):251–269, 1979.

[111] J. Gimsa, P. Marszalek, U. Loewe, and T. Y. Tsong. Dielectrophoresis and electrorotation of neurospora slime and murine myeloma cells. *Biophysical Journal*, 60(4):749–760, 1991.

[112] Y. Huang, R. Holzel, R. Pethig, and X. B. Wang. Differences in the ac electrodynamics of viable and nonviable yeast-cells determined through combined dielectrophoresis and electrorotation studies. *Physics in Medicine and Biology*, 37(7):1499–1517, 1992.

[113] J. C. Maxwell. *A tritise on electricity and magnetism*, volume 1. Clarendon Press, Oxford, 1881.

[114] M. Simeonova, D. Wachner, and J. Gimsa. Cellular absorption of electric field energy: influence of molecular properties of the cytoplasm. *Bioelectrochemistry*, 56(1-2):215–218, 2002.

[115] T. Sun. *Single Cell Impedance Spectroscopy*. PhD thesis, University of Southampton, 2007.

[116] J. R. Macdonald. Impedance spectroscopy - old problems and new developments. *Electrochimica Acta*, 35(10):1483–1492, 1990. Ea224 Times Cited:100 Cited References Count:61.

[117] H. P. Schwan. 4-electrode null technique for impedance measurements with high resolution. *Review of scientific instruments*, 39(4):481, 1968.

[118] H. P. Schwan. Electrode polarisation impedance and measurements in biological materials. *Annals of the New York Academiy of Science*, 148(A1):191–193, 1968.

[119] J. C. Wang. Impedance of a fractal electrolyte-electrode interface. *Electrochimica Acta*, 33(5), 1988.

[120] L. Nyikos and T. Pajkossy. Fractal dimension and fractional power frequency-dependent impedance of blocking electrodes. *Electrochimica Acta*, 30(11):1533–1540, 1985.

[121] T. Pajkossy and L. Nyikos. Impedance of planar electrodes with scale-invariant capacitance distribution. *Journal of Electroanalytical Chemistry*, 332(1-2):55–61, 1992.

[122] S. Gawad. *Dielectric spectroscopy in a microfabricated flow cytometer*. PhD thesis, Ecole politechnique federale de Lausanne, 2004.

[123] M. S. Howard. *Practical flow cytometry*. John Wiley & Sons, 2003.

[124] Z. Wang, J. El-Ali, M. Engelund, T. Gotsaed, I. R. Perch-Nielsen, K. B. Mogensen, D. Snakenborg, J. P. Kutter, and A. Wolff. Measurements of scattered light on a microchip flow cytometer with integrated polymer based optical elements. *Lab on a Chip*, 4(4):372–377, 2004.

[125] A. Kummrow, J. Theisen, M. Frankowski, A. Tuchscheerer, H. Yildirim, K. Brattke, M. Schmidt, and J. Neukammer. Microfluidic structures for flow cytometric analysis of hydrodynamically focussed blood cells fabricated by ultraprecision micromachining. *Lab on a Chip*, 9(7):972–981, 2009.

[126] D. Holmes, H. Morgan, and N. G. Green. High throughput particle analysis: Combining dielectrophoretic particle focussing with confocal optical detection. *Biosensors & Bioelectronics*, 21(8):1621–1630, 2006.

[127] S. Gawad, P. Batard, U. Seger, S. Metz, and P. Renaud. Leukocytes discrimination by impedance spectroscopy flow cytometry. Nara, Japan, 2002. Kluwer Academic Publisher.

[128] N. G. Green, A. Ramos, A. Gonzalez, H. Morgan, and A. Castellanos. Fluid flow induced by nonuniform ac electric fields in electrolytes on microelectrodes. i. experimental measurements. *Physical Review E*, 61(4):4011–4018, 2000.

[129] A. Ramos, A. Gonzalez, A. Castellanos, N. G. Green, and H. Morgan. Pumping of liquids with ac voltages applied to asymmetric pairs of microelectrodes. *Physical Review E*, 67(5):–, 2003.

[130] A. Ramos, A. Gonzalez, A. Castellanos, H. Morgan, and N. G. Green. Fluid flow driven by a.c. electric fields in microelectrodes. *Electrostatics 1999*, 163:137–140, 1999.

[131] U. Tallarek, E. Rapp, T. Scheenen, E. Bayer, and H. Van As. Electroosmotic and pressure-driven flow in open and packed capillaries: Velocity distributions and fluid dispersion. *Analytical Chemistry*, 72(10):2292–2301, 2000.

[132] T. Braschler, J. Theytaz, R. Zvitov-Marabi, H. Van Lintel, G. Loche, A. Kunze, N. Demierre, R. Tornay, M. Schlund, and P. Renaud. A virtual valve for smooth contamination-free flow switching. *Lab on a Chip*, 7(9):1111–1113, 2007.

[133] C. Futterer, N. Minc, V. Bormuth, J. H. Codarbox, P. Laval, J. Rossier, and J. L. Viovy. Injection and flow control system for microchannels. *Lab on a Chip*, 4(4):351–356, 2004.

[134] N. Watkins, B. M. Venkatesan, M. Toner, W. Rodriguez, and R. Bashir. A robust electrical microcytometer with 3-dimensional hydrofocusing. *Lab on a Chip*, 9(22):3177–3184, 2009.

[135] J. Jin. *The finite element method in electromagnetics*. John Wiley & Sons, New York, 2002.

[136] N. G. Green, A. Ramos, A. Gonzalez, A. Castellanos, and H. Morgan. Electrothermally induced fluid flow on microelectrodes. *Journal of Electrostatics*, 53(2):71–87, 2001.

[137] W. Bai, K. S. Zhao, and K. Asami. Effects of copper on dielectric properties of e. coli cells. *Colloids and Surfaces B-Biointerfaces*, 58(2):105–115, 2007.

[138] Sambrook and Russell. *Molecular cloning: a laboratory manual*. Cold Spring Harbor Laboratory Press, New York, 2001.

[139] G. Segre and A. Silberberg. Radial particle displacements in poiseuille flow of suspensions. *Nature*, 189(189):209–210, 1961.

[140] D. Di Carlo, D. Irimia, R. G. Tompkins, and M. Toner. Continuous inertial focusing, ordering, and separation of particles in microchannels. *Proceedings of the National Academy of Sciences of the United States of America*, 104(48):18892–18897, 2007.

[141] T. Sun, S. Gawad, N. G. Green, and H. Morgan. Dielectric spectroscopy of single cells: time domain analysis using maxwell's mixture equation. *Journal of Physics D-Applied Physics*, 40(1):1–8, 2007.

[142] W. Meier. Polymer nanocapsules. *Chemical Society Reviews*, 29(5):295–303, 2000.

[143] M. Nasseau, Y. Boublik, W. Meier, M. Winterhalter, and D. Fournier. Substrate-permeable encapsulation of enzymes maintains effective activity, stabilizes against denaturation, and protects against proteolytic degradation. *Biotechnology and Bioengineering*, 75(5):615–618, 2001.

[144] S. Forster and M. Konrad. From self-organizing polymers to nano- and biomaterials. *Journal of Materials Chemistry*, 13(11):2671–2688, 2003.

[145] E. Donath, G. B. Sukhorukov, F. Caruso, S. A. Davis, and H. Mohwald. Novel hollow polymer shells by colloid-templated assembly of polyelectrolytes. *Angewandte Chemie-International Edition*, 37(16):2202–2205, 1998.

[146] R. K. Iler. *J. Colloid Interface Sci.*, 21:569, 1966.

[147] G. Decher and J. D. Hong. Buildup of ultrathin multilayer films by a self-assembly process .1. consecutive adsorption of anionic and cationic bipolar amphiphiles on charged surfaces. *Makromolekulare Chemie-Macromolecular Symposia*, 46:321–327, 1991.

[148] G. Decher, J. D. Hong, and J. Schmitt. Buildup of ultrathin multilayer films by a self-assembly process .3. consecutively alternating adsorption of anionic and cationic polyelectrolytes on charged surfaces. *Thin Solid Films*, 210(1-2):831–835, 1992.

[149] L. Netzer and J. Sagiv. A new approach to construction of artificial monolayer assemblies. *Journal of the American Chemical Society*, 105(3):674–676, 1983.

[150] R. Cao, Z. Y. Huang, X. J. Lei, B. S. Kang, M. C. Hong, and H. Q. Liu. Structure of a dinuclear nickel compound, ni2(pph3)2(sc3h6s)2. *Acta Crystallographica Section C-Crystal Structure Communications*, 48:1654–1655, 1992.

[151] S. T. Dubas and J. B. Schlenoff. Polyelectrolyte multilayers containing a weak polyacid: Construction and deconstruction. *Macromolecules*, 34(11):3736–3740, 2001.

[152] J. D. Mendelsohn, C. J. Barrett, V. V. Chan, A. J. Pal, A. M. Mayes, and M. F. Rubner. Fabrication of microporous thin films from polyelectrolyte multilayers. *Langmuir*, 16(11):5017–5023, 2000.

[153] S. T. Dubas and J. B. Schlenoff. Factors controlling the growth of polyelectrolyte multilayers. *Macromolecules*, 32(24):8153–8160, 1999.

[154] D. Korneev, Y. Lvov, G. Decher, J. Schmitt, and S. Yaradaikin. Neutron reflectivity analysis of self-assembled film superlattices with alternate layers of deuterated and hydrogenated polysterenesulfonate and polyallylamine. *Physica B*, 213:954–956, 1995.

[155] R. Kugler, J. Schmitt, and W. Knoll. The swelling behavior of polyelectrolyte multilayers in air of different relative humidity and in water. *Macromolecular Chemistry and Physics*, 203(2):413–419, 2002.

[156] G. Ibarz, L. Dahne, E. Donath, and H. Mohwald. Controlled permeability of polyelectrolyte capsules via defined annealing. *Chemistry of Materials*, 14(10):4059–4062, 2002.

[157] F. Caruso, R. A. Caruso, and H. Mohwald. Nanoengineering of inorganic and hybrid hollow spheres by colloidal templating. *Science*, 282(5391):1111–1114, 1998.

[158] G. B. Sukhorukov, E. Donath, S. Davis, H. Lichtenfeld, F. Caruso, V. I. Popov, and H. Mohwald. Stepwise polyelectrolyte assembly on particle surfaces: a novel approach to colloid design. *Polymers for Advanced Technologies*, 9(10-11):759–767, 1998.

[159] T. Mauser, C. Dejugnat, and G. B. Sukhorukov. Reversible ph-dependent properties of multilayer microcapsules made of weak polyelectrolytes. *Macromolecular Rapid Communications*, 25(20):1781–1785, 2004.

[160] C. Y. Gao, S. Leporatti, S. Moya, E. Donath, and H. Mohwald. Swelling and shrinking of polyelectrolyte microcapsules in response to changes in temperature and ionic strength. *Chemistry-a European Journal*, 9(4):915–920, 2003.

[161] K. Kohler, D. Shchukin, G. B. Sukhorukov, and H. Mohwald. Drastic morphological modification of polyelectrolyte microcapsules induced by high temperature. *Macromolecules*, 37:9546–9550, 2004.

[162] S. Moya, G. B. Sukhorukov, M. Auch, E. Donath, and H. Mohwald. Microencapsulation of organic solvents in polyelectrolyte multilayer micrometer-sized shells. *Journal of Colloid and Interface Science*, 216(2):297–302, 1999.

[163] G. B. Sukhorukov, M. Brumen, E. Donath, and H. Mohwald. Hollow polyelectrolyte shells: Exclusion of polymers and donnan equilibrium. *Journal of Physical Chemistry B*, 103(31):6434–6440, 1999.

[164] K Kohler, D. G. Shchukin, H. Mohwald, and G. B. Sukhorukov. Thermal behavior of polyelectrolyte multilayer microcapsules. 1. effect of odd and even layer number. *J. Phys. Chem. B*, 109:18250–18259, 2005.

[165] R. Georgieva, S. Moya, S. Leporatti, B. Neu, H. Baumler, C. Reichle, E. Donath, and H. Mohwald. Conductance and capacitance of polyelectrolyte and lipid-polyelectrolyte composite capsules as measured by electrorotation. *Langmuir*, 16(17):7075–7081, 2000.

[166] G. B. Sukhorukov, A. A. Antipov, A. Voigt, E. Donath, and H. Mohwald. ph-controlled macromolecule encapsulation in and release from polyelectrolyte multilayer nanocapsules. *Macromolecular Rapid Communications*, 22(1):44–46, 2001.

[167] C. Dejugnat, D. Halozan, and G. B. Sukhorukov. Defined picogram dose inclusion and release of macromolecules using polyelectrolyte microcapsules. *Macromolecular Rapid Communications*, 26(12):961–967, 2005.

[168] G. Ibarz, L. Dahne, E. Donath, and H. Mohwald. Smart micro- and nanocontainers for storage, transport, and release. *Advanced Materials*, 13(17):1324–1327, 2001.

[169] A. A. Antipov, G. B. Sukhorukov, S. Leporatti, I. L. Radtchenko, E. Donath, and H. Mohwald. Polyelectrolyte multilayer capsule permeability control. *Colloids and Surfaces a-Physicochemical and Engineering Aspects*, 198:535–541, 2002.

[170] A. S. Angelatos, B. Radt, and F. Caruso. Light-responsive polyelectrolyte/gold nanoparticle microcapsules. *Journal of Physical Chemistry B*, 109(7):3071–3076, 2005.

[171] A. G. Skirtach, C. Dejugnat, D. Braun, A. S. Susha, A. L. Rogach, W. J. Parak, H. Mohwald, and G. B. Sukhorukov. The role of metal nanoparticles in remote release of encapsulated materials. *Nano Letters*, 5(7):1371–1377, 2005.

[172] Z. H. Lu, M. D. Prouty, Z. H. Guo, V. O. Golub, C. S. S. R. Kumar, and Y. M. Lvov. Magnetic switch of permeability for polyelectrolyte microcapsules embedded with co@au nanoparticles. *Langmuir*, 21(5):2042–2050, 2005.

[173] R. Georgieva, S. Moya, E. Donath, and H. Baumler. Permeability and conductivity of red blood cell templated polyelectrolyte capsules coated with supplementary layers. *Langmuir*, 20(5):1895–1900, 2004.

[174] F. Dubreuil, N. Elsner, and A. Fery. Elastic properties of polyelectrolyte capsules studied by atomic-force microscopy and ricm. *European Physical Journal E*, 12(2):215–221, 2003.

[175] R. Georgieva, S. E. Moya, H. Baumler, H. Mohwald, and E. Donath. Controlling ionic conductivity in lipid polyelectrolyte composite capsules by cholesterol. *Journal of Physical Chemistry B*, 109(38):18025–18030, 2005.

[176] I. Estrela-Lopis, S. Leporatti, S. Moya, A. Brandt, E. Donath, and H. Mohwald. Sans studies of polyelectrolyte multilayers on colloidal templates. *Langmuir*, 18(21):7861–7866, 2002.

[177] I. Estrela-Lopis, S. Leporatti, D. Clemens, and E. Donath. Polyelectrolyte multilayer hollow capsules studied by small-angle neutron scattering (sans). *Soft Matter*, 5(1):214–219, 2009.

[178] C. Dejugnat and G. B. Sukhorukov. Ph-responsive properties of hollow polyelectrolyte microcapsules templated on various cores. *Langmuir*, 20(17):7265–7269, 2004.

[179] K. Kohler, P. M. Biesheuvel, R. Weinkamer, H. Mohwald, and G. B. Sukhorukov. Salt-induced swelling-to-shrinking transition in polyelectrolyte multilayer capsules. *Physical Review Letters*, 97(18):–, 2006.

[180] R. Georgieva, R. Dimova, G. Sukhorukov, G. Ibarz, and H. Mohwald. Influence of different salts on micro-sized polyelectrolyte hollow capsules. *Journal of Materials Chemistry*, 15(40):4301–4310, 2005.

[181] J. Yang, Y. Huang, X. B. Wang, F. F. Becker, and P. R. C. Gascoyne. Differential analysis of human leukocytes by dielectrophoretic field-flow-fractionation. *Biophysical Journal*, 78(5):2680–2689, 2000.

[182] J. Ruths, F. Essler, G. Decher, and H. Riegler. Polyelectrolytes i: Polyanion/polycation multilayers at the air/monolayer/water interface as elements for quantitative polymer adsorption studies and preparation of hetero-superlattices on solid surfaces. *Langmuir*, 16(23):8871–8878, 2000.

[183] S. Leporatti, C. Gao, A. Voigt, E. Donath, and H. Mohwald. Shrinking of ultrathin polyelectrolyte multilayer capsules upon annealing: A confocal laser scanning microscopy and scanning force microscopy study. *European Physical Journal E*, 5(1):13–20, 2001.